PLASMONIC HYBRID NANOCONSTRUCTS FOR SUBWAVELENGTH MANIPULATION OF OPTICAL PROPERTIES

A Dissertation
Presented to
The Academic Faculty

by

Shuaidi Zhang

In Partial Fulfillment
of the Requirements for the Degree
Doctor of Philosophy in the
School of Materials Science and Engineering

Georgia Institute of Technology
August 2019

COPYRIGHT © 2019 BY SHUAIDI ZHANG

PLASMONIC HYBRID NANOCONSTRUCTS FOR SUBWAVELENGTH MANIPULATION OF OPTICAL PROPERTIES

Approved by:

Dr. Vladimir V. Tsukruk, Advisor
School of Materials Science and Engineering
Georgia Institute of Technology

Dr. Zhiqun Lin
School of Materials Science and Engineering
Georgia Institute of Technology

Dr. Wenshan Cai
School of Electrical and Computer Engineering
School of Materials Science and Engineering
Georgia Institute of Technology

Dr. Younan Xia
The Wallace H. Coulter Department of Biomedical Engineering
School of Chemistry and Biochemistry
Georgia Institute of Technology

Dr. Ali Adibi
School of Electrical and Computer Engineering
Georgia Institute of Technology

Date Approved: April 15, 2019

Dedicated to my family, mentors, and friends

ACKNOWLEDGEMENTS

I would like to take this opportunity to thank my advisor Prof. Vladimir V. Tsukruk, who have provided me with consistent guidance and inspiration over the last four and half years, without which I will not be able to achieve what I have accomplished today. Simultaneously, I appreciate the financial support of National Science Foundation (CBET-1401720, CHE-1506046) and U.S. Department of Energy (DE-FG02-09ER46604) for all the studies I have conducted during my PhD pursuit. In addition, I want to thank my PhD dissertation committee members: Prof. Z. Lin, Prof. W. Cai., Prof. Y. Xia, Prof. A. Adibi for their helpful suggestions and critique.

I would also like to thank all my collaborators for their vital contribution to the project we worked on, specifically: Dr. Mahmoud A. Mahmoud, Dr. Sajanlal R. Panikkanvalappil, and Mohammadreza Nazemi from Prof. M. A. El-Sayed's group for providing various plasmonic nanocrystals. Dr. Jorge L. Chávez from Dr. N Kelley-Loughnane's group for helpful discussion on surface chemistry pertinent to nanocrystal functionalization. And all the SEMA lab members, in particular, Dr. Jeffery Geldmeier for help with electrodynamic simulation; Dr. Rui Xiong for help with interfacial design of nanocomposites; Dr. Chun-Hao Lin for helpful discussion on top-down nanofabrication techniques and photonic resonator physics.

Lastly, I am deeply grateful to the unconditional support of my parents, who are courageous enough to give me the true freedom to pursue the life I aspired; to allow their only child to be separated from them by half a globe and for nearly half a decade. This is a sacrifice I can never hope to repay.

TABLE OF CONTENTS

LIST OF TABLES

LIST OF FIGURES

LIST OF SYMBOLS AND ABBREVIATIONS

ε’	real part of complex permittivity
ε”	imaginary part of complex permittivity
λ	wavelength
ACN	acetonitrile
AFM	atomic force microscopy
AuNR	gold nanorod
AuNS	gold nanosphere
CNF	cellulose nanofiber
CTAB	cetyltrimethylammonium bromide
DBR	distributed Bragg reflectors
DMF	N,N-dimethylformamide
EBL	electron beam lithography
ECP	electrochromic polymers
FDTD	Finite-difference time-domain
FIB	focused ion beam
FP	Fabry-Pérot
FSR	free spectral range
FWHM	full width at half maximum
GPC	gel permeation chromatography
LSPR	localized surface plasmon resonance
MCH	6-mercapto-1-hexanol
MTP	multiply twinned particles

NHA	nanohole array
ODT	1-octadecanethiol
P4VP	poly(4-vinylpyridine)
PAA	poly(acrylic acid)
PC	propylene carbonate
PDDA	polydiallyldimethylammonium chloride
PEG	poly(ethylene glycol)
PEI	poly(ethyleneimine)
pHEMA	poly(2-hydroxyethyl methacrylate)
PML	perfect matched layer
PMMA	poly(methyl methacrylate)
PS	polystyrene
PVA	polyvinyl alcohol
PVP	polyvinylpyrrolidone
RIS	refractive index sensitivity
RIU	refractive index unit
SAM	self-assembled monolayer
SEIRAS	surface enhanced infrared absorption spectroscopy
SEM	scanning electron microscopy
SERS	surface enhanced Raman spectroscopy/scattering
SIMS	secondary ion mass spectrometry
SPP	surface plasmon polariton
$TBAPF_6$	tetrabutylammonium hexafluorophosphate
TEM	transmission electron microscopy
THF	tetrahydrofuran

SUMMARY

Plasmonic nanostructures give rise to intriguing unconventional optical phenomena such as deep-subwavelength light focusing, precisely tunable scattering/absorption, and super-linearity enhancement. These properties could be harnessed by combining plasmonic components with functional organics into plasmonic hybrid nanoconstructs for practical applications, such as molecular sensing, advanced displays, and photonic logic processing. However, to fully realize the potential of these plasmonic hybrid nanoconstructs, critical questions on fundamental aspects of organic-inorganic assembly and their coupling behavior need to be addressed.

Therefore, the primary goal of this work is to understand some of these aspects and fill knowledge gaps regarding the efficient microfabrication and utilization of hybrid plasmonic nanoconstructs. The work is partitioned into three consecutive tasks:

- Wet chemistry synthesis and fabrication of high quality plasmonic nanostructures and compatible organic components. Emphasis is placed on ensuring the monodispersity of colloidally synthesized nanocrystals of precisely defined shapes and synthesizing electrochromic polymers with desired bandgap and solvent compatibility
- Understand the unknown reaction dynamics in common ligand exchange processes used to make and functionalize plasmonic nanostructures. This include development of advanced high-resolution experimental routines that can characterize the morphology and composition changes on the same individual nanocrystal with nm-precision as surface reaction progresses. Examine the host-

guest interaction as plasmonically active nanoparticles are embedded in functional organic matrices.

- Using knowledge gained in previous tasks to fabricate and assemble hybrid plasmonic nanoconstructs that integrates active soft components that can be modulated via external stimuli to achieve desired optical properties such as absorption modulation, directional scattering, and E-field enhancement.

Specifically, an advanced nanoscale characterization method based on scanning probe microscopy and secondary ion mass-spectrometry is developed to monitor the morphological and compositional changes on the surface of the exact same plasmonic nanocrystal as thiol-based ligand exchange reaction proceeds, leading to new discoveries on thiol-polymeric surfactant replacement reaction dynamics. Detailed characterization of nanoparticle distribution in organic matrices and corresponding electrodynamic modeling have also been combined to aid the rational design of a cellulose nanofiber-gold nanorod hybrid surface enhanced Raman spectroscopy based molecular sensing platform that outperforms traditional design by two orders of magnitude. New discoveries have also been made regarding the optical response of electrochromic polymer infused plasmonic nanohole arrays upon complex permittivity modulation: the forward and backward scattering shows drastically different response whose origin is explained by advanced electrodynamic simulation. Finally, using high resolution hyperspectral mapping and high-fidelity sub-nm resolution electrodynamic simulation, we furthered the understanding of coupling between plasmonic nanocrystals and photonic microcavities and proposed a new method that uses the near-field coupling between plasmonic nanoparticle antennas to

regulate the optical output of a plasmonic-photonic hybrid cavity, which could lead to extremely compact designs for nanolasers.

CHAPTER 1. INTRODUCTION

1.1 Plasmonic Nanostructures

1.1.1 Brief Introduction to Plasmonics

It is well known that noble metal nanostructures with characteristic dimensions below 100 nm possess several distinct optical phenomena including the guided propagation of surface plasmon polaritons (SPP) and localized surface plasmon resonance (LSPR) in the extended visible and near-IR spectral ranges (Figure 1.1).[1, 2, 3, 4, 5]

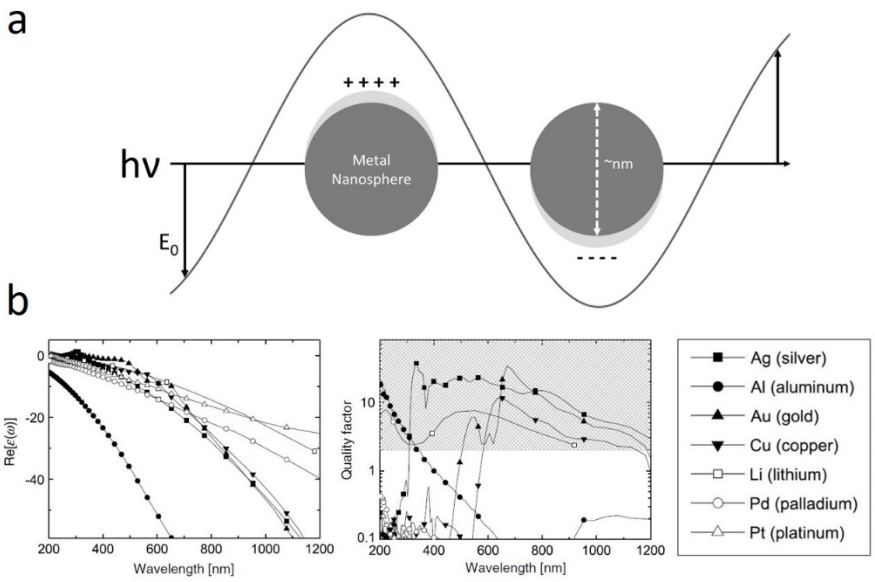

Figure 1.1 (a) The excitation of LSPR in metal nanoparticles. (b) Real relative permittivity and LSPR quality factor of several common metals in the extended visible range. Adapted from ref 8. Copyright 2009 Elsevier.

The origin of SPP and LSPR phenomena stems from the unique dielectric response of noble metals.[6, 7] Because of their high carrier concentration, metals display negative real permittivity (ε') in certain wavelength ranges depending up their electronic band structures,

thereby allowing their electrons to be excited into collective oscillation by impinging light, leading to plasmonic behavior (Figure 1.1a).[8] For example, LSPR enables noble metal nanostructures to exhibit distinct colorimetric responses to changing environments and coupling conditions and causes the dramatic enhancement seen in the surface enhanced Raman spectroscopy (SERS) and surface enhanced infrared absorption spectroscopy (SEIRAS) analysis techniques.[9,10, 11] SPP phenomena allow sensitive probing of antibody-antigen complexation on metal films and are also promising for future optical circuitry.[12, 13]

However, not every metal can be used for plasmonic applications. The strength of an LSPR response and the attenuation of an SPP depend strongly on the imaginary permittivity (ε"). While almost all metals display negative real permittivity in the certain optical range, most have a very high imaginary permittivity. Based on classical electrodynamics, it is possible to define a shape-independent quality factor $Q = \frac{\omega \left(\frac{d\varepsilon'}{d\omega}\right)}{2\varepsilon''}$, with ω representing the incident light frequency, that characterizes the strength of the resonance.[14] The second panel of Figure 1.1b depicts the quality factor of common metal LSPR in the 200-1200 nm wavelength regime. As seen, Ag and Au are the two most suitable materials for plasmonic-based applications due to their high quality factors in the visible-IR range, and these popular nanostructures will be a focus of the discussion below.

The nanoparticle size and shape also have a significant impact on the extinction properties of a nanoparticle.[15] An increase in size generally corresponds to an increase in overall extinction and a redshift of the LSPR peak wavelength. For instance, a Au sphere increasing from 10 nm to 100 nm in diameter will exhibit a 47 nm LSRP red shift.[16] Larger

nanoparticles also exhibit broader LSPR peaks due to radiative damping of their dipole oscillations.[17]

Finally, large nanoparticles may even exhibit several modes. For instance, Ag nanocubes typically exhibit a large dipolar peak and a smaller quadrupole one, but peak splitting can be induced in the dipole peak as the nanocube size is increased, which can be attributed to the separation of the absorption and scattering spectra from one another as the size is increased.[18] With these combined effects, the plasmonic peak of Ag nanocube can be seen to significantly broaden as the size is increased from 36 to 172 nm (Figure 1.2a).[19]

The shape of the nanoparticle has the largest influence on the LSPR resonances, and therefore the controlled synthesis of differently shaped nanoparticles has been of the utmost interest for the past decades.[20] Silver nanoparticles of various shapes and sizes display plasmonic resonances that span the entire wavelength range of 320-1100 nm (Figure 1.2b).[21,22,]

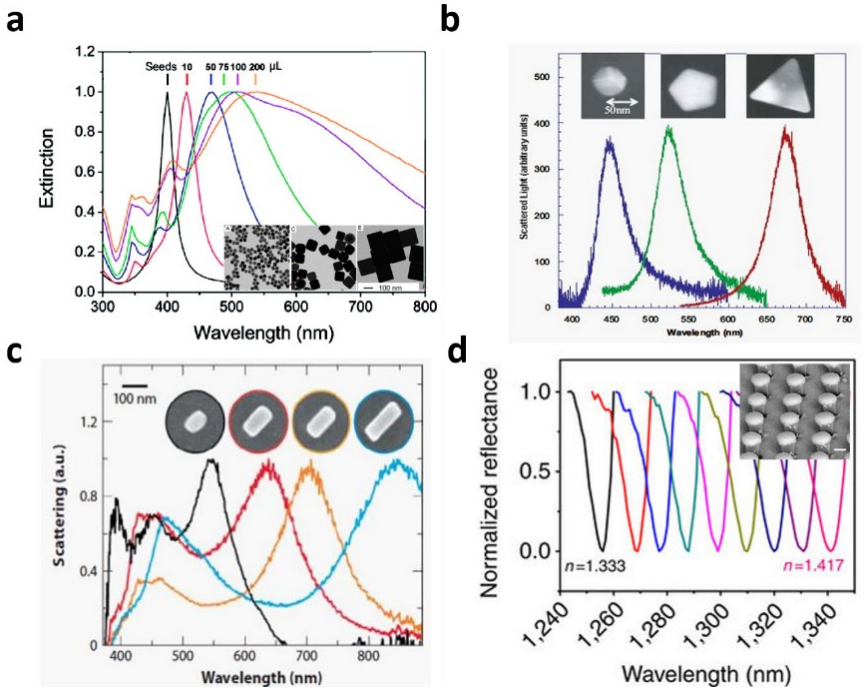

Figure 1.2 (a) The extinction spectra of Ag nanocubes as their size is increased. The insets from left to right correspond respectively with the pink, green, and orange spectra. Adapted from ref 16. Copyright 2006 American Chemical Society. (b) The extinction spectra of Ag nanospheres, pentagons, and triangular prisms of approximately the same size. Adapted from ref 21. Copyright 2002 American Institute of Physics. (c) The longitudinal LSPR of Ag nanobars redshifts as their aspect ratio is increased. Adapted from ref 28. Copyright 2006 American Chemical Society (d). The extinction spectra of a gold mushroom array as a function of the environment refractive index. Adapted from ref 29. Copyright 2013 Macmillan Publishing Ltd.

The rounding of nanoparticle edges and corners can have a drastic influence on LSPR spectra as well. In general, rounding removes regions of high charge density that can collect on sharp facets from the so-called "lightning rod effect" and results in an LSPR blue shift and the reduction of higher order modes.[23, 24, 25] Also, when a nanoparticle becomes anisotropic (i.e. high-aspect ratio nanorods), it exhibits two modes, a longitudinal mode and a transverse mode.[18, 26, 27, 20] The intensity and spectral position of these resonances depend on the aspect ratio of the particle; when a particle's aspect ratio is increased, the

longitudinal mode will redshift significantly while the transverse mode remains at the same spectral position, as seen in the case of Ag nanobars (Figure 1.2c).[28]

Another important consideration for nanoparticle plasmonic phenomena is the effect of the surrounding. Generally, an increase of the refractive index of the environment red shifts the plasmon peak wavelength, with the shift magnitude being determined by the nanoparticle's refractive index sensitivity (RIS). For a homogeneous environment, the RIS can be determined by $\Delta\lambda_{LSPR} = m\Delta n$, where $\Delta\lambda_{LSPR}$ is the change in the LSPR peak wavelength, *m* is the RIS, and Δn is the change in the refractive index of the environment (Figure 1.2d).[29] Also, adjacent plasmonic nanocrystals can have their LSPR modes coupled together in what are known as "bonding" and "anti-bonding" modes thus modulating overall spectral response depending upon the interparticle distance and the refractive environment.[8, 30]

Complex LSPR resonance modes arise in plasmonic nanoparticle clusters, anisotropic nanoparticles, and hollow nanostructures due to the coupling between narrow subradiant antibonding modes and broad superradiant bonding modes.[31, 32] With specific coupling parameters, resultant Fano resonances can be engineered to have extremely narrow spectral widths and to provide ultra-high sensitivity to the variable refractive index of the surrounding.[33, 34, 35] Additionally, nonlinear plasmonic phenomena, such as second or third harmonic mode generation, have also been used for enhanced dielectric sensing.[36, 37]

The aforementioned dielectric properties of metals also mean that incident light can lead to the formation of light propagating along the dielectric-metal interface provided that the normal momentum mismatch is compensated for by a prism or grating. SPP modes enable

a range of exciting applications such as the focusing of plasmon energy for optical lenses[38] and the ultrasensitive detection of refractive index changes caused by selective adsorption of biomolecules.[39] Also, the LSPR behavior of metal nanoparticles can couple to SPP in nearby metallic thin films to form hybridized modes with tunable electric field hot spots.[40,41]

1.1.2 Synthesis and Fabrication of Plasmonic Metal Nanostructures

The field of metal nanocrystal colloidal synthesis has progressed rapidly in recent years, fueled both by the facile nature of this process and the highly-ordered structures with well-controlled plasmonic properties it yields.[42, 43, 44, 45] Over the past decade, many different types of metal nanocrystals such as nanocubes, nanoplates, nanostars, and nanowires have been synthesized using wet chemistry approaches.[21, 46]

Colloidal synthesis relies on the chemical reduction of metal salts in solution under the presence of stabilizing surfactants.[47] The thermodynamics and kinetics of reduction reactions can be controlled by a wide range of factors including the temperature, reaction time, concentration, and stoichiometry of the reactants, types of surfactanst used, activity of the reductant, and the presence of seed crystals. Due to this variability, wet chemistry methods are extremely versatile and capable of generating a vast library of nanocrystals with different shapes and sizes. In recent years, new insights into the formation mechanisms, synthetic methods, and the role of various reactants and trace amount of impurities have helped produce nanocrystals with complex shapes while boosting their yields and improving monodispersity. Below, we provide a brief overview of chemical

synthesis of noble metal nanostructures with a focus on some of the most recent advances in the field.

The simplest version of colloidal synthesis can be accomplished in one step within a single reaction vessel and is referred to as one-pot synthesis. In this process, the reduction of metal ions in solution is achieved by a strong reductant with the additional presence of a stabilizing surfactant. Two of the most widely used and established methods for the synthesis of Au nanospheres (AuNS) are the Turkevich method[48,49] and the Brust-Schiffrin method.[50] Both approaches use $AuCl_4^-$ as a source for gold ions and use citrate and dodecanethiol as respective capping agents to stabilize the Au^0 clusters formed in solution.[51, 52]

The shape of nanocrystals can be controlled by selecting surfactants that display preferential binding for certain crystallographic facets. Notably, direct reduction of Ag ions in solution has been known to produce multiply twinned particles (MTPs) bound by low energy {111} facets.[53] However, further growth can be inhibited by the addition of a polyvinylpyrrolidone (PVP) surfactant. The PVP selectively binds to the Ag {100} surfaces and reduces the growth rate in the <100> direction, resulting in {100} capped single crystalline Ag nanocubes (Figure 1.3a, b).[53]

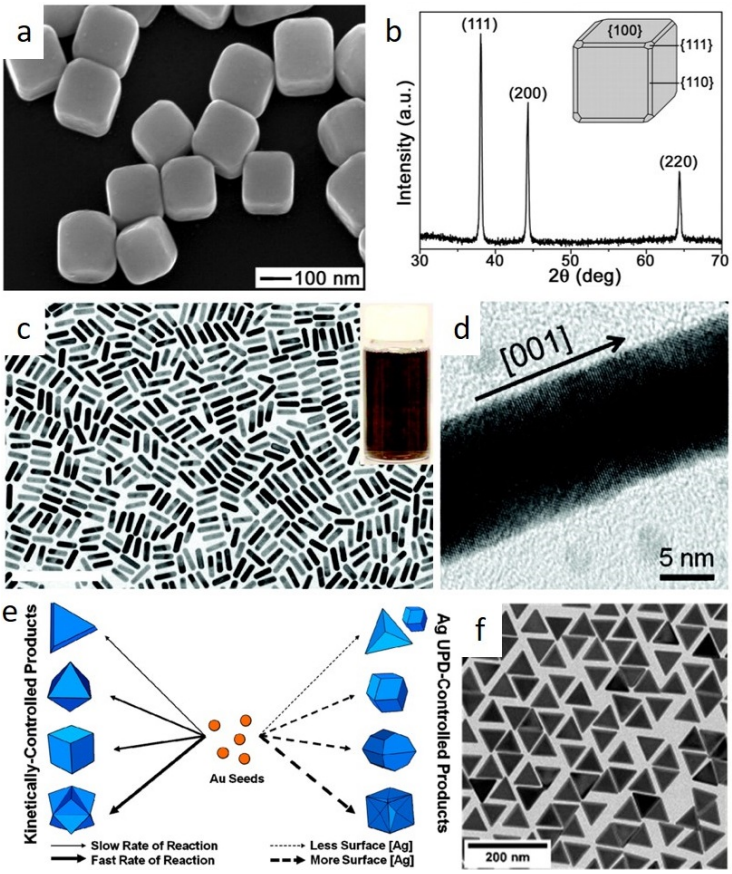

Figure 1.3 (a) SEM image and (b) XRD of Ag nanocubes synthesized by the polyol process. Adapted from ref 53. Copyright 2002 American Association for the Advancement of Science. (c) Transmission electron microscopy (TEM) and (d) high-resolution TEM (HRTEM) images of AuNRs with a high monodispersity synthesized by seed-mediated growth. Inset: photograph of corresponding solution. Adapted from ref 72. Copyright 2012 American Chemical Society. (e) Halides and silver ion influence on the eventual shape of the Au nanocrystal synthesized by seed-mediated growth. Adapted from ref 74. Copyright 2012 American Chemical Society. (f) TEM image of monodisperse Au nanotriangles. Adapted from ref 75. Copyright 2014 American Chemical Society.

This synthesis method of using polyol as both a reductant and a capping agent is very versatile and simply referred to as polyol synthesis.[54, 55, 56, 57, 58, 59] In the case of silver, a simple change of initial concentration of Ag ions to below 0.1 M in the aforementioned polyol process will result in the formation of (111) twinned pentagonal Ag nanowires.[60, 61, 62]

The simplicity of the one-pot synthesis method warranted its adoption in many early studies of plasmonic nanostructures. However, the monodispersity of the synthesized nanoparticles is limited by the duration of the initial nucleation and any procedural changes inevitably alter both the nucleation and growth processes, making one-pot synthesis highly sensitive to the environment.[63] To overcome this limitation, seed-mediated growth methods, where the nucleation of seeds and subsequent nanocrystal growth are decoupled into two separate processes, have been developed.[64] The nucleation conditions can thereby be optimized to promote seed crystals with preferable symmetries and sizes without having subsequent effects on the crystal growth. The seeds can also be purified *post hoc* using techniques such as differential centrifugation if necessary. After their synthesis, seeds are introduced to growth solutions containing metal salts with milder reducing agents that promote their growth without inducing spontaneous nucleation.

One of the most recognized uses of the seed-mediated synthesis method has been the synthesis of Au nanorods (AuNRs) with controlled aspect ratios and, consequently, tunable positions of the longitudinal and transverse plasmonic bands.[65,66] Depending on the type of seed and the presence of $AgNO_3$ in the growth solution, single crystalline and penta-twinned AuNRs can be synthesized.[67, 68, 69, 70, 71] More precise control of the nanorod length can be obtained by arresting growth at specific times, yielding highly monodisperse nanoparticles (Figure 1.3c, d).[65, 72, 73]

Besides in the creation of nanorods, seed-mediated methods have been extensively used in the synthesis of more complex nanostructures such as octahedra, cubes, and trisoctahedra. The crystal formation dynamics during the growth phase can be systematically controlled by adjusting the concentrations of ascorbic acid and halide ions.[74] Even more complex Au

nanostructures defined by high-index surfaces such as truncated ditetragonal prisms, concave cubes, and tetrahexahedra can be synthesized by introducing trace amounts of Ag^+ (Figure 1.3e).[74] Nanostructures with sharp edges and corners such as triangular Au nanoplates have also been synthesized with fine control over their dimensions (Figure 1.3f).[75] These nanostructures are actually {111} faceted truncated bitetrahedra with a twin plane in the middle parallel to the top and bottom surfaces.[74, 76] The size of these nanotriangles can be tuned within 60-150 nm by varying the amount of seeds added to the final growth solution.

Highly branched Au nanostars can be obtained by growing 15 nm PVP-coated Au seeds in N,N-dimethylformamide (DMF) solution containing PVP and $HAuCl_4$ at room temperature.[77, 78] More recent efforts have aimed to achieve a certain level of control over the branching structure of nanoparticles. Both quadruple-branched nanocrosses and highly defined symmetrical nanostars were synthesized (Figure 1.4a, b).[79, 80] Due to their higher chemical reactivity, multi-pod Ag nanocrystals can be obtained through anisotropic chemical etching of single-crystalline octapod-shaped nanoparticles (Figure 1.4c).[81, 82]

Ultrasmall Au nanoparticles (~2 nm diameter) have also been pursued recently[83, 84, 85,86, 87] These nanoclusters are in the quantum regime and exhibit molecular-like discrete electron energy levels. [88 , 89] For instance, monodisperse 2.4 nm diameter dectahedral Au nanoparticles weighing 115 kDa and containing 500±10 Au atoms have recently been reported to exhibit distinct plasmonic properties (Figure 1.4d).[84]

Moreover, smaller Au clusters stabilized by thiolates such as $Au_{36,}$[90] Au_{130},[91] Au_{133},[85] and Au_{144}[92] can be synthesized with true atomic precision, and these organized clusters exhibit

interesting transition behavior that bridges plasmonic and molecular optical responses.[86] Further variability of the plasmonic properties of noble metal nanostructures can be introduced through the synthesis of multicomponent nanocrystals such as bimetallic ones.[93] For instance, Tsao et al. showed that various Au/Ag core/shell structures ranging from cubes to octahedra can be synthesized by varying the concentration and amount of reagents (Figure 1.5a).[94] Similarly, other Au/Pd core/shell and alloyed nanostructures can be synthesized using this approach by reducing Pd onto Au nanocrystals.[95, 96, 97,98,99]

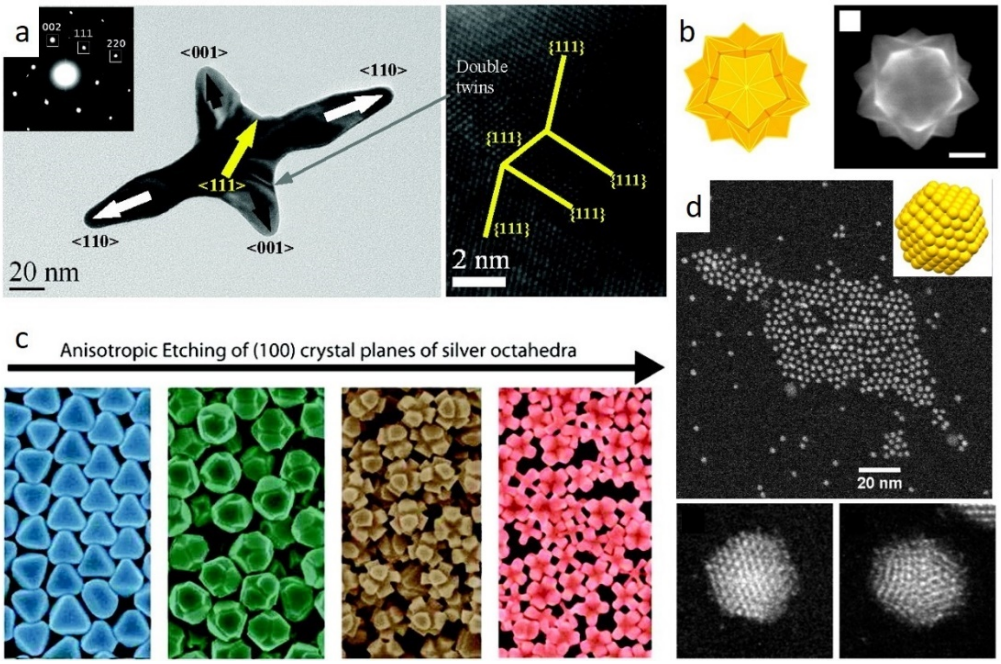

Figure 1.4 (a) TEM, select area electron diffraction (SAED), and HRTEM images of Au nanocrosses. Adapted from ref 79. Copyright 2011 American Chemical Society. (b) SEM image and corresponding geometric model of symmetric Au nanostars. Scale bar: 50 nm. Adapted from ref 79. Copyright 2015 American Chemical Society. (c) SEM images of single-crystal Ag octahedra after different chemical etching times. Adapted from ref 81. Copyright 2010 American Chemical Society. (d) TEM image of $Au_{\sim 500}(SR)_{\sim 120}$. TEM images depicting individual 5 nm particles. Adapted from ref 84. Copyright 2014 American Chemical Society.

Further bimetallic hollow structures such as nanoshells,[100] nanorattles,[101] nanocages,[102] and nanoboxes have also been actively sought within this general approach.[103] A typical synthesis method to make hollow nanostructures is through the galvanic replacement of Ag^0 by Au^{3+} on Ag nanocrystals templates to yield Au nanoshells and Au nanoframes.[100, 122]

More recent efforts have focused on the use of various capping agents to achieve the selective dealloying of Ag and the deposition of Au. For example, Hong et al. reported the synthesis of single-crystalline octahedral Au-Ag alloy nanoframes (Figure 1.5b).[104, 105] In a more complex approach, galvanic replacement can be completely inhibited by kinetic methods, thereby realizing inverted bimetallic structures such as Ag nanocubes with ultrathin Au shells (Figure 1.5c).[106]

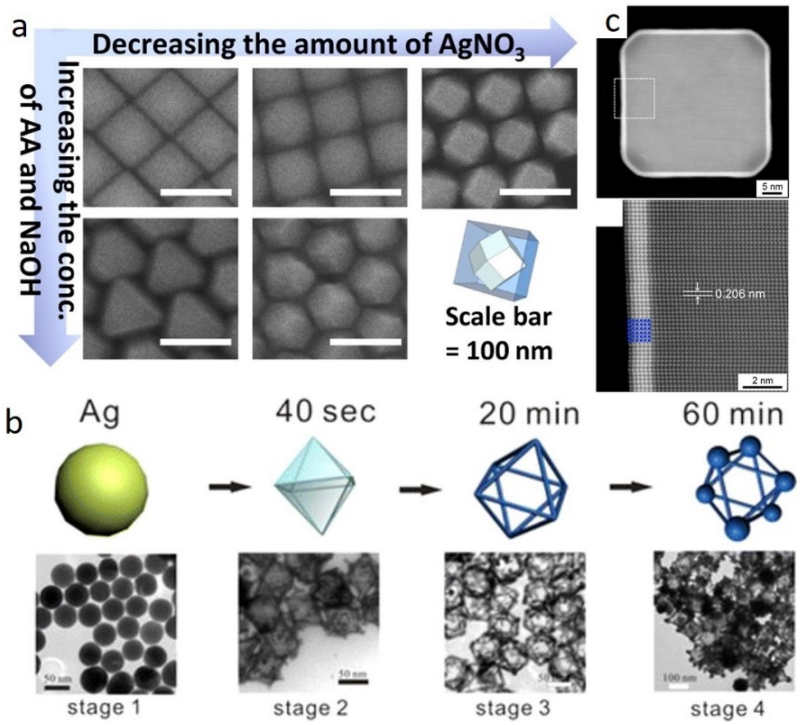

Figure 1.5 (a) SEM images of Au/Ag core/shell nanocrystals with different shapes and their formation conditions. Adapted from ref 94. Copyright 2014 American Chemical Society. (b) Schematics and corresponding TEM images of the Au-Ag nanoframe formation process. Adapted from ref 104. Copyright 2012 American Chemical Society. (c) STEM image of a Ag/Au nanocube and a higher magnification image showing six atomic layers of the Au shell. Adapted from ref 106. Copyright 2014 American Chemical Society.

On the other hand, traditional top-down scanning beam lithographic approaches such as electron beam lithography (EBL) and focused ion beam (FIB) milling are considered powerful tools for nanostructure fabrication outside of colloidal synthesis.[107] In EBL fabrication, a thin polymer resist is deposited on a substrate and subsequently exposed to a tightly focused electron beam (Figure 1.6a).

The developed resist is then used as a shadow mask for metal deposition and later lifted off, leaving behind patterned metal nanostructures that can reach sub-10 nm spatial resolution (Figure 1.6b).[108, 109, 110] In the case of FIB, a focused ion beam is used to directly

mill desired patterns on metallic substrates such as evaporated Au films or single crystal Au nanoplates.[111, 112] It is worth noting that a recent development, the sketch-and-peel method, can drastically improve the throughput of this approach (Figure 1.6c).[113]

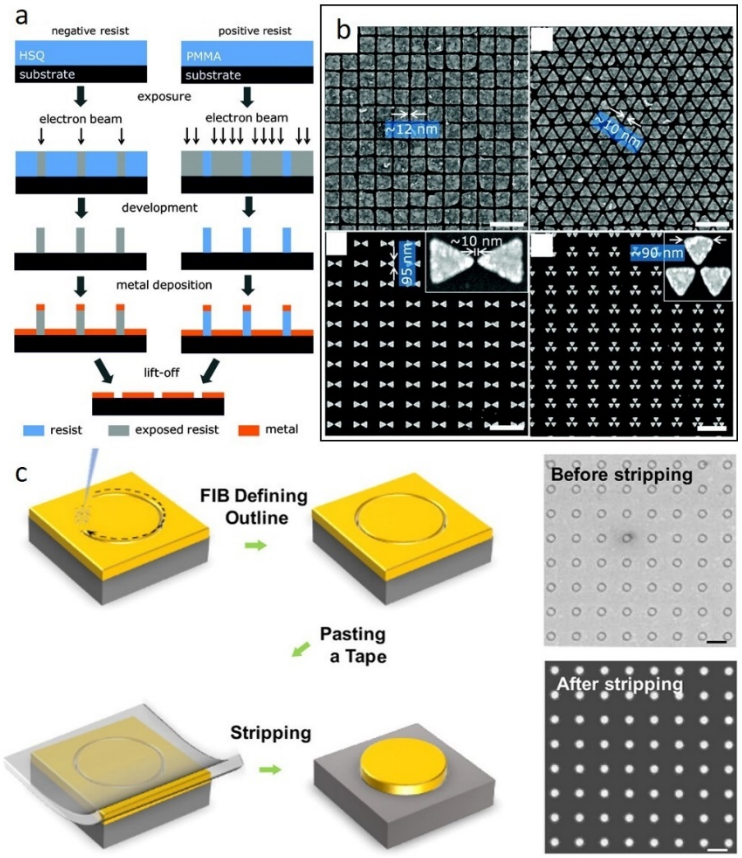

Figure 1.6 (a) A typical EBL manufacturing process using either a positive or a negative resist. (b) SEM images of different Au nanostructures with ~10 nm gaps fabricated by HSQ resist-based EBL. Scale bars: (top) 200 nm; (bottom) 500 nm. Adapted from ref 108. Copyright 2011 American Chemical Society. (c) The "sketch and peel" FIB process. Adapted from ref 107. Copyright 2016 American Chemical Society

The huge varieties of nanostructures mentioned above can serve many different functions to enable biosensing. For example, Ag nanocubes and AuNRs are the two most widely used SERS nanostructures for plasmonic enhancement of Raman signals and can be tailored to different excitation wavelengths. Ag nanowires can play an important role in

facilitating nanoelectrodes with high conductivity and flexibility.[114, 115] The nanowires can also act as antennas or waveguides to direct the propagation of plasmon polaritons, which can be used for SPR-based sensing methods.[114, 116,117, 118, 119, 120, 121] Hollow plasmonic nanostructures are highly sensitive towards surrounding refractive index changes, making them excellent reporters.[122, 123] Typical shifts in the LSPR peak per refractive index unit (RIU) for solid AuNS are 40-80 nm/RIU (RIS values) while hollow gold shells of a similar size exhibit a much higher RIS of ~400 nm/RIU.[100] Moreover, bimetallic nanostructures have also been shown to possess extremely high RIS values (500-600 nm/RIU).[124]

1.2 Functional Organics

1.2.1 Ligands

As mentioned earlier, plasmonic nanocrystals synthesized via colloidal chemistry rely on ligands for both their shape control and solution stability, without which they will spontaneously and irreversibly aggregate into agglomerates.[125] Besides stabilization, the ligands are also used to introduce various additional functionalities, such as serving as anchoring points for immobilization or further surface modification.[126] A variety of organic molecules are employed for such purposes. They can be partitioned into three distinct types based on their stabilization mechanism: electrostatic, steric, electrosteric.

Electrostatic ligands achieve colloidal nanoparticle stabilization by ionizing in the dispersion medium and selectively absorb onto the particle surface, therefore imparting a net charge on the particle and causing an electric double layer to form. Because the particles carry the same charge, the repulsive Coulombic force between them counterbalances the Van der Waals attraction, preventing aggregation.[125] Common electrostatic ligands used in

plasmonic nanocrystal syntheses include cetyltrimethylammonium bromide (CTAB), trisodium citrate, and their derivatives along with amines and thiols with charged functional groups.

CTAB is mostly used seed mediated synthesis of Au or Ag nanorods in aqueous solutions due to its ability to form micelles.[127, 128] It is understood that a bilayer forms aground the nanoparticle during growth with the ammonium polar head on both side interfacing with the metal and water respectively. The density of this bilayer and the number of Br^- counter ions attached to it are believed to vary upon growth of the nanorods, though detailed mechanism is not very well understood.[129] Trisodium citrate on the other hand directly participate in the reduction of Au salts while chelated to Au atoms. The detailed structure of citrate adlayers on colloidal gold is much less understood compared to CTAB adlayers. However, recent studies suggest citrate anions absorb initially onto Au nanoparticle via central carboxylate groups and transform from monodentate to tetradentate coordination to form a self-assembled layer mediated by hydrogen bonding under basic conditions.[130] Finally, linear thiol and amines can adsorb onto the clean metal surface to form self-assembled monolayers (SAMs) via nitrogen lone pair interaction and covalent bonding, respectively.[131, 132] Both SAMs has been well studied on ultra-clean bulk metal surfaces.[133] However, complete understanding on their bonding to colloidal metal nanoparticle is still lacking.

On the other hand, steric stabilization involves the use of non-ionic solvophilic polymers that attach to the nanoparticle surface. Since the polymer is solvophilic, long loops or tails of molecular chains extends into the solvent. The repulsion force is provided by the entropic penalties from compressing extended polymer chains into smaller volumes.[134] For

this type of stabilization to work effectively, the polymers used should have anchoring groups that attach strongly to the nanoparticle surface while simultaneously have chains that are highly soluble in the dispersion medium. Common steric ligands used in plasmonic nanocrystal synthesis include PVP, polyvinyl alcohol (PVA), and poly(ethylene glycol) (PEG). As mentioned before, PVP is extensively used in Ag nanoparticle synthesis. The oxygen atom of the carbonyl group in the pyrrolidone unit can bind strongly to noble metals via charge transfer mechanism.[135, 136] PVA and PEG do not possess native strong interaction with metallic surfaces and has to be attached via terminal or branched thiol, amine, or carboxylic acid groups.[137, 138, 139]

Finally, in the case of electrosteric stabilization, polyelectrolytes are used to encase the nanoparticles, providing both electrostatic and steric repulsion with their charged polymer chains.[140] Common electrosteric ligands used include polyanions such as poly(acrylic acid) (PAA),[141] and polycations such as poly(ethyleneimine) (PEI),[142] polydiallyldimethylammonium chloride (PDDA),[143] and poly(4-vinylpyridine) (P4VP).[144]

1.2.2 Structural and Functional Matrices

Besides interfacing with its native or modified immediate ligand shell, plasmonic nanoparticles are frequently further embedded in various extended structural organic matrices to form nanocomposites with various interesting properties. There are mainly three ways to combine plasmonic nanocrystals with polymer matrices: the nanocrystals can be either synthesized *in situ* inside an existing polymer network or blended into one afterwards. Or reversely, the organic matrix can be constructed via *in situ* polymerization around existing nanocrystal suspension.

In the *in situ* nanoparticle synthesis method, metal salts are first loaded into a polymer matrix of choice, and then the entire system is brought to a condition where the loaded salts can be reduced into metal nanoparticles.[145] This approach is very popular in the metallization of hydrogels as their natural organization contains large amount of "free spaces" which can be easily accessed via solution. Essentially, these "free spaces" can serve as "nanoreactors" to confine the reduction reaction, allowing nanoparticles to form more or less uniformly throughout the matrix.[145] For example, silver nitrate has been reduced poly[N-isopropylacrylamide-co-(sodium acrylate)] hydrogels networks to form well dispersed spherical Ag nanoparticles.[146] By the same reduction method, Ag and Au nanoparticles can be loaded into chitosan networks,[147] PVA networks,[148] and block copolymer networks.[149]

After successful application of this method in simple organic networks, it is quickly realized that additional functionalities beside simple mechanical support can be enabled by employing polymers with responsive behaviors. By reducing gold salts in poly(N-isopropylacrylamide) hydrogels, thermal response behavior can be realized.[150] On the other hand, if photo responsive polymer such as DNQ-novolac photoresist is used, the nanocomposite can be patterned using photolithography after the formation of plasmonic nanoparticles.[151] Obviously other chemical functionalities such as pH/ionic strength responsiveness can be enabled as well, but the basic concept remains the same.[145]

The problem with *in situ* synthesis is that such processes generally produces nanoparticles with much higher size dispersity than those produced using traditional means. Also, there is almost no shape control over the formation of the nanoparticles due to the lack of proper capping agent, as a result, the nanoparticles made are almost exclusively spherical or near

spherical in form. To combat this issue, majority of research in the field of hybrid plasmonic nanocomposite focused on blending plasmonic nanocrystals into functional polymer networks post nanocrystal synthesis and purification. In the blending approach, the ligand layer encasing the nanoparticles can be carefully engineered to mediate the interaction of nanoparticle with the organic matrix. If properly managed, not only can they avoid nanoparticle aggregation and phase separation, but also allow controlled heterogenous distribution.[145, 152] For example, by varying the ligand type, nanoparticles can be preferentially dispersed in one domain of block-co-polymers, forming plasmonically active periodic morphologies.[153]

Using the blending method, nanoparticles with precisely engineered size, shape, and plasmonic response have been successfully incorporated into organic matrices of all sorts of mechanical, thermal and dielectric properties for various functionalities. For instance, Au nanoparticle and merocyanine were incorporated into PEG diacrylate crosslinked PEG methyl ether methacrylate gel to construct light controlled self-erasable information storage medium.[154] Similarly, AuNR has been loaded into PVA film as laser writable film.[155] Both AuNS and AuNR have been embedded into poly(methyl methacrylate) (PMMA) films to fabricate plasmonic arrays with specific optical response.[156] Ag nanoparticles have been impregnated into poly(2-hydroxyethyl methacrylate) (pHEMA) for holographic and sensing applications.[157, 158] Naturally occurring polymeric matrices such as agarose, gelatin and collagens have also seen use as plasmonic nanocrystal embedding substrate.[159, 160, 161] Multiple other systems are also developed on matrices not listed here, interested readers are referred to recent published reviews.[162, 163]

One particular organic matrix, electrochromic polymers (ECP), are worth mentioning, as these polymers dielectric responses that are based on their oxidation state, some of which are reversibly accessible by applying external electric potentials. These include but not limited to: polyaniline, polythiophenes, polypyrroles, poly((alkylenedioxy)benzene)s, poly(phenylenevinylene)s, polyselenophenes and their derivatives.[164, 165] Combination of ECP with plasmonic nanoparticle is also frequently done via the third incorporation method: *in situ* polymerization. Because oscillation conditions of LSPR of nanoparticles depend heavily on the dielectric environment, the ability to quickly and reversibly modulate complex permittivity of the matrix surrounding the plasmonic nanoparticles is invaluable to achieving electrically tunable plasmonic response in hybrid nanoconstructs.[166, 167]

1.3 Integration of Plasmonic Nanostructures with Functional Organics

1.3.1 Surface Functionalization Chemistry

Noble metal surfaces can be readily functionalized by thiol ligands through strong sulfur-metal bond interactions to form SAMs.[168, 169] By employing alkanethiols with different terminal groups, metallic surfaces can be converted to have a wide range of surface chemistries.[170] In the context of surface activation for organic layer integration, these modifications demonstrate that employing different alkanethiols results in adlayers of different packing densities and dielectric properties that can be utilized to tune the final surface accessibility.

The surface physiochemical properties of plasmonic nanostructures are of significant importance to their further functionalization. For instance, the existence of adsorbate

organic species or natural oxide layers can lead to drastically different surface chemistries for the same nominal "bulk" composition. Yet too often, the practical surface properties and morphologies of nanostructures are simply overlooked in designing conjugated biorecognition matrices.

Moreover, with the wide adoption of bottom-up chemical synthetic approaches, as-synthesized plasmonic nanostructures may themselves possess complicated surface chemistries. Depending on the synthesis procedure, as-fabricated nanoscale metallic surfaces can be contaminated with residual reagents such as surfactants (intentional or unintentional) and catalysts, which is especially an issue for nanocrystals synthesized by wet-chemistry methods. As mentioned in Section 1.2.1, Various surfactants and shape-controlling agents are often added in order to stabilize the nanocrystals in solution and to control the growth kinetics of different facets. Generally, several washing steps conducted after synthesis are intended to remove the bulk of extra reagents present in solution but cannot effectively remove the firmly adsorbed affine layers.

For this reason, synthesis residual materials must be considered when conducting surface modification treatments. For example, a popular stabilizing agent for Au nanocrystal synthesis, citrate anions, was recently found to display strong resistance to desorption under thiol functionalization.[171] Exposure of citrate-stabilized ~40 nm Au nanoparticles to alkyl and aryl thiols yielded only 50-65% surface coverage with thiol SAMs. It was suggested that citrate anions readily form dihydrogen bonded species on the Au surface and consequently form a stable network that is resistant towards thiol displacement.[171]

Likewise, the presence of CTAB bilayers on as-synthesized Au nanorods poses a significant challenge to their subsequent functionalization with synthetic and biological ligands. The persistence of CTAB coverage on the {100} and {110} side faces of Au nanorods under thiol treatment has been frequently reported.[172, 173, 174] Often, such partial exchange is necessary to maintain the solubility of metal nanocrystals for solution-based applications. For complete functionalization of Au nanorods while avoiding irreversible aggregation, charged thiol systems such as 3-Amino-5-mercapto-1,2,4-triazole or two-step thiol-PEG-stabilized ligand-exchange processes can be used.[175, 176] Still, the residual amount of CTAB remaining on nanorod surfaces after treatment is usually unknown and difficult to determine.[177] Additionally, PVP used in polyol synthesis has been detected in SERS studies even after a 60 min exchange reaction by cysteamine and thiolated PEG.[178]

The existence of these synthetic residuals can have a significant impact on the performance and functionality of the underlying nanostructures and behavior of grafted bioconjugated components.[179] For example, the native oleylamine capping agents on metallic nanocrystals has been shown to significantly reduce their electrochemical active surface area (EASA),[180, 181] which can adversely influence their use in electrochemical-based biomolecular sensors. In fact, Wilson et al. demonstrated that a CTA^+ surfactant layer effectively blocks electrogenerated chemiluminescence (ECL) reactions on single Au nanowire electrodes.[182] Moreover, CTAB is also known to be cytotoxic, meaning its continued existence on reporter surfaces even in trace amounts may limit their use in cellular and *in vivo* environments.[183]

These examples suggest that the real surface and interface conditions of colloidal nanocrystals are often affected by the existence of various surface agents used in their

synthesis and during storage that must be taken into account for their organic functionalization.[179] Capping agents on colloidal metallic nanocrystals often cause difficulties in subsequent functionalization and induce adverse effects on the desired performance. Thus, such effects must be considered during the functionalization of plasmonic nanostructures, and appropriate surface chemical reaction or cleaning methods should be adopted.

1.3.2 Directed Assembly of Colloidal Nanostructures

Unique nanoscale properties can also stem from the near-field coupling of plasmonic modes of nanostructures when they are placed in close proximity and enable techniques such as field-enhanced spectroscopy and photochemistry that are vital to molecular sensing.[184] Thus, in this section, we discuss in detail the assembly of plasmonic nanocrystals with different shapes and sizes into different spatial configurations.

For example, monodisperse polyhedral nanocrystals can be readily assembled into monolayers with different packing densities at the water-air interface using the Langmuir-Blodgett (LB) technique (**Figure 8a-c**).[185] The type of the superlattice formed depends on the physical dimension of the nanocrystal and the surface pressure. At relatively low surface pressures, the nanocrystals adopt an ordered hexagonal superlattice structure due to hard-sphere interactions, with the collective plasmon properties of the film being characterized by distinct long-range order and the formation of corresponding “lattice modes”. As the surface pressure increases, close-packed islands of nanocrystals start to nucleate, and these islands give rise to intense plasmonic coupling at local hot spots rather than promoting a coherent optical response from the entire monolayer lattice. Further

compression results in the entire film coalescing into a uniform metallic structure (**Figure 8a-c**).

Such uniformly packed films have been shown to support propagating surface plasmons similar to those observed in continuous metal films with non-localized plasmonic modes.[185] Au or Ag nanorods can self-align and assemble into densely packed 3D structures upon solvent evaporation. [186] Pietrobon et al. showed that pentagonal Ag nanorods can be assembled into hexagonal close-packed 3D layers resembling layered smectic mesophases (**Figure 8d**).[187]

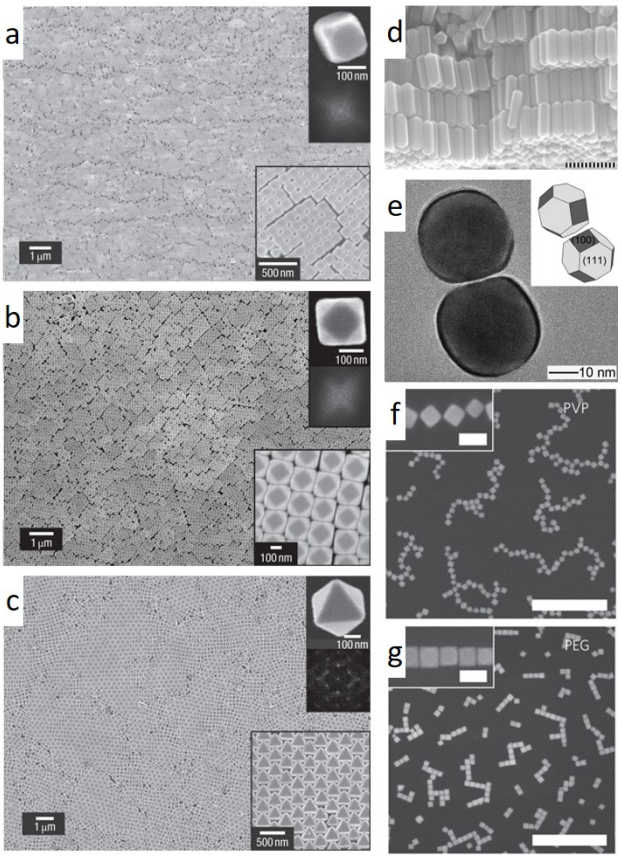

Figure 1.7 SEM images and Fourier transforms of closely packed monolayers of Ag (a) nanocubes, (b) cuboctahedra, and (c) octahedra. Adapted from ref 185. Copyright 2007 Macmillan Publishing Ltd. (d) SEM image of densely packed Ag nanorods. Adapted from ref 187. Copyright 2009 American Chemical Society. (e) TEM image

of a Ag nanosphere dimer. Adapted from ref 188. Copyright 2009 American Chemical Society. SEM images of Ag nanocube chains assembled by polymer surface modification with (f) edge-edge and (g) face-face configurations. Adapted from ref 190. Copyright 2012 Macmillan Publishing Ltd.

Direct methods such as bifunctional chemical linkage have been demonstrated to result in well-controlled dimers with nanoscale gaps (**Figure 8e**). [188, 189] Later, Gao et al. successfully assembled ~80 nm Ag nanocubes grafted with hydrophilic polymers into self-oriented 1D chains by spontaneous phase segregation within a polystyrene film (**Figure 8f, g**).[190] Assemblies of more complex heterostructures composed of two or more types of nanocrystals have been demonstrated by deploying molecular linkers such as p-aminothiophenol (**Figure 9a)**.[191]

In a different approach, concentrated nanoparticle solutions can be drawn over hard recess templates while the solvent evaporates, and the particles will be driven into these recesses by capillary forces, or in case of a tilted substrate, by gravity.[192, 193, 194] For example, by tuning the size and depth of the pre-patterned circular holes on a Si substrate, Ag octahedra clusters with different arrangements can be fabricated, allowing the reproducible assembly of well-defined and strongly coupled plasmonic 3D nanostructures with precise placement of components (**Figure 9b**).[194]

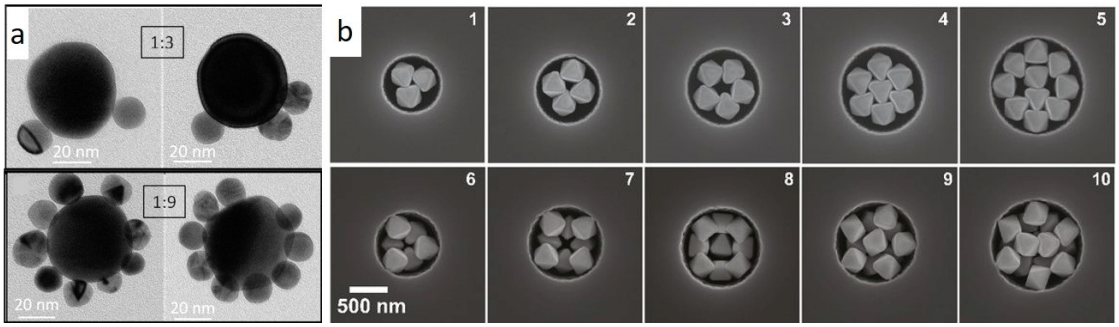

Figure 1.8 (a) TEM image of Au core-satellite heterostructures assembled at different stoichiometries. Adapted from ref 191. Copyright 2012 American Chemical Society. (b) SEM images of Ag octahedra packed into circular pits of varying diameter and depth. Adapted from ref 194. Copyright 2013 National Academy of Sciences of the United States of America.

An alternative, facile method of producing periodic linear assemblies of plasmonic nanoparticles is to use the relaxation wrinkles made by plasma etching stretched polydimethylsiloxane (PDMS) stamps as elastomeric templates (**Figure 10a**).[195] Such regular templates enable directed assembly of ~80 nm diameter Au nanoparticle into linear chains of various widths by simple spin coating, after which the resulting structures can be transferred onto other substrates by contact printing (**Figure 10b**).[195] Muller et al. has shown that post-assembly growth of close-packed Au nanoparticle monolayers can be used to fabricate gradient plasmonic arrays (**Figure 10c**).[196,196] This approach yielded a large-area plasmonic array with gradual changes in apparent color due to increasing Au nanoparticle sizes and decreasing inter-particle distances depending on the amount of time the nanoparticles had spent in the growth solution (**Figure 10d**).[196]

More complex assemblies of nanocrystals into higher-order structures can be realized by the modification of their surface with the use of DNA-directed assembly.[197] In this method, the nanocrystal surfaces are functionalized with single strand DNA sequences, and these functionalized nanocrystals are then used for assembly with either nanocrystals

functionalized with complimentary DNA strands or with a DNA origami scaffold. Because DNA hybridization is highly specific and programmable, the assembly of sophisticated and precisely defined nanostructures such as 3D chiral plasmonic pyramids,[198] nanohelices,[199] and AuNR dimers[200] can be achieved.

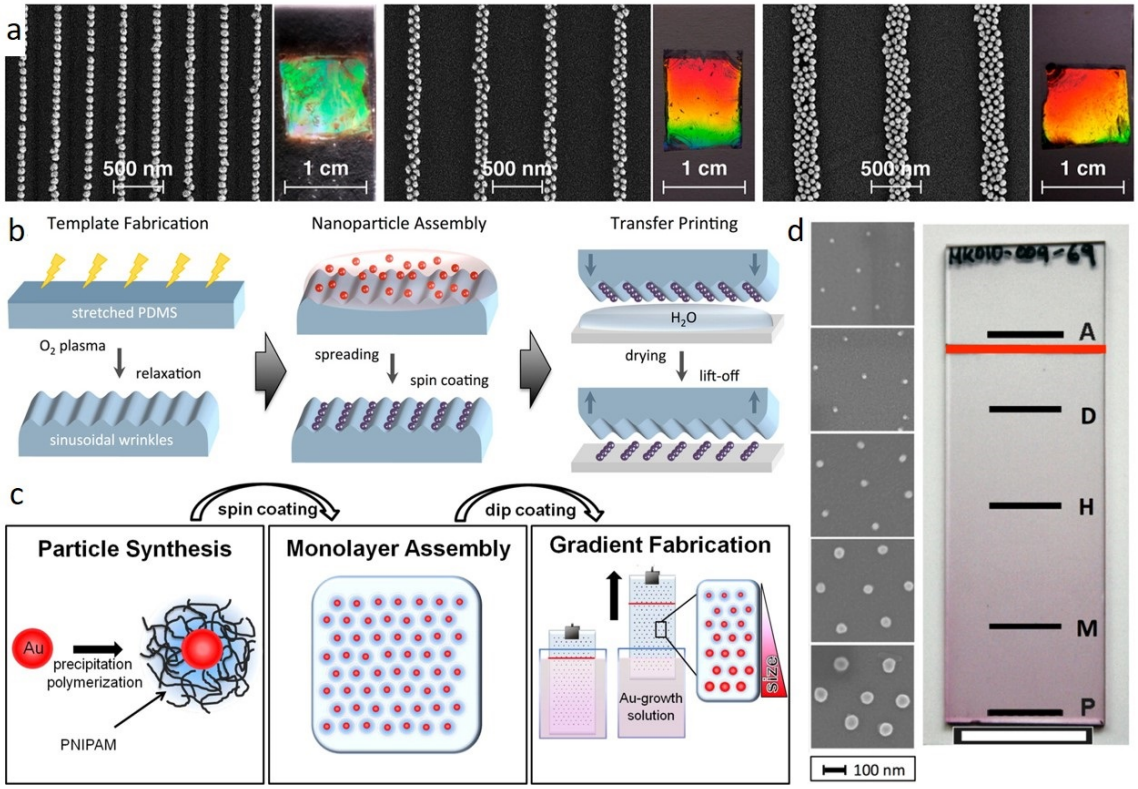

Figure 1.9 (a) SEM and optical images of assembled Au nanoparticle chains. (b) The wrinkle-assisted assembly process of the nanoparticle chains. Adapted from ref 195. Copyright 2014 American Chemical Society. (c) The fabrication of gradient plasmonic arrays. (d) Photograph of the gradient plasmonic array and corresponding SEM images from each line position. Adapted from ref 196. Copyright 2014 American Chemical Society.

Finally, precise positioning of individual nanocrystals can be accomplished by direct mechanical manipulation with multiple-probe nanomanipulators composed of sharp (tip radius <50 nm) tungsten probes mounted on individual triple-axis stages inside a high-resolution SEM.[201] The motion of the probes can be independently controlled with a

precision down to ~5 nm via fine actuators. With such a tool, nanocrystals can be placed at arbitrary locations through either push contact or electrostatic interactions.

Lately, 3D additive manufacturing has also been reported as an alternative approach for the direct fabrication of complex structures.[202, 203, 204] This approach can be a promising way to create assemblies of plasmonic structures or to even build active hybrid nanoscale metamaterials. The 3D printing of nanoparticles has vastly improved over recent years, although high spatial resolution at the nanoscale remains a challenge.[205, 206, 207] However, this technique has great potential for future nanoscale biosensing if the spatial resolution can be significantly improved and the low throughput issue can be resolved to a degree that allows efficient scaled production.[208, 209, 210, 211, 212, 213]

1.4 Summary of Present Challenges

It is evident that organic-inorganic hybrid plasmonic nanostructures hold great promise for future application in a wide range of areas including molecular sensing and nanophotonic circuitry. However, several critical problems need to be resolved if these complex nanoconstructs are to see wide practical applications.

First, there is a serious lack of understanding on the nanoscale surface chemistry happing at the inorganic-organic interface, especially for colloidally synthesized nanocrystals. Even fundamental aspects such as bonding mechanism and charge transfer between organic ligand and noble metals are not completely understood. Much less is known about the specific configuration ligand molecules adopt on the surface of these plasmonic nanostructures. Many higher-level structures are constructed based on the assumption that ligand morphology will be the same as derived by studies conducted on ultra clean metallic

surfaces under vacuum. However, as outline in previous sections, more and more evidences suggest, both the nanoscale curvature of the plasmonic structure and the initial condition of the metallic surface can have a significant impact on the physiochemical property of the hybrid nanoconstruct, especially considering such constructs function in the nanoscale regime where, unlike in bulk devices, nm-sized imperfections might render crucial component inoperable.

Secondly, despite the abundance of reports on novel systems that combines plasmonic nanostructures with functional organic matrices, the construction of hybrid systems based on rational design and optimization to increase device robustness remains rare. For example, in the field of molecular sensing, plasmonic nanostructure embedded in organic matrices have clocked many impressive metrics when operated in simple environment. However, in practical environment, they still face huge problems in terms of selective analyte retainment, substrate noise, and repeatability. Additionally, a lot of reported systems are based on stochastic assemblies or absorption process in which little or no nanocrystal positioning control is present. This either leads to extremely inefficient use of high-quality plasmonic nanocrystals or poor performance. Thus, a lot remains to be explored in the deterministic assembly of plasmonically active nanostructures and functional organic matrices that allows both components to be used efficiently.

Finally, even higher-level integrations such as the coupling behavior of hybrid plasmonic systems to external optical/electrical inputs such as assembly with photonic microcavity or electrochromic polymer remains to be systematically understood. For instance, shape, size, and interparticle coupling of plasmonic nanoparticles and their relative position to other photonic components such as microcavity, photonic crystals, functional dielectrics, and

gain medium can lead to dramatically different optical field distributions, which will in return cause light to interact differently with different components. Such deeply coupled system will allow an extreme range of optically or electrically addressable tunability. Systematic understanding of hybrid structures at this level may give rise to intriguing optical phenomena that are of practical interests.

CHAPTER 2. RESEARCH GOALS, OBJECTIVES, AND OVERVIEW

2.1 Research Goals

The ultimate goal of this study is to develop an understanding of fundamental light-matter interaction in plasmonically active inorganic-organic hybrid composites and structures. This goal is advanced by a step-wise systematic approach as illustrated in Scheme 2.1. Firstly, on the individual element level, plasmonic nanostructure with desired properties are obtained by tuning their size, shape and material while appropriate organic molecules are selected for various functionalities such as nanofiltration or electrochromism. Subsequently, research effort is focused on the understanding of the coupling and cooperative interactions between these two components. Aspects like surface chemistry, plasmonic near field coupling, and dielectric environment modulation are investigated using various advanced characterization techniques such as nanoscale morphology monitoring. Specific emphasis is placed on understanding associated fundamental nanoscale phenomena. This effort is heavily aided by electrodynamic simulations both to elucidate properties that are difficult to obtain experimentally such as E-field distribution, and to optimize subsequent experimental design. Finally, based on knowledge gained from completing previous tasks, novel plasmonic hybrid nanoconstructs are assembled using microfabrication techniques and their structural and optical properties are thoroughly characterized by advanced metrology. The knowledge derived is extremely useful in aiding the design of advanced deep-subwavelength scale optical components for molecular sensing and nanophotonic applications (Scheme 2.1).

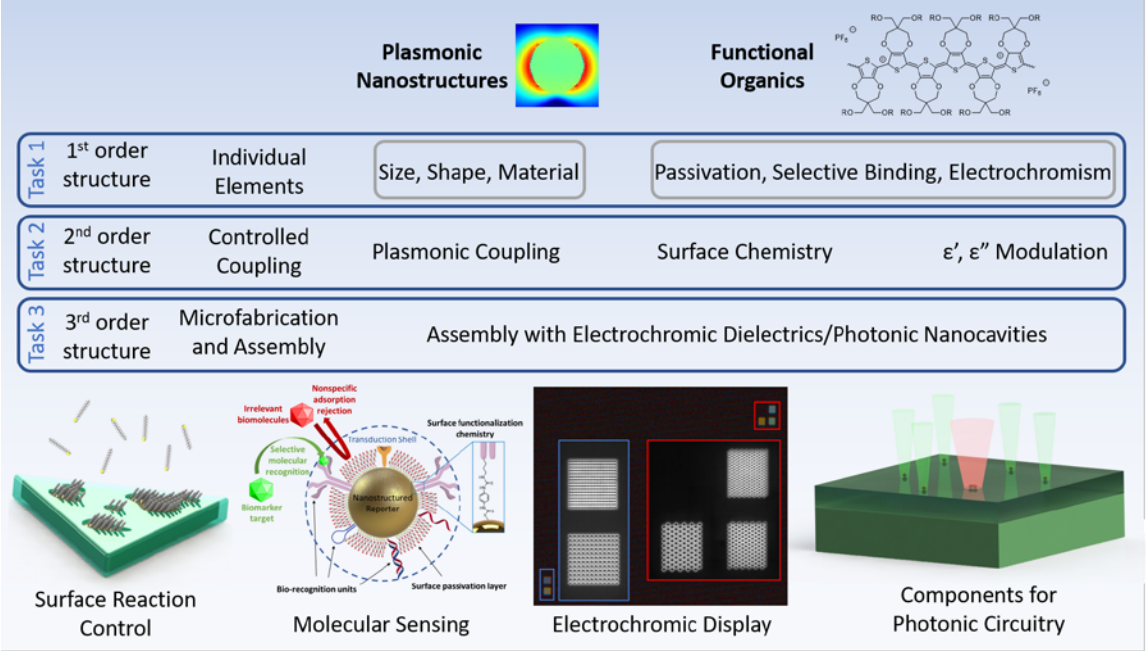

Scheme 2.1 Schematic illustration of systematic research approach to understanding and engineering the optical responses of plasmonic hybrid nanostructures

2.2 Technical Objectives

The primary goal of this work can be partitioned into three tasks: synthesis of plasmonic nanostructures and functional organic molecules (Task 1), investigation of fundamental aspect associated with coupling between components (Task 2), and examination of novel hybrid nanoconstruct fabricated based on knowledge gained from previous tasks (Task 3).

Specially, Task 1 seeks to optimize the wet chemistry synthesis of plasmonic nanocrystals, top-down lithographic fabrication of periodic plasmonic nanostructures, and chemical synthesis of functional macromolecules so high-quality components can be obtained for subsequent investigations.

Task 2 seeks to understand the fundamental interactions between plasmonic nanostructures and functional organic components so more advanced nanoconstructs could be built based

on rational design. Aspects such as the coupling between individual plasmonic nanostructures, the surface chemistry on metallic nanocrystals, and the effect of complex permittivity modulation initiated by organic components on the plasmonic response of metal nanoconstructs are to be investigated.

Task 3 seeks to assemble plasmonic nanostructures and functional organic components into novel hybrid structures using microfabrication techniques based on knowledge gained from Task 1 and Task 2. And subsequently to explore and control interesting optical properties that arise from the cooperative interactions between different elements in the plasmonic hybrid nanoconstruct.

Specific objectives are listed below:

Task 1: Synthesis of plasmonic nanostructures and functional organic molecules:

- Synthesize high quality single crystalline Au nanoplates with large flat top surfaces for the investigation of surface functionalization chemistry reactions on colloidal nanocrystals.
- Synthesize highly monodisperse plasmonically active gold nanorods and nanospheres with well-defined ligand layers to improve wet chemistry assembly with functional organic components.
- Optimize the parameters used in FIB fabrication such as current, acceleration voltage, ion lens configuration, and beam dwell time.
- Select and modify novel electrochromic polymers that have desired bandgap, solvent compatibility, and chemical stability.

Task 2: Fundamental analysis on controlled coupling:

- Develop high resolution morphology and composition characterization method to monitor the functionalization dynamics on the surface of the exact same nanocrystal with nm-precision.
- Investigate the near field coupling between plasmonic components in organic matrices and how the resulting electromagnetic field distribution affects optical properties.
- Examine and understand the optical response of plasmonic nanostructure upon modulation of dielectric environment via electrodynamics simulation.

Task 3: Microfabrication and assembly of novel hybrid plasmonic nanoconstructs:

- Guided by previous experimental results and electrodynamic modeling, fabricate high-performance SERS-based hybrid sensing platforms by efficiently assembling plasmonic nanostructure with polymeric matrices resulting in desired organic-inorganic interfaces and nanoparticle distribution.
- Guided by previous experimental results and electrodynamic modeling, assemble novel plasmonic hybrid nanoconstructs that incorporates sophisticated components such as electrochromic materials or photonic microcavities using microfabrication techniques.
- Using correlated high resolution structural and optical characterization, aided by advanced electrodynamic modeling, to systematically study new optical phenomena that arise from the cooperative interactions between different components within the newly fabricated hybrid nanoconstructs.

2.3 Organization and Composition of Dissertation

Chapter 1 reviews the general concept and recent literature on the development of hybrid plasmonic nanostructures. The synthesis and fabrication of plasmonic nanostructure and functional organic components are introduced, along with some fundamental physics on plasmonics. Afterwards, past research on assembly and integration of these two components to form hybrid nanostructures are presented.

Chapter 2 outline the goals and objectives of this research. The objectives are grouped into three sequential tasks. A directory schematic is included to illustrate the systematic approach of the entire project. Short synopsis regarding each chapter are also provided.

Chapter 3 outlines the synthesis/fabrication techniques and general characterization methods used in this research. Some of the syntheses described are done by collaborators as noted in section 3.X. Materials used and details regarding specific experiments that are not generically applicable are included in relevant sections in respective chapters.

Chapter 4 describes direct high-resolution monitoring of an evolving mixed nanodomain surface morphology during thiol adsorption on PVP-stabilized single crystal gold nanocrystals. Revealing the thiol adsorption and replacement dynamics to be much more complex than a simple complete substitution of the initial polymer ligand. The ligand-exchange dynamics and the unusual equilibrium morphology revealed provide important insights into both displacement dynamics of surface-bound molecules and the nanoscale peculiarities of surface functionalization of colloidal metal substrates.

Chapter 5 demonstrates that cellulose nanofiber (CNF) biomaterials with high transparency and mechanical robustness can be combined with gold nanorods to form a multifunctional porous membrane for dual-mode SERS detection of both small molecules and cells. Upon drastically lowering the spectral background noise and utilizing nanofiltration, the plasmonic CNF membranes reported show significantly improved SERS sensitivity and detection fidelity as compared to traditional metal, metal oxide, synthetic polymer, and paper SERS substrates.

Chapter 6 report the observation of peculiar and drastically different forward and backward scattering behavior of polymer-infused nanohole arrays (NHAs) when a surrounding electrochromic polymer matrix was subjected to electrical potential, thereby changing the permittivity of the environment. Forward scattering at normal incidence angle of the NHAs is dominated by the extinction of the polymer coating, while concurrently monitored backward scattering at a highly oblique angle showed significant red-shifting in addition to attenuation.

Chapter 7 report the fabrication of a hybrid plasmonic-photonic cavity whose output mode can be selected by different geometrical configuration of nanoscale plasmonic resonators. The hybrid cavity has a Fabry-Pérot like configuration with SiO_2/Si dielectric interface at one end and plasmonically active Au individual or coupled nanospheres (AuNS) on the other end. The behavior of this hybrid antenna can be altered by coupling two AuNS together to form a dimer, allowing different mode output to be selected. Potential for such hybrid cavities to incorporate gain mediums is also demonstrated, as its prospective application would be for localized low threshold lasing used in photonic nanocircuits, near field spectroscopy and molecular sensing.

Chapter 8 summarizes the conclusions of this study from preceding chapters and provides a general discussion on the significance of this research and its broader impact. Implications for future research are also outlined.

CHAPTER 3. EXPERIMENTAL METHODS

This chapter lists common fabrication methods and characterization techniques used in this work. Specific materials and modification to common procedures pertinent to individual studies are listed in experimental details in respective chapters

3.1 Synthesis of Plasmonic Nanocrystals

3.1.1 Au Nanoplates

Single crystal colloidal Au nanoplates were synthesized according to polyol process previously reported.[214] Typically, 110 mg of PVP was mixed with 10 mL ethylene glycol in a scintillation vial and magnetically stirred for 20 min. 200 µL of 250 mM $HAuCl_4$ aqueous solution was added to the mixture, after which, the vial was capped and heated to 120 °C in oil bath without ambient light. After approximately 12 hrs of reaction, triangular and hexagonal Au nanoplates with edge length from 15 µm to 25 µm and thickness from 30 nm to 200 nm were formed. These were collected from solution, washed with ethanol for 3 times, and re-dispersed in pure ethanol for future use.

3.1.2 Au Nanorods

The AuNRs were synthesized according to a seed-mediated growth technique previously reported in the literature.[215] First, the gold seeds were prepared: in a 30 mL vial, 2.5 mL of 1.0 mM aqueous solution of $HAuCl_4$ was mixed with 5 mL of 0.2 M aqueous solution of CTAB. Then, under stirring, 0.6 mL of 10 mM ice-cold $NaBH_4$ solution was added. The seeds were formed after 5 min of stirring. The growth solution was prepared by mixing 400

mL of 1.0 mM HAuCl4 aqueous solution with 400 mL of 0.2 M CTAB in a 1 L flask. 24 mL of silver nitrate (4.0 mM) was then added, followed by 5.6 mL of 78.8 mM ascorbic acid. The AuNRs were obtained by adding 0.64 mL seed solution to the growth solution and leaving the mixture to react overnight in accordance with procedures reported in the literature. [66, 215] The as-synthesized AuNRs were centrifuged three times at a speed of 6000 rpm to remove the excess CTAB.

3.1.3 Au Nanospheres

AuNSs were prepared by a modified version of the seed-mediated method reported in the literature.[216] Briefly, the seed nanoparticles were prepared by adding 600 µL of an ice cold 10 mM $NaBH_4$ solution to 250 µL of $HAuCl_4.3H_2O$ (10 mM) dissolved in 7 mL of 100 mM CTAB solution under vigorous stirring for 2 minutes. Afterwards, 0.40 mL of tenfold diluted seed solution allowed to grow for 8 h in a growth solution. The growth solution was prepared by mixing $HAuCl_4.3H_2O$ solution (10 mL, 0.01 M) with CTAB solution (80 mL of 0.1 M CTAB solution dissolved in 400 mL of DI water) followed by adding 60 mL (0.1 M) ascorbic acid. This solution was aged for 3 weeks under room temperature for the nanocrystals to reach equilibrium shape and the resultant AuNSs were purified by centrifugation (8000 rpm for 10 min) and re-dispersed in Nanopure water.

3.2 Focused Ion Beam Milling (FIB)

FEI Nova 200 NanoLab DualBeam^{TM}-SEM/FIB is used for FIB patterning. Specific patterns were etched by $^{69}Ga^{+}$ ion beam operated at 30 kV 10pA following corresponding bitmap files in a point by point fashion. Specifically, a dwell time was set, and the beam was blanked at points where no etching was supposed to occur.

3.3 Optical Microscopy

Optical microscopy images (brightfield/darkfield) were taken using either a Leica DM4000M microscope with a Leica DFC480 camera or an Olympus BX51 microscope (CytoViva hyperspectral scanning system, see below) with a Dagexcel-M Digital Firewire camera.

3.4 Hyperspectral Imaging

The extinction spectra of NHAs and spectral mapping were acquired by CytoViva hyperspectral scanning system with a SPECIM Imspector V10E spectrograph (30μm slit width, spectral range: 400–1000 nm, dispersion: 97.5 nm/mm, spectral resolution: 2.8 nm) coupled with a PCO.pixelfly camera using a 50× (NA = 0.8) objective which has a fixed ~73° incidence cone when used in dark field mode. All element mounted on an Olympus BX51 microscope. A Fiber-Lite DC-950 halogen lamp is used as the light source. The Lamp spectrum is collected in the transmission setup without any substrate. All the spectra were collected at max output of the lamp and normalized by dividing the lamp spectrum.

3.5 Atomic Force Microscopy (AFM)

AFM scans were carried out using Icon AFM (Bruker). Silicon tip with spring constant of 9.53 N/m (XSC11 Cantilever C, MikroMasch) was operated in the tapping mode in air at 0.45-0.75 Hz scan rate and at 90° scan angle. Scan size ranges from 20 μm × 20 μm to 500 nm × 500 nm at 512 × 512 or 1024 ×1024 pixel resolution.

3.6 Scanning Electron Microscopy (SEM)

Samples were imaged using Hitachi S3400 SEM operated at 15 kV (regular resolution) or Hitachi SU8230 SEM operated at 1.5 kV or 5 kV (high resolution). Nonconductive sample are first coated with a 2-nm thick Pd/Au alloy film via sputtering.

3.7 Transmission Electron Microscopy (TEM)

The TEM images and electron diffraction patterns were acquired using a Hitachi HT770 transmission electron microscope operated at 120 kV with samples drop-cast on Formvar/Carbon coated 200 mesh copper grids (Ted Pella, Inc. Product # 01800-F). The grids were dried at room temperature in air before imaging.

3.8 Secondary Ion Mass Spectrometry (SIMS)

SIMS data were collected by a TOF-SIMS5 time-of-flight secondary ion mass spectrometer (Ion-tof GmbH) with Bi^+ ion source. The analyzer was operated at 10 kV acceleration voltage in negative polarity mode. The ion distribution maps were collected at 20 μm × 20 μm raster size in burst alignment mode with 7 ion pulses per burst. Pixel resolution was set at 256 × 256. When reconstructed, every 4 neighboring pixels were integrated to provide better contrast. Mass spectra were calibrated by C^-, CH^- CH^{2-} CH^{3-} OH^- and Au^- peaks.

3.9 Confocal Raman

Raman spectroscopy were conducted using a 20x objective (NA = 0.40, laser spot size ~ 21 μm^2) on a WiTec confocal Raman microscope (Alpha 300R) with an fiber coupled Nd:YAG laser (λ = 532 nm) and an infrared diode laser (λ = 785 nm) according to usual procedure.[217] Signal-to-noise (S/N) ratios are calculated by comparing the average above

background intensity of specific Raman peaks through 3 separate measurements with the average fluctuations of backgrounds in the immediate vicinity of the same Raman peak.

3.10 Spectroscopic Ellipsometry

Spectroscopic ellipsometry was performed using a Woollam M-2000U ellipsometer (spectral range: 245–1000 nm). Ellipsometry data from all samples were acquired at 65°, 70°, and 75° angles of incidence. The refractive index of the silicon and silicon oxide was taken from the V.A.SE database (WVASE32 Version 3.768) The data were fitted with a two-layer model that consists of a semi-infinite silicon substrate and a silicon oxide layer with initial thickness of 2 μm. The thickness of silicon oxide layer was then parameterized until proper fit tolerance was achieved.

3.11 UV-vis and Fluorescence Spectroscopy

Extinction spectra were collected using a Shimadzu UV–vis-2450 spectrometer with D2 and tungsten lamps (wavelength range: 300–1100 nm). Photoluminescence spectra were collected using a Shimadzu RF-5301PC spectrofluorophotometer with a spectral range of 400–750 nm (1 nm intervals).

3.12 Electrodynamic Simulation

Finite-difference time-domain (FDTD) simulations were conducted using Lumerical FDTD Solutions (Version 8.12).[167] Individual AuNR or AuNS was modeled with a uniform 2 nm CTAB coating. The refractive index values of water, cellulose, CTAB, SiO_2 and gold were taken from previous reports or built-in CRC Handbook values.[218, 219] Dimensions for the individual nanorod or nanosphere were estimated from TEM, with the end facet of

AuNR approximated as a hemisphere. All simulations were conducted with a 0.5 nm mesh size in the x-, y-, and z-directions.[220, 166] A total-field scattered-field plane wave light source with a wavelength range of 300–1000 nm or 440–810 nm was used for illumination. Anti-symmetric and symmetric symmetries are applied to reduce simulation time. 12-layer perfect matched layer (PML) boundary condition was applied at the simulation boundary to absorb radiation energy with minimum scattering.

CHAPTER 4. LIGAND-EXCHANGE DYNAMICS ON GOLD NANOCRYSTALS

4.1 Introduction

The surface functionalization of metallic surfaces and nanostructures has important applications in molecular electronics, catalysis, and nanoscale biochemical sensors.[221,222,223] Because of its simplicity, compositional variability, and bond strength, thiol-based functionalization has been widely used to position functional or passivating ligands on various active detector surfaces,[224, 225] and molecular tunnel junctions.[226,227] The formation of functional self-assembled monolayers (SAMs) by thiols on Au surfaces has been extensively studied for many years with their lattice arrangement,[228, 229, 230] self-alignment kinetics,[231, 232] phase separations[233, 234, 235] and structural defects[236, 237] well-characterized. In the vast majority of studies, the Au surfaces were carefully prepared and thiolated under demanding conditions such as gas phase transport in near vacuum or ultra-pure solutions to ensure surface cleanness.[231,238] Yet a large number of practical devices currently explored use functionalized surfaces harboring physisorbed species from ambient air or previous wet chemistry processing steps. This is especially the case in nanodevices that employ colloidal nanocrystals stabilized by physisorbed surfactants.[21,46] Often, the presence of this native ligand is simply ignored and complete replacement of any surface contaminates or surfactants is assumed because the Au-thiol bonding strength is much stronger than those between Au and common surfactants (Scheme 4.1).[171, 238, 239, 240]

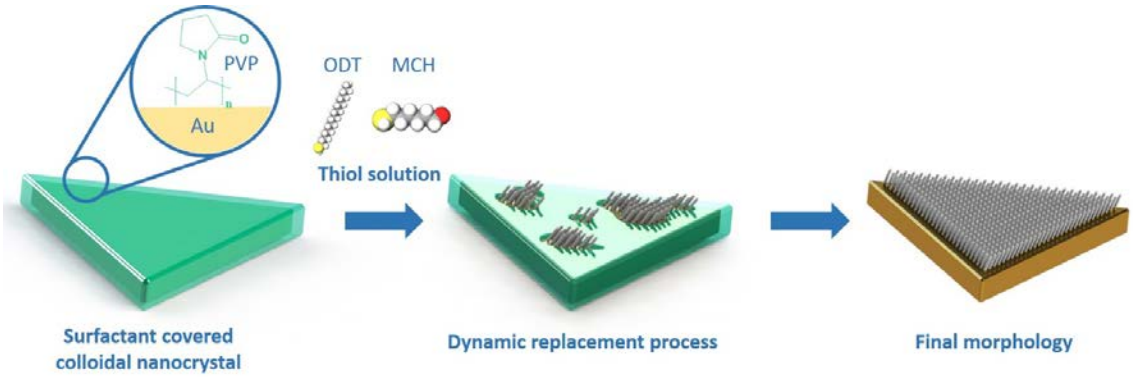

Scheme 4.1 Idealized thiol ligand-exchange process of surfactant covered colloidal nanocrystals.

However, despite the prevalent adoption of this assumption, its validity, along with the displacement dynamics and the eventual morphology of the thiol monolayer layer after "completed" surface reaction remains largely unexplored due to experimental challenges such as direct high-resolution monitoring of nanocrystal surfaces during reaction. Therefore, in this work, we analyzed the dynamics of ligand-exchange reaction of different kinds of linear alkanethiols on polyvinylpyrrolidone (PVP) covered single crystal gold nanoplates with high resolution atomic force microscopy (AFM) and secondary-ion mass spectrometry (SIMS) in a semi-*in situ* approach. In contrast to most of previous studies,[241, 242] we exploited single crystal gold nanoplates as a model substrate that provided large areas of uniform Au (111) crystallographic plane. The atomically flat nature of Au nanoplates enabled fine monitoring of subtle (sub-nanometer) changes on metallic surfaces coated with PVP, which is one of the most widely used polymer surfactant in colloidal nanoparticle synthesis.[243] Two common classes of thiol ligands are investigated in this work: 1-octadecanethiol (ODT), which represents classic long-chain alkanethiols with methyl terminal groups that has been widely studied for hydrophobic SAM formation,[244, 245, 246] and 6-mercapto-1-hexanol (MCH), which is shorter, contains a hydrophilic terminal

group, and is commonly used as a spacer molecule in functional SAMs.[247] These thiols represent the limiting cases in terms of mobility and hydrophobic-hydrophilic balance.

By monitoring the evolution of the nanoscale surface in the same surface region, we have demonstrated that during ligand-exchange, thiol molecules do not form uniform SAMs with complete PVP replacement. Instead, random network of elongated PVP domains a hundred nanometers long, ten nanometers wide and four nanometers high were formed as a result of partial displacement by growing thiol SAM domains that surround the PVP islands. Smaller, dome-like nanoscale PVP domains (around 10 nm diameter and 1-2 nm in height) were formed during MCH adsorption. By revealing the variation of surface profile of thiol-ligand layers with reaction time, we demonstrated that the full thiol-PVP ligand-exchange could not be completed. The stable mixed surface morphology was observed in both cases and related to interplay of enthalpic and entropic factors during polymer-thiol exchange.

4.2 Experimental Details

4.2.1 Materials

1-Octadecanethiol (98%), 6-Mercapto-1-hexanol (97%), Ethanol (200 Proof, OmniPur), Ethylene glycol (anhydrous, 99.8%), Polyvinylpyrrolidone (Molecular weight: 40,000) Tetrachloroauric acid (≥49.0% Au basis). All chemicals except ethanol were purchased from Sigma-Aldrich, and were used as-received without further purification.

4.2.2 Ligand-exchange of Au nanoplates

200 µL of colloidal Au nanoplates were cast on UV-Ozone cleaned (30 minutes, Novascan PSD-UV) 1 cm × 1 cm silicon wafer and, after solvent evaporates, rinsed by 10 mL of pure ethanol. The wafer was then put into respective thiol solution for ligand-exchange. Afterwards, it was retrieved, rinsed by 10 mL of pure ethanol and dried under nitrogen. Solution phase ligand-exchange was performed by injecting 500 µL concentrated Au nanoplate ethanol suspension into 20 mL of respective thiol solution under rapid magnetic stirring. The nanoplates were retrieved afterwards, cast on Si wafer, rinsed with ethanol and dried under nitrogen for further characterization. All ligand-exchanges are performed under room temperature without ambient light.

4.2.3 Characterization

AFM height distribution histograms were extracted at fixed 300-pixel resolution across the Z range of the selected area. To prevent any cross-contamination, a new tip was used for each sample. AFM surfactant cleaning was carried out using XSC11 Cantilever A (spring constant = 0.22 N/m) at 1000 nm deflection set point and XSC11 Cantilever C at 50-100 nm set point (470 nN – 950 nN) in contact mode. Peak force nanoscale mechanical measurement was carried out using SNL-10 Cantilever D (spring constant = 0.06 N/m, Bruker) in air at 120 pN peak force set point and 1 kHz peak force frequency. Surface reconstructions and tip deconvolutions of AFM topographical images were carried out using standard algorithms,[248, 249] assuming tip apex radius of 8 nm and tip slope of 20° (manufacturer's specifications).

4.3 Results and Discussion

4.3.1 Atomically flat single crystal Au nanoplates

The single crystal gold nanoplates synthesized here are 30 nm - 200 nm thick, have typical edge lengths ranging of 10 μm - 25 μm, and show triangular or hexagonal shapes due to single crystalline symmetry (Figure 4.1a, b). The hexagonal symmetry and six bright {220} Bragg diffraction spots (blue box) in the electron diffraction pattern confirm both the single crystallinity and the [111] zone axis of the crystal (Figure 4.1c, inset).[250] Six fainter inner-most diffraction spots (red box) are 1/3{422} forbidden reflections resulted from local hexagonal symmetries that are only present in Au or Ag nanocrystals bounded by atomically flat surfaces.[25]

Large area diffraction patterns also show complete first order Laue zone with high index diffraction spots, further confirming the single crystallinity of the individual nanoplates (Figure A.1). During deposition process, smaller nanoplates or nanobelts from solution might adhere to larger crystals (Figure 4.1c). Nevertheless, clean individual nanoplates can be easily found and selected under an optical microscope for further single nanoplate studies (Figure 4.1d).

Colloidal nanocrystals are known to have a native layer of residual surfactant present on their surface even after several rounds of washing.[251] The PVP shell in such cases is usually considered to be ~ 1 nm thick. As a result, the top surface of these Au nanoplates provided a micron-sized atomically flat area with ultrathin PVP coating, an ideal model system for nanoscale morphology monitoring and surface modification. Root-mean-squared roughness (R_{rms}) measured within 1 μm × 1 μm surface area was determined to be around 0.3 nm (Figure 4.1a, inset). This value is comparable to the top surface of atomically flat single crystal silicon wafer (0.1-0.2 nm)[252] and further confirms the near-ideal planarity of

the substrate, which is critically important for quantitative morphology monitoring in this study.

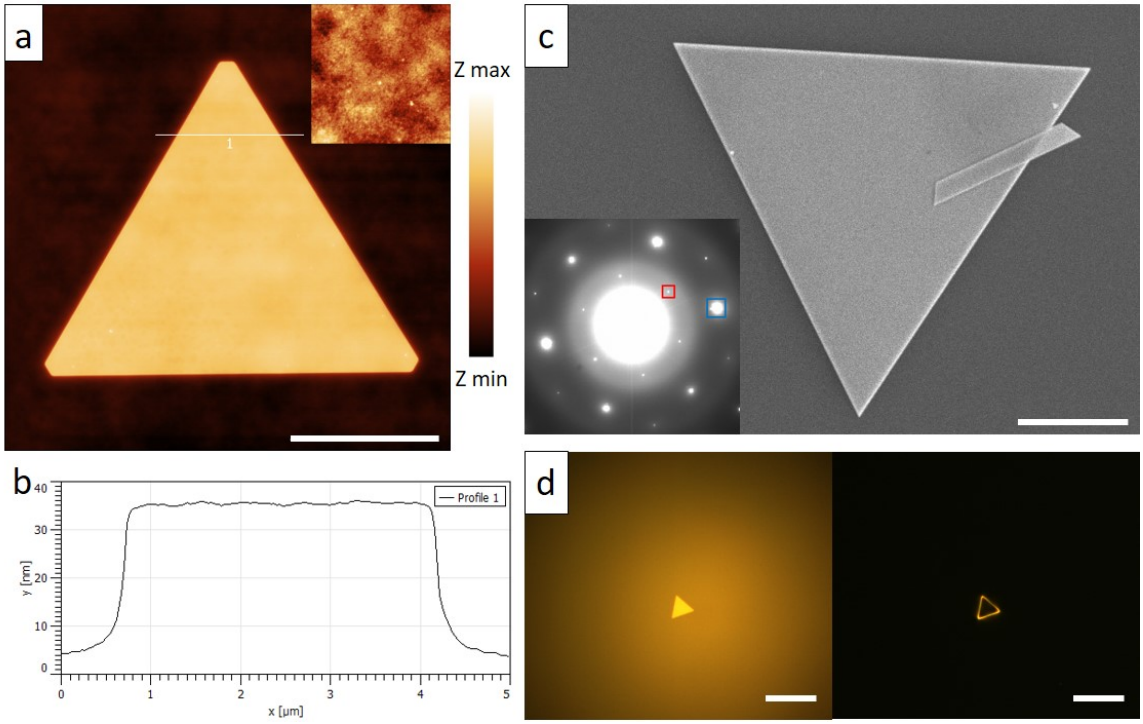

Figure 4.1 As-synthesized Au nanoplates, (a) AFM topographical image. Scale bar: 5 µm; Z scale: 50 nm. (All AFM images presented use the same false color gradient) Inset: 1 µm × 1 µm AFM topographical image of the top surface. Z scale: 3 nm R_{rms}: 0.3 nm (b) cross-section profile from line 1 in (a). (c) SEM image of individual nanoplate. Scale bar: 5 µm. Inset: electron diffraction pattern from a single Au nanoplate. (d) bright (left) and dark (right) field optical microscopy images of an individual nanoplate. Scale bars for both images are 25 µm.

4.3.2 Spatially and temporally resolved surface reaction monitoring

We monitored the surface morphology of PVP-coated Au single crystal exposed to thiol solution by repeating AFM scans at the same area of the same nanoplate after different reaction times (Figure 4.2). The images were acquired by exposing Au nanoplates deposited on silicon wafer to 1 mM ODT ethanol solution, a concentration that is commonly used for thiol functionalization,[221,242,253,254] and stopping the reaction at specific

times to image the same selected areas of the targeted individual nanoplate. After imaging, the reaction was resumed and stopped at next point later in time for repeated imaging. A series of these snapshots was used to reconstruct the evolution of surface morphology with great precision, and identify localized surface morphology transformations in the course of reaction.

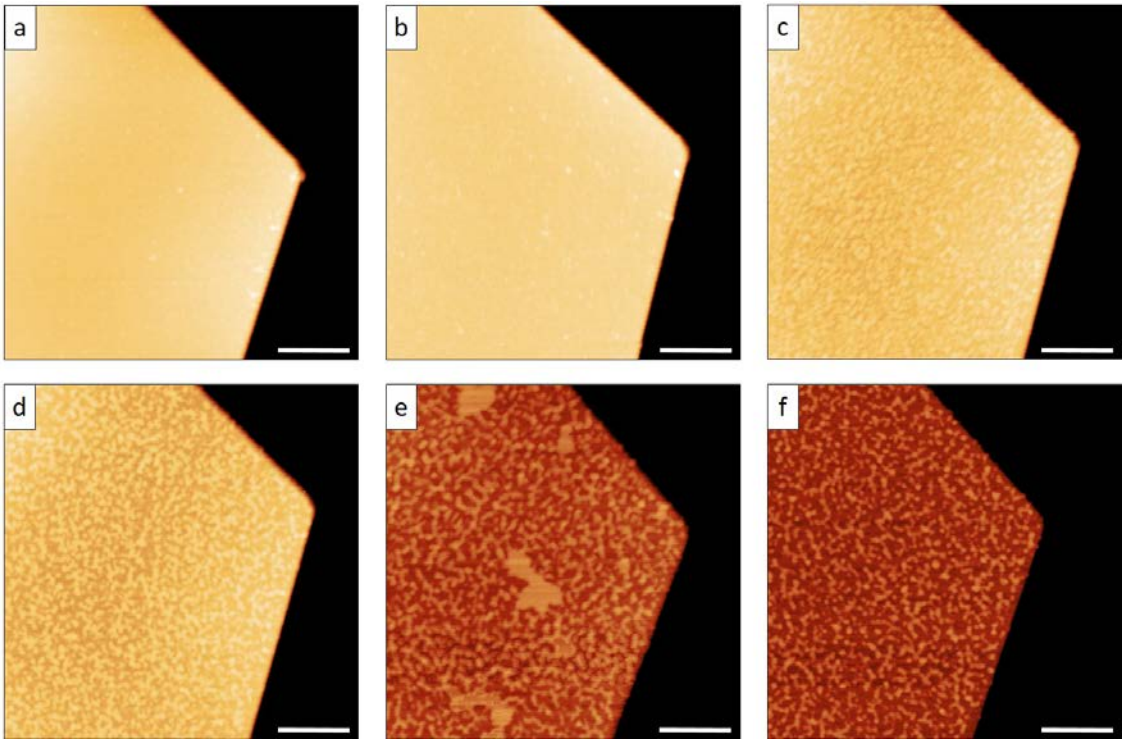

Figure 4.2 AFM topographical image of ODT adsorption layers on PVP-Au nanoplates after (a) 0 sec, (b) 30 sec, (c) 300 sec, (d) 3000 sec, (e) 30,000 sec and (f) 90,000 sec exposure to 1 mM ODT ethanol solution. Scale bar: 200 nm; Z scale: 180 nm (Color range 160-180 nm selected for surface feature contrast).

As we observed, after mere 30 secs of exposure to thiol solution, the uniform and smooth PVP-coated surface of the Au nanoplate started to become noticeably roughened and non-uniform. Globular surface features typically ~ 17 nm in lateral dimension (deconvoluted true dimension) can be seen randomly forming across the entire nanoplate, with about 0.5

nm height differences compared to surrounding surfaces. This is especially evident in high resolution 500 nm × 500 nm scan Figure A.2a). After 300 secs of exposure, the globular features shrank in lateral size to around ~ 10 nm but increased in height to ~ 2 nm, and became clearly discernable in the 1 µm × 1 µm scan. However, in both cases, the globular structures were so densely packed that the tip could not reach the underlying surface and thus height evaluation might be inaccurate (Figure 4.3a, inset).

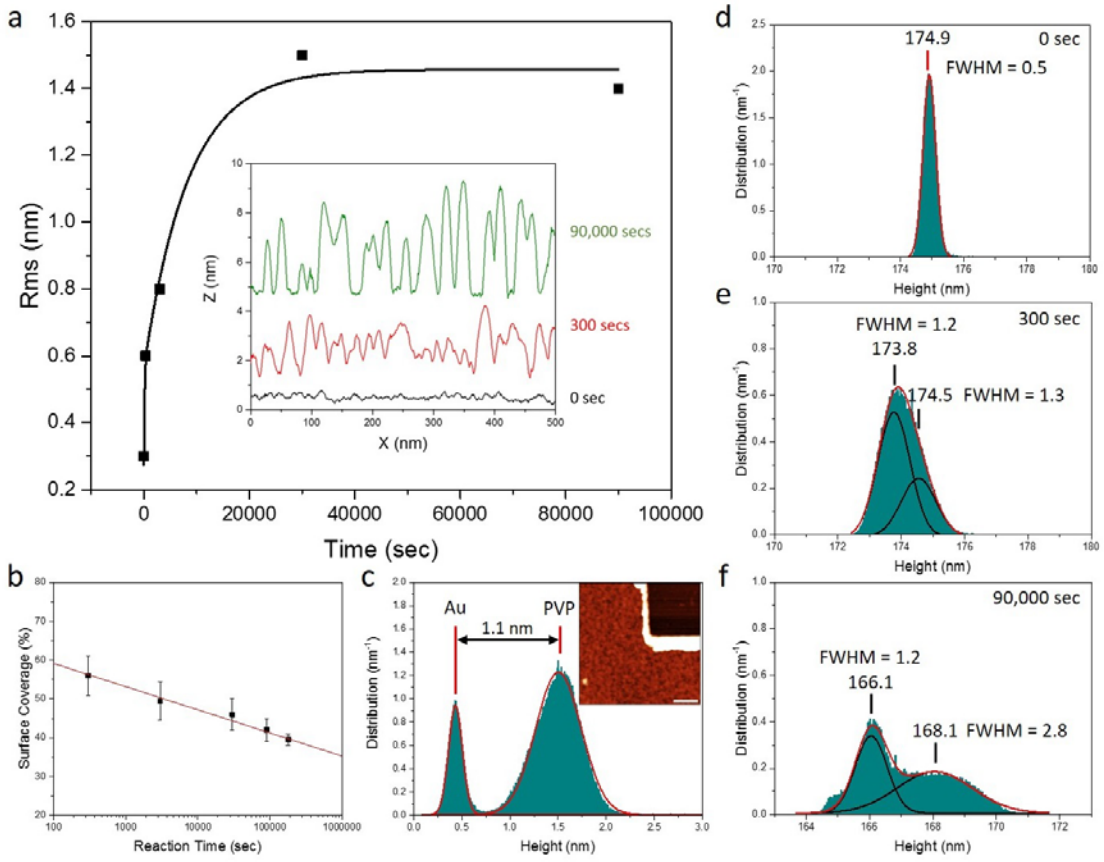

Figure 4.3 (a) Au nanoplate R_{rms} as a function of reaction time with ODT solution. Trend line is plotted as a guide to the eye. Inset: typical 500 nm cross-section profiles of Au nanoplate surface at different reaction times (off-set for clarity). (b) Surface coverage percentage of globular features at various reaction times. (c) PVP surfactant layer thickness as determined from the histogram of the AFM topographical image of a partially cleaned area immediately after AFM cleaning (Inset, scale bar: 100 nm). (d-f) Gaussian fit of the height histograms of AFM image at different reaction times

As the surface reaction proceeds further, the globular surface features remained roughly the same lateral size but steadily increased in the height to approximately 4 nm. During the later stages (> 8 hrs), large jointed islands approximately 200 nm wide occasionally formed and subsequently dissolved (Figure 4.2e, f). However, the appearance of these islands was random and cannot be consistently observed during repetitive experiments. The fact that they were not present in the final equilibrated morphology, suggests that they were probably metastable intermediate structures formed during the adsorption or random aggregates formed in solution.

After 90,000 secs (25 hrs) of exposure to thiol solution, the surface globules grew into random network of elevated curved structures of about 70 nm long and 10-15 nm wide and further increased in relative height to about 4 nm (Figure 4.3a, inset). Additionally, the spacing between individual surface features increased to 20-40 nm, wide enough for the AFM tip to reach the underlying surface and thus measure heights accurately. Overall, changes in surface morphology show that the globules were being squeezed and merged in the lateral direction while simultaneously being extended in the vertical direction. The surface features seem to have reached stable dimensions and overall distributions after 25 hrs of ligand exchange reaction (Figure A.2f, g, h). The true surface coverage of globular structures can be calculated by reconstructing the AFM topographical map using the modeled tip, and decreased logarithmically from 56% at 300 sec to 39% at 180,000 sec (Figure 4.3b, Figure A.4).

This final random island network surface morphology is highly uncharacteristic for supposedly “completed” thiol ligand-exchange reaction with formation of fully covering SAM. As known, when alkanethiols absorb on clean Au surface, they will first cover the

surface within a few minutes to form a low grafting density monolayer and some densely packed islands, and in the next few hours the alkane chains will undergo an assembly process to form an highly ordered and uniform monolayer.[221,255] Because hydrophilic or amphiphilic ligands have considerable solubility in ethanol solution, they should readily leave the surface during the thiol adsorption and assembly phase, thus leaving behind complete SAM after 24 hrs.[255] If such is the case, the surface monolayer would conform to the underlying Au (111) crystallographic plane, and should be near atomically flat with occasional defects. Yet, the final surface morphology we observe after excessive adsorption time were still dominated by globular structures of 3 to 4 nm in height aggregated into random networks (Figure 4.2f).

To quantify the change in surface morphology, R_{rms} was computed within 500 nm × 500 nm Au top surface area selected from each AFM topographical image (to ensure sampled region have the same geometrical dimension and includes only the top surface of the Au nanocrystal) and plotted against adsorption time in Figure 4.3a. The points representing 0 sec and 30 secs effectively overlap due to both the scale of the time axis and their near identical R_{rms} values. As we observed, over the monitored time interval, the R_{rms} of the nanoplate top surface increased dramatically during the first 8 hrs from 0.3 nm to 1.5 nm due to the initial rapid formation of globular surface structures. The micro-roughness subsequently stabilized at 1.5 ± 0.1 nm at longer times.

Before quantitative analysis of the height distribution data, we determined the thickness of PVP surfactant layer covering the Au nanocrystal by removing part of the coating in a selected surface area with the AFM tip (Figure 4.3c). The height distribution histogram from a 500 nm × 500 nm surface area of an Au nanoplate, with PVP removed at top right

corner of the image (Figure 4.3c, inset), shows two well separated Gaussian peaks, indicating the presence of two surfaces. The first peak corresponds to lower elevation of the bare Au surface cleaned from PVP coating and has a very narrow distribution with full width at half maximum (FWHM) of only 0.2 nm, common for atomically flat Au surfaces. The second peak corresponds to higher elevation of the PVP coated surface with much higher FWHM of 0.5 nm. Distance between the two peaks shows the average thickness of the PVP coating of 1.1 nm, close to commonly reported values in the literature (1~3 nm).[251]

Figure 4.3d, e and f show the height histograms of the AFM topographical images taken at 0, 300 and 90,000 secs respectively. The histogram peak representing the top surface was narrow (the FWHM of 0.5 nm) at the start of the reaction, suggesting a flat and uniform surface. As the reaction proceeds, the single peak initially broadens and could be deconvoluted into two overlapping peaks (bare surface and elevated surface features), reflecting the initial formation of the globular structures. The smaller deconvoluted peak represents the average height of the observed globular features. The horizontal peak separation indicates the globules are 0.7 nm above the underlying PVP surface. The two peaks have FWHMs of 1.2 and 1.3 nm respectively, and extensively overlap with each other, signaling a smooth and continuous transition.

As the surface reaction proceeds further, at 90,000 secs, the height distribution of the same surface area shows two distinct peaks (Figure 4.3f). The main peak representing the underlying nanoplate top surface largely maintains its shape and peak width (FWHM = 1.2 nm). In contrast, the secondary peak broadened considerably, with its FWHM more than doubled to 2.8 nm (Figure 4.3f). This change reflects evolution of the surface morphology as the globular structure's irregular geometry started to appear (Figure 4.2c-f). The

structures were also much taller, as indicated by the increased peak separation to 2 nm, which corresponds to the ~4 nm apex to base height difference shown in the cross-section profile (Figure 4.3a, inset).

4.3.3 Selective surface modification of PVP ligand layer

To understand the composition of these globular surface structures, we performed high force contact mode AFM local cleaning of Au nanoplates.[256,257] Briefly, a sharp Si tip of 8 nm radius is moved in raster manner across a square area at very high force (200-700 nN) effectively shoveling any organic surface coating and leaving behind the exposed bare Au substrate (Figure 4.4a). To make sure the removal of PVP was indeed complete, we conducted double cleaning on a separate nanoplate within a 1 μm × 1 μm selected area at the center of a 2 μm × 2 μm previously cleaned pattern. No new debris accumulation was visible from the second cleaning, signaling bare Au surface was indeed obtained during the first cleaning scan (Figure A.5a). Moreover, while the entire cleaned area maintains a clear AFM phase contrast with the PVP covered region, no phase contrast was observed within the 1 μm × 1 μm double-cleaned region, suggesting the surface composition uniformity of the bare Au surface after sequential cleanings (Figure A.5b).

The Au nanoplate with the cleaned surface region was then immediately treated with 1 mM ODT ethanol solution for 24 hrs in order to directly observe the surface morphological evolution differences between the clean Au surface and PVP coated Au surface on the same nanocrystal (Figure 4.4b). Figure 4.4c, d are 1 μm × 1 μm scans corresponding to black and blue squares in Figure 4.4b, respectively. Remarkably, we only see the formation of characteristic globular surface structures outside of the pre-cleaned area. The outside

region (blue square) displayed similar networked 4 nm height curved structures as seen in Figure 4.2f. By comparison, the inside pre-cleaned region (black square) was much smoother (sub nanometer local height differences) and devoid of complex surface morphologies. In fact, the R_{rms} measured within 1 µm × 1 µm area inside the cleaned region was only 0.5 nm whereas the R_{rms} measured within 1 µm × 1 µm area from the PVP covered region was much higher (1.3 nm), similar to those discussed previously (Figure 4.4c, d).

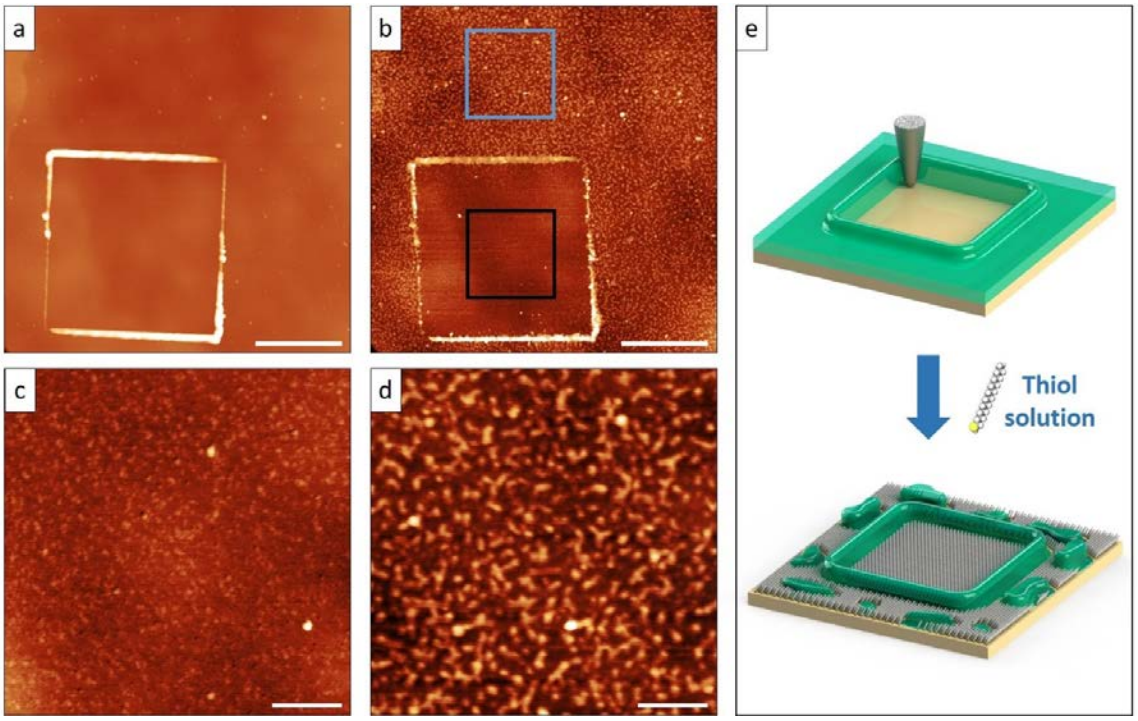

Figure 4.4 AFM topographical image of a Au nanoplate (a) immediately after 2 µm × 2 µm AFM cleaning, (b) same area after 24 hrs exposure to 1 mM ODT ethanol solution. 1 µm × 1 µm zoom-in AFM scan of (b), (c) inside AFM cleaned area (black box) and (d) outside AFM cleaned area (blue box). Scale bar: 1 µm (a,b), 200 nm (c,d); Z scale: 20 nm (a,b), 10 nm (c,d). (e) Schematics of AFM cleaning and subsequent ODT ligand-exchange process.

It is clear that the presence of the PVP coating defined the eventual complex surface morphology after thiol adsorption. Furthermore, the fact that the thiol SAMs in the pre-cleaned surface region was of roughly the same height as the underlying surface (valleys)

of the outside regions strongly suggests that the regions between the globular features were in fact ODT monolayer. Consequently, the globular structures are likely to be the residual islands of initial polymer coating (Figure 4.4e).

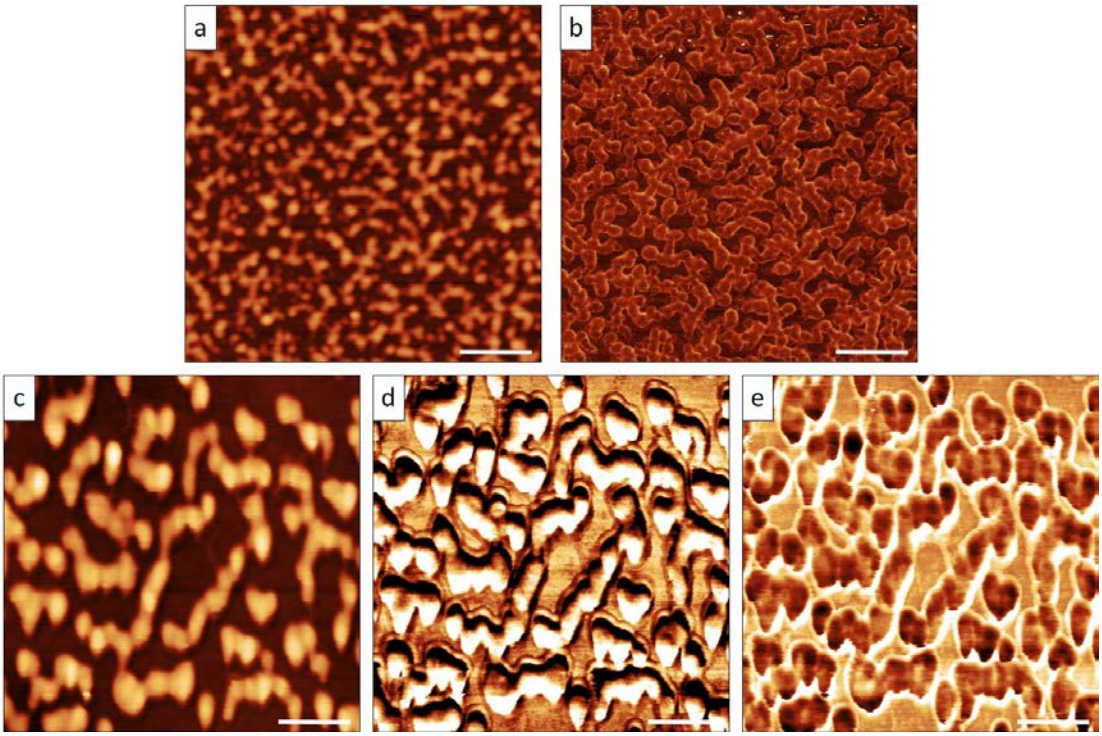

Figure 4.5 High resolution AFM (a) topographical and (b) phase image of final Au nanoplate top surface after 25 hrs of ODT exposure obtained from tapping mode. Z scale: 10 nm (a), 10° (b). QNM characterization of thiol surface adsorption layers on Au nanoplate after 3 solution exchanges and 72 hrs of exposure to 1 mM ODT ethanol solution, (c) topographical image, Z scale: 10 nm; (d) Derjaguin-Muller-Toporov (DMT) modulus image, Z scale: 25-40 MPa; (e) adhesion image, Z scale: 0.5-2 nN. Scale bar for all subfigures: 100 nm

The different nature of materials within curved globular aggregates and surrounding regions was confirmed by contrast in AFM phase imaging (Figure 4.5a, b, Figure A.2, Figure A.3). However, due to the complex nature of the phase shift in the tapping mode. No definitive identifications can be made about the origin of these contrasts other than the two features are made of different materials.

To elucidate the composition of different surface regions, we applied surface force spectroscopy (SFS) mapping with AFM and full spectrum SIMS mapping. The chemical composition of the surface layer was first probed through SFS quantitative nanoscale mechanical (QNM) characterizations where the contact mechanics of the AFM tip and the sample can be evaluated with high spatial resolution (down to a few nanometers). In these high resolution mappings (1 pixel corresponds to 1 nm), the elevated surface structures can be distinctively resolved in topographical, modulus, and adhesive measurements (Figure 4.5c, d, e). These measurements indicated that globular aggregated features possess much higher apparent elastic modulus (roughly twofold) than surrounding regions in the tens of MPa region. On the other hand, they show much lower adhesion (about 50%) in the 1 nN region. Typical force distance curves and tip loading curve for globules and surrounding areas indicate that tip penetration is lower than 2 nm, suggesting the SFS mapping is indeed measuring the mechanical properties of the ligand layer rather than the underlying gold surface (Figure A.6).

Even though true quantification of absolute values of elastic modulus and adhesion can be ambiguous in QNM measurements, the relative variation of these characteristics in the same image can be used for the identification of different material compositions on the surface.[258] Therefore, we can suggest that stiffer but less adhesive globular aggregates correspond to the PVP aggregates and softer but more adhesive surrounding reflects the presence of ODT SAM. Indeed, the PVP chain in this state is well below its glass transition point and is considered to be generally stiff with an elastic modulus from lower 1GPa up to 3 GPa, common for bulk glassy polymers.[259] On the other hand, the elastic modulus of various organic monolayers were reported within the range from 200 MPa to 2 GPa with

trend of less densely grafted organic monolayers having much lower elastic modulus.[260,261,262] Subsequently, the contact area between the tip and the PVP regions would be smaller compared with regions covered by low-grafted thiols due to higher apparent stiffness, resulting in lower effective adhesion or pull-off forces (Figure 4.5c).

Ideally, one would also like to conduct direct chemical characterization of the surface through molecular vibrational spectroscopy. However, the amount of PVP retained on the surface is way below the detection limit of standard spectroscopic measurement such as confocal Raman mapping (Figure A.7). For this reason, we employ highly surface sensitive SIMS analysis, which can yield chemistry dependent secondary ion information at the micrometer resolution.

SIMS maps in negative polarity were collected from an ODT exposed triangular Au nanoplate with 5 μm × 5 μm pre-cleaned surface area (Figure 4.6). The large patterning area was used to compensate for the limited (~ 0.5 μm) spatial resolution of SIMS.[263] In Figure 4.6, the cleaned area is marked by square 2, while an outside region of identical dimension is marked by square 1. The respective AuS^- ion count ratio, which directly corresponds to the relative abundance of thiol component, of square 2 to square 1 is 14:11, suggesting that the cleaned area was enriched in thiols (Figure 4.6a).

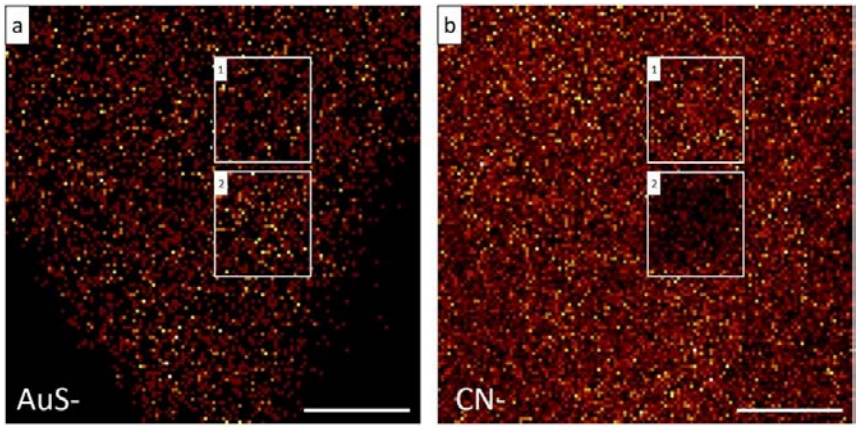

Figure 4.6 SIMS map of (a) AuS^- ion and (b) CN^- ion from 5 µm × 5 µm AFM cleaned Au nanoplate exposed to 1mM ODT solution for 12 hrs. Integrated over five 256 × 256 pixel scan. Scale bar: 5 µm

The respective CN^- ion count ratio, which corresponds to the abundance of PVP repeating units, of square 2 to square 1 is 1:2, suggesting that cleaned area was depleted in PVP coating while the outside area still had detectable PVP presence (Figure 4.6b). This provides direct chemical evidence to our previous conclusions, strongly supporting that the globular structure observed were indeed aggregates of PVP coils. Thus, a combination of different results supports our suggestions that mixed surface morphology observed in this study is composed of phase separated nanoscale globular PVP aggregates surrounded by the grafted thiol SAM domains.

As a control experiment, we performed the identical ODT absorption on bare Au substrate made by physical vapor deposition (PVD). However, the polycrystalline nature of the PVD film at the nanoscale generates a roughness texture that makes it difficult to distinctively isolate and analyze the surface features. Nevertheless, the AFM topographical images collected before and after ODT treatment were very similar, and we do not conclusively observe the formation of defined surface structures (Figure A.8). In addition, when the

PVD Au film was initially coated with PVP by immersion into PVP ethylene glycol solution used in Au nanoplate synthesis (see EXPERIMENTAL), subsequent exposure to ODT resulted in surface morphology changes that were similar to those observed on the Au nanoplates (Figure A.9). Again, the uneven surface made it difficult to obtain the true physical dimension of the PVP globules, and therefore yield any quantitative results. This is also precisely the reason why single crystal flat Au surfaces was needed in this study. Further study on PVD Au film revealed that post hoc exposure to PVP ethylene glycol solution after initial formation of ODT monolayer resulted in globules with drastically different size and distribution, suggesting the observed morphology was not a result of simple surfactant re-adsorption (Figure A.10).

4.3.4 Thiol ligand-exchange dynamics and mixed surface morphology

Based on both the surface morphology, SIMS and SFS results, we propose the following evolution of the surface morphology during thiol functionalization of colloidal nanocrystals with ethanol mediated alkanethiol-polymer ligand-exchange (Scheme 4.2).

Scheme 4.2 Proposed thiol adsorption dynamics and formation of mixed surface morphology. (a) Au nanoplate surface with PVP surfactant from colloidal synthesis. (b) Initial surfactant displacement and thiol island formation (c) Final mixed surface morphology after 24 hrs of thiol solution exposure.

We suggest that when PVP coated Au nanocrystals are exposed to thiol solutions, thiol molecules start to replace the adsorbed PVP monolayer (1.1 nm thick) at random sites all

over the crystal surface to form nanoscale SAM thiol domains (Scheme 4.2b). Because thiol-Au bond (bond energy ~ 44 kcal/mol)[168] is enthalpically more favorable than pyrrolidone oxygen/nitrogen Au coordination (coordination energy ~ 15 kcal/mol)[264] initial displacement happens very fast (several seconds).[255] These initial thiol domains are buried and surrounded by the native PVP surfactants. However, their existence does cause the initially uniform PVP coating to be disrupted into around 20 nm sized globules with apparent excessive height of 0.5 nm above the surrounding ODT SAM, which is itself 2.2 nm high (Figure 4.2c).[265] As the reaction continues, the thiol domains grow laterally and horizontally compress the PVP globules to roughly 10 nm sizes and cause the globules to be squeezed and expand in the vertical direction to approximately 4 nm above the surrounding SAM. During this period, neighboring PVP globules merge and rearrange into longer and more curved networks (Figure 4.2f, Scheme 4.2c). Importantly, unlike commonly believed, this phase separated ligand layer turned out to be the final morphology even when the nanocrystals were exposed to thiol solutions for 50 hrs (Figure A.2g).

We suggest this dynamic surface phase separation and the formation of mixed surface morphology is likely caused by incomplete displacement of PVP chains during ligand-exchange followed by micro-phase separation of residual PVP materials into aggregated nanoscale domains. In the process, PVP chains are horizontally and vertically displaced by forming thiol SAM domains into globular like structures with the bottom segments of the chain still strongly bonded to the Au surface, confined by both pyrrolidone-Au coordination bonding and entropic displacement barrier for PVP random coils. A considerable amount of PVP coils remains in this phase separated state bound to bare Au surface to make the nanocrystal surface partially solvophilic, reducing its interface energy

with ethanol solution, balancing the unfavorable interactions of polar solvent and the methyl terminal groups of ODT SAM.

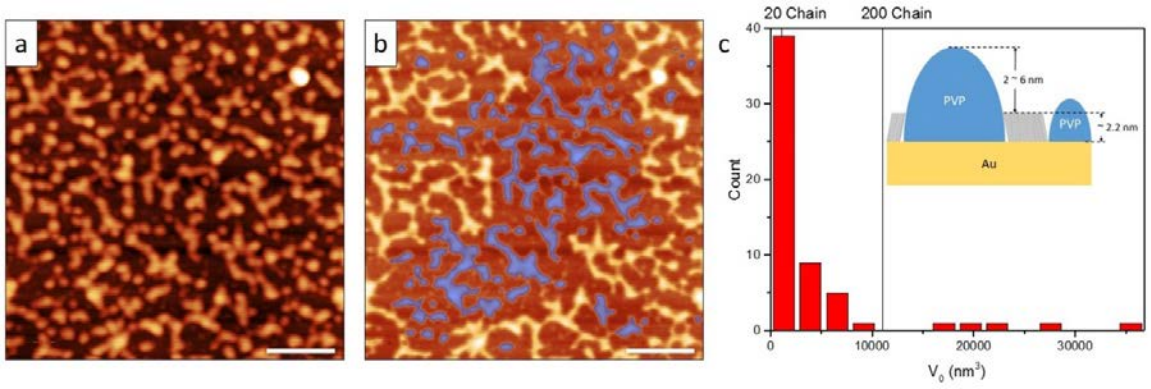

Figure 4.7 (a) AFM image of Au nanoplate after 50 hrs of consecutive ODT exposure (b) Surface profile reconstructed from (a) using a model tip with 8 nm apex radius and 20° tip slope. Only globular structures that falls completely inside the frame are selected (blue). Scale bar: 100 nm. Z scale: 10 nm. (c) Zero basis volume histogram from selected globules. Inset: schematics demonstrating the true vertical dimension of PVP globules.

To further understand the quantities of PVP chains remaining on the nanocrystal surface, true surface map of final equilibrated ligand layer was generated by deconvoluting the AFM topographical image of nanocrystal top surface after 50 hrs of ODT exposure (Figure 4.7a). All the globular features that were not edge touching were selected, and the height data was subsequently leveled by aligning minimum values for all globules selected (Figure 4.7b). True volume of individual globule was calculated by taking into account the Z location of the true Au (111) surface, which is 2.2 nm beneath the top surface of surrounding ODT SAM domains (Figure 4.7c, inset). Based on the bulk density (1.2 g/cm^3) and molecular weight of PVP used, we roughly estimated that the number of remaining PVP chains in each of the globule feature is on the order of magnitude of 10 to 10^2 (Figure 4.7c). In fact, if we compute the total adjusted volume of all the globular features presented

in Figure 4.7b, the result (248,000 nm^3) is very close to the original PVP adlayer volume (275,000 nm^3, assuming 1.1 nm thickness) as if most of the PVP just deformed on the surface rather than being displaced into the solution. However, these values should not be taken literally, since the surface reconstruction is not exact, and the zero-basis calculation tends to overestimate the volume. Nevertheless, this is definitely a non-negligible amount. Since most thiol-functionalization or ligand-exchange processes for colloidal nanocrystals are conducted under the conditions tested here, both in terms of substrate exposure[266] and solution mixing,[178, 267] it is very likely that these ligand-exchange reactions previously perceived as "complete" are not actually complete.

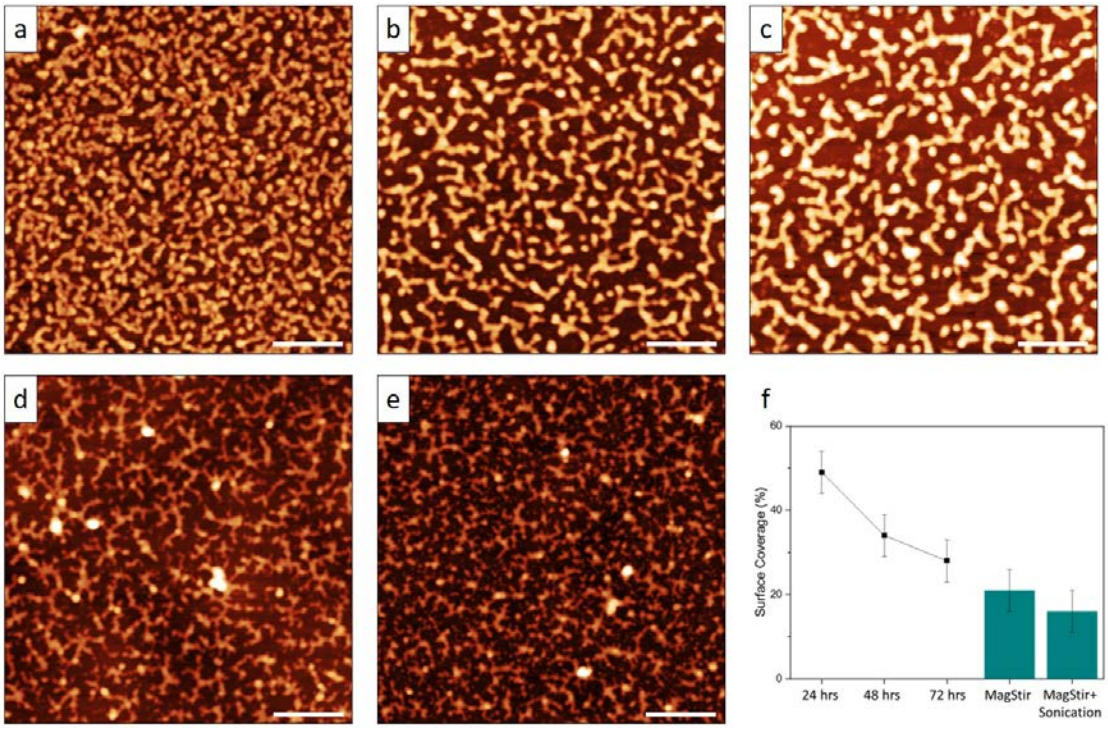

Figure 4.8 AFM topographical image of thiol surface adsorption layers on Au nanoplate after (a) 24 hrs exposure to 1 mM ODT ethanol solution, (b) additional 24 hrs exposure to fresh 1 mM ODT ethanol solution following (a), (c) additional 24 hrs exposure to fresh 1 mM ODT ethanol solution following (b), totaling 72 hrs of consecutive exposure, (d) solution phase thiol ligand-exchange under rapid magnetic stirring for 72 hrs, (e) solution phase thiol ligand-exchange under 72 hrs of rapid

magnetic stirring followed by 5 mins of sonication. Scale bar: 200 nm. Z scale: 10 nm (f) Surface coverage of globular structures in (a) to (e) calculated after tip deconvolution.

Then, we considered whether the remaining PVP domains can be completely removed after the formation of mixed morphology by refreshing ODT solution at each step, rapid magnetic stirring or sonication (Figure 4.8). After each AFM imaging, the substrate was put into a fresh vial of ODT solution to reduce PVP concentration in the solution. This approach resulted in the formation of larger 40-50 nm globules with 6-7 nm height (Figure 4.8a-c). The surface coverage of the PVP globules decreased from 49% ± 5% at 24 hrs to 28% ± 5% at 72 hrs with the overall character of mixed surface morphology remaining unchanged (Figure 4.8f). Similar minor changes were observed after external agitation but the mixed PVP-ODT surface morphology remained very similar to the morphologies observed in the basic procedure (Figure 4.8d-f). Additionally, consecutive AFM monitoring of individual globules has demonstrated that the PVP domains are mostly pinned on the Au surface with very limited surface mobility, suggesting strong interactions (Figure A.11).

In this regard, recognizing the true microstructure of the ligand layer can be extremely important. As surfactant still presenting on the surface may alter the chemical and physical behavior of functional ligand layer in significant ways. For instance, residual surfactant will almost certainly disrupt the chemical properties of the engineered surface, comprising the affinity or selectivity of active sensing surfaces, or it can introduce extra electrical or optical noises in molecular junctions. The incredible resilience of polymeric surfactant on colloidal nanocrystal surface demonstrated here shows that simple thiol replacement

chemistry can no longer be assumed from a theoretical point of view, but rather, formation of engineered SAM surfaces on nanocrystals need to be experimentally verified.

Ligand exchange performed with MCH yielded qualitatively similar results with a few noticeable differences. The globular features produced by MCH ligand-exchange on Au nanoplates were much smaller and denser than those observed for ODT, they consist of domes 10 nm in diameter and 1-2 nm in height (Figure 4.9a). The QNM images showed stiffness and adhesion contrast similar to those observed during ODT adsorption, suggesting analogous micro-phase separation behavior (Figure 4.9b, c). The same roughness contrast is also present for AFM cleaned nanoplates after MCH adsorption (Figure 4.9d, e). R_{rms} inside the pre-cleaned area was 0.15 nm (200 nm × 200 nm, randomly sampled, standard deviation < 0.01 nm) whereas R_{rms} of the un-patterned area was 0.24 nm (200 nm × 200 nm, randomly sampled, standard deviation < 0.01 nm).

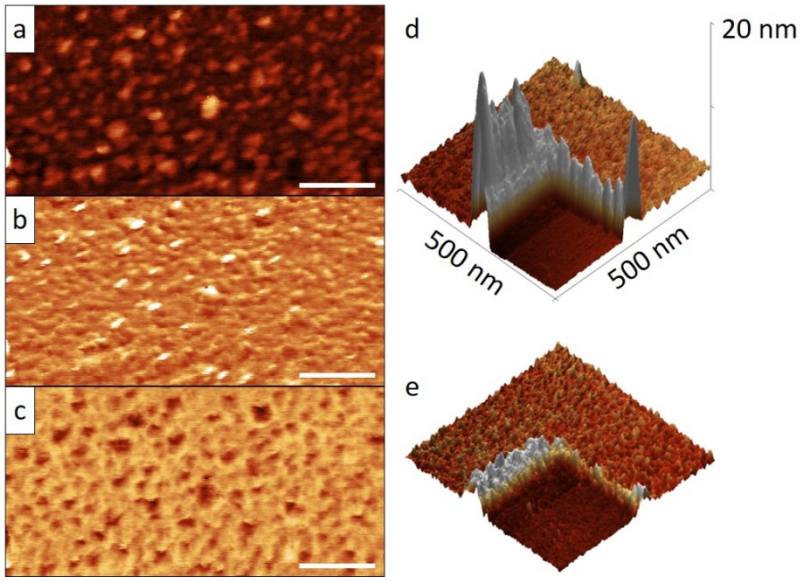

Figure 4.9 QNM Characterization of thiol surface adsorption layers on Au nanoplate after 2 solution exchanges and 48 hrs of exposure to 1 mM MCH ethanol solution, (a) topographical image, Z scale: 10 nm; (b) DMT modulus image, Z scale: 1-20 MPa; (c)

adhesion image, Z scale: 0.5-1.2 nN. Scale bar: 100 nm. 3D AFM topography showing in initial formation of MCH adsorption layer on top of partially cleaned Au nanoplate: (d) as cleaned, (e) after 300 secs of solution exposure.

The difference in globular sizes can be understood by considering the structure integrity of the thiol monolayer and major energetic factors contributing to the formation of SAMs with polymethylene backbones. We consider two interactions, the S-Au bonding, which roughly contributes 44 kcal/mol, and inter-alkanechain hydrophobic-hydrophobic interactions, which contributes about 1 kcal/mol per methylene group, for ODT and MCH molecules studied here.**Error! Bookmark not defined.**,[268] For this reason, the monolayer formed by M CH is significantly more disordered and less dense than those formed by ODT due to enthalpy,[245,270,269] meaning MCH SAMs will have less driving force compared to long-chain alkanethiols to horizontally displace PVP chains. Thus the PVP chains might intercalate more into the MCH SAM domains, degrading the monolayer integrity and resulting in significantly smaller and denser globular features. Also, MCH's hydrophilic hydroxyl head groups has much higher affinity to pyrrolidone unit than ODT's hydrophobic methyl head group.[270] Therefore, it would be favorable for PVP chains to surface migrate back onto the formed MCH SAM simply due to entropic reasons. In fact, we observed the surface migration of PVP globules back into the AFM cleaned areas during the later stages (>300 sec) of MCH ligand exchange (Figure A.12). In Addition, equimolar mixed ODT/MCH solution (total thiol concentration = 1 mM) was also tested and produced a surface morphology contrast similar to those observed in ODT study (Figure A.13).

As a control sample, we tested the exposure of AFM cleaned nanoplate to pure ethanol for 24 hrs (Figure A.14). Because bare Au surface is highly susceptible towards nonspecific

adsorption of organics,[271] we expect the clean region to attract a lot more carbonaceous contaminates from solution and air than the regions protected by surfactants.[272] Indeed, we see accumulation of particulates and a relative increase in roughness in the clean region, demonstrating that the opposite roughness change observed during thiol ligand-exchange was indeed due to the presence of thiols.

4.4 Conclusions

By studying the adsorption behavior of two types of representative linear thiol molecules on colloidal single crystalline Au substrate, we have demonstrated that, contrary to common belief, linear thiols do not completely replace polymeric surfactant (PVP) during ligand-exchange of colloidal nanocrystals to form uniform monolayers. Instead, the thiol molecules apparently nucleate on crystallographic surfaces to form small domains of SAMs that both horizontally and vertically displaces PVP coating into globular structures of several nanometers in height. Astonishingly, this network of residual PVP domains persists even after 72 hrs of exposure, as well as several rounds of solution replacement and sonication. The exact dimension of the polymeric globules and their distribution depends on the order and hydrophobicity of the formed SAM domains. Long-chain alkanethiols with hydrophobic head groups such as ODT can displace 1 nm thick native PVP surfactant layers into sparse network-like globules 3-4 nm in height, 10-15 nm in width and ~ 70 nm in length with AFM-measurable highly ordered SAM domains in between. Whereas short-chain alcohol-thiols such as MCH can only displace the same PVP surfactant layers into densely packed dome-like globules ~ 10 nm in diameter and 1-2 nm in height with SAM domains buried in between that are inaccessible to ordinary AFM tips.

In essence, this study offered some of the important answers to a critical question concerning thiol-based ligand-exchanges that has been difficult to address before and demonstrated the complex interplay between linear thiol domains and PVP surfactant on colloidal nanocrystals. The traditional view regarding thiol ligand-exchange on pre-coated Au surfaces is almost certainly flawed. Ethanol mediated exchange process between linear thiols and PVP surfactant produces nanoscale ligand layer phase separation patterns rather than uniform SAM on colloidal nanocrystals.

CHAPTER 5. DUAL-EXCITATION NANOCELLULOSE PLASMONIC MEMBRANES FOR MOLECULAR AND CELLULAR SERS DETECTION

5.1 Introduction

The free electrons in noble metal nanostructures can be resonantly excited by light in the visible-near infrared (vis-NIR) range to produce localized, high intensity electromagnetic (EM) fields through a phenomenon called localized surface plasmon resonance (LSPR).[273] The high field enhancement can be utilized to significantly enhance the Raman scattering of nearby molecules in surface-enhanced Raman scattering (SERS).[10, 225, 274, 275, 276] However, getting plasmonic nanoparticles to efficiently interact with analytes in a quantifiable and predictable manager has always been an issue.[276] Many attempts have been made to find suitable substrates that facilitates ideal nanoparticle-analyte interactions.[274, 277, 278]

Porous substrates with large surface areas such as common filter papers,[279, 280] porous alumina membranes,[281, 282] and filter membranes[283] have all been experimented as SERS platforms for both solutions and vapors. However, problems like high fluorescence/Raman background and poor retention of both nanoparticle and analytes often remain unsolved.[284, 285, 286] Therefore, high loading density of metal nanostructures has often been required for acceptable performance.[287] The high loading in return promotes high optical absorbance thus limiting the probing depth and volume. Moreover, the excessive loading of nanoparticles results in a mixture of nanoparticle clusters with varying degrees of

aggregation.[288] Due to plasmonic coupling, each of these clusters will have different plasmonic responses,[289] making it difficult to optimize excitation wavelengths for efficient SERS detection.

Here, we report a novel SERS substrate based on the incorporation of gold nanorods into nanoporous network of cellulose nanofibers that significantly improves the utilization efficiency of plasmonic nanostructures and effectively pre-concentrates the targeted analytes (Scheme 5.1). The AuNR/CNF membranes are fabricated via direct vacuum assisted filtration.[290, 291] First, CNF dispersion in water is filtrated through a polycarbonate (PC) filter with ~200 nm diameter holes. This allows the CNFs to assemble into a layered membrane with interdigitated fibers. Before the CNF membrane is completely dry, aqueous AuNR solution is added to form a nanocomposite membrane infiltrated with individual nanorods or nanorod clusters.

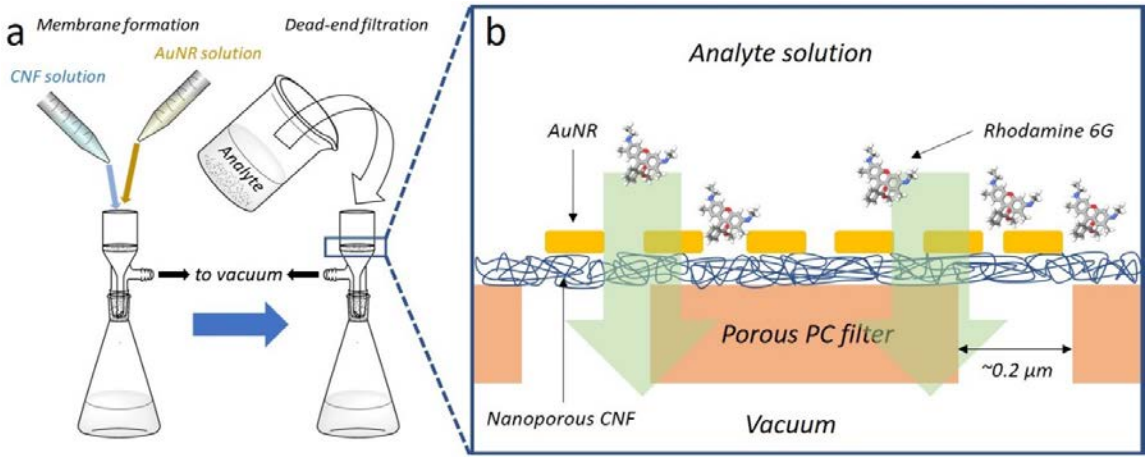

Scheme 5.1 (a) Fabrication of AuNR/CNF membrane, and its subsequent use in analyte solution filtration. (b) Schematics of the analyte (R6G) solution pre-concentration.

The plasmonic nanofiber membranes possess several exceptional optical properties, which includes high transmission in the vis-NIR range, low scattering, and near absence of both fluorescence and Raman backgrounds. The design also takes advantage of the nanoporous morphology of CNF matrix that helps retain and pre-concentrate the analyte for efficient SERS detection (Scheme 5.1b).

5.2 Experimental Details

5.2.1 Materials

CTAB (hexadecyltrimethylammonium bromide ⩾99%), $NaBH_4$ (granular, 99.99% trace metal basis), $HAuCl_4–3H_2O$ (⩾99.9% trace metals basis), ascorbic acid (ACS reagent, ⩾ 99%), silver nitrate (⩾99.5%), 2,2,6,6-tetramethylpiperidine-1-oxyl (98%), NaBr (⩾ 99%), NaClO-H_2O (⩾98%), NaOH(⩾98%), hydrochloric acid (36.5-38.0% ACS, BDH Aristar), All chemicals beside hydrochloric acid were purchased from Sigma-Aldrich and were used as-received without further purification.

5.2.2 Synthesis of CNFs

Cellulose nanofibers were prepared from never dried softwood pulp by 2,2,6,6-tetramethylpiperidine-1-oxyl radical (TEMPO)-mediated oxidation and ultrasonication according to the previous report.[292] Briefly, TEMPO (0.016 g, 0.1 mmol) and sodium bromide (0.1 g, 1 mmol) were added 0.3 wt% wood pulp (200 mL). TEMPO-mediated oxidation was started by adding the 6 ml 12% NaClO solution, and the pH was adjusted to pH 10 by the addition of 0.1 M HCl under continues stirring at room temperature. The pH was maintained at 10 by adding 0.5 M NaOH using a pH stat until no NaOH consumption

was observed. The TEMPO-oxidized cellulose was purified by centrifuge at 10000 rpm for 10 min. The final cellulose nanofibers were prepared by treating the TEMPO-oxidized cellulose in the ultrasonicator (QSonica, Q125) for 1h. The concentration of the as-prepared cellulose nanofibers was determined to be 1.8 wt%.

5.2.3 Fabrication of CNF/AuNR composite membranes

CNF/AuNR membranes are manufactured via vacuum assisted filtration at a pressure difference of ~1 bar. A track-etched polycarbonate membrane filter with 200 nm pore size was used. First, 5 mL of 1.8 wt% CNF dispersion was filtrated. 3 mL of AuNR solution is immediately added after the CNF dispersion is drained, AuNR/CNF composite membrane is formed at the end of the filtration. Additional filtration of analyte solution is completely by adding 20 mL of respective solution to the filtration feed after the AuNR/CNF membrane formation.

5.2.4 E. Coli. cultivation

Escherichia coli (*E. Coli.*) was cultured in Luria-Bertani Broth for 24 hr at 37°C under shaking at 180 rpm until they reached their stationary growth stage. This corresponds to a concentration of approximately $10^7 \sim 10^8$ CFU/mL ($OD_{600} = 0.97$).[293] 40 mL of the original culture is pelleted at 3400 RCF for 10 min, and re-dispersed in the same amount of PBS solutions for SERS detection.

5.2.5 Characterization

Tensile properties of CNF membranes were measured at a gauge length of 10 mm and at a cross-head speed of 0.0254 mm/s (strain rate: 0.15%/min), using a RSA III solids analyzer (Rheometric Scientific Co.).

5.3 Results and Discussion

5.3.1 Morphology and Properties of materials and membranes

The AuNRs used in this study have aspect ratio of 3.5:1, and are hemi-spherically shaped at both ends (Figure 5.1a). The UV-vis spectrum of the native AuNR solution shows two distinct peaks at 798 nm and 510 nm, corresponding to the longitudinal and transverse LSPR modes (Figure 5.1b).[294] As the AuNR are filtrated into the CNF network, a visible red-shift in both peaks is observed due to transferring to an environment with higher refractive index.[220]

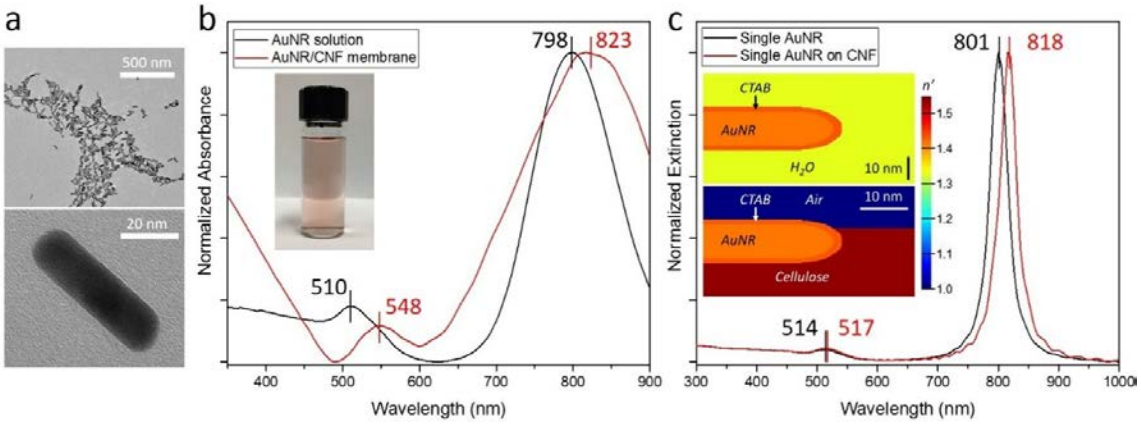

Figure 5.1 (a) TEM images of the AuNRs used in this study. (b) Extinction spectra of AuNR solution and AuNR/CNF membrane. Inset: optical image of AuNR solution (c) Calculated extinction spectrum of single AuNR (in water) and single AuNR on CNF (in air) from FDTD simulation. Inset: respective cross-section showing the geometrical setup used for the simulation, color maps the real part refractive indices of the components.

The calculated extinction spectrum with AuNR suspended in H_2O showed corresponding peaks at 514 nm and 801 nm, albeit with much sharper profile, which is due to the fact that only a single nanorod is simulated (Figure 5.1c). The calculated single nanorod extinction curve also shifts to the red when AuNR is transferred to the CNF/air interface.

CNF used in this study are made by TEMPO oxidation treatment followed by direct mechanical exfoliation, which yields much thinner and more uniform fibers than those produced by acid hydrolysis or bacterial synthesis.[295, 296, 297, 298] The nanofibers are on average longer than 1 μm, and are very uniform both in terms of size distribution and diameter variation (4 ± 0.8 nm) (Figure 5.2a). The resulting CNF membranes are colorless and optically uniform (Figure 5.2b). Figure 5.2c shows the SEM image of AuNR/CNF membrane slightly separated from the underlying PC filter membrane with total thickness close to 1 μm.

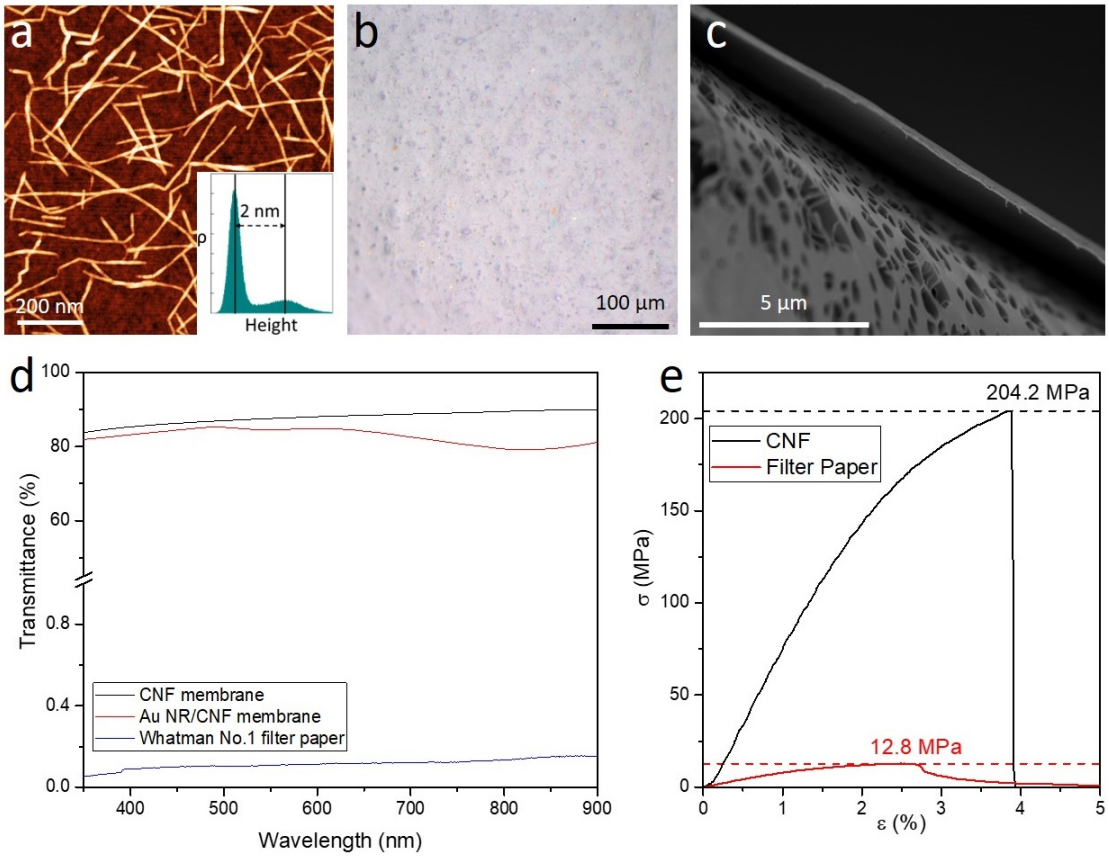

Figure 5.2 (a) AFM topographical image of individual CNF fibers. Inset: height histogram of (a), indicating the fibers are on average ~4 nm in diameter. (b) Optical micrograph of AuNR/CNF membrane. (c) Side-view SEM image of AuNR/CNF membrane on top of PC filter. (d) Transmittance of pure CNF membrane, AuNR/CNF membrane, and common filter paper. (e) Stress-strain curves of CNF membrane and common filter paper.

The uniformity of CNF fibers allows the fabrication of highly transparent membranes with minimum scattering. Neat CNF membrane has ~ 87% and ~ 89% transmission at the 532 nm and 785 nm Raman excitation wavelengths. Even after loading with gold nanorods, the transmission remains high at ~ 85% and ~ 80%, respectively (Figure 5.2d). In contrast, ordinary lab filter papers frequently used as SERS substrate shows very low transmittance (< 0.2%) in the Vis-NIR range even before the loading of plasmonic nanocrystals (Figure 5.2d).

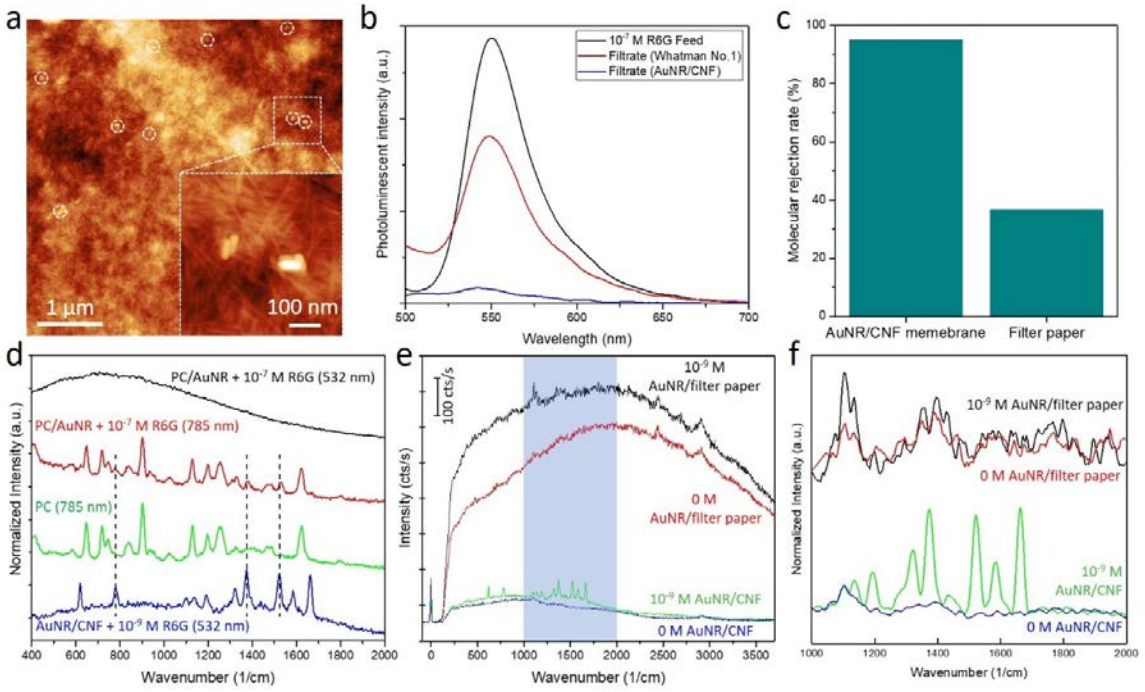

Figure 5.3 (a) AFM topographical image of AuNR/CNF membrane, individual AuNRs and their aggregates are marked out by open white circles. Z scale: 50 nm. Inset: High resolution AFM scan of the area marked by open square. Z scale: 40 nm. (b) Photoluminescence spectrum of 10^{-7} M R6G analyte feed (black) and filtrate from filter paper (red) and AuNR/CNF membrane (blue). (c) Molecular rejection rates of R6G molecules. (d) Raman spectrum of PC/AuNR membrane after 10^{-7} M R6G analyte solution filtration excited at 532 nm (black) and 785 nm (red); pure PC membrane excited at 785 nm (green); AuNR/CNF membrane after 10^{-9} M R6G solution filtration at 532 nm (blue). (e) Raw spectra collected from AuNR/filter paper and AuNR/CNF membrane after 10^{-9} M (black/green) and 0 M (red/blue) R6G solution filtration respectively. (f) Spectral region between 1000 cm^{-1} and 2000 cm^{-1} in (e) after smoothing and background subtraction, spectra from different substrates are offset for clarity, color code same as in (e).

Other cellulose based SERS substrates reported in the literature often have significantly reduced transmission due to the high loading of plasmonic nanocrystals, and the membrane usually appears black due to broadband absorptions.[299] For SERS membrane that have thickness less than the focal depth of confocal Raman microscope (~ 1 μm), high optical transparency means that the entire membrane, rather than just the surface region, can contribute to the generation of the Raman signal. Additionally, the AuNR/CNF membrane

fabricated here is mechanically robust, with ultimate tensile strength measured at ~ 200 MPa, an order of magnitude higher than that of regular filter paper (Figure 5.2e). This mechanical strength allows the membrane, which is less than 1μm thick, to be free-standing and easily transferable to other surfaces for Raman analysis. AFM topographical image of the AuNR/CNF membrane shows densely packed cellulose nanofiber network with embedded individual AuNRs and their aggregates (Figure 5.3a, white circles). Many AuNRs are in the clustered form with two or three AuNR packed together. There are approximately 20 discernable AuNR in this 5 μm × 5 μm scan, giving a low loading density estimation of 0.8 nanorods/μm^2. The volume density of AuNR in the membrane can also be estimated from the concentration of AuNR in the feed solution to be approximately 8.5 nanorods/μm^3 (see Figure B.1 and relevant discussion in Appendix B). In comparison, typical loading densities of nanoparticle based SERS substrates are at least tens of nanoparticles per μm^2 or hundreds of nanoparticles per μm^3.[280, 299]

Structurally, the network of randomly packed CNFs acts like ~ nm sized sieves that serves as efficient pre-concentrators for the analytes. Figure 5.3b shows the photoluminescence spectra of 10^{-7} M R6G aqueous solution feed and filtrates by AuNR/CNF membrane in comparison with standard Whatman No.1 filter paper. The fluorescence peak at ~ 550 nm originates from R6G molecules and can be linearly correlated with R6G concentration. Filtration by regular filter paper resulted in 63% retention of the original fluorescence intensity, signifying a molecular rejection rate of 37% (Figure 5.3c). In contrast, after filtration with the AuNR/CNF membrane, which has ~0.6% of the thickness of the regular filter paper, the fluorescence intensity in the filtrate is only 5% of the original solution, signifying a much higher molecular rejection rate of 95 %. Such high rejection rate means

the membrane is performing actual nanofiltration, as most of the analyte molecules are effectively retained on the membrane for subsequent detection.

The main advantage of using CNF network in comparison with traditional porous materials such as PC, PTFE, nylon or filter paper, is its synergic quality of excellent molecular rejection rate and the lack of fluorescence and Raman backgrounds. This is hard to achieve with polymer films, as the most of them contain functional groups with strong fluorescence and Raman activity.[300] For example, direct combination of track-etched PC filter with plasmonic nanocrystals results in poor SERS performance because the PC substrate produces a very strong fluorescence background that drowns out all the Raman signals and prevents sensitive measurements (Figure 5.3d, solid black curve). The problem of high fluorescence background can be mediated by using long wavelength 785 nm excitation.[301] However, PC itself will produce multiple Raman band that convolutes with those of the analytes (Figure 5.3d). This greatly reduces the sensitivity of the SERS substrate, making the analyte hard to identify even at relatively high concentration in analyte solution. In contrast, the AuNR/CNF membrane is almost free from fluorescence and Raman backgrounds, and produces detectable Raman spectra with all the characteristic peaks of the R6G analyte even at $1/100^{th}$ (1 nM) of the detection limit (100 nM) for PC based substrates (Figure 5.3d solid blue curve).

Similarly, when substrates made of PTFE, Nylon 6,6, or carbon nanotube matrix are used for plasmonic nanoparticle immobilization and SERS detection, Raman backgrounds must be separately measured and subtracted using a blank sample.[283, 302] However, such background subtraction is fundamentally limited by the statistical fluctuations of the

background itself. This means the method will only work at fairly high analyte concentrations, leading to poor sensitivity despite the excellent filtration properties.[283]

Filter paper, being mostly composed of natural cellulose, is largely free of Raman backgrounds, but instead has considerable fluorescence backgrounds due to manufacturing additives.[303] Figure 5.3e shows the raw Raman spectra obtained from both AuNR/filter paper and AuNR/CNF before and after R6G filtration. It is immediately evident from the control sample in the graph that filter paper based SERS substrate showed significant fluorescence background, and weak interfering broad impurity Raman peaks at 1356 cm^{-1}, 1433 cm^{-1} and 2441 cm^{-1} whereas CNF membrane has a very low fluorescence background and almost featureless background in a window from 250 cm^{-1} to 2570 cm^{-1} (Figure 5.3e).

Figure 5.3f shows the spectra of the four samples in Figure 5.3e in the region between 1000 cm^{-1} and 2000 cm^{-1} after background subtraction and 10 point 2nd order Savitzky–Golay smoothing. Using the control sample as baseline, 6 characteristic R6G Raman peaks can be easily distinguished in the case of CNF based substrate. However, in the case of filter paper substrate, even though a lot of spectral features are present, none of the distinctive R6G Raman peaks can be observed (Figure 5.3f).

We also tested the SERS performance of pure AuNR film on two rigid substrates: Si wafer, which produces a low fluorescence background, and glass slide, which has similar refractive index to cellulose (Figure B.2). The analyte solutions were introduced either through dropcasting or dip and dry. Both substrates exhibited significantly poorer performance compared to AuNR/CNF, unable to resolve even the strongest Raman signatures of R6G molecules at 1 nM concentration (see Supporting Information for

detailed discussion). This means the excellent performance of AuNR/CNF cannot simply be attributed to the intrinsic properties of the AuNR, but rather involves both their favorable distribution in the CNF matrix and the analyte preconcentration facilitated by the nanofiltration.

5.3.2 Dual mode plasmonic response of AuNR/CNF film at different excitations

The high loading rate in traditional filtration based SERS substrate inevitably leads to clustering and board band optical response, meaning most of the plasmonic nanostructures are not driven resonantly. In this case, most of the Raman enhancement actually comes from the few nm sized gaps between coupled nanoparticles, these nano-gaps can support much higher EM field amplification than isolated nanoparticles, and are usually referred to as SERS hotspots.[304, 305] Therefore, even though the optical absorbance of the substrate might be dominated by individual nanoparticles, they contribute little to the actual SERS enhancement. In addition, the optimal excitation wavelength may not be at the maxima of the optical absorbance.

However, in our system, the optical properties of CNF membrane allow much lower nanoparticle loading rates to be used, leading to isolated nanorods and their small clusters (Figure 5.3a). The sparse distribution likely represents the natural state of AuNR in the feed solution, meaning the dimers or trimers probably originated from the solution and just got deposited into the CNF matrix. In this sense, the deposition is much more predictable than the high loading cases, where AuNRs interact with each other through capillary forces to form random large aggregates upon immobilization. We suspect, as long as the AuNR solution fed into the CNF membrane remains in the dilute regime, the relative distribution

of AuNR in the CNF matrix (dimers vs monomers etc.) will remain the same, because it is directly transferred from the solution. Thus, we did not further optimize the loading density, as the existing concentration already produces good results.

AFM topographical images of the AuNR/CNF membranes show monomer, dimer and imbedded monomer (Figure 5.4a, insets). Figure 5.4a shows the comparison between the experimentally measured extinction spectrum of AuNR/CNF membrane and those calculated by FDTD simulation for the three most representative AuNR arrangements. The broadening of the longitudinal mode peak can be readily explained by the formation of parallel AuNR dimers and the formation of completely imbedded AuNRs. More importantly, we observed a shift in transverse mode from 510 nm to 548 nm when AuNRs are transferred from solution to the CNF substrate (Figure 5.1b). Such a large shift cannot be explained by changes in refractive index environment alone, as even completely embedded nanorods show transverse mode at 518 nm (Figure 5.4a). Instead, this shift is largely due to nanorod side-to-side packing, as both our simulations and the literature data show such clustering leads to significant red shift of the transverse mode.[306, 307]

We mostly focus on dimers not only because it is the most abundant geometry in the observed clusters, but also because it is the only structure that is almost exactly resonantly driven at the 532 nm laser excitation wavelength (Figure 5.4a). In addition, the longitudinal mode of the dimer can still be efficiently driven at 785 nm, even though it is slightly off resonance. Figure 5.4b shows the field distribution of parallel AuNR dimers at the two laser wavelengths.

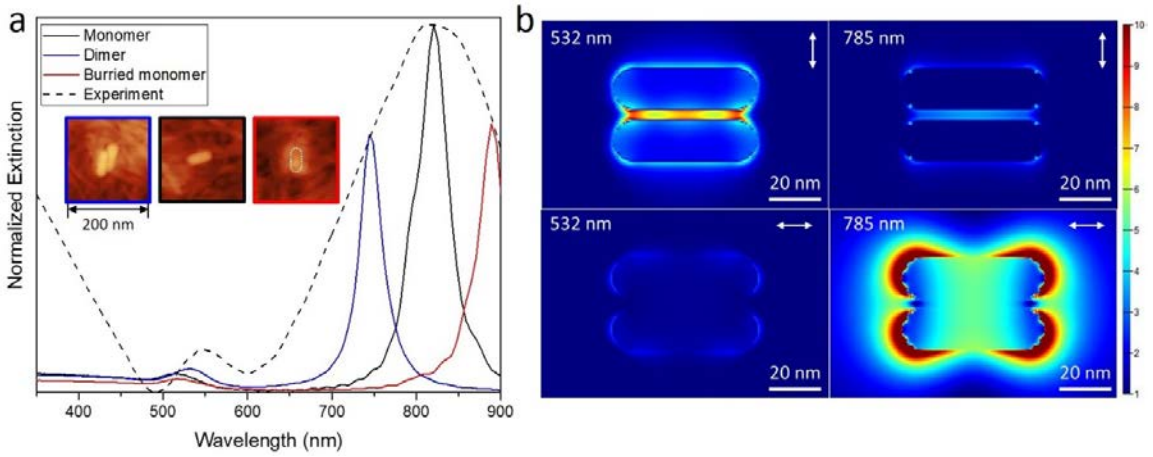

Figure 5.4 (a) UV-vis extinction spectrum of AuNR/CNF membrane and calculated extinction spectra of individual nanostructures. Inset: AFM topographica images of typical AuNR structures on CNF, color code of the outline corresponds to the color code in the calculated spectra. Z scale: 40 nm. (b) E-field distribution of AuNR dimers on CNF substrate, excited at two different Raman wavelengths. White arrow indicates laser polarization.

At 532 nm, the transverse modes of the AuNRs hybridizes to form a low energy (red shift) bonding plasmon mode, and regions of high E-field strengths (hotspots) appears inside the gap. At 785 nm, the longitudinal modes of the AuNRs hybridizes to form a high energy (blue shift) antibonding plasmon mode, and E-field hotspots are produced at the ends of the dimer.[306, 307] Such effective field-enhancement at both excitation wavelengths allows the AuNR/CNF membrane to be operated in dual excitation mode. Such a unique ability allows the AuNR/CNF membrane to utilize the high excitation efficiency of the 532 nm laser when detecting small molecules, and the fluorescence suppression of 785 nm laser when detecting biological cells and micro-organisms.

5.3.3 SERS detection of small molecules at 532 nm

The further SERS detection was evaluated by filtrating 20 mL of R6G solutions of different concentrations (Figure 5.5a). The inset of Figure 5.5a shows the detailed spectra between

1000 – 2000 cm^{-1} from 10^{-11} M concentration run (blue) and 10^{-12} M concentration run (brown) after background subtraction and smoothing. As expected, with decreasing concentration, the prominence of the R6G Raman peaks steadily decreased. The switch between the presence and the absence of six characteristic peaks in these two runs suggests a limit of detection (LoD) below 10 pM (S/N>3).[308]

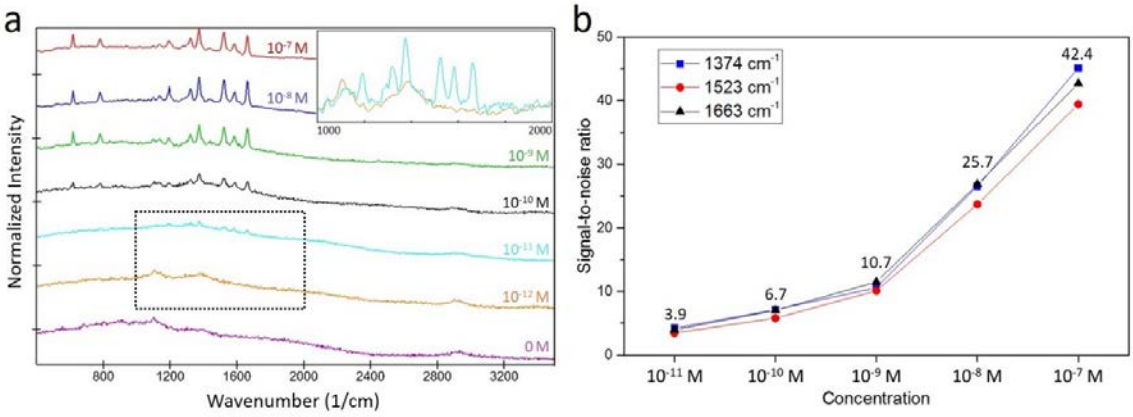

Figure 5.5 (a) Raman spectra collected from AuNR/CNF membrane after filtration of R6G solutions of various concentrations. Inset: Spectra region marked by the open black box after smoothing and background subtraction. (b) S/N ratio of three characteristic R6G Raman peaks as a function of R6G concentration, numbers at each point denotes the average S/N ratio of the three peaks.

It is important to note here that unlike common report of "theoretical LoD" where only one single strongest peak has S/N ratio larger than 3, the LoD we report here is the practical limit where the analyte can be identified from characteristic fingerprint.[276] At 10 pM concentration, all six characteristic Raman peaks in the window have S/N ratio larger than 3 and three of the strongest Raman peaks corresponding to R6G xanthene ring stretch mode at 1374 cm^{-1}, 1523 cm^{-1}, and 1663 cm^{-1} are quantifiable, leading to direct, unambiguous chemical identification.[309] In terms of such unambiguous organic molecule identification,

most SERS substrates reported in the literature are still limited in the μM range, while our sample is able to reliably perform in the pM - nM range.[283, 310, 311, 312]

Furthermore, the S/N ratios of the three characteristic peaks with the highest intensities at different R6G concentrations are plotted in Figure 5.5b. At the high concentration end (0.1 μM), the S/N ratio of the peaks at 1374 cm^{-1}, 1523 cm^{-1}, and 1663 cm^{-1} are 45.1, 39.5, and 42.7, respectively, corresponding to the relative intensity of the three Raman modes. As the analyte concentration lowers, the S/N ratio of the three peaks converge due to the relative increase in noise intensity. However, their intensity order (1374>1663>1523) remains the same, even down to 10 pM concentration (S/N ratio at 4.3, 3.5, and 4.0 respectively), meaning the target-identifying Raman fingerprint "shape" is preserved.

It is worth to note that unreliable quantification of analyte concentration, particularly at sub nM levels, has frequently plagued traditional SERS substrates that are not precisely defined, because of the random distribution of extremely sensitive SERS hotspots created by arbitrary interparticle coupling.[276] This issue is usually tackled by lithographically defined patterns or carefully controlled colloidal assembly.[313, 314] However, we can relax such requirements due to the uniform, predictable, and sparse distribution of AuNR in our CNF substrate. The data in Figure 5.5b shows a strict monotonic relation between analyte concentration and S/N ratio, meaning simple linear extrapolation will be able to yield semi-quantitative (order of magnitude) estimate on the R6G concentration of any unknown sample.

Moreover, we also tested the performance of AuNR/CNF membrane in detecting methylene blue (MB), which is non-resonant at 532 nm. Compared to R6G, MB has

significantly smaller Raman cross-sections. Non-resonant SERS detection limits in the 10^{-3} M to 10^{-5} M range are commonly reported in literature.[315, 316] However, with our AuNR/CNF membrane, the strongest peak at 1632 cm^{-1}, which corresponds to C-C ring stretching, can still be detected down to the 10^{-7} M concentration (Figure B.3).[315] This is noteworthy especially considering such results are obtained by an Au-based system at fluorescence-inducing blue-shifted off-resonance excitation. Thus, AuNR/CNF membrane not only demonstrates excellent performance of detection of resonantly excited R6G Raman markers but also displays great utility in detecting non-resonant organic molecules with relatively weak Raman scattering.

5.3.4 SERS detection of cells at 785 nm

Next, we tested the capability of AuNR/CNF membrane to detect waterborne bacteria at NIR excitation conditions. Raman identification of biological cells has always been problematic due to two reasons. First, Raman active molecules in living cells exist in a complex mixture and have very low individual concentrations, meaning extremely long integration times ranging from tens of minutes to even hours are required.[317, 318] Second, many cellular components are autofluorescent, laser excitation at short wavelengths can easily cause fluorescence background that drowns out whatever weak Raman signal the cell might produce.[319, 320] This can be mitigated by increasing the laser excitation wavelength. However, as mentioned, long wavelength lasers have low Raman scattering efficiency, thus requiring even longer integration times. Here, we address this problem by utilizing the large EM enhancement from the longitudinal mode of nanorods to compensate for the loss in Raman scattering cross-sections caused by the long wavelength excitation.

We filtrated *E Coli.* spiked solution through the AuNR/CNF membrane and performed Raman spectroscopy using both 532 nm and 785 nm excitations (Figure 5.6). When 532 nm excitation is used, significant fluorescence is induced (Figure 5.6a). After background subtraction, two very weak broad peaks in the 800 cm^{-1} to 2000 cm^{-1} region can be observed (Figure 5.6b). However, there is almost perfect spectra overlap with the control sample (red curve, only pure H_2O is filtrated) in this region, meaning these two peaks originated from the membrane itself. In fact, they can all be assigned to vibrational bands in cellulose: the peak at 1112 cm^{-1} can be assigned to the C–O–C glycosidic ring stretch,[321] while the peak at 1395 cm^{-1} can be assigned to H-C-C, H-C-O, H-O-C bending.[322, 323] No additional Raman peaks are observed that can be assigned to *E.Coli.* This likely means the strong autofluorescence induced by the 532 nm completely masks the weak Raman scattering from the cell.

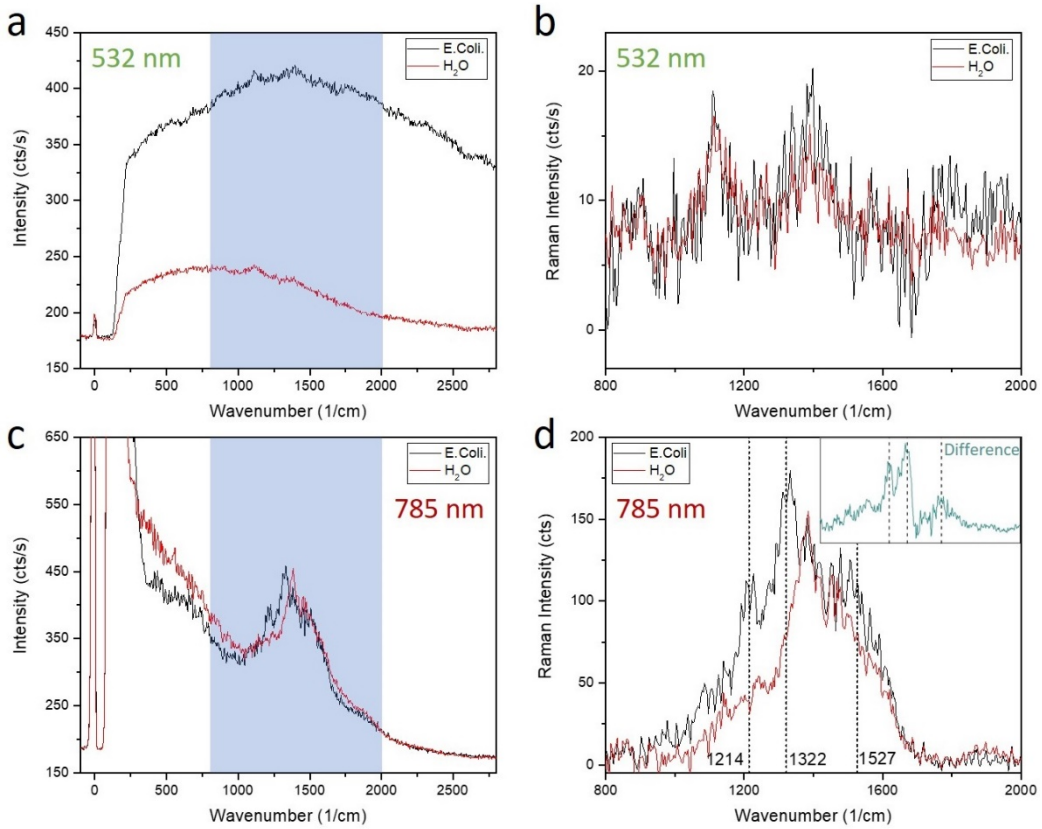

Figure 5.6 (a) Raw spectra collected from AuNR/CNF membrane after filtration of *E.Coli* spiked solution (black) and H_2O (red), excited at 532 nm. (b) Spectral region between 800 cm^{-1} and 2000 cm^{-1} after background subtraction from (a). (c) Raw spectra collected from AuNR/CNF membrane after filtration of *E.Coli* spiked solution (black) and H_2O (red), excited at 785 nm. (d) Spectral region between 800 cm^{-1} and 2000 cm^{-1} after background subtraction from (c). Inset: spectra difference obtained by subtracting the red curve from the black curve; dashed lines correspond to the same spectral locations in (d).

However, when the same sample was tested with 785 nm excitation, no fluorescence background increase was observed compared to the control sample, signifying successful fluorescence suppression (Figure 5.6c). Further examination of detailed spectra between 800 cm^{-1} and 2000 cm^{-1} shows several characteristic peaks above the red control baseline (Figure 5.6d). By subtracting the baseline red curve from the black curve, three distinctive peaks can be identified that are in accordance with reported *E. Coli.* Raman spectra in the literature (Figure 5.6d, inset).[324] The peak at 1214 cm^{-1} has been traditionally assigned to

the amino acid tyrosine,[325] but assignments to phenylalanine and tryptophan have also been suggested.[317] The peak at 1322 cm^{-1} and 1527 cm^{-1} can be assigned to guanine.[326, 327]

It is important to note that in our experiment, only 100-200 seconds integration time is needed to produce identifiable signal, instead of hours as required by traditional Raman.[317] The CNF matrix will produce some broad spectral features, but because of the low background noise, such features do not interfere with the identification of unique Raman bands. Additionally, the bacteria are directly captured by the porous membrane, drastically simplifying sample collection process. Such capabilities can be immensely useful for fast in-field sample collection.

5.4 Conclusions

In summary, we fabricated a novel CNF based molecular filtration and SERS detection platform. The nanofiltration capabilities of the CNF matrix allows for effective pre-concentration of the analyte molecules. Combined with the optical properties of CNF, such as high transparency, low light scattering, low fluorescence background, and cellulose's low Raman background, excellent sensing performance can be achieved with low loading density of plasmonic nanocrystals. The limited nanorod aggregation also allows the unique dual mode near resonate excitation of nanorod dimers for high E-field enhancement at two common Raman wavelengths, which facilitates the versatile detection of different analytes, ranging from molecules to biological cells. To the best of our knowledge, SERS performance is at least 2 orders of magnitude better than traditional porous SERS substrates.

CHAPTER 6. HETEROGENEOUS FORWARD AND BACKWARD SCATTERING MODULATION BY POLYMER-INFUSED PLASMONIC NANOHOLE ARRAYS

6.1 Introduction

Controlled light transmission through sub-wavelength orifices in thin metallic films has been well documented.[328, 329, 330] This intriguing phenomenon is due to the excitation of a special kind of light coupled electron resonances at the metal-dielectric interface known as surface plasmonic polaritons (SPP).[331] By arranging plasmonic nanoholes of varying dimensions into large arrays of different periodicity and symmetry, different plasmon resonances can be excited by incident light, thus different light transmission properties can be achieved.[332, 333] Several pioneering papers have already examined in detail the theoretical aspects of such optical element.[334] Some even explored more advanced geometries such as aligned multilayered nanohole array (NHA), where the intercoupling between SPPs at different interfaces can modulate the transmission peak or even lead to new resonant modes;[335] or air gap coupled NHA, where the width of the air gap can be used to induce constructive or destructive interference.[336]

Because transmission spectra can be modified by changing the nanohole array geometry, there has been great interest to utilize them as pre-programmed color filters for advanced imaging and display technologies.[337, 338, 339, 340, 341] Multiple studies have been conducted on the use of diverse NHAs coupled with nematic liquid crystals, electrochromic polymers, and Fabry–Pérot devices as plasmonic filters that can be turned on and off by electrical

signals.[342, 343, 344, 345, 346] Recent explorations in novel NHA structures, such as asymmetric nanoholes, demonstrated polarization dependent colors.[347] Fabricated metal-insulator-metal multilayered nanoholes have demonstrated the ability to support Fano resonances with enhanced sensitivity to refractive index changes of the surrounding media.[348]

However, while these studies focused on the forward scattering properties of NHAs, which are immediately relevant to backlit color displays, little attention has been paid to their backward scattering properties, especially when illuminated at oblique angles. In fact, there is a good reason to expect the optical response of periodic plasmonic nanoarrays to be drastically different when they are used as backward scatterers, since it is already known that the transmission profiles of plasmonic NHAs are angle dependent.[349] However, monitoring of both forward and backward scattering under variable refractive conditions is rarely conducted due to experimental challenges.

In this study, we investigate both the forward and backward scattering of NHAs infused with a redox active electrochromic polymer (ECP), poly(2,2'-bis(2-ethyl-hexyloxymethyl)-3,4-propylenedioxythiophene) (ECP-M), which switches between a purple/magenta neutral state and a highly transmissive oxidized state, with modulated refractive index (Figure 6.1). The modulation of the dielectric environment is accomplished conveniently and reversibly via applied electrochemical potential in an electrolyte.[350, 351, 352, 353] It was found that there are indeed significant differences in backward and forward scattering characteristics, especially in their relative sensitivity to refractive index modulations. When subjected to an applied potential, spectra measured in the forward scattering mode shows selective attenuation, while spectra measured in the backward scattering mode shows single-peak red-shifting. Electrodynamic simulations show that

these differences are due to the highly oblique illumination used for backward scattering, exciting multiple complex plasmon resonances that collectively influence the integrated optical output.

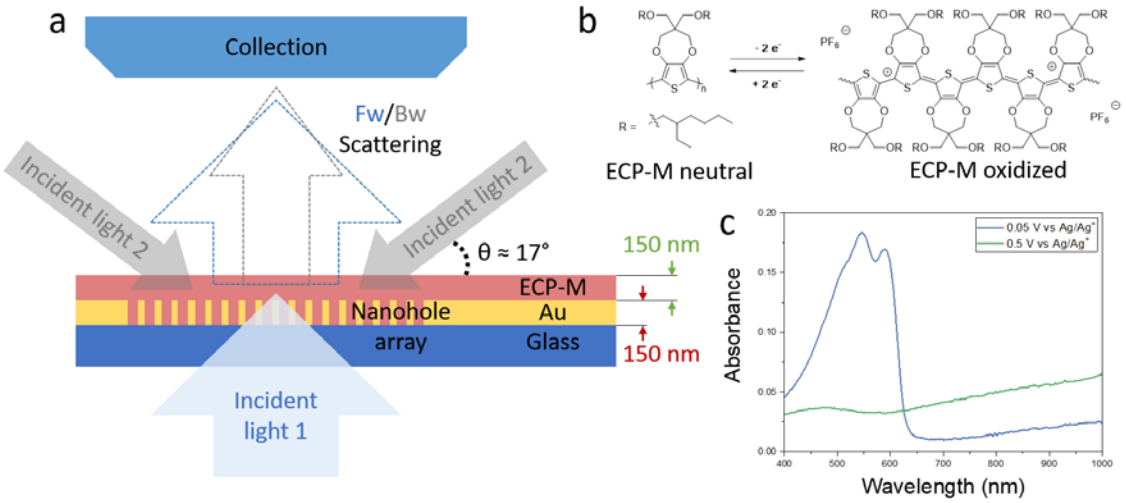

Figure 6.1 (a) The experimental setup of ECP-M infused Au NHA on glass slides. In forward scattering measurement, light comes in from the bottom (incident light 1) and is collected at the top (blue dashed arrow). In backward scattering measurement, light comes from the top at 73° incidence angle (incident light 2) and is collected at the top (grey dashed arrow). (b) Molecular structure and electrochemical switching of ECP-M. (c) UV-vis spectra of ECP-M in neutral (blue) and oxidized (green) states.

6.2 Experimental Details

6.2.1 Materials

Tetrabutylammonium hexafluorophosphate ($TBAPF_6$) acetonitrile (ACN) and propylene carbonate (PC) were purchased from Sigma Aldrich and used without further purification. The ECP-M electrochromic polymer was synthesized as described previously from the corresponding alkoxy-substituted 3,4-propylenedioxythiophene monomer by oxidative polymerization with iron(III)chloride.[353] The molecular mass of the polymer is 12.4 kDa

with a dispersity (Đ) of 1.8 as determined by gel permeation chromatography (GPC) in tetrahydrofuran (THF) versus polystyrene (PS) standards.[166]

6.2.2 Fabrication of NHA

The plasmonic NHA was manufactured via focused ion beam direct writing lithography. First, 150 nm thick of Au film is evaporated onto glass slides using Denton Explorer E-beam evaporator at a rate of 0.5 Å/s at 10^{-6} Torr. The deposition is monitored by a quartz microbalance mass sensor. Next, the substrate is transferred to the FIB for patterning. After initial optical characterization of the pristine nanoholes. 20 µL of concentrated ECP-M toluene solution was spincoated onto the NHA substrate at 2000 rpm, resulting in a 150-nm thick film.

6.2.3 Electrochemical switching

Electrochemical measurements were carried out using a VersaSTAT3-200 (Princeton Applied Research) with Versastudio software in a three-electrode cell with a Ag/Ag^+ reference electrode (10 mM $AgNO_3$ in 0.5 M $TBAPF_6$/ACN, $E_{1/2}$ is 76 mV for ferrocene), a Pt wire as the counter electrode, and Au coated substrate with patterned NHAs as the working electrode.[356] The electrolyte is 0.5 M $TBAPF_6$ in PC, individual switching is done using chronoamperometry setting holding the working electrode at designated potential against reference electrode for 10 s. Cycling experiment was performed using cyclovoltammetry setting at scan speed of 0.2 V/s.

6.2.4 Optical characterization

All optical measurements done in air, the oxidative state of the substrate is switched in an electrochemical cell between measurements in electrolyte and systems were completely dried before optical measurements. The extinction spectra of ECP-M are collected using 150 nm pure ECP-M film on ITO substrate with extinction from the blank ITO subtracted. The substrate is then placed into the electrochemical cell, switched to another oxidation state, dried, and measured again.

6.2.5 FDTD simulations

An array of 9 nanoholes (3 holes each in two primary axis) of specified periodicity, diameter and symmetry were modeled as through holes in a 150-nm thick Au film on top of 1-micron thick SiO_2 and filled with respective dielectric materials (air, ECP-ox, ECP-neu). An additional 150-nm thick ECP film of respective oxidative states is constructed on top of the Au film when simulating ECP coated NHAs. The refractive index values of ECP-M at oxidized and neutral states were taken from previous work where they were measured for thin films with spectroscopic ellipsometry.[166]

The simulation region was restricted to the center unit cell defined in the x,y Cartesian coordinates with 1 micron z span. A mesh override was applied to the nanoholes with a 10 nm mesh size and 10 nm buffer in the x-, y-, and z-directions. For simulation of forward scattering, a broadband Bloch planewave source with 400-1000 nm wavelength span was used for illumination. The injection plane was placed inside the SiO_2 substrate with propagation direction pointing upward at normal incidence angle. Periodic boundary conditions were applied in both x and y directions. Anti-symmetric and symmetric symmetries are applied to reduce simulation time. 12-layer perfect matched layer (PML)

boundary condition was applied in the z direction to absorb radiation energy with minimum scattering. For simulation of backward scattering, a narrowband (band width: 8.825 THz) Bloch planewave source defined in the time domain with 50 fs pulse length and 100 fs offset is used for illumination. The injection plane was placed above the structures in air with propagation direction pointing downward at 73° incidence angle. Bloch boundary conditions were applied in both x and y directions. Anti-symmetric symmetry was applied to reduce simulation time. 36-layer PML boundary condition was applied in the z direction to absorb radiation energy with minimum scattering. The source frequency was swept from 300 THz to 750 THz in 200 individual simulations data at center frequency was recorded and complied to yield a full spectrum.

6.3 Results and Discussion

6.3.1 NHA, ECP-M, and illumination setup

NHAs with different diameter, periodicity, and symmetry are fabricated on 150 nm thick E-beam evaporated Au on glass substrates using focused ion beam milling. Four different arrays were fabricated: p250s, p350s, p340h, and p420h. The arrays were identified by their periodicity and symmetry as demonstrated in Figure 6.2a and Table 1. For example, p250s is a square (s) array with 250 nm periodicity, while p420h is a hexagonal (h) array with 420 nm periodicity. These geometric parameters of the NHAs are arbitrarily chosen based on previous research to test the universality of the ECP tuning effect.[337]

Table 1 Geometries of NHAs

NHA Designation	Periodicity (P)	Diameter (D)	Symmetry
p250s	P_x=P_y=250 nm	125 nm	Square
p350s	P_x=P_y=350 nm	175 nm	Square
p340h	340 nm	180 nm	Hexagonal
p420h	420 nm	240 nm	Hexagonal

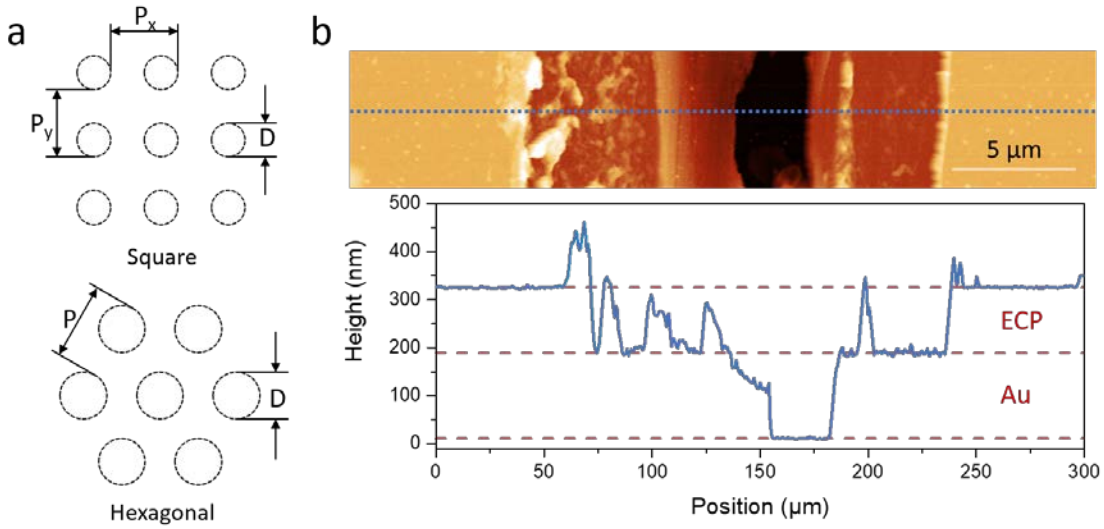

Figure 6.2 (a) The geometries and dimensions of the nanohole arrays. (b) AFM image of scratched ECP-Au-Glass structure, (Z scale: 500 nm) and cross-section profile along the dotted line, clearly showing the 3-layer structure.

After initial hyperspectral characterization of the as-fabricated NHAs, the entire substrate was coated with an additional ~150 nm ECP film. Figure 6.2b shows the AFM image and

the corresponding cross-sectional profile of a scratched line test on the pristine area of the substrate. A wide strip of ECP film cleanly separated at the ECP-Au interface upon incision and drag of the blade and reveals the Au film underneath. In the middle of the scratch line, where the tip of the blade sits, a narrow strip of Au is also scratched away, revealing the glass base.

Two illumination schemes are used to study the directional optical response of the ECP-M coated NHAs with all measurements conducted in air after film drying (Figure 6.1, see Experimental). In the forward scattering setup, broadband light from a halogen lamp illuminates the NHA at zero incidence through a glass substrate from beneath (Figure 6.1a, solid blue arrow). This essentially corresponds to the brightfield transmission mode in microscopy. The light is transmitted/forward scattered by the NHA and collected from above by an objective (Figure 6.1a, open blue arrow). In the backward scattering setup, light from the same source is introduced to the NHA at ~73° (fixed by dark field objective) incidence through air from above (two solid gray arrows), scattered by the NHA, and collected by the same objective from above (Figure 6.1a, open gray arrow). This corresponds to the darkfield reflection mode in microscopy

Figure 6.3 shows the SEM and corresponding hyperspectral images of the as-fabricated NHAs (without ECP coating) at the two illumination conditions described above. Upon illumination, NHAs of different structural geometries display different colors, a clear indication of plasmonic effects. As the illumination condition changes, the observed color also changes correspondingly for each NHA. The colors are fairly consistent within each NHA. However, brightness non-uniformities and small color variations are present. These are mainly caused by defects and inhomogeneities during FIB milling. Unlike other finely

grained metals like Al, E-beam evaporated Au films have grain size on the order of ~30 nm (Figure C.1a), ion milling of structures on a similar scale will inevitably yield less well-defined structures as the sputtering rate depends on the crystallographic orientation of the grain. As shown in Figure 6.3a, this nonuniformity in milling efficiency directly translates to some limited areas having blind holes instead of through holes, especially for arrays with smallest periodicity. Since plasmon resonances are dictated by structure geometry, such nonuniformity leads to the observed color/brightness differences. The effect is mitigated with larger hole diameter, causing p420h to have the highest brightness/color uniformity (Figure 6.3b, c).

In the backward scattering setup, we see another effect of imperfect FIB milling, the NHAs are surrounding by bright edges. This is due to the fact that despite the primary ion beam being blanked, the “un-milled” areas inside the arrays will still be partially etched from secondary sputtering, resulting in NHAs having lower elevations than the rest of the Au film (Figure C.2b-c). The elevation difference creates a step at the edge, which specularly reflects the oblique illumination into the collection objective. In addition, point like particulate contamination on Au surface can also be seen (Figure 6.3c). However, these contaminates do not appear to interfere with the NHA structures. These defects can all be eliminated by using single crystalline gold substrates in clean packaged environment, or by switching to other non-sticking, small grained plasmonic metals such as aluminum, should practical needs arise.

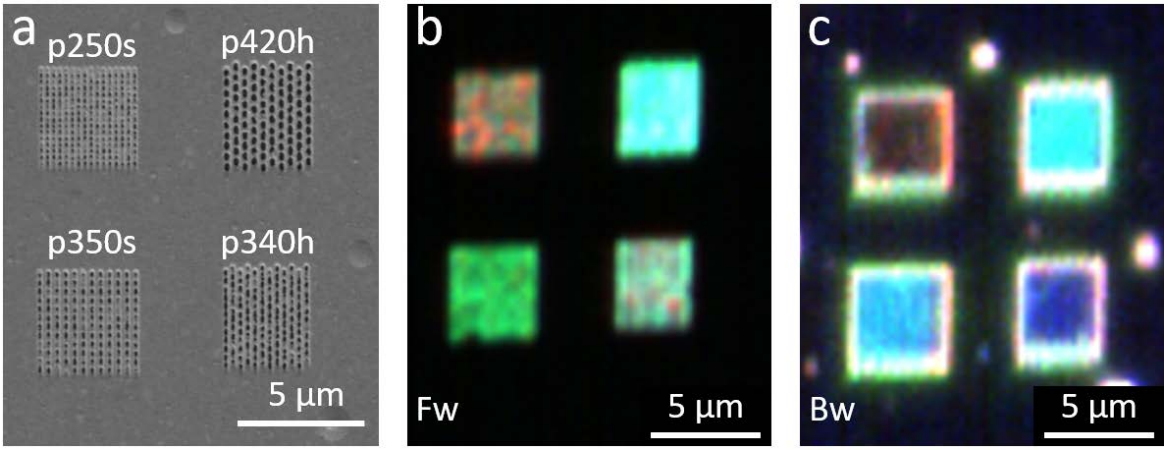

Figure 6.3 SEM image of NHAs with different geometries (see Figure 6.2a) (a). Hyperspectral image of the corresponding pristine arrays under forward (b) and backward (c) scattering illumination conditions.

The electron-rich alkoxy-substituted ECP-M was chosen as the electrochemically-controlled medium due to its excellent solvent compatibility, electrochemical stability, and low oxidation potential as was demonstrated earlier (see chemical structures in Figure 6.1b).[166] The polymer appears magenta/purple in its charge neutral state and, therefore, is termed ECP-Magenta (ECP-M).[166] ECP-M can be switched between neutral and oxidized states by applying an electrochemical potential at 0.05 V and 0.5 V vs. Ag/Ag^{+}, respectively (Figure C.2). In the neutral state, ECP-M has a broad absorption band from 410~620 nm with two absorption peaks at 547 nm and 588 nm (Figure 6.1c). Upon removal of electrons from the conjugated backbone, ECP-M transitions into a colorless and transmissive oxidized state at 0.5 V (Figure 6.1c). A low residual absorption remains across the visible spectrum, resulting in near-complete visual transparency under these conditions (Figure 6.1c).

6.3.2 Electrochemical switching of ECP-M infused NHA

Figure 6.4 shows the hyperspectral spectra and corresponding image from two different NHAs with the smallest (p250s) and the largest (p420h) hole diameters collected at two different illumination conditions and different dielectric environments: bare nanoholes and nanoholes covered by ECP coating in the oxidized state (ECP-ox) and in the neutral state (ECP-neu). Before coating with the ECP, the forward scattering spectrum of p250s NHA shows two broad plasmon resonances at ~510 nm and ~720 nm due to the excitation of surface plasmon resonances at the metal/air and at the metal/glass interface, respectively (Figure 6.4a).[338] ECP-M in its oxidized state does not affect these two peaks besides overall modest intensity damping due to non-specific light absorption (Figure 6.4a). The lack of modulation is also evident from the absence of color change between the forward scattering images of the respective array in Figure 6.3b and Figure 6.4b.

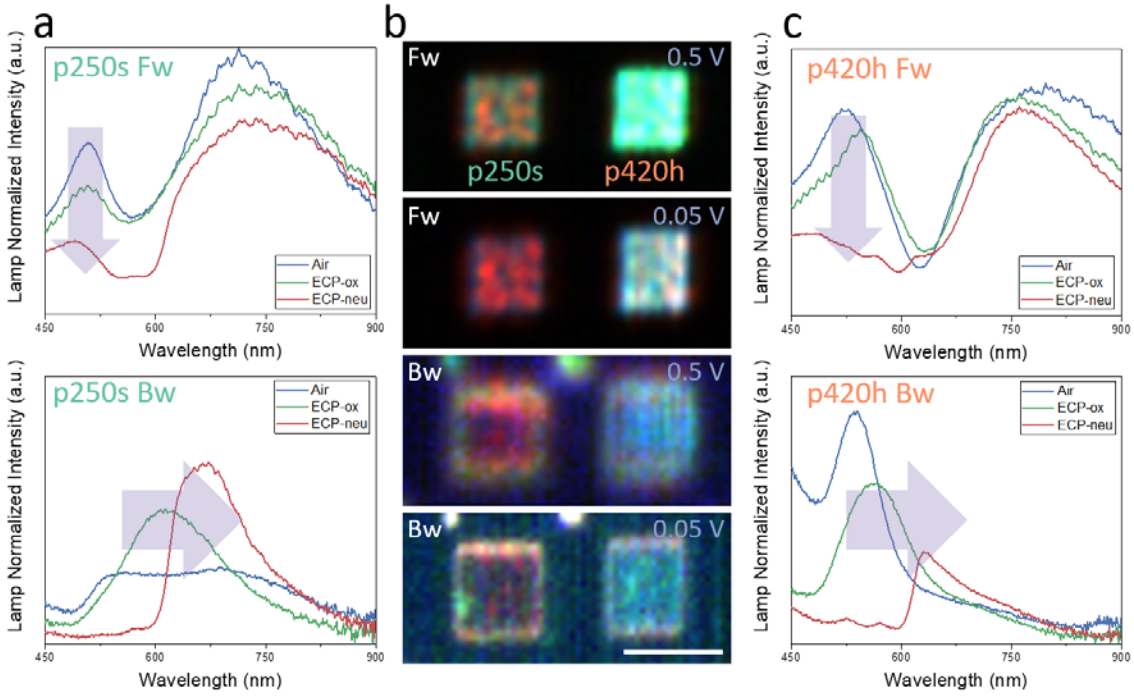

Figure 6.4 (a) Forward (Fw) and backward (Bw) scattering spectra of the p250s array in different dielectric environments: air, ECP-M in oxidized state (ECP-ox), and ECP-M in reduced state (ECP-neu). (b) Color image of p250s and p420h arrays under

different ECP oxidation states: 0.5V (oxidized), 0.05 V (reduced). Scale bar: 5 μm. (c) Fw and Bw scattering spectra of the p420h array in different dielectric environments.

In contrast, when the ECP-M coating is switched to the neutral state by applying an electrical potential of 0.05 V, the plasmon peak at ~510 nm became severely attenuated while the peak at ~720 nm remained largely unaffected (Figure 6.4a). The selective damping of the ~510 nm peak occurs because the presence of ECP-M's absorption band is in this wavelength range (Figure 6.1c). Such selective damping causes the substantial changes in the color of the NHA, changing it from brown to red (Figure 6.4b)

When the illumination conditions are switched to those in backward scattering measurements (Figure 6.1a, incident light 2), completely different optical responses are observed (Figure 6.4a). Backward scattering showed a single plasmon peak with sequential redshift from initial 548 nm for bare NHA to ~611 nm for ECP-oxidized state, and further to ~664 nm for ECP-neutral state (Figure 6.4a). The oxidized/neutral state switching of the ECP media also resulted in significant visual color change (from red to brown color, Figure 6.4b bottom two figures).

The same trends are even more pronounced in the optical responses of the p420h array with larger spacing and hole diameter of 240 nm (Figure 6.4c). In the forward scattering spectrum, we again see damping in the 450-600 nm range caused by increasing light absorption by the ECP coating. The intensity ratio between the two plasmon peaks at ~530 nm and ~765 nm changed about twofold, from 0.85 in the oxidized state to 0.40 in the neutral state. In the backward scattering, a single peak also sequentially redshifted to ~561 nm and ~633 nm after covering with ECP-ox and ECP-neu coatings (Figure 6.4c).

Figure 6.5 shows the forwarding and backward scattering spectra of all 4 NHAs of different periodicities, hole diameters and symmetries. All of them showed similar behavior, mainly peak attenuation in the 450-600 nm range for forward scattering (arrows in Figure 6.5a-d), and peak attenuation plus significant red-shifting in backward scattering (arrows in Figure 6.5e-h), suggesting such trends are a general property of polymer-infused NHAs and not restricted to a specific array configuration.

It is known that, because plasmon polaritons exist at metal surfaces, the mode frequency in any plasmonic system will necessarily depend on its dielectric environment.[354] As shown in our previous work with plasmonic nanostructures embedded in ECP coatings, this property can be exploited to electrically tune the wavelength of the extinction plasmonic peaks of nanoparticles.[220, 166, 355, 356] By changing the refractive index of the medium the plasmonic nanoparticles are dispersed in, their localized surface plasmonic resonance (LSPR) peak can be shifted to higher or lower wavelengths depending on the changes in refractive index in the spectral region of interest and the geometry of the nanoparticle.[357] For instance, previous results employing Au nanorods coated by ECP-M shells showed plasmonic peak shifts of up to 30 nm.[166]

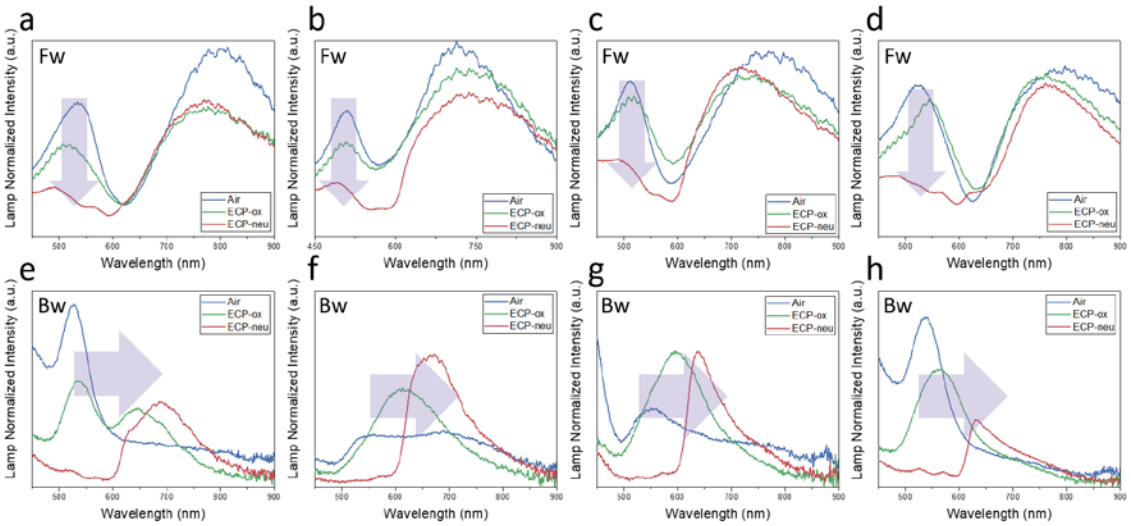

Figure 6.5 Forward scattering spectra of (a) p350s, (b) p250s, (c) p340h, (d) p420h arrays in air (blue), ECPox (green), and ECPrd (red). Backward scattering spectra of (e) p350s, (f) p250s, (g) p340h, (h) p420h arrays in air (blue), ECPox (green), and ECPrd (red).

Considering the present results, the NHA's response to changes in the dielectric environment is unexpected and cannot be explained by simple unidirectional radiation model that applies well to the individual randomly-oriented nanoparticles. In contrast, the spectral responses of the uniformly ordered NHAs are found to be highly dependent on the illumination conditions. For forward scattering, the lack of peak shifts means the plasmon resonance modes excited have low sensitivity towards the refractive index change, instead, the spectral changes are mainly produced by the attenuation by the ECP-M absorption. Yet, for backward scattering, the same ECP modulation produced very large red-shifts of the plasmon peak (70-120 nm), suggesting the plasmon modes excited in this illumination configuration are extremely sensitive to refractive index modulation.

For reference, we also calculated the color coordinates from the normalized spectrum of all the ECP infused NHAs in CIE 1931 color space (Figure C.3). As expected, when ECP

is switched from oxidized form to neutral form, the color coordinates shifted correspondingly. It is interesting to note that the shifts in color space are much larger in the backward scattering configuration as large spectral shifts are induced in addition to total intensity attenuation. The color range presented here are somewhat limited as we are primarily focused on the optical response of NHA under oblique illumination. For a wide range color palettes from plasmonic structures see several excellent examples.[341, 358, 359, 360]

6.3.3 Theoretical aspects

To better understand the possible electrodynamics behind such behaviors, we further performed finite difference time domain (FDTD) simulations on the representative p250s NHA array. The simulation of forward scattering is straightforward, as light is injected and collected at the normal angle (Figure 6.6).[361, 362]

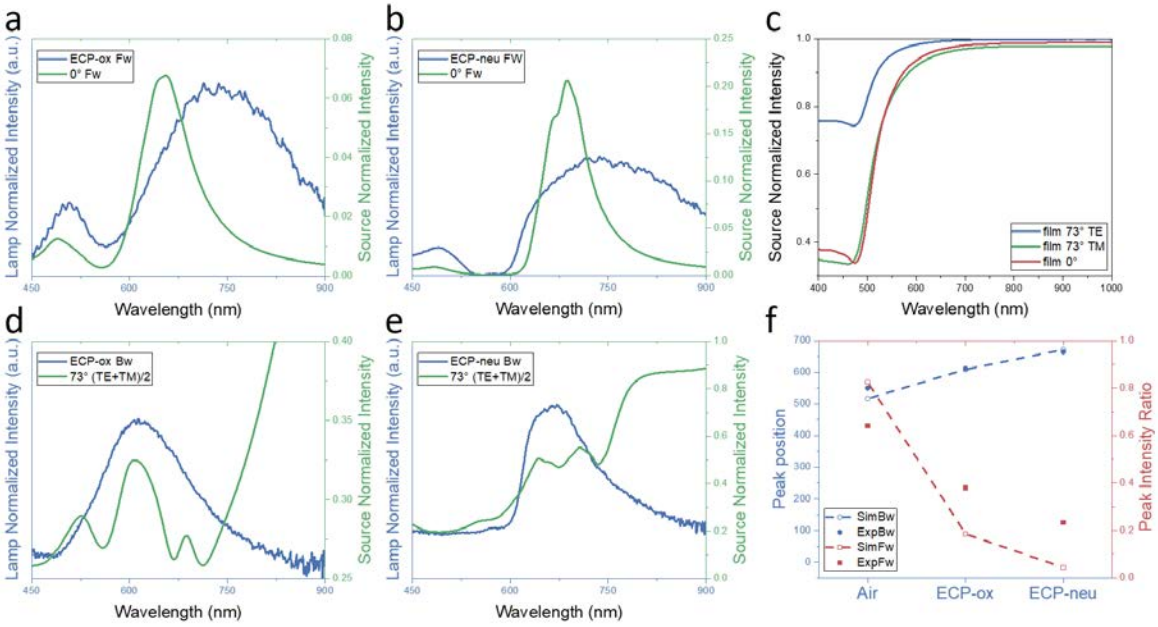

Figure 6.6 Measured forward scattering spectra (blue) of p250s array compared with FDTD results (green) for ECP oxidized (a) and reduced (b) states. (c) FDTD backward scattering results of 150 nm thick Au film at different angles and

polarizations. Measured backward scattering spectra (blue) of p250s array compared with FDTD results (green) for ECP oxidized (d) and reduced (e) states. (f) Trends in experimental data and FDTD simulations in terms of peak intensity ratio for forward scattering and in terms of peak position for backward scattering.

Because the angle of incidence is 0°, there will be no phase difference on the incident light both spatially and temporally. In comparison, simulation of backward scattering is significantly more complex due to both interference from specular refection and the phase difference build up among the frequency components at high incidence angle (see Figure C.4 and relevant discussion in Appendix C).

Furthermore, Figure 6.6 a, b shows the comparison between the FDTD simulations and measured results of the forward scattering of NHAs at different ECP oxidation states. As we can see from this comparison, the general spectral features, such as the existence of two plasmonic peaks and their relative intensities are well reproduced by FDTD. The simulation clearly showed the attenuation in the 450-600 nm range as the ECP coating is switched from ECP-ox to ECP-neu state. However, there is a blue-shift in the peaks and the measured spectra are broader than those simulated. These differences can be mainly attributed to defects in the NHAs with the holes being slightly larger than specified, causing a red shift from the ideal structures. In addition, the relatively large grain sizes of the evaporated Au film and resulting variations in hole dimensions broaden the plasmonic peak (Figure 6.3a).

On the other hand, in backwards scattering simulation, due to the periodic nature of the setup, light from specular reflection is included in simulated spectra (see discussion in SI). Thus, the spectra simulated all bear the hallmark, such as skewed high intensity in the infrared, of the reflection spectrum of bulk Au (Figure 6.6c red curve). In addition, because

TE and TM polarized modes behave differently, we averaged simulation results from both modes to generate un-polarized spectra (Figure 6.6c blue and green curves). Un-polarized backward scattering spectra of NHAs were simulated for both ECP-ox and ECP-neu states of the polymer coating (Figure 6.6d,e). It is clear from direct comparison, a general fair match in the main peak locations is observed for both states with excessive reflection at longer wavelength as discussed above. In addition, the simulated spectra showed multiple secondary modes underlying a single peak not detected in experimental spectra due probably to preferential source polarization (as discussed later), limited spectral resolution, and NHA fabrication imperfections.

Despite these complications, the calculated spectra are broadly in agreement with our experimental observation of significant differences in the modulation behavior of forward vs. backward scattering of polymer infused NHAs under variable electrochemical potential. Both the relative ratio between the two peaks (as a measurement of attenuation) in the forward scattering, and the peak position (as a measurement of refractive index induced plasmonic peak shifting) in the backward scattering, are replicated and suggest that plasmon modes excited in the backscattering setup are more sensitive towards changes in the refractive index compared to those excited in the forward scattering (Figure 6.6f).

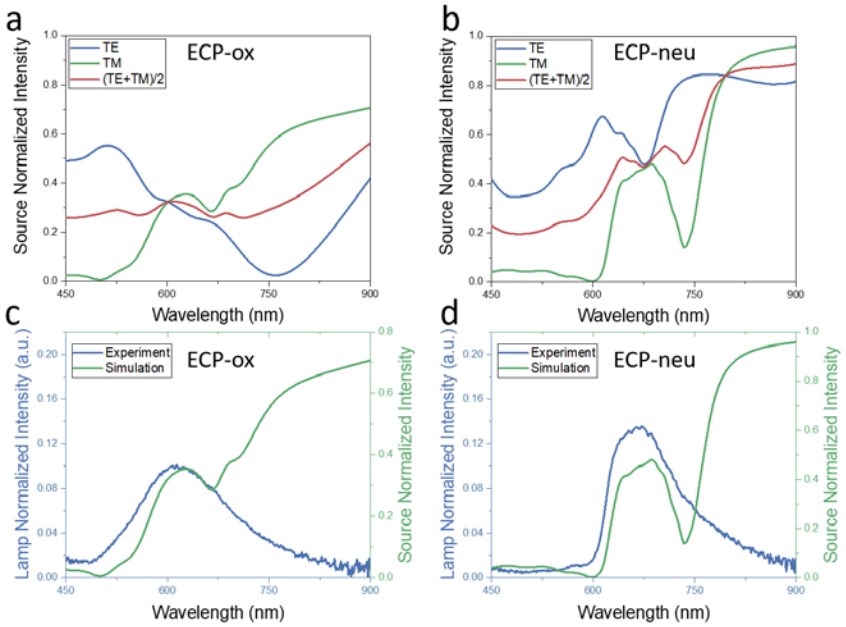

Figure 6.7 Decomposition of FDTD simulated unpolarized back scattering spectra of p250s array into TE and TM polarized components for ECP oxidized (a) and neutral (b) states. Measured backward scattering spectra (blue) of p250s array compared with FDTD results of pure TM polarized light (green) for ECP oxidized (c) and neutral (d) states.

In addition, the simulation suggests the plasmonic resonances excited by TE and TM polarization modes behave very differently from each other (Figure 6.7a, b). Changes in refractive index also prompted much larger response when the two modes are individually considered. It is possible that at highly oblique angle of illumination, slight changes in the permittivity of the infused polymer can cause totally different plasmonic modes to be excited in the NHA. Interestingly, further comparison of the simulated spectrum with experimental results indicated sources with pure TM polarization produced a better fit than unpolarized sources, suggesting preferential TM polarized illumination. This is expected, as in our reflected darkfield setup, the illumination light column goes through a reflector lens assembly that partially polarizes the illuminating light. However, quantitative ratio of

this polarization is unknown, so simulations using unpolarized sources are still presented here for demonstration of the universality.

A natural supplement to this work would be to investigate the optical properties of NHAs under transmission darkfield setup, in which light is coming from beneath the substrate at a highly oblique angle and the spectrum is collected by objectives lens above the substrate (Figure C.5a). Due to limitations in our hyperspectral system setup, we cannot conduct such an experiment. However, we did simulate the response of p250s array under such conditions (Figure C.5). The results suggest the transmission intensities are very low (< 1%), and there exist a cut-off frequency where almost no light is transmitted. ECP modulations do seem to produce large spectral variations and have some interesting characteristics of interest for future research (see Figure C.5 and relevant discussion in Appendix C).

6.4 Conclusions

In summary, we have observed dramatic differences in the forward and backward scattering properties of polymer-infused plasmonic NHAs under variable matrix permittivity modulated by electrochemical potential. The modulation of backward scattering is significantly different compared to scattering in the forward direction. Although for forward scattering, the effect of ECP modulation is mostly dominated by attenuation of plasmonic peaks, the backward scattering of NHAs show large peak shifts due to the changes in plasmon resonance conditions. These asymmetrical optical response of polymer-metal NHA structures can be useful for various prospective applications, such as logic operations in photonic circuits.[363, 364, 365] The polarization and angle dependent

backscattering response might find use in configuring plasmonic-based color filter with novel illumination geometries.[366] Finally, the extreme refractive index sensitivity of polymer-metal NHAs in the backward scattering setup could be further extended to SPR-type molecular sensors [367, 368, 369] with improved performance in the detection of subtle refractive index modulation caused by absorption events.[276, 370, 371, 372, 373, 374]

CHAPTER 7. MODULATION OF PHOTONIC CAVITY MODES BY NANOSTRUCTURED PLASMONIC RESONATOR

7.1 Introduction

Due to their capability to confine light to deep subwavelength volumes, plasmonic nanostructures have important application in nanophotonics.[4] Briefly, when metallic nanoparticles are excited by electromagnetic wave of optical frequency, their conduction electrons, being confined in nanoscale space by the physical volume of the nanoparticle, can oscillate collectively to produce localized surface plasmon resonance (LSPR).[375] This phenomena is especially evident in noble metal nanoparticles due to their relative low damping loss.[2-41] Such resonance are extremely useful, as they can produce very high E-field around the nanoparticle that greatly promotes light-matter interactions.[376] For this reason, the field of plasmonics mostly has found applications in colorimetric sensing,[273, 276 , 377, 378] energy conversion,[379, 380, 381] and near field imaging.[382, 383, 384] Photonic cavities, on the other hand, has been the foundation of modern optics, and a major component of lasers.[385] They operate based on the principle of standing wave resonance and is capable of providing amplified modes of very narrow spectral spread.[386]

Similar to the trend seen in microelectronics, the miniaturization of optical components has also been aggressively pursued, as smaller components offer higher energy confinement and faster response.[387, 388] Therefore, there has been great interest to combine plasmonic nanostructures with photonic cavities to produce both strong optical confinement and high-quality select amplified modes.[389, 390, 391, 392] For instance, 2D crystal cavities has been

coupled with Au nanorods [393], Au bowties, [394] and Pt/Au wire [395] to achieve field localization. Extensive works have also been done on incorporating plasmonic components with Fabry-Pérot (FP) cavities to achieve mode splitting, [396, 397, 398, 399] enhanced refractive index sensing, [400, 401] and spontaneous emission enhancement. [402] Turns out, these hybrid systems are capable of supporting a wide variety of resonances depending on where the plasmonic nanostructure is positioned and its coupling strength with the standing waves. [402, 403, 404] However, a lot remains to be explored in this field, and a system that is capable of tunable localized output is yet to be demonstrated.

In this study, we propose a novel scheme that uses the geometrical arrangement of a simple plasmonic resonator, AuNS, to efficiently modulate the output modes of a FP photonic cavity by controlling the plasmonic near-field coupling. The individual or coupled AuNS are deposited on top of a FP cavity ~2 μm in length to form a hybrid cavity whose modes are distinctively different than the original pure FP cavity (Figure 1). Output of this hybrid cavity is then selected by selecting different plasmonic resonator configurations such as monomers and dimers. This approach is different than other studies that focuses on ensemble properties with plasmonic active layers, as we focus on output enabled by individual nanoscale plasmonic resonators. By isolating individual/paired nanoparticles, we are not only able to eliminate spectral broadening caused by statistical variation, but also localize the output of the hybrid cavity to nanometer precision. In our system, different localized output from the same cavity can be simply achieved by altering the positioning, and hence the plasmonic coupling between AuNSs. Such unique capability allows for ultra-compact microcavities with separate, localized, and tunable output, which is crucial for their integration into nanophotonic chips.

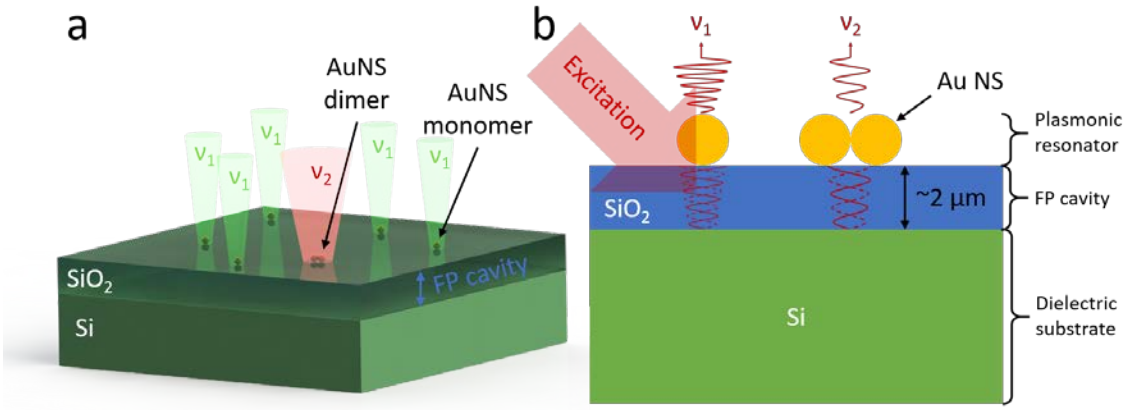

Figure 7.1 (a) Schematics showing individual AuNS monomers and a dimer on FP photonic cavity. Light cone of different color represents different optical outputs by monomers and dimers. (b) Cross-sectional view of (a).

7.2 Experimental Details

7.2.1 Materials

CTAB (hexadecyltrimethylammonium bromide ⩾99%), $NaBH_4$ (granular, 99.99% trace metal basis), $HAuCl_4 \cdot 3H_2O$ (⩾99.9% trace metals basis), ascorbic acid (ACS reagent, ⩾99%), Rhodamine 6G (Dye content 99%). All chemicals were purchased from Sigma-Aldrich and were used as-received without further purification. 4-inch Si wafers with 2.2 um thermal oxide were purchased from University Wafer, Inc. (thickness variation: ± 3% wiw, ± 5% wtw.)

7.2.2 Fabrication of AuNS-FP Resonator and AuNS-glass Reference

Thermo oxide wafers were first cut into 1 cm by 1 cm pieces, cleaned in piranha solution for 1 hr, rinsed, and stored. When needed, individual wafers were retrieved and treated by UV-Ozone (Novascan PSD-UV) for 30 min to make their surface hydrophilic. 20 µL

aqueous AuNS solution of appropriate concentration (OD = 2.0 for 1 cm path length at resonance wavelength) were then spin-coated onto the SiO_2 wafer at 3000 rpm till dry (this typically takes less than 20 sec). The same spin-coat procedure was used for cover glass to make the AuNS-glass reference samples. R6G incorporated AuNS-FP resonator was fabricated by spin-coating 20 µL 10^{-3} M aqueous R6G solution onto the SiO_2 wafer before the spin-coating of AuNS dispersion.

7.3 Results and Discussion

The colloidally synthesized AuNS used in this study has a mean diameter of 52 ± 2 nm as determined by TEM (Figure 2a, Figure D.1). The UV-vis spectrum of AuNS suspended in aqueous solution is shown in Figure 2b and clearly shows a LSPR peak at 531 nm. Similarly, in our FDTD simulation, 52 nm sized AuNS capped with 2 nm thick CTAB layers yielded a calculated extinction cross section maximum at 536 nm, which is in good agreement with the experimental data (Figure 2b).[405] An examination of the E-field distribution profile (Figure 2b, inset) at the spectral maximum reveals the peak observed is a simple dipole resonance induced in AuNS as expected from theory.[184]

The FP micro-cavity is formed by having an optically transparently medium sandwiched in between two parallel reflective surfaces. In our case, an amorphous 2 µm thick SiO_2 layer is sandwiched in between the SiO_2/Si interface and the Air/SiO_2 (later Au-Air/SiO_2) interface. Precise thickness of this SiO_2 layer is determined via spectroscopic ellipsometry to be 2170 ± 70 nm (See Methods, Figure D.2).

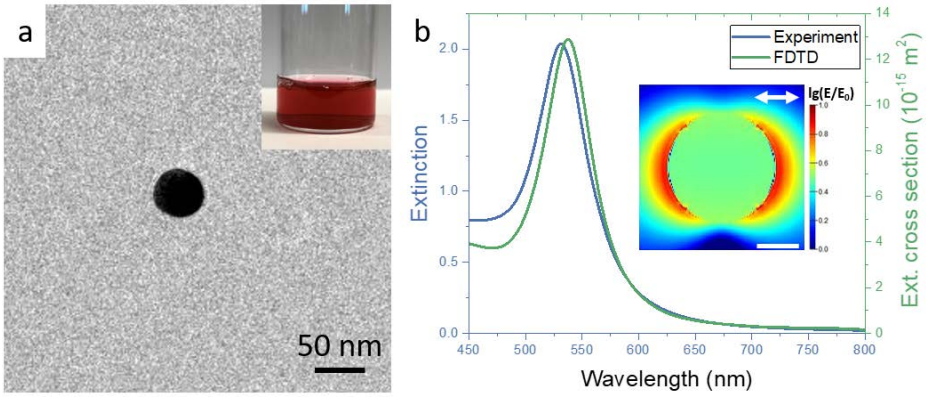

Figure 7.2 (a) TEM image of a typical AuNS. Inset: Optical photograph of AuNS solution. (b) Measured extinction spectrum of AuNS solution (blue curve) and FDTD calculation of the extinction cross section (green curve). Inset: E-field profile around the AuNS at resonance wavelength. Scale bar: 20 nm. Polarization of incident light indicated by white arrow.

The darkfield microscopic image of the AuNS-FP substrate and an AuNS-glass slide reference after assembly show densely coated nanoparticles, which acts as scattering centers (Figure 3a, b). While most of the scattering centers appear green, we see red colored ones sparsely distributed in the mix. AFM scan of the same select area shows spherical nanoparticles ~50 nm in height, confirming these are indeed individual AuNSs (Figure 3f, Figure D.3).

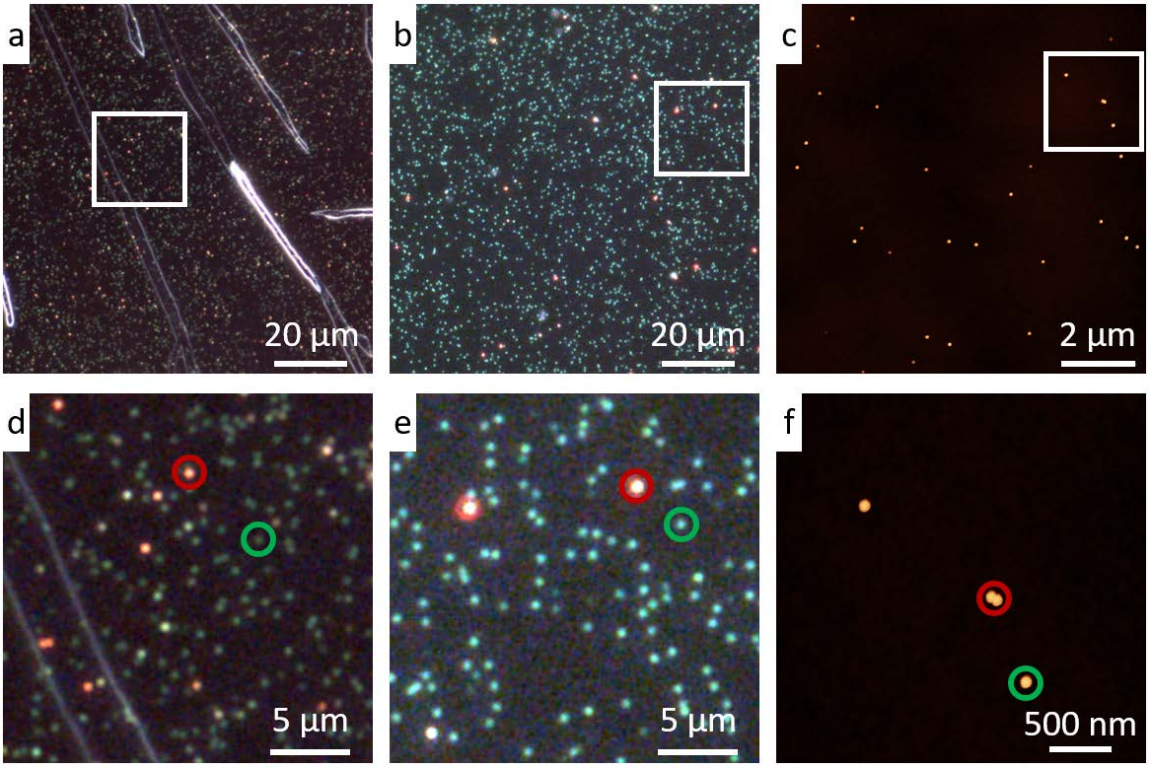

Figure 7.3 (a) Darkfield microscopic image of AuNS spin-coated on (a) glass and on (b) FP cavity. (c) AFM topographical image of AuNS spin-coated on FP cavity. Z scale: 70 nm (d-f) Zoom-in image of area marked by white square in (a), (b), and (c), respectively. Both dimers (red circle) and monomers (green circle) can be seen.

From both optical and AFM image, we can clearly see most of the AuNSs are optically isolated from each other; in the optical image, they each possesses point-like scattering signatures of a single particle dipole resonance at around 530 nm close to the solution extinction peak (Figure 3a-b, 2b). Therefore, they appear green. We refer to these isolated AuNSs as monomers (Green circles in Figure 3d-f).

The second most common species are AuNS-AuNS dimers with characteristic red scattering centers, which originates from them being excited by light polarized along the axis of contact (Figure 3d, e red circle).[184] This is further confirmed by the AFM scan of the select surface areas identified in optical images with clear identification of nanosphere

dimers (Figure 3f red circle, Figure D.3). Furthermore, in the optical images, we do not see scattering centers of any other color, and throughout all the AFM images we randomly collected on the surface, we have yet to find a trimer or any assemblies with more than two AuNSs.

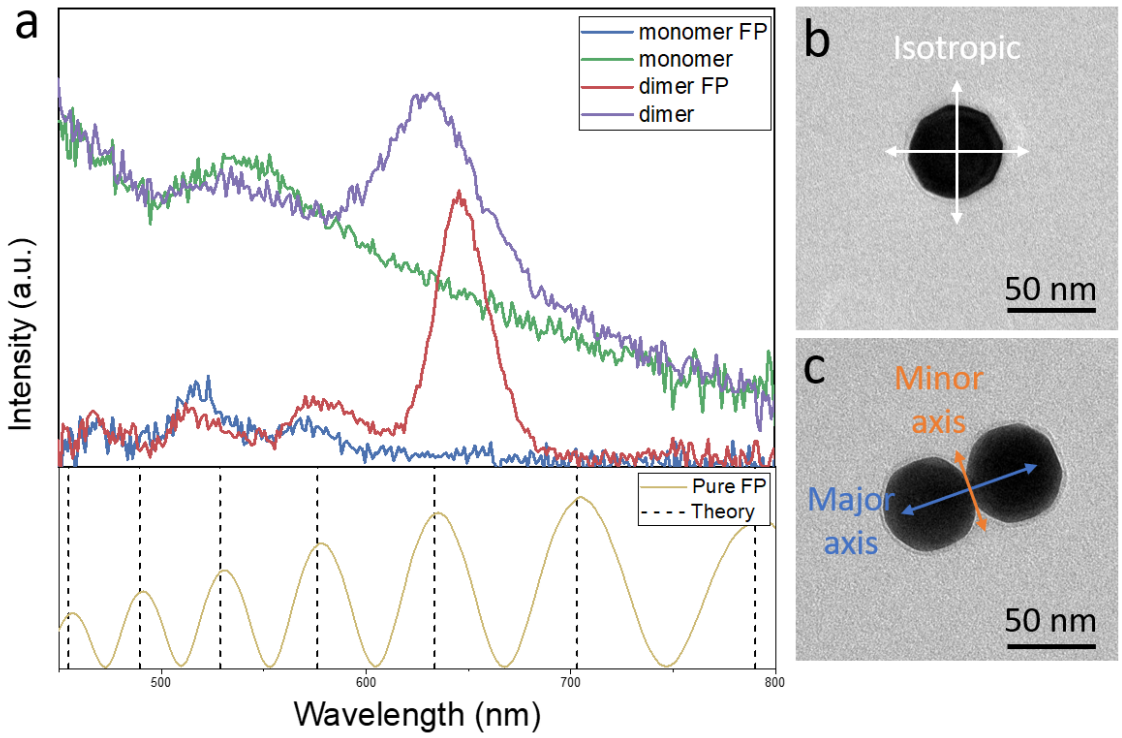

Figure 7.4 (a) TOP: Spectra from individual monomer on glass (green curve), dimer on glass (purple curve), monomer on FP (blue curve), and dimer on FP (red curve). BOTTOM: Spectrum of pure FP cavity without AuNS. The vertical dashed lines represent theoretically calculated mode positions. TEM image of (b) a typical monomer and (c) a typical dimer, with arrows marking their symmetry.

Having successfully assembled monomers and dimers with FP cavity and glass substrate, we performed hyperspectral mapping on the two samples and obtained spectra for individual monomer and dimer on both substrates (Figure 4a). For AuNS-glass reference sample, we see a single LSPR peak for the monomer at 538 nm corresponding to the dipole

resonance we observed in the UV-vis spectrum of the solution; unlike dimers, the spectra of monomers are polarization independent due to their isotropic symmetry (Figure 4b).

On the other hand, for dimers, we see two peaks, one at 534 nm corresponding to the transverse mode excited by light polarized along the minor axis, and a much more prominent new peak at 630 nm corresponding to the longitudinal mode excited by light polarized along the major axis, just as predicted by theory (Figure 4c).[184,406] The tilted backgrounds are due to fluorescence background from the substrate.

For monomer and dimers assembled onto the FP cavity, discretized peaks of regular periodicity arise due to the standing wave resonance condition imposed by the FP cavity (Figure 4a). However, when compared to the spectra of FP cavity without the AuNS (Figure 4a, yellow curve), these modes are heavily modulated by the coupling between the photonic cavity and the plasmonic resonators. Both the monomer and the dimer appear to have modes at same spectral positions, albeit with different intensities. We see relative enhancement of the modes at wavelength close to the original LSPR, and relative suppression of modes away from the original LSPR. For monomers, modes at 470 nm, 518 nm, and 572 nm are selected, with the one at 518 nm having the highest intensity. All other modes are almost completely suppressed. For dimers, an additional mode at 646 nm is also selected as the longitudinal LSPR mode of the dimer envelopes this spectral region.

The intensity of the modes is also directly correlated to the intensity of the LSPR peaks, with the mode at 646 nm having much higher intensity than the rest of the modes (Figure 4a, red and purple curve). These modes have significantly reduced peak width with FWHM at ~28 nm compared to those of pure LSPR, which have FWHM at ~61 nm. Even so, the

finesse of these modes is still relatively low compared to high quality laser etalons. This is mainly due to the low reflectance at the SiO_2/Si dielectric interface. As shown in Figure D.4, even for perfectly flat SiO_2/Si interface the reflectance is around 0.27 at 450 nm and monotonically decreases to 0.18 at 800 nm. However, higher finesse can be easily achieved by employing dielectric materials with higher refractive index contrast.[407]

The positions of the modes are also modified. From Figure 4 and Figure D.5, we can see there is apparent misalignment between the pure FP modes and the hybrid modes as well as changes in the free spectral range (FSR). If we convert the spectrum to wavenumber space where the FSR is constant (ignoring variable dispersion), the FSR of the pure FP modes can be measured to be around 1550 cm^{-1}, whereas the FSR of the hybrid modes are around 1950 cm^{-1} (Figure D.5). This conclusively establishes that strong coupling between the plasmonic resonator and the photonic cavity has taken place.[401] The modulation is not due to simple spectra addition (which will not modify FSR or mode position), but rather due to introductions of additional phase shifts by AuNS that directly change the standing-wave resonance condition of the cavity, resulting in hybrid modes that are distinctively different than the original FP modes.[401] Interestingly, the spectral position of the hybrid modes does not seem to be affected by lateral plasmonic coupling between the AuNSs (Figure 4a, red and blue curves). Thus, by simply arranging the coupling between plasmonic resonators, different output can be selected from the same set of hybrid modes. Such a property is very useful, it essentially means internal mode selectivity for the microcavity can be achieved in an extremely localized fashion that is not possible with traditional interferometer-based methods.[408]

Furthermore, we performed detailed FDTD simulation of individual monomer and dimer on the two substrates (Figure 5). The resulting trends agree well with the experiments. Figure 5a shows the simulated scattering cross sections for single monomer and dimer on semi-infinite glass substrates. As expected, the monomer shows a single LSPR peak at 524 nm from dipole resonance (Figure 5a, blue curve). The blueshift from 537 nm in the experimental spectra is likely due to the particular AuNS measured being smaller than the mean size of the AuNS ensemble used for simulation setup.

Simulation of the dimer is conducted separately for incident lights polarized along the two axes of symmetry (Figure 4c). In this figure, 90° denotes polarization parallel to the minor axis while 0° denotes polarization parallel to the major axis. For 90° polarization, there is minimum coupling between the two nanospheres, and the same kind of dipole resonance similar to those seen in monomers can be excited in the transverse direction at 522 nm (Figure 5a, red curve). The slight blueshift compared to 524 nm of the monomer is due to the weak repulsive coupling between the two dipoles oscillating in parallel pushing the resonance to a higher energy level.[2] In a dimer, the scattering cross section is approximately double that of the monomer. For 0° polarization, strong dipole-dipole coupling of the plasmons of the two AuNS can be excited in the longitudinal direction, and since the dipoles interact attractively in this direction (oscillating in tandem), the resonance condition is pulled to a lower energy level, causing the LSPR to red-shift to 577 nm. The coupling also causes the system to have much larger polarizability in this direction, which in return yields a much larger scattering cross section (Figure 5a, green curve).[409] We also see a blueshift in the simulated longitudinal mode compared to experimental spectrum, this is likely caused by two factors, the size variation we mentioned before, and the closer

separation between the AuNSs in the experiment.[410] In analyzing the TEM and AFM images, we noticed when AuNSs assemble into dimers, the CTAB surfactant layer often intermingled and deformed at the point of contact, resulting in much closer gap (< 2 nm) than the total thickness of two CTAB surfactant layers (2+2 nm) that we assume in the simulation.

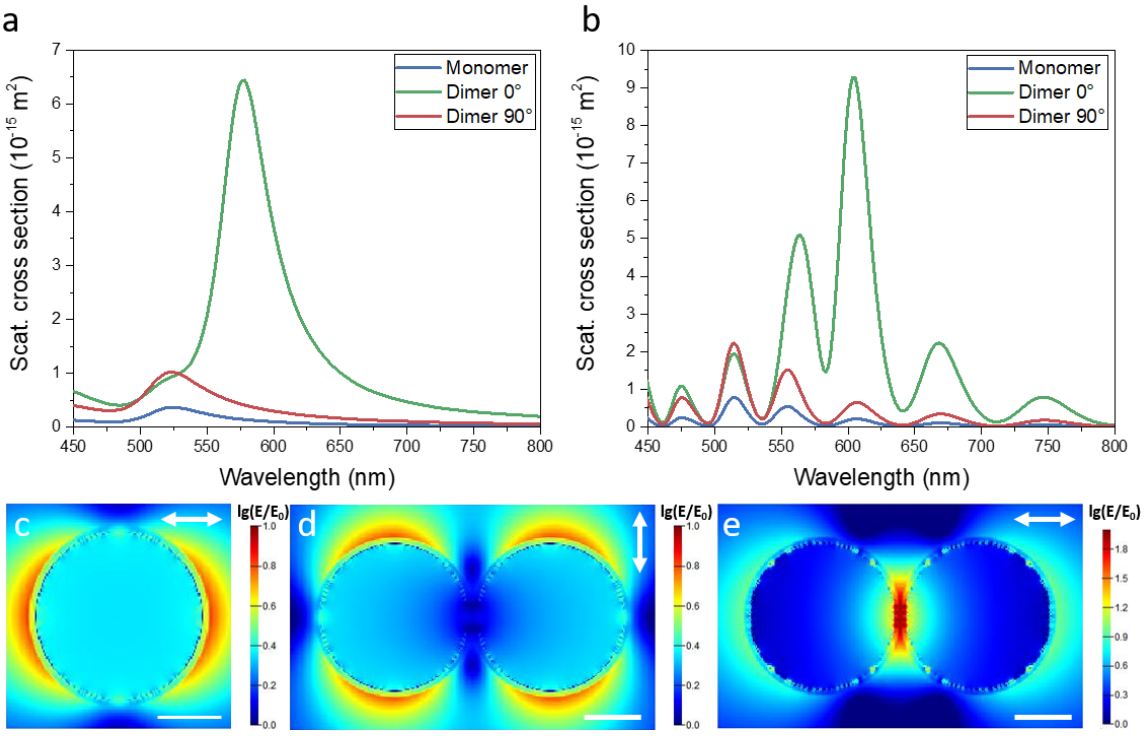

Figure 7.5 (a) FDTD simulated scattering spectra of AuNS on glass substrate: monomer (blue curve), dimer at 0° polarization angle (green curve), and dimer at 90° polarization angle. (b) FDTD simulated spectra of AuNS on FP substrate: monomer (blue curve), dimer at 0° polarization angle (green curve), and dimer at 90° polarization angle. (c) E-field profile around AuS monomer at max intensity resonance wavelength. Scale bar: 20 nm (d,e) E-field profile around AuS dimer at respective max intensity resonance wavelength for 90° and 0° polarization.

For monomer and dimer nanospheres coupled to FP, the same dipole resonances are happening, except here, the resonances are also regulated by the photonic modes of FP cavity. Figure 5b shows the simulated spectra for single monomer and dimer coupled to

the FP cavity of 2170 nm thickness. As expected, the spectra look very similar to those observed in experiment, the board LSPR peaks are discretized into fringes through coupling with the photonic cavity, forming hybrid modes that reduces the FWHM from ~45 nm to ~ 25 nm. Again, monomer and dimers have identical mode positions, only the intensity of the modes are modulated differently. Mode intensity is proportional to the intensity of pure LSPR peak calculated for AuNS-glass reference, with modes closer to the LSPR peak being selectively enhanced, and modes away from it being selectively suppressed. As a result, the monomer selects a primary mode at 514 nm and the dimer selects a primary mode at 603 nm (Figure 5b).

A further look at the field distribution profile in the horizontal plane cutting through the center of the AuNSs can yield more insight on the operation of such hybrid cavities. Essentially, the plasmonic resonator act as an optical antenna that out-couples the standing waves in the FP cavity to the far-field.[411, 412, 413] In Figure 5c, we can directly observe the radiating dipole moments from E-field visualization. As mentioned earlier, due the symmetry of the AuNS, the response of monomer is polarization independent; the dimer, on the other hand, can support two different resonances depending on polarization direction (Figure 5d, e).

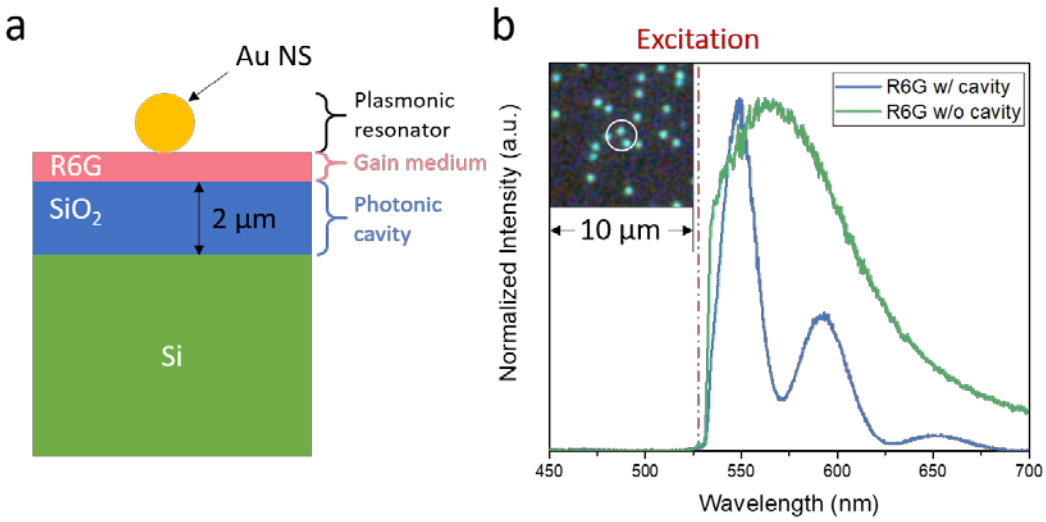

Figure 7.6 (a) Schematics showing the insertion of a gain medium into the photonic-plasmonic hybrid resonator. (b) Normalized emission spectra of R6G at 532 nm excitation with (blue curve) and without (green curve) hybrid resonator. Inset: approximate laser spot size (white circle) superimposed on dark field image taken using x50 objective.

Considering the most relevant practical applications for optical resonator systems are lasers, we investigated the effect of incorporation of gain medium into our plasmonic-FP hybrid cavity. As shown by the schematics in Figure 6a, an optically transparent layer of Rhodamine 6G (R6G) few nanometers thick is introduced between AuNS and the SiO_2.[414]. A confocal Raman system coupled with a 532 nm laser is then used to excite the R6G at its absorption peak.[415] Since the system is incapable of darkfield imaging, we positioned the beam on the surface and identified statistically the relative amount of monomer and dimers (Figure 6 inset). The signal collected almost certainly originated from one or several monomers. Indeed, we see a high intensity mode at 548 nm, agreeing with the spectra of monomers. The slight shift in mode position compared to previous result is likely due to wafer-to-wafer oxide thickness non-uniformity (±5%). Nevertheless, the spectral narrowing is obvious, the FWHM decreased from ~104 nm for R6G film without cavity to

~22 nm for R6G film coupled to cavity. Unfortunately, we are not able to achieve high intensity lasing with the system due to the fast photobleaching of R6G. However, the system clearly demonstrates potential to be integrated with gain mediums. In future studies, it should be relatively easy to introduce a quantum well emission layer made of inorganic semiconductors using physical deposition at the SiO_2/Au interface, making a true nano-laser.[416]

7.4 Conclusions

In summary, we have reported the fabrication of a hybrid nanostructured AuNS-FP optical cavity whose output mode can be selected by altering the plasmonic near-field coupling between nanospheres. The introduction of AuNS at one end of the FP cavity was able to alter the standing wave resonance condition inside the FP cavity, forming highly localized hybrid modes with distinctively different resonances and spectral positions compared to the original pure FP photonic modes. The AuNS act as a radiating optical antenna that out-couples the standing wave inside the cavity to the far-field.

Moreover, the behavior of this antenna can be changed by laterally coupling two AuNS together to form a dimer. The monomer and dimer have identical hybrid mode positions. However, the relative intensity of the modes is modulated by their respective LSPR intensities, which roughly translates to the efficiency at which they can radiate at specific wavelengths, causing different primary mode to be selected from the same set of modes. It is worth noting that such modulation mechanism is not limited to monomers and dimers but applies to all sorts of plasmonic nanostructures, offering virtually limitless tunability. We also demonstrate the potential to incorporate gain medium into the cavity for lasing.

For better performance, dielectric interface with higher reflectivity and high quality plasmonic nanocrystals with narrow LSPR such as gold nanorods can be used.[417] It's easy to envision, when combined with robust gain medium and nanocrystal patterning capabilities such as those enabled by template assisted assembly and substrate-to-substrate nanoparticle transfer, an extremely compact tunable nano-laser can be constructed.[195] System like this is immensely useful. Instead of bulky distributed Bragg reflectors (DBRs) which are several microns in thickness, compact plasmonic nanocrystals can be used to select different mode output from the same optical microcavity.

By varying the lateral coupling between the plasmonic nanocrystals, different laser modes can be selected at different locations from the same cavity layer. The plasmonic nature of the AuNS can even allow localized near field output to plasmonic waveguides such as single crystalline Ag nanowires in the deep subwavelength regime. Such ultra-compact tunable lasing system is bound to find abundant applications in optical interconnects, near-field spectroscopy, and other nanophotonic related engineering fields.

CHAPTER 8. GENERAL CONCLUSIONS AND BROADER IMPACT

8.1 General Conclusions

In summary, the research presented in this thesis focused on advancing the understanding on utilizing plasmonic hybrid nanoconstruct for controlling light-matter interaction in the subwavelength regime. Detailed studies are conducted on all levels of organization: controlled synthesis of individual plasmonic nanostructure or functional organics, organic-inorganic assembly behavior and interface chemistry, and localized coupling of plasmonic nanostructure with elements such as photonic microcavity and electrochromic polymers.

Major areas focused on were:

- Surface chemistry on the functionalization of colloidally synthesized nanocrystals with organic ligands in aqueous solutions.
- Rational design of organic matrices that immobilize and support the plasmonic nanocrystals to facilitate their efficient utilization.
- Changes in angular dependent optical output of plasmonic nanostructures upon modulation of their immediate dielectric environment.
- Coupling of plasmonically active nanocrystals to dielectric nanophotonic components such as optical microcavities.

Specific techniques used to investigate these areas include:

- AFM based temporally resolved stop-and-go nanoscale morphology monitoring that directly visualizes the changes in surface morphology with nm-precision as chemical reactions take place.
- Combination of AFM based mechanical processing and SIMS characterization to achieve super-resolution surface composition analysis that is beyond the capability of ordinary SIMS.
- Thorough 3D characterization on the structural properties of plasmonically active nanostructures and their placement in organic matrices using AFM, SEM and TEM.
- High-resolution hyperspectral mapping of output spectrum from single plasmonic nanostructures under various conditions.
- Further theoretical analysis of experimental result aided by FDTD modeling that reveals the electrodynamic process happening within the system with sub-fs resolution and provides frequency domain information such as optical field (E, H, and P) distributions with sub-nm resolution.

First, we examined the ligand exchange process happening on colloidally synthesized plasmonically active nanocrystals, PVP capped single crystalline triangular gold nanoplates with (111) top surface was used as a model system to investigate the absorption of thiols, which is a commonly used anchoring group for functional organics, on plasmonic nanostructures. Using temporally resolved **stop-and-go high resolution AFM microscopy**, we observed that during ligand exchange with linear thiol, the nanocrystal surface evolved from an initial 1 nm uniform PVP coating into **a remarkably stable network of globular PVP domains** 20–100 nm in size and ~4 nm in height surrounded by thiol self-assembled monolayers. The final stability of such a mixed thiol–PVP surface

morphology can possibly be attributed to the interfacial energy reduction from partially solvophilic surfaces and the entropic gain from mixed ligand surface layers. The ligand-exchange dynamics and the **unusual equilibrium morphology** revealed provided important insights into displacement dynamics of surface-bound molecules on colloidal metal substrates.

Next, we investigated how plasmonic nanocrystals can be efficiently integrated with functional organic matrices. By carefully **controlling inorganic-organic interactions and the assembly methods**, we successfully demonstrated a hybrid CNF based **multifunctional porous membrane** that hosts AuNR dimers and enables their efficient use for **dual-mode SERS detection** of both small molecules and cells.

The nanoporous nature of the nanofiber membranes allows for effective molecular filtration and preconcentration of the analytes, further boosting the SERS performance. Specifically, because of the low fluorescence and Raman background of the CNF matrix, extremely low loading density of AuNRs can be used. The nanorod assemblies within the CNF network can be resonantly driven by a 532 nm laser (transverse plasmonic mode) and near resonantly driven at by a 785 nm laser (longitudinal mode), facilitating dual operational modes at two excitation wavelengths. The shorter wavelength excitation mode yields better Raman scattering efficiency and has been demonstrated to be capable of detecting rhodamine 6G (R6G) dyes **down to picomolar concentrations**. On the other hand, the longer wavelength excitation mode provides autofluorescence suppression for the better detection of microorganisms such as *Escherichia coli*, shortening the required integration time **from hours to minutes**. The hybrid plasmonic CNF membranes reported show **significantly improved SERS sensitivity and detection fidelity** as compared to

traditional SERS substrates, demonstrating the importance of optimizing the cooperative effects between plasmonic nanoparticles and organic matrix.

We then focused on understanding the optical response of plasmonic nanostructure upon modulation of its immediate dielectric environment. For this task we combined ECP with NHAs of different geometry and observed **drastically different forward and backward scattering behavior of polymer-infused NHAs** when the surrounding electrochromic polymer matrix was subjected to electrical potential, thereby changing the effective permittivity of the environment. Our experiments show forward scattering at normal incidence angle of the NHAs is mostly controlled by ECP attenuation, while the backward scattering at a highly oblique angle show significant red-shifting in addition to attenuation upon switching of ECP states. We are able to systematically understand the origin of this interesting asymmetric optical modulation through detailed FDTD simulation, which revealed **highly oblique illumination can excite polarization dependent complex plasmon resonances** that are highly sensitive to the modulation of the refractive index of the surrounding media.

Finally, we report the integration of colloidally synthesized highly monodisperse AuNS with a FP-type photonic cavity. Upon assembly, the **plasmonic peaks of the AuNSs are discretized by the photonic cavity**, forming hybrid modes that are distinctively different from the original modes supported by the FP cavity. In this configuration, the plasmonic nanocrystal essentially act as an optical antenna that out-couples the **new hybrid modes** inside the cavity to the far-field. Different modes can therefore be selected by utilizing plasmonic near-field coupling between two nanocrystals by placing them closely to each other to form a dimer. The exact **output mode selected is based on the spectral envelope**

imposed by the plasmonic oscillation from respective AuNS assemblies (monomer or dimer). The ability to integrate gain mediums into such a hybrid system is also demonstrated, showing great promise for the application of hybrid plasmonic-photonic cavity in the realization of ultra-efficient nanolasers.

8.2 Significance and Broader Impact

The combination of crystalline inorganic plasmonic nanostructures with soft organic macromolecules has tremendous potential in the miniaturization and improvement of molecular sensors, displays, and nanophotonic circuitry. This research is therefore attempting to answer some of the critical questions involving the fabrication, assembly, and integration of these devices. It is only when these fundamental issues are addressed properly, can the true potential of hybrid plasmonic nanoconstructs and their ability to control optical field at nanometer precision be unlocked.

One could argue, the most fundamental aspect of building the hybrid nanostructure is understanding the interface at the organic-inorganic interface. Before our study on the ligand replacement dynamics, there is very little information available on the exact morphologies of ligand structure and the completeness of ligand replacement reaction. Frequently, the ideal case of complete ligand replacement is assumed and presented in simple schematics. However, by systematically investigating the replacement of original polymeric surfactant by linear thiols, we have shown the actual reaction dynamics on the surface of these nanocrystals to be significantly more complicated, and the ligand replacement reaction is far from complete even after reaching equilibrium. This finding can potentially **address many discrepancies** reported in literature and offer explanation

on the performance deviations observed from ideal ligand layers. More importantly, it calls into **question the long-held belief** that solution-based ligand replacement is a fast, clean, and simple reaction. It suggests existing capping agent must be taken into consideration when functionalizing colloidally synthesized nanoparticles. In general, the formation of self-assembled ligand monolayer on metallic surface is not nearly as robust as believed, thus any pre-existing surface contaminates is likely to have an impact on the functionalization process.

Besides the conclusion from the experiment, the techniques we developed during the study also has broader applications. For example, the AFM based mechanical cleaning procedure and the single flake reaction monitoring technique can be easily applied to the investigation of other surface chemistry dynamics. The combination of the creation of nanoscale cleaned pattern by AFM and SIMS **provide a powerful technique** to investigate the chemical nature of nanoscale features resulting from any reactions. In the field of hybrid plasmonic nanostructure based biomolecular sensing, these advanced characterization techniques will help establish a better understanding of the morphology, mobility, stability, and specific activity of nanostructure surface-bound biomolecules. More importantly, they will allow a better understanding of some of the crucial mechanistic aspects of biomolecular reactions as well as biofouling on nanostructured surfaces and its prevention. Such fundamental understanding is the **key to break through the critical barriers** of current nanoscale biosensing and to deliver high device robustness under complex environment and signal reproducibility.

Our second study on the integration of high quality CNF network with near monodisperse AuNR produced a molecular filtration based SERS detection platform that has

significantly better performance (2 orders of magnitude lower LoD) than traditional porous SERS substrates. More importantly, our study demonstrated that rationally optimizing the material and the organization of polymer networks and the nanocrystal loading method can be much more effective than simply increasing the loading density of the plasmonic nanocrystals. By utilizing the CNF network's nanofiltration capability and loading sparsely distributed AuNR dimers on the surface, **much more efficient utilization** of AuNR was achieved with unique dual-mode near resonant operation. This is a big stride forward in terms of utilization of plasmonic nanocrystals in hybrid detection platforms that can be used for practical purposes.

Moreover, the same platform is not limited to AuNR and can be widely applicable to other nanocrystals that needed highly transparent free-standing support with minimum optical interference. It is also worth noting that using the systematized approach we adopted in designing the plasmonic hybrid platform: by maximizing the number of molecules retained near plasmonic hotspot, minimizing the fluorescence and Raman background, and utilizing resonant excitation, superior performance can be achieved without high density loading of plasmonic nanocrystals. In fact, we demonstrate the high density loading is probably detrimental to the overall device performance, as it introduces irregular aggregations and prevents the structure to be excited resonantly. By demonstrating the effectiveness of our approach, we introduce a **new design strategy based on guest/host complimentary functionalities** that can be broadly applied to a wide variety of organic-inorganic hybrid devices.

Based on this strategy of rational design, in the long term, we suggest that constant improvements in chemical synthesis, protein engineering, and bioconjugation techniques

will necessarily yield novel nanoengineered components of much higher quality, low polydispersity, tailored functionality, reproducibility, and consistency. Coupled with a comprehensive understanding of multicomponent interfacial interactions and realistic nanoscale organization obtained from experimental and computational studies playing in tandem, researchers will be able to design fully integrated plasmonic hybrid sensing nanostructures optimized for specific biodetection and biocomputing functions under a wide range of operating bioenvironments. Moreover, combined with newly emerging advanced manufacturing technologies, such as 3D/4D printing and DNA-directed hierarchical assembly, multicomponent, mesoscale structures capable of coordinating with each nanostructured constituent are hopefully to be demonstrated in near future.

Even in the near term, current research activities and investments in the area of advanced molecular sensing with plasmonic nanostructures can be rewarding. Improvements in the multiplexing capabilities and cost reduction strategies in current biochip design with the use of nanostructured hybrid plasmonic elements by themselves will likely be sufficient to push nano-biosensing platform past the present technology barriers to realize economical lab-on-a-chip replacements for many of today's clinical lab-based and in-field procedures for control and real-time monitoring. Such robust, sensitive, highly selective, multi-analyte, portable and multifunctional biosensing nanomaterials and devices will likely play a crucial part in improving diagnostic and healthcare, environmental monitoring, drug and food inspection, and real-time fast in-field molecular screening.

In our next study, we examined some of the overlooked aspect of a well-studied area, namely the integration of NHAs and ECPs, whose dielectric property can be electrochemically modulated. Even though the forward scattering/transmission property of

ECP infused NHAs are well studied for their potential application in next generation display technologies, the backscattering/reflection has not received the same amount of attention. We investigated this aspect and found drastically different optical responses in these two illumination configurations upon ECP modulation. Such heterogenous response can be useful for various prospective applications, such as logic operations in photonic circuits. The optical response's angular and polarization dependence might **inspire novel plasmonic display illumination** geometries and could find uses in **dramatically improving SPR-type molecular sensors**. In addition, the high performance ECP our collaborator synthesized offer many improvements to traditional PANI based systems and can be tailored to have specific physiochemical properties such as solubility and bandgap. Synthesis procedures of these novel ECPs are published and can be of further use to future research.

Another contribution to the wider scientific community is the **advanced FDTD simulation method** we used to model excitation of a period plasmonic structure at a highly oblique angle using a plane wave source with bloch simulation boundaries. Traditionally, such highly oblique angle coupled with period boundary conditions are very difficult to simulate as the frequency dependent angle variance can easily lead to divergence. However, in our study we developed a method that uses narrow band pulse sources and frequency sweep to address this problem. Application of this method is **not limited to this specific study** but can be used to **simulate various arbitrary periodic structures** under oblique illumination, which we believe will lead to much **better understanding of the angular dependence** of the optical responses of plasmonic nanostructures.

Lastly, in our final study, we demonstrated that by exploiting plasmonic near-field coupling, simple geometrical arrangement of AuNS into monomer and dimers can be used to select different output modes from hybrid FP-AuNS cavity. The fundamental aspects of the coupling interaction between plasmonic optical antenna and the FP-cavity is elucidated, and the formation of hybrid modes are investigated thoroughly with FDTD simulation. While plasmonic nanoparticle has been assembled with FP before, we believe this is **the first time** the effect of plasmonic coupling between nanoparticles that are **concurrently coupled** with FP has been investigated with **single nanoparticle resolution**. Due to the change in plasmon oscillation characteristic upon lateral AuNS coupling, the radiation efficiency of the optical antenna shifts correspondingly, allowing different modes to be selected.

Modulation of cavity output using this method means optical oscillator system can be made to be extremely compact, without the need for bulky external dielectric mechanism (such as DBR) for mode selection. The hybrid design we proposed can also be extended to FP cavities with higher refractive index materials (ZrO_2, HfO_2 etc), other photonic cavities (WGM cavity, 2D photonic crystal cavity, etc), and other plasmonic nanocrystals (AuNR, Ag nanocube, etc). It can also potentially allow plasmonic output via near-field coupling to plasmonic waveguides. Thus, **facilitating a rich variation** that can be utilized by different nanophotonic applications with specific requirement on output modes or emission directional profiles. Most importantly, we further demonstrated the capability for such hybrid microcavity to incorporate gain medium, which **directly leads to lasing applications**, and by extension to a wide range of fields that benefits from efficient ultra-compact nanolasers.

8.3 Dissemination of work

This work has resulted in 12 peer-reviewed publications (6 as first author) and 6 conference presentations (2 as first author).

8.3.1 Publications Directly Relevant to This Work:

Zhang, S.; Panikkanvalappil, S. R.; Kang, S.; Smith, M. J.; Yu S.; El-Sayed, M.; Tsukruk V. V. Modulation of Photonic Cavity Modes by Nanostructured Plasmonic Resonator. *ACS Photonics.* **2019**, *Submitted*

Zhang, S.; Yu S.; Zhou J.; Ponder, J. F.; Smith, M. J.; Reynolds, J. R.; Tsukruk, V. V. Heterogeneous Forward and Backward Scattering Modulation by Polymer-Infused Plasmonic Nanohole Arrays. *J. Mater. Chem. C* **2019**, *7*, 3090-3099.

Zhang, S.; Xiong, R.; Mahmoud, M. A.; Quigley, N. E.; Chang, H.; El-Sayed, M.; Tsukruk V. V. Dual-Excitation Nanocellulose Plasmonic Membranes for Molecular and Cellular SERS Detection. *ACS Appl. Mater. Interfaces* **2018**, *10*, 18380-18389.

Zhang, S.; Geryak, R.; Geldmeier, J.; Kim, S.; Tsukruk, V. V. Synthesis, Assembly, and Applications of Hybrid Nanostructures for Biosensing. *Chem. Rev.* **2017**, *117*, 12942-13038. (Invited Review)

Zhang, S.; Kim, S.; Tsukruk, V. V. Ligand-Exchange Dynamics on Gold Nanocrystals: Direct Monitoring of Nanoscale Polyvinylpyrrolidone–Thiol Domain Surface Morphology. *Langmuir* **2017**, *33*, 3576-3587.

Zhang, S.; Tsukruk, V. V. Biofunctionalized Brush Surfaces for Biomolecular Sensing in *Polymer and Biopolymer Brushes: for Materials Science and Biotechnology*; John Wiley & Sons, Inc.: Hoboken, NJ, USA, 2017; Ch16, p433-477. ISBN: 978-1119455011 (Invited Review)

Xiong, R.; Hu, K.; **Zhang, S.**; Lu, C.; Tsukruk, V. V. Ultrastrong Freestanding Graphene Oxide Nanomembranes with Surface-Enhanced Raman Scattering Functionality by Solvent-Assisted Single-Component Layer-by-Layer Assembly. *ACS Nano* **2016**, *10*, 6702-6715.

Xiong, R.; Grant, A.; Ma, R.; **Zhang, S.**; Tsukruk, V. V. Naturally-derived biopolymer nanocomposites: interfacial design, properties and emerging applications. *Mater. Sci. Eng. R Rep.* **2018**, *125*, 1-41. (Invited Review)

8.3.2 Other Related Publications

Xiong, R.; Kim, H.; Korolovych, V.; **Zhang, S.**; Yingling. Y; Tsukruk V. V. Wrapping Nanocellulose Nets around Graphene Oxide Sheets *Angew. Chem. Int. Ed.* **2018**, *57*, 1-7.

Xiong, R.; Kim, H. S.; **Zhang, S.**; Kim, S.; Korolovych, V. F.; Ma, R.; Yingling, Y. G.; Lu, C.; Tsukruk, V. V. Template-Guided Assembly of Silk Fibroin on Cellulose Nanofibers for Robust Nanostructures with Ultrafast Water Transport. *ACS Nano* **2017**, *11*, 12008-12019.

Kim, S.; Geryak, R. D.; **Zhang, S.**; Ma, R.; Calabrese, R.; Kaplan, D. L.; Tsukruk, V. V. Interfacial Shear Strength and Adhesive Behavior of Silk Ionomer Surfaces. *Biomacromolecules* **2017**, *18*, 2876-2886.

Hu, K.; Xiong, R.; Guo, H.; Ma, R.; **Zhang, S.**; Wang, Z. L.; Tsukruk, V. V. Self-Powered Electronic Skin with Biotactile Selectivity. *Adv. Mater.* **2016**, *28*, 3549-3556. (Cover Story)

8.3.3 Conference Presentations:

Zhang, S.; Tsukruk, V. V. Adsorption Behavior of Mixed Thiols on SERS Active Single Crystal Gold Nanoplatelets. 252nd American Chemical Society National Meeting & Exposition, 2016. (Oral presentation)

Zhang, S.; Chávez, J. L.; Kelley-Loughnane, N.; Tsukruk, V. V. Aptamer Functionalized Ligand Layers on SERS Active Colloidal Nanocrystals. 252nd American Chemical Society National Meeting & Exposition, 2016. (Poster presentation)

Xiong, R.; **Zhang, S.**; Tsukruk, V. V. Cellulose Nanofiber-Templated Silk Fibroin Shish-kebab Nanostructure with Exceptional Mechanical Robustness and Ultrafast Water Transport. MRS Fall Meeting & Exhibit, 2017. (Oral presentation)

Xiong, R.; Kim, H.; Zhang, L.; Korolovych, V.; **Zhang, S.**; Yingling, Y. G.; Tsukruk, V. V. Hairy Graphenes: Wrapping Nanocellulose Nets Around Graphene Oxide Sheets. 257th American Chemical Society National Meeting & Exposition, 2019. (Poster presentation)

Xiong, R.; Kim, H.; Zhang, L.; Korolovych, V. F.; **Zhang, S.**; Yingling, Y. G.; Tsukruk, V. V. Hairy Graphenes: Wrapping Nanocellulose Nets Around Graphene Oxide Sheets. MRS Spring Meeting & Exhibit, 2019. (Oral presentation)

Xiong, R.; Yu, S.; **Zhang, S.**; Korolovych V.; Yingling, Y. G.; Tsukruk, V. V. Hierarchical Nanocellulose Materials for Strong Photonic Chiral Nematic Films. MRS Spring Meeting & Exhibit, 2019. (Poster presentation)

APPENDIX A. CHAPTER 4 SUPPORTING INFORMATION

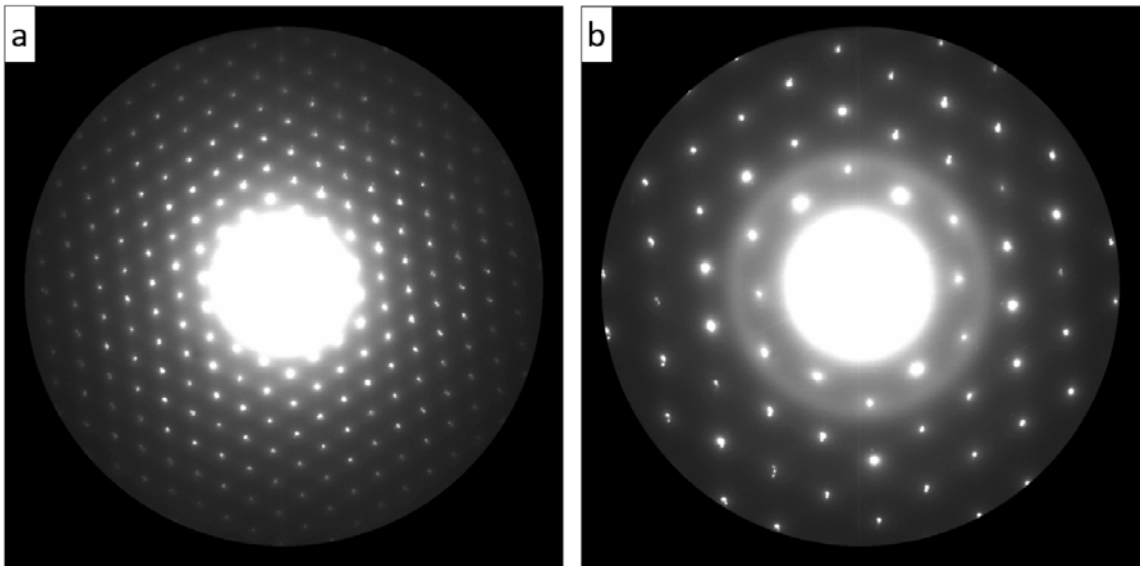

Figure A.1 Large area electron (120 kV) diffraction pattern from a typical synthesized Au nanoplate drop-cast on TEM grid. (a) and (b) are from the same spot but captured at different camera length.

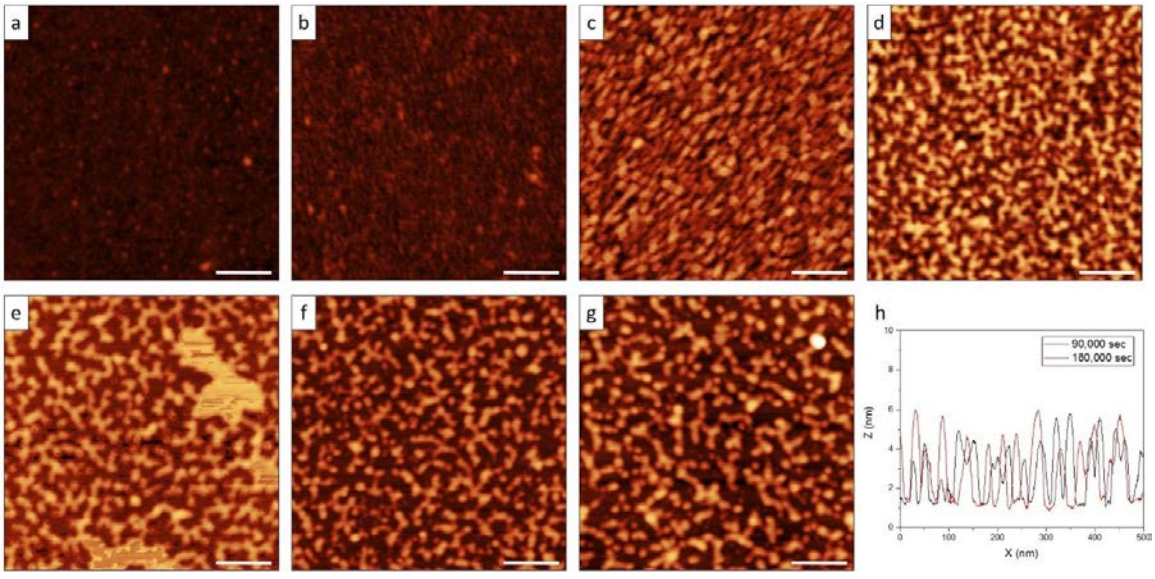

Figure A.2 High resolution AFM topographical images of ODT adsorption layers on Au nanoplates after (a) 0 sec (bare crystal), (b) 30 sec, (c) 300 sec, (d) 3000 sec, (e) 30,000 sec, (f) 90,000 sec and (g) 180,000 sec exposure to 1 mM ODT ethanol solution.

Scale bar: 100 nm; Z scale: 5 nm (a, b, c, d), 10 nm (e, f, g). (h) Typical cross section profile from (f) and (g).

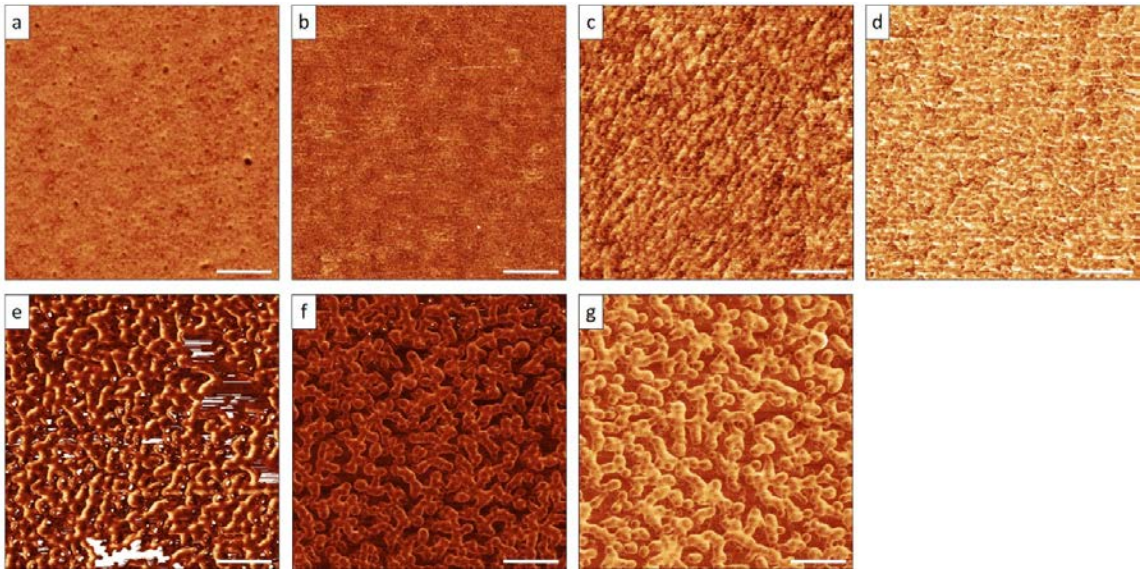

Figure A.3 High resolution AFM phase images corresponding to Figure A.2: (a) 0 sec, (b) 30 sec, (c) 300 sec, (d) 3000 sec, (e) 30,000 sec, (f) 90,000 sec, (g) 180,000 sec. Scale bar: 100 nm; Z scale: 10° (a, b, c, d), 20° (e, f, g)

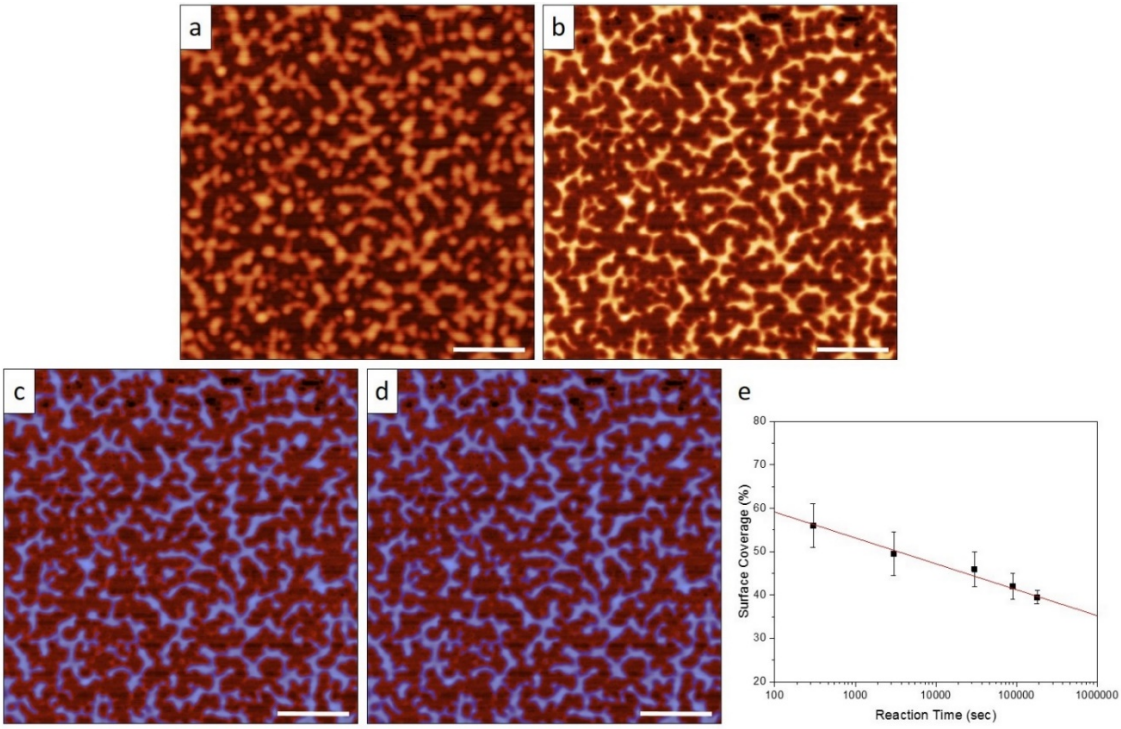

Figure A.4 Calculation of surface coverage of globule features. (a) Raw AFM image from Figure A.2f showing nanoplate surface morphology at 90,000 sec reaction time. (b) Corrected AFM topographical image reconstructed from (a) using 8 nm tip radius and 20° tip slope. Height mask of globular features giving surface coverage value of (c) 39% (lower limit) and (d) 45% (higher limit). This gives the error bar. (e) Surface coverage of globular features from 300 sec to 180,000 sec all calculated using this method. Solid red trend line serves as a guide to the eye. Scale bar: 100 nm; Z scale: 10 nm

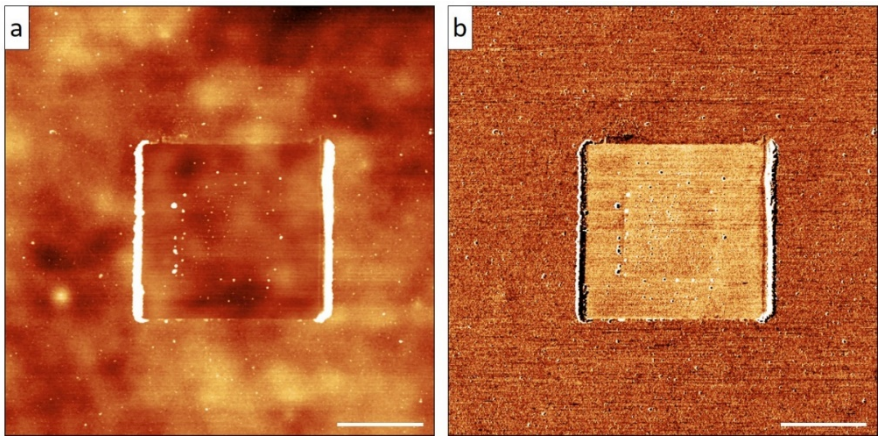

Figure A.5 AFM (a) topographical and (b) phase image of Au nanoplate surface that has gone through double AFM cleaning. First, a 2 × 2 µm area is cleaned. Afterwards,

the AFM tip is moved to the center of the pattern and instructed to clean a new 1 × 1 μm area. Scale bar: 1 μm; Z scale: 10 nm (a), 5° (b).

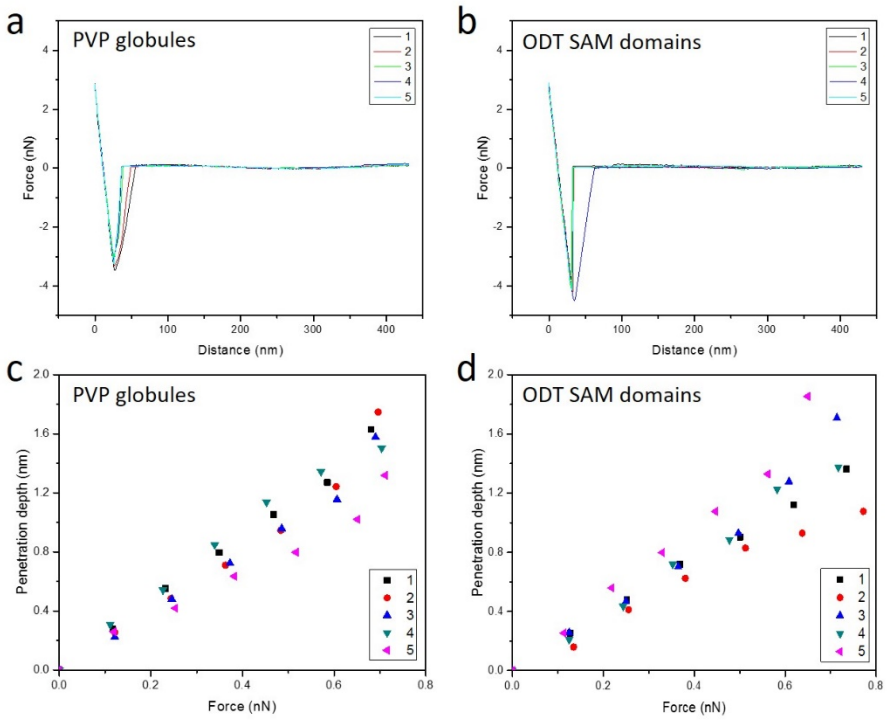

Figure A.6 QNM force distance curves of (a) PVP globules and (b) surrounding ODT SAM domains. QNM tip loading curve of (c) PVP globules and (b) surrounding ODT SAM domains. Five independent measurements are plotted for each case.

As shown in Figure A.7, we attempted to probe the adlayer using Raman spectroscopy on one of the flakes. It is evident from the confocal Raman map and corresponding spectrums that even when the Au nanoplates were functionalized with molecules with high Raman cross-section (thiophenol), we cannot observe any signal from the adlayer. This is expected; because the Au nanoplates are atomically flat and several microns in lateral size, they do not provide any plasmonic Raman enhancement.[418] Therefore, it would be close to impossible to quantitatively detect the PVP adlayer presented in this paper using standard confocal Raman spectroscopy. Similar argument applies to FTIR measurements.

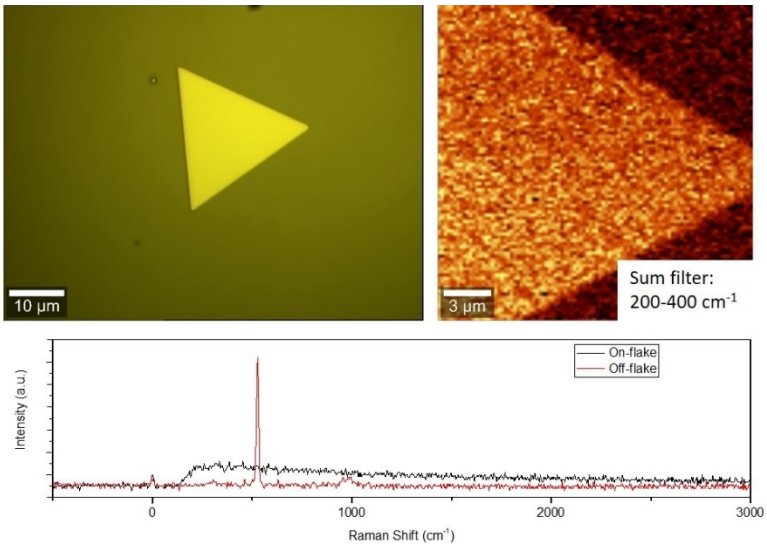

Figure A.7 Optical image and confocal Raman map of thiophenol functionalized Au nanoplate, 1 sec integration time, Raman mapping resolution: 200 nm × 200 nm per pixel. The off-flake spectrum shows characteristic first-order peak from crystalline Si at 520 cm^{-1} and second-order peak at 900~1000 cm^{-1}

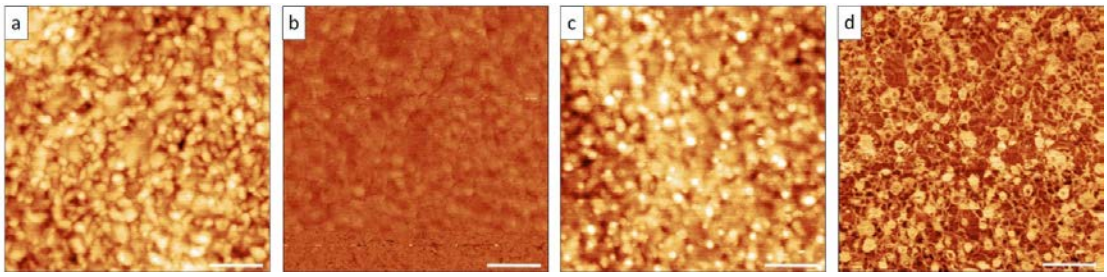

Figure A.8 AFM (a,c) topographical and (b,d) phase images of E-beam evaporated 20 nm Au film on Si wafer with 5.7 nm Ti adhesion layer. (a,b) as-evaporated. (c,d) after 24 hrs 1 mM ODT solution exposure, Scale bar: 100 nm; Z scale: 5 nm (a,c), 10° (b), 20° (d)

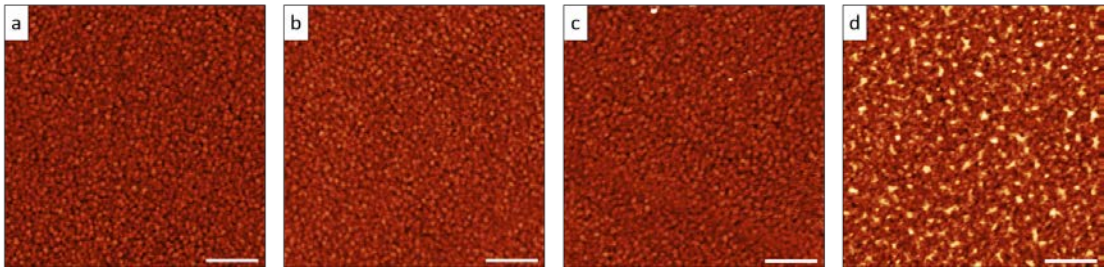

Figure A.9 AFM topographical images of cold sputtered 70 nm Au film on Si wafer. (a) as-sputtered. (b) after 24 hrs of 1 mM ODT solution exposure, (c) after 12 hrs of PVP ethylene glycol solution exposure, (d) after 12 hrs of PVP ethylene glycol solution exposure and subsequently 24 hrs of 1mM ODT solution exposure. Scale bar: 200 nm; Z scale: 10 nm

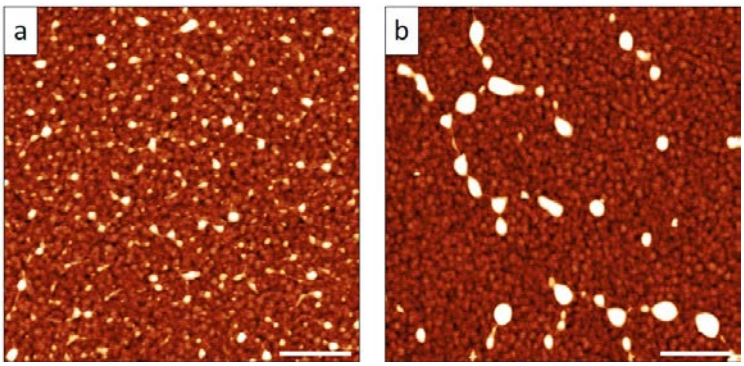

Figure A.10 AFM topographical images of sample in Figure A.9d (a) and sample in Figure A.9b (b) after further 12 hrs of exposure to PVP ethylene glycol solution. Scale bar: 200 nm; Z scale: 10 nm

Figure A.11 shows the same-area surface morphology evolution of an AFM cleaned Au nanoplate after 5000 sec and 60,000 sec exposure to 1 mM ODT ethanol solution. The area marked by the white rectangular is an artificially induced PVP accumulation caused by the controlled irregular movement of the AFM tip during the surface cleaning process and serves as a convenient monitoring position for detailed morphological changes of individual PVP globules. It is evident from the magnified image that PVP domains have limited mobility on the surface (Figure A.11, inset). The domains seem to be pinned on the surface. Over the course of more than 15 hrs of solution ligand-exchange, the PVP domains

in this 200 nm × 500 nm area obvious have gone through morphological changes similar to those shown in Figure A.2, but their 2D arrangement on the Au surface appears to be preserved, suggesting the formed PVP domains are largely immobile.

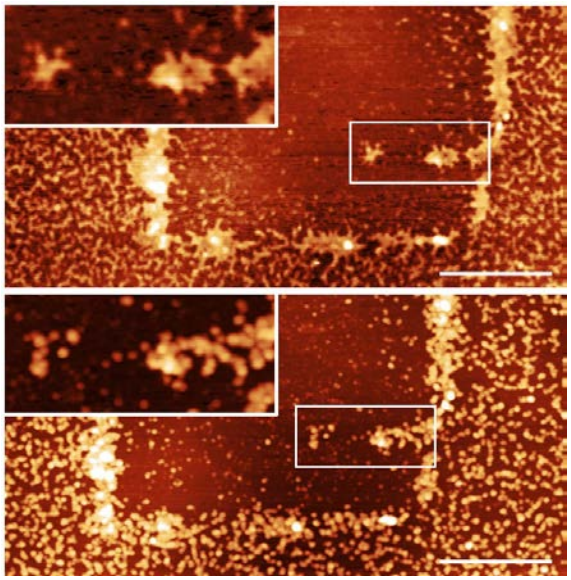

Figure A.11 AFM topographical images of same area of AFM cleaned Au nanoplate after 5000 sec (top). and 60,000 sec (bottom) exposure to 1 mM ODT ethanol solution. Inset: magnified image of the marked areas. Scale bar: 400 nm; Z scale: 10 nm

Figure A.12b-f shows surface morphology "snapshots" at specific points of time into the reaction. At 300 secs, as MCH just starting to deforming PVP into globules, there was a significant morphological difference between the pre-cleaned and PVP coated areas similar to those previously observed in ODT study (Figure A.12c). The R_{rms} inside the pre-cleaned area was 0.15 nm (200 nm × 200 nm, randomly sampled, standard deviation < 0.01 nm) whereas R_{rms} of the PVP coated area was 0.24 nm (200 nm × 200 nm, randomly sampled, standard deviation < 0.01 nm). However, at later stages the roughness inside and outside the AFM cleaned area gradually equalized as smaller coils started to migrate inside. At 120,000 secs the R_{rms} for the two regions were even inversed, at 0.46 nm and 0.42 nm

respectively (Figure A.12f, 200 nm × 200 nm, randomly sampled, standard deviation < 0.01 nm). The inversion was probably due to the fact that globular structures outside of the pre-cleaned region are more densely packed than those in the pre-cleaned region, therefore not registering that much of a height difference.

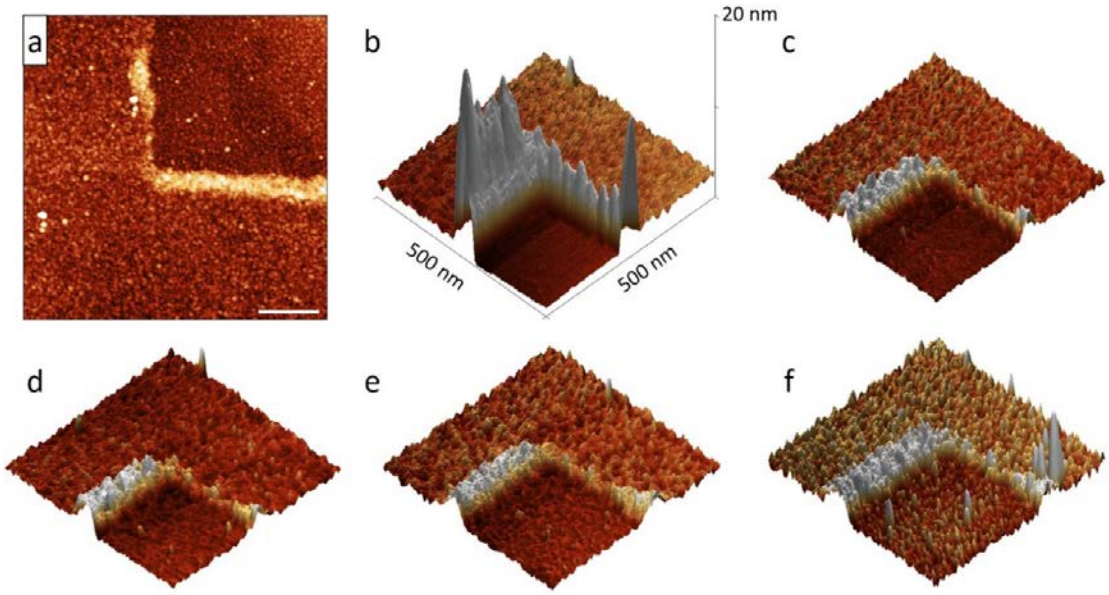

Figure A.12 (a) AFM topographical image of AFM cleaned Au nanoplate after 24 hrs exposure to MCH solution. Scale bar: 200 nm; Z scale: 10 nm. 500 nm × 500 nm 3D AFM topography of MCH adsorption layer on top of partially cleaned Au nanoplate at different reaction times: (b) 0 secs, (c) 300 secs, (d) 3000 secs, (e) 30,000 secs, (f) 120,000 secs, Z scale: 20 nm

Given the majorities of functional SAMs are mixed systems of functional and passivating ligands, we also studied the ligand-exchange from mixed thiol solutions. Equimolar ODT and MCH (total thiol concentration = 1 mM) produced a surface morphology contrast similar to those observed in ODT study (Figure A.13a). Analogous network-like globular structures appeared only outside of the pre-clean area, generating a 1 μm × 1 μm R_{rms} of 0.84 nm (Figure A.13b_1), while inside the pre-clean area, 1 μm × 1 μm R_{rms} remains 0.27 nm (Figure A.13c_1). This resemblance is likely due to the differences in SAM formation

energy and relative solubility of different thiols in ethanol. Thiol component with relatively long methylene chain will be preferentially absorbed onto the Au surface from equimolar solutions.[265] The fact that MCH contains a hydroxyl group further decreases its ratio in the mixed SAM due to the increased solubility in ethanol.[419] Thus, the final chemical composition of SAM domains should be largely ODT, providing a large enough hydrophobic repulsion force to prevent the surface migration of PVP into the pre-cleaned region. Nevertheless, the effect of MCH can be found, the globular structures generated are considerably more densely packed and lower in height (~ 2 nm compared to ~ 4 nm) compared with pure ODT ligand-exchange, suggesting a less ordered mixed-SAM layer and better intermixing with residual PVP chains (Figure A.13c).

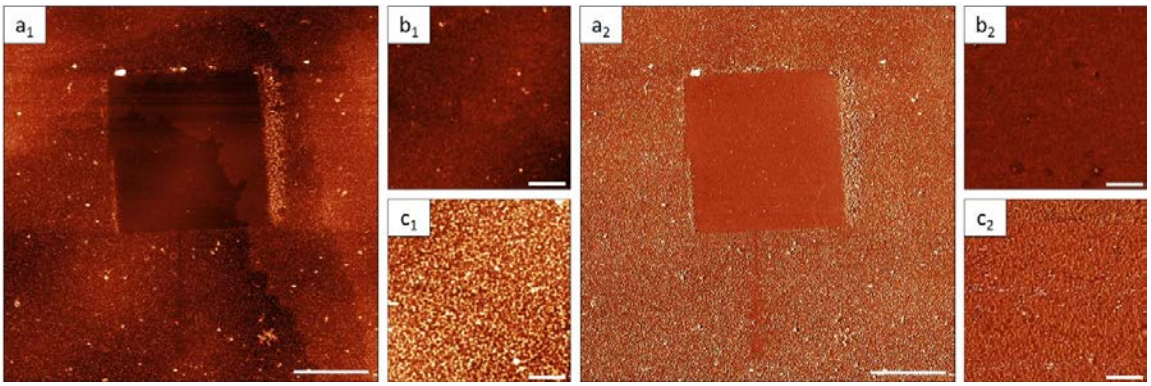

Figure A.13 (a) AFM topographical (subset1) and phase (subset2) image of 2 × 2 µm AFM cleaned Au nanoplates after 24 hrs of exposure to 1 mM equimolar MCH/ODT. Respective detailed map (b) inside and (c) outside of the cleaned surface area. Scale bar: 1 µm (a), 200 nm (b, c). Z scale: 10 nm and 30° (a), 5 nm and 20° (b, c).

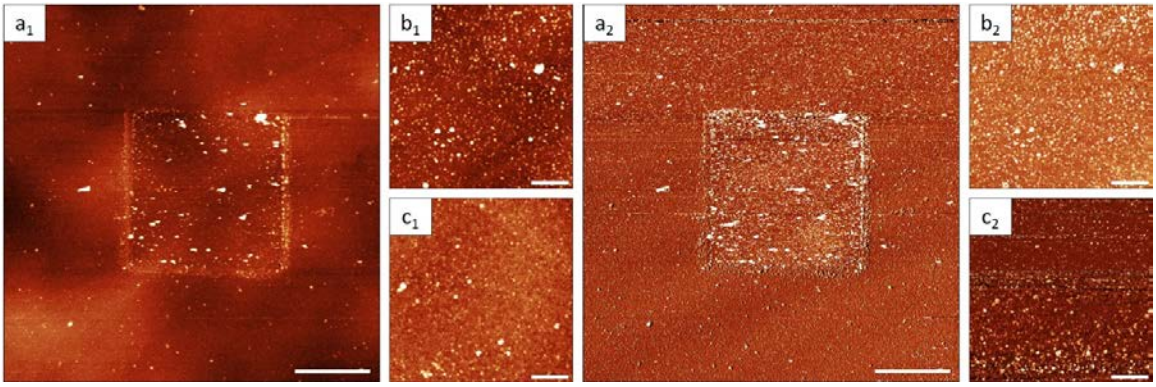

Figure A.14 (a) AFM topographical (subset1) and phase (subset2) image of 2 × 2 µm AFM cleaned Au nanoplates after 24 hrs of exposure to pure solvent (ethanol). Respective detailed map inside (b) and outside (c) of the cleaned area. Scale bar: 1 µm (a), 200 nm (b, c). Z scale: 10 nm and 20° (a), 5 nm and 20° (b, c).

APPENDIX B. CHAPTER 5 SUPPORTING INFORMATION

B.1 Estimation of Volume Density of AuNR in AuNR/CNF Membrane

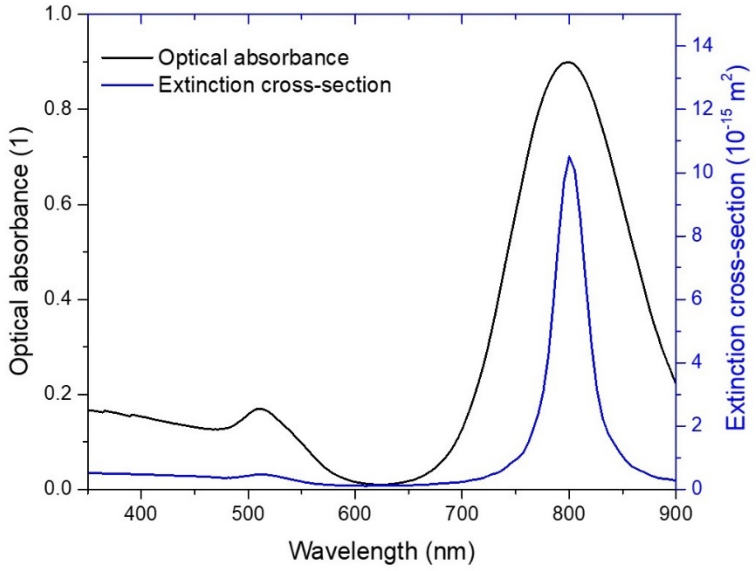

Figure B.1 Optical absorbance of the AuNR feed solution (black). Extinction cross-section obtained from unpolarized FDTD simulation of a single AuNR in water (Blue).

The numerical concentration (n) of AuNR in the feed solution can be calculated based on the optical absorbance measured by UV-vis spectroscopy and the expected extinction cross-section of individual AuNR (σ) (Figure B.1):

Optical absorbance measured by UV-vis at 798 nm: $A = \log_{10}(I_0/I) = 0.90$

optical pathlength of UV-vis cuvette: z = 10 mm

Extinction cross-section of individual AuNR at 798 nm: $\sigma = 1.05 \times 10^{-14}$ m^{-2} (obtained from FDTD simulation)

Optical extinction measured: $\ln(I_0/I) = \log_{10}(I_0/I) \times \ln 10 = 2.07$

$\ln(I_0/I) = n\sigma z = n \times 1.05 \times 10^{-16}\ m^3 \Rightarrow n = 1.971 \times 10^{16}\ m^{-3} = 1.971 \times 10^{10}\ mL^{-1}$ (AuNR concentration in solution)

Once the numerical concentration of AuNR in the feed solution is determined. The volume density of AuNR in the CNF membrane can be estimated by knowing the physical dimension of the membrane and assuming 100% retention of all the AuNR from the feed solution:

Total AuNR solution added: 3 mL, Radius of membrane: 47 mm, Thickness of membrane: 1 µm

Volume density of AuNR = $\frac{3 \times 1.971 \times 10^{10}}{\pi \times 47000^2 \times 1} \approx 8.5\ \mu m^{-3}$

B.2 SERS Performance of Dropcasted AuNR Film on Si Wafer and Glass

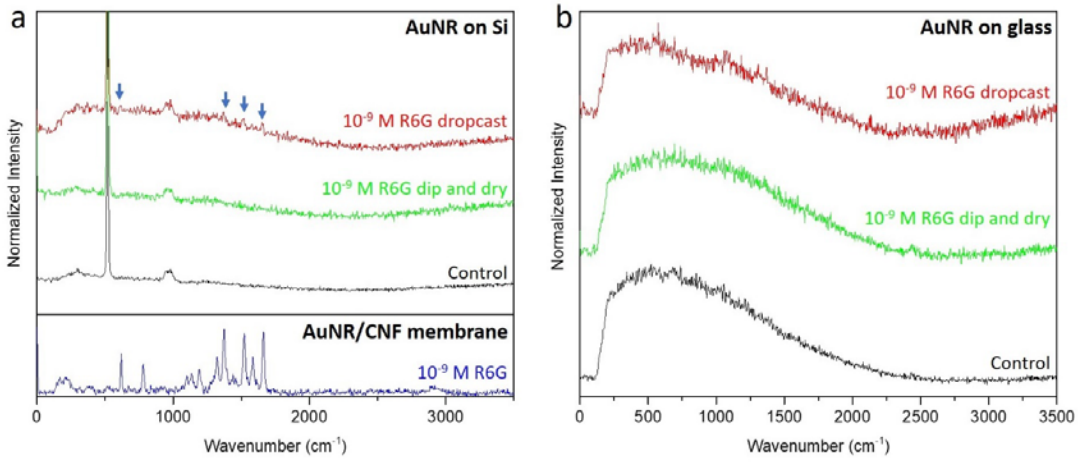

Figure B.2 (a) Raman spectra of dropcasted AuNR film on Si wafer in its native state (black), dipped and dried with 10^{-9} M R6G solution (green), dropcasted and dried with 10^{-9} M R6G solution (red), and AuNR/CNF membrane after 10^{-9} M R6G solution filtration. (b) Raman spectra of dropcasted AuNR film on glass in its native state (black), dipped and dried with 10^{-9} M R6G solution (green), dropcasted and dried with 10^{-9} M R6G solution (red).

The SERS performance of dropcasted AuNR film on rigid substrate was tested using Si wafer and glass. Figure B.2 shows the detection of 10^{-9} M R6G using 532 nm laser excitation. Two common method of introducing analytes were attempted: dip and dry, in which the substrate is dipped into the analyte solution and allowed to dry under ambient conditions, and dropcast, in which a droplet of analyte solution is directly dropcasted onto the substrate and allowed to dry under ambient condition. In this case, the dropcast method enables much stronger analyte-AuNR interactions as all the analytes are retained on the substrate, but takes much longer, as the entire droplet needs to evaporate. In Figure B.2a, the Raman peak at 520 cm^{-1} and ~1000 cm^{-1} are from the underlying Si wafer, only in dropcast sample do we see 4 extremely weak peak (S/N < 3, marked by blue arrows) that can be attributed to R6G molecules. In comparison, the entire R6G spectrum can be clearly identified in the AuNR/CNF membrane sample (Figure B.2a, blue curve). The same two methods were tested with glass substrate, which has similar refractive index to cellulose (Figure B.2b). However, both method produced negative results, besides, significant fluorescence was observed.

B.3 SERS Performance of AuNR/CNF Membrane in Detecting Non-resonant Organic Molecules with Weak Raman Scattering

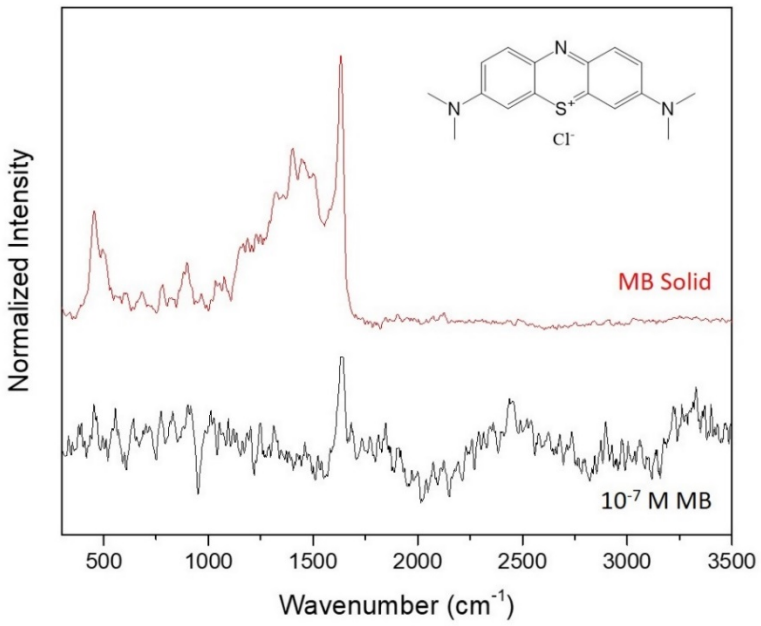

Figure B.3 Raman spectrum obtained from bulk MB salts (red). And SERS spectrum obtained from AuNR/CNF after 10^{-7} M MB solution filtration (black). Inset: chemical structure of MB

APPENDIX C. CHAPTER 6 SUPPORTING INFORMATION

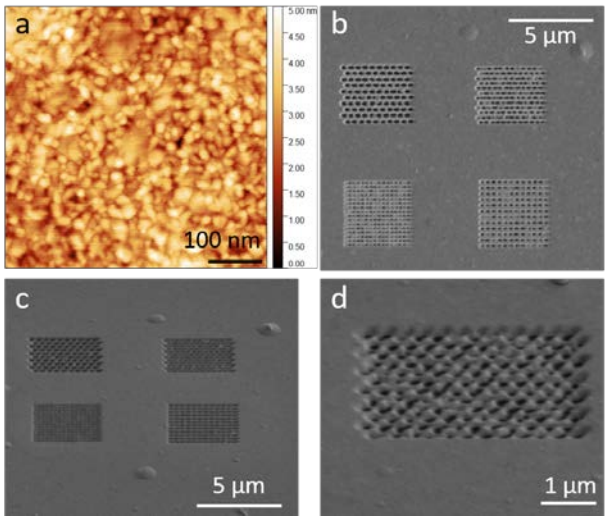

Figure C.1 (a) AFM topographical image of E-beam evaporated gold on Si substrate. (b) Top-view SEM image of NHAs. (c) Oblique side-view SEM image of NHAs. (d) Oblique side-view SEM image of p340h

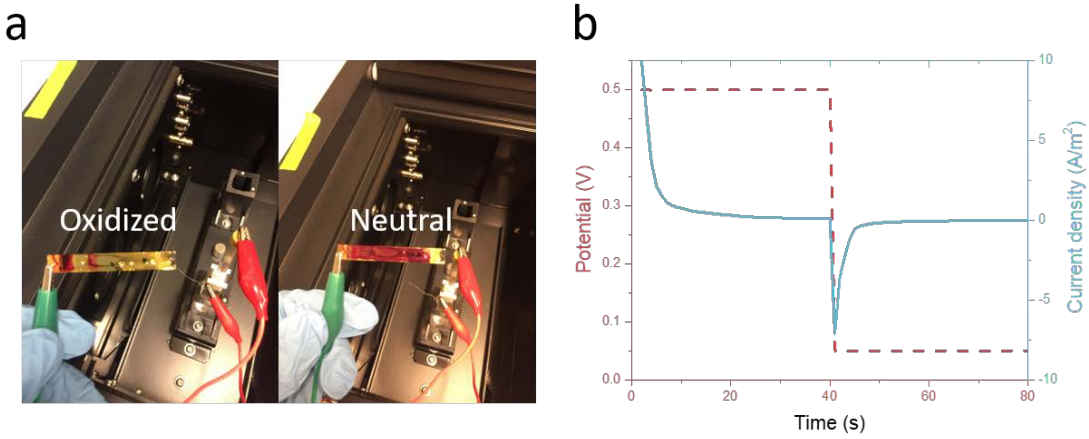

Figure C.2 (a) Optical photograph showing the ECP coated nanohole array substrate in the oxidized and neutral state. (b) Current density changes vs time in response to applied potential.

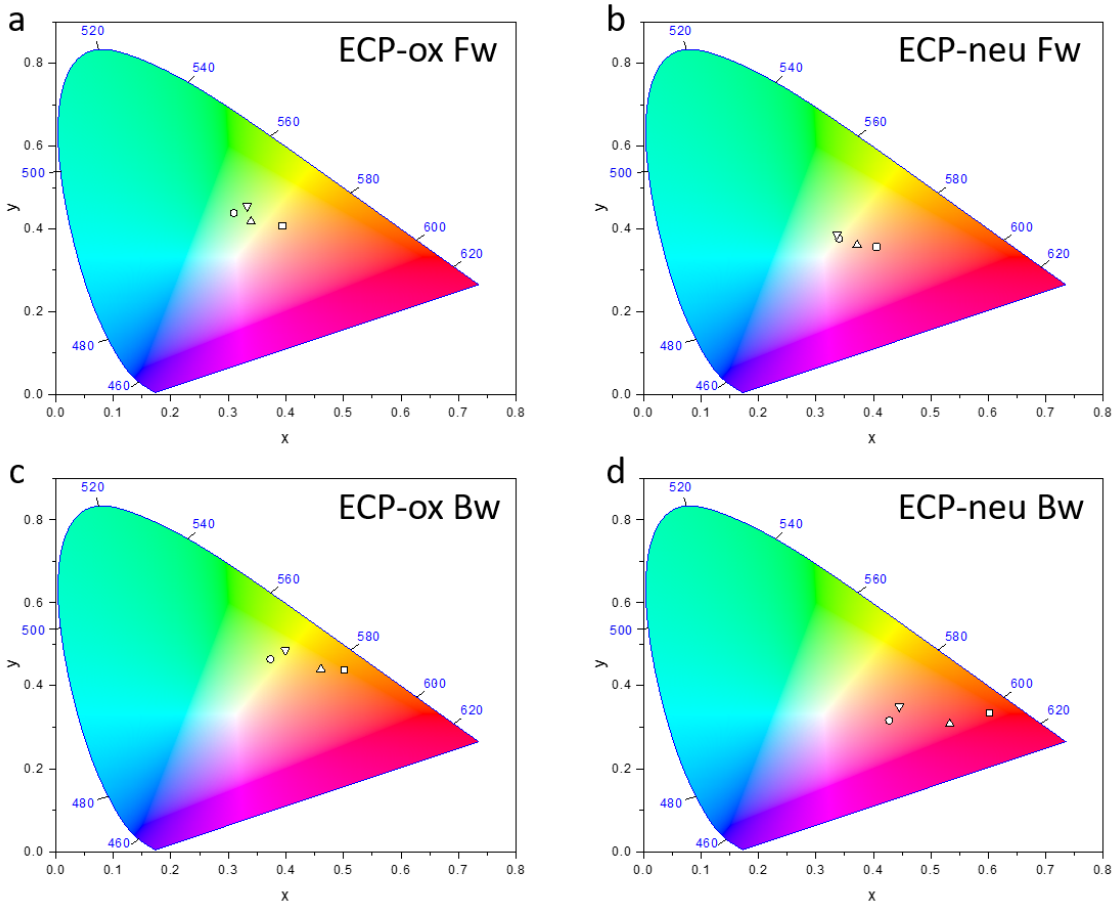

Figure C.3 CIE 1931 coordinates (standard illuminant E) calculated from normalized spectrum of NHAs under different conditions □: p250, ○: p350, △: p340h, ▽: p420h (a) ECP-ox Fw, (b) ECP-neu Fw, (c) ECP-ox Bw, (d) ECP-neu Bw

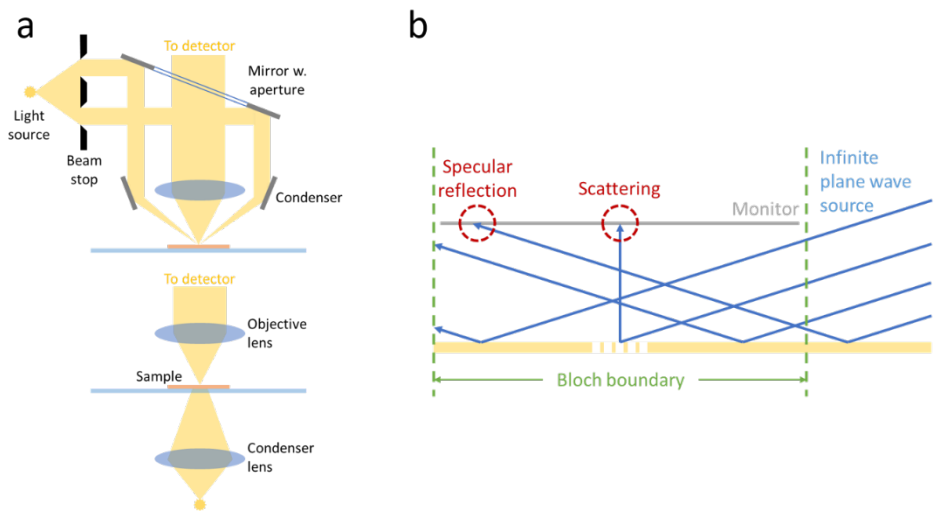

Figure C.4 (a) Schematics showing backward scattering (top) and forward scattering (bottom) illumination setup. (b) Schematics showing the FDTD simulation setup in back scattering illumination condition.

Compared to forward scattering, backward scattering is much more challenging to simulate and is rarely performed. This is because when a plane wave source is injected at an incidence angle other than 0°, different frequency components of the source pulse will have different angles of incidence due to phase differences. Since the angle of incidence of the center frequency is already very high (73°), incidence angle for some of the frequency components can easily approach 90°, coupled with periodic boundaries, these components can propagate indefinitely in the XY plane, easily leading to divergence. Thus, to perform such simulation, extreme narrowband sources need to be used, leading to long pulse length (50 fs), and individual simulation must be run at each frequency point to produce the spectrum in a specific range, quickly draining computational resources and increasing computational time.

Another problem with simulating backward scattering is that the periodic boundary condition will necessarily cause specular reflection to be collected. As shown in Figure

C.4, when both the planewave source and the structure is infinite in the XY plane, 2D monitors will unavoidably collect radiations from specular reflection. Such effect is demonstrated in Figure 6c, in which we simulated the "back scattering spectrum" of a solid perfectly smooth 150-nm thick Au film (Bulk Au). Because such film is incapable of producing back scattered light, as all the light will either be absorbed or specularly reflected, the intensity should be zero across the board. However, we do see spectrum features, meaning specular reflection is collected.

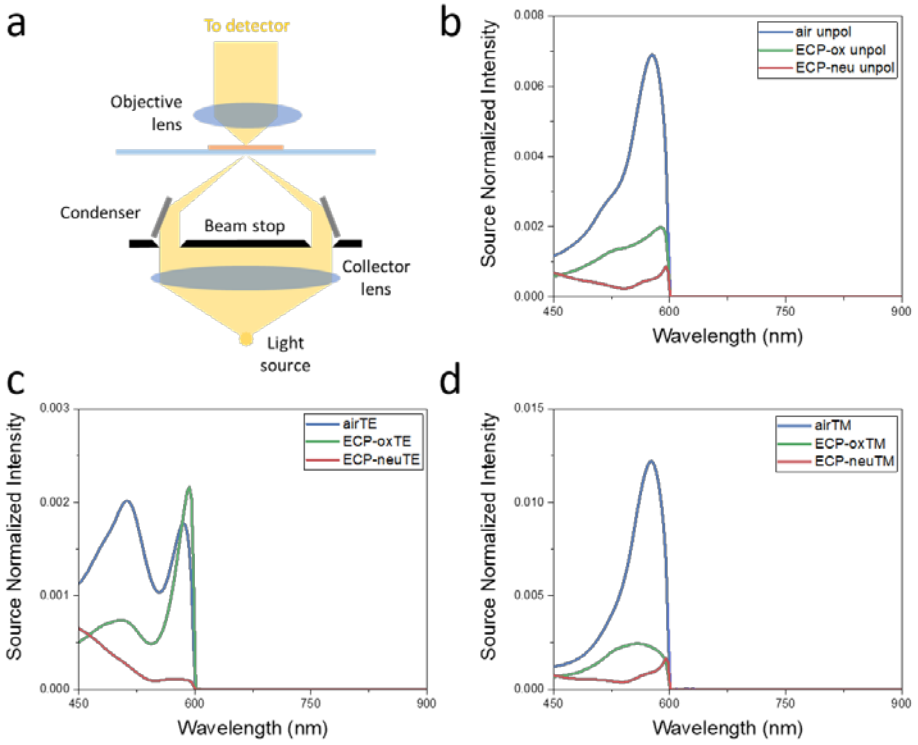

Figure C.5 (a) Schematics showing the transmission darkfield illumination condition. (b) Unpolarized scattering spectra of p250s array in air (blue), ECP-ox (green), and ECP-neu (red) from FDTD simulation. Decomposition of FDTD simulated spectra into (c) TE and (d) TM components.

We also simulated the spectra for the darkfield transmission setup (Figure C.5a), in which light is coming from beneath the substrate at a highly oblique angle and the spectrum is

collected by objectives lens above the substrate. Figure C.5b shows the transmission spectrum for unpolarized illumination. In general, the transmission intensities are very low, less than 1% of the source intensity is transmitted across the spectrum with pristine NHAs. When ECP is added, the transmission dropped even lower to below 0.2%. This is intuitive, as grazing angle incidence can be shown to enhance reflectivity by simple Fresnel equation analysis using complex refractive indices. There also appears to be a cut-off frequency below which transmission intensity is negligible. Figure C.5c, d shows the decomposition of the simulated spectra into TE and TM components. By comparing with the unpolarized spectra, we can see the general spectra trend is dominated by TM components where TE components only have a small contribution. However, we want to accentuate here that these simulations are not experimentally verified, sharp transitions such as the one shown in ECP-neu TM mode might be due to simulation instabilities and may not be physically accurate. Nevertheless, these preliminary results are fascinating, especially the appearance of a cut-off frequency and the markedly different TM/TE response and would be of great interest for future research.

APPENDIX D. CHAPTER 7 SUPPORTING INFORMATION

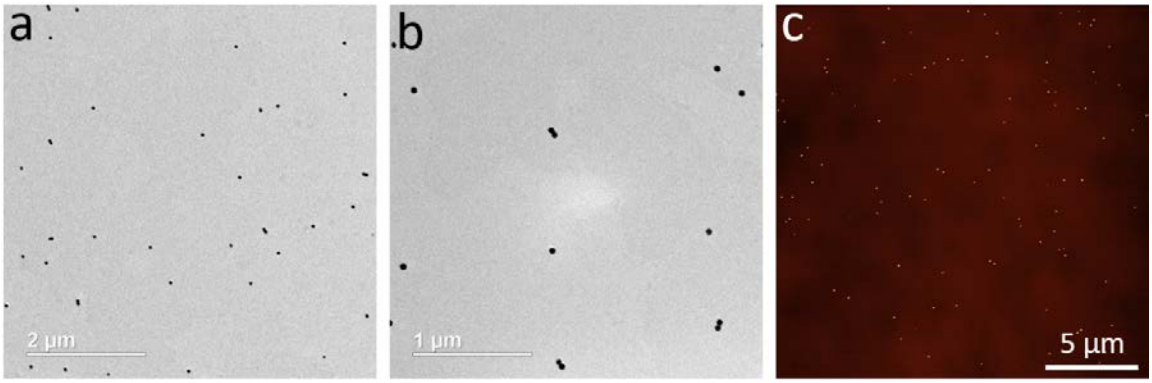

Figure D.1 (a) Representative TEM image showing the AuNS to have a mean size of 52 nm. (b) TEM image of larger magnification showing the presence of dimers among monomers. (c) Large area AFM topographical scan of AuNS spin-coated on FP cavity. Z scale: 70 nm.

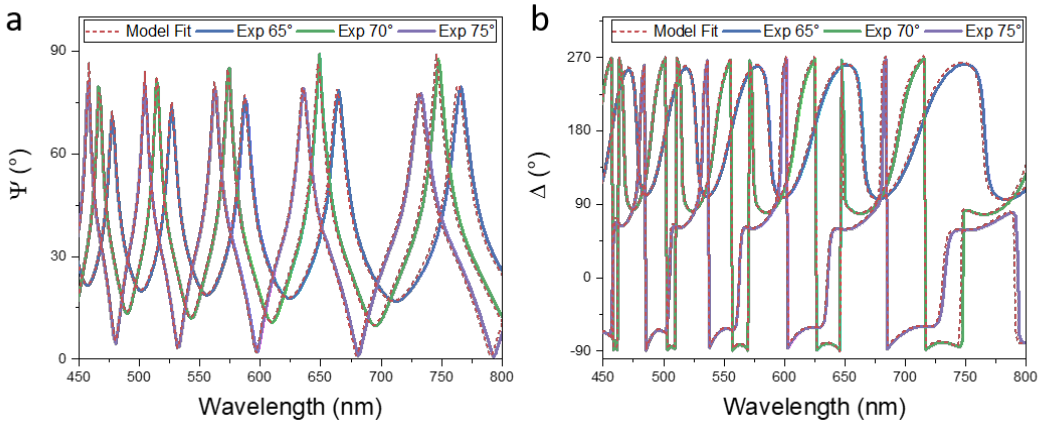

Figure D.2 Spectroscopic ellipsometry measurement of thermally oxidized SiO2 wafer at 65°(blue solid curve), 70°(green solid curve), 75°(purple solid curve) incident angles, and fit curve with 2170 nm-thick SiO2 on Si model (red dashed curve) for Ψ (a) and Δ (b) respectively.

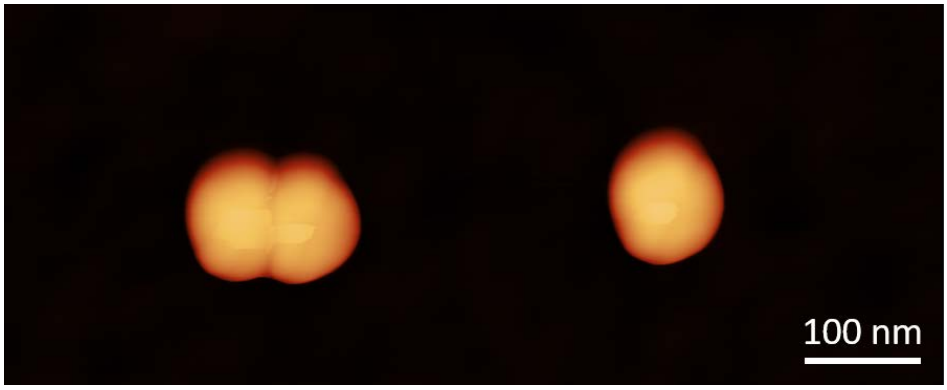

Figure D.3 High resolution AFM topographical image of a dimer and a monomer in the same frame. Z scale: 70 nm

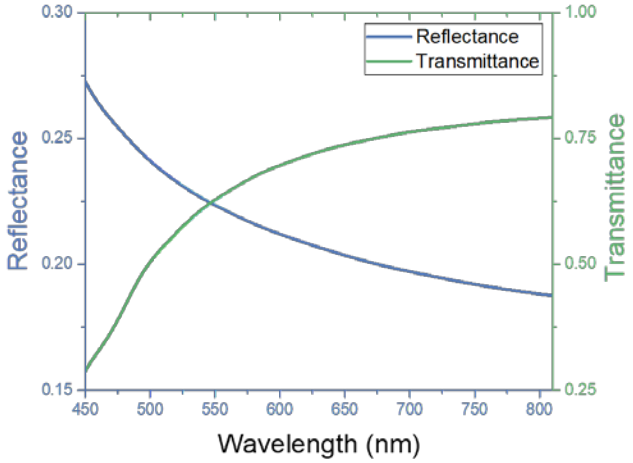

Figure D.4 Calculated reflectance and transmittance of perfectly flat, semi-infinite, SiO_2/Si interface (light going from SiO_2 into Si)

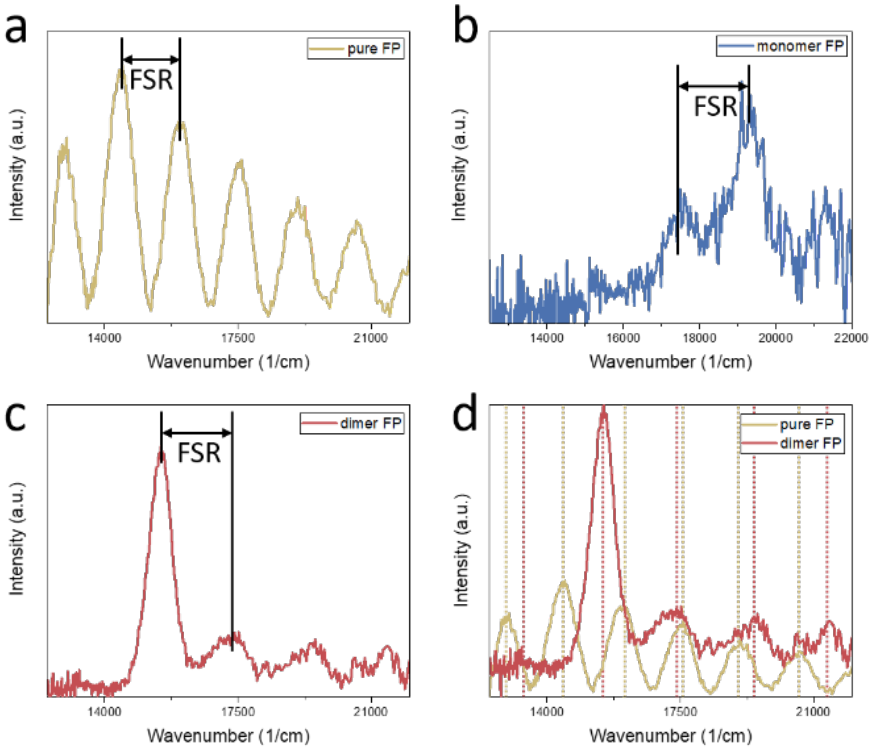

Figure D.5 Spectra from Figure 4 converted to wavenumber space: (a) pure FP, (b) individual monomer on FP, (c) individual dimer on FP. (d) Superimposed spectra of dimer on FP and pure FP with vertical dashed lines of respective color marking their mode positions.

REFERENCES

(1) *Plasmonics: theory and applications*; Shahbazyan, T. V.; Stockman, M. I., Eds.; Challenges and Advances in Computational Chemistry and Physics; Springer: Dordrecht, Netherlands, 2013; Vol. 15.

(2) Ghosh, S. K.; Pal, T. Interparticle coupling effect on the surface plasmon resonance of gold nanoparticles: from theory to applications. *Chem. Rev.* **2007,** *107*, 4797-4862.

(3) Li, E.-P.; Chu, H.-S. *Plasmonic nanoelectronics and sensing*; Cambridge University Press: Cambridge, U.K., 2014.

(4) Maier, S. A.; Brongersma, M. L.; Kik, P. G.; Meltzer, S.; Requicha, A. A.; Atwater, H. A. Plasmonics—a route to nanoscale optical devices. *Adv. Mater.* **2001,** *13*, 1501-1505.

(5) Pelton, M.; Bryant, G. W. *Introduction to metal-nanoparticle plasmonics*; John Wiley & Sons: Hoboken, NJ, 2013.

(6) Maier, S. A. *Plasmonics: fundamentals and applications*; Springer US: New York, **2007**.

(7) Atwater, H. A. The promise of plasmonics. *Sci. Am.* **2007,** *296*, 56-62.

(8) Le Ru, E. C.; Etchegoin, P. G. Principles of surface-enhanced Raman spectroscopy: and related plasmonic effects. 1st ed. *Elsevier*: Amsterdam. **2009**.

(9) Maier, S. A.; Kik, P. G.; Atwater, H. A.; Meltzer, S.; Harel, E.; Koel, B. E.; Requicha, A. A. G. Local detection of electromagnetic energy transport below the diffraction limit in metal nanoparticle plasmon waveguides. *Nat. Mater.* **2003**, *2*, 229-232.

(10) Campion, A.; Kambhampati, P. Surface-enhanced Raman scattering. *Chem. Soc. Rev.* **1998**, *27*, 241-250.

(11) D'Andrea, C.; Bochterle, J.; Toma, A.; Huck, C.; Neubrech, F.; Messina, E.; Fazio, B.; Maragò, O. M.; Di Fabrizio, E.; Lamy de La Chapelle, M. et al. Optical

Nanoantennas for Multiband Surface-Enhanced Infrared and Raman Spectroscopy. *ACS Nano* **2013,** *7*, 3522-3531.

(12) Ozbay, E. Plasmonics: merging photonics and electronics at nanoscale dimensions. *Science* **2006,** *311*, 189-193.

(13) Bozhevolnyi, S. I. Frontiers in Optics 2008/Laser Science XXIV/Plasmonics and Metamaterials/Optical Fabrication and Testing, Rochester, New York, 2008; p MWD3.

(14) Wang, F.; Shen, Y. R. General Properties of Local Plasmons in Metal Nanostructures. *Phys. Rev. Lett.* **2006,** *97*, 206806.

(15) Jain, P. K.; Lee, K. S.; El-Sayed, I. H.; El-Sayed, M. A. Calculated Absorption and Scattering Properties of Gold Nanoparticles of Different Size, Shape, and Composition: Applications in Biological Imaging and Biomedicine. *J. Phys. Chem. B* **2006,** *110*, 7238-7248.

(16) Liz-Marzán, L. M. Tailoring Surface Plasmons through the Morphology and Assembly of Metal Nanoparticles. *Langmuir* **2006,** *22*, 32-41.

(17) Kreibig, U.; Vollmer, M., *Optical properties of metal clusters*. Springer-Verlag: Berlin, Germany 1995.

(18) Zhou, F.; Li, Z.-Y.; Liu, Y.; Xia, Y. Quantitative analysis of dipole and quadrupole excitation in the surface plasmon resonance of metal nanoparticles. *J. Phys. Chem. C* **2008,** *112*, 20233-20240.

(19) Zhang, Q.; Li, W.; Moran, C.; Zeng, J.; Chen, J.; Wen, L.-P.; Xia, Y. Seed-mediated synthesis of Ag nanocubes with controllable edge lengths in the range of 30− 200 nm and comparison of their optical properties. *J. Am. Chem. Soc.* **2010,** *132*, 11372-11378.

(20) Kelly, K. L.; Coronado, E.; Zhao, L. L.; Schatz, G. C. The Optical Properties of Metal Nanoparticles: The Influence of Size, Shape, and Dielectric Environment. *J. Phys. Chem. B* **2003,** *107*, 668-677.

(21) Rycenga, M.; Cobley, C. M.; Zeng, J.; Li, W.; Moran, C. H.; Zhang, Q.; Qin, D.; Xia, Y. Controlling the Synthesis and Assembly of Silver Nanostructures for Plasmonic Applications. *Chem. Rev.* **2011,** *111*, 3669-3712.

(22) Mock, J. J.; Barbic, M.; Smith, D. R.; Schultz, D. A.; Schultz, S. Shape effects in plasmon resonance of individual colloidal silver nanoparticles. *J. Chem. Phys.* **2002,** *116*, 6755-6759.

(23) Liao, P. F.; Wokaun, A. Lightning rod effect in surface enhanced Raman scattering. *J. Chem. Phys.* **1982,** *76*, 751-752.

(24) Grillet, N.; Manchon, D.; Bertorelle, F.; Bonnet, C.; Broyer, M.; Cottancin, E.; Lermé, J.; Hillenkamp, M.; Pellarin, M. Plasmon coupling in silver nanocube dimers: resonance splitting induced by edge rounding. *ACS Nano* **2011,** *5*, 9450-9462.

(25) Jin, R.; Cao, Y.; Mirkin, C. A.; Kelly, K.; Schatz, G. C.; Zheng, J. Photoinduced conversion of silver nanospheres to nanoprisms. *Science* **2001,** *294*, 1901-1903.

(26) Alvarez, M. M.; Khoury, J. T.; Schaaff, T. G.; Shafigullin, M. N.; Vezmar, I.; Whetten, R. L. Optical absorption spectra of nanocrystal gold molecules. *J. Phys. Chem. B* **1997,** *101*, 3706-3712.

(27) Link, S.; El-Sayed, M. A. Spectral Properties and Relaxation Dynamics of Surface Plasmon Electronic Oscillations in Gold and Silver Nanodots and Nanorods. *J. Phys. Chem. B* **1999,** *103*, 8410-8426.

(28) Wiley, B. J.; Chen, Y.; McLellan, J. M.; Xiong, Y.; Li, Z.-Y.; Ginger, D.; Xia, Y. Synthesis and Optical Properties of Silver Nanobars and Nanorice. *Nano Lett.* **2007,** *7*, 1032-1036.

(29) Shen, Y.; Zhou, J.; Liu, T.; Tao, Y.; Jiang, R.; Liu, M.; Xiao, G.; Zhu, J.; Zhou, Z.-K.; Wang, X. Plasmonic gold mushroom arrays with refractive index sensing figures of merit approaching the theoretical limit. *Nat. Commun.* **2013,** *4*, 2381.

(30) Li, Q.; Zhang, Z. Bonding and Anti-bonding Modes of Plasmon Coupling Effects in TiO2-Ag Core-shell Dimers. *Sci. Rep.* **2016,** *6*, 19433.

(31) Luk'yanchuk, B.; Zheludev, N. I.; Maier, S. A.; Halas, N. J.; Nordlander, P.; Giessen, H.; Chong, C. T. The Fano resonance in plasmonic nanostructures and metamaterials. *Nat. Mater.* **2010,** *9*, 707-715.

(32) Chang, W.-S.; Lassiter, J. B.; Swanglap, P.; Sobhani, H.; Khatua, S.; Nordlander, P.; Halas, N. J.; Link, S. A Plasmonic Fano Switch. *Nano Lett.* **2012,** *12*, 4977-4982.

(33) Cetin, A. E.; Altug, H. Fano Resonant Ring/Disk Plasmonic Nanocavities on Conducting Substrates for Advanced Biosensing. *ACS Nano* **2012,** *6*, 9989-9995.

(34) Yanik, A. A.; Cetin, A. E.; Huang, M.; Artar, A.; Mousavi, S. H.; Khanikaev, A.; Connor, J. H.; Shvets, G.; Altug, H. Seeing protein monolayers with naked eye through plasmonic Fano resonances. *Proc. Natl. Acad. Sci. U.S.A.* **2011,** *108*, 11784-11789.

(35) Fan, J. A.; He, Y.; Bao, K.; Wu, C.; Bao, J.; Schade, N. B.; Manoharan, V. N.; Shvets, G.; Nordlander, P.; Liu, D. R.et al. DNA-Enabled Self-Assembly of Plasmonic Nanoclusters. *Nano Lett.* **2011,** *11*, 4859-4864.

(36) Yu, R.; Cox, J. D.; de Abajo, F. J. G. Nonlinear Plasmonic Sensing with Nanographene. *Phys. Rev. Lett.* **2016,** *117*, 123904.

(37) Mesch, M.; Metzger, B.; Hentschel, M.; Giessen, H. Nonlinear Plasmonic Sensing. *Nano Lett.* **2016,** *16*, 3155-3159.

(38) Liu, Z.; Steele, J. M.; Srituravanich, W.; Pikus, Y.; Sun, C.; Zhang, X. Focusing Surface Plasmons with a Plasmonic Lens. *Nano Lett.* **2005,** *5*, 1726-1729.

(39) Homola, J.; Piliarik, M. Surface Plasmon Resonance (SPR) Sensors. In *Surface plasmon resonance based sensors*; Homola, J., Ed; Springer Series on Chemical Sensors and Biosensors; Springer-Verlag: Berlin, Germany, 2006; Vol. 4.

(40) Nordlander, P.; Prodan, E.: Plasmon Hybridization in Nanoparticles near Metallic Surfaces. *Nano Lett.* **2004**, *4*, 2209-2213.

(41) Hu, M.; Ghoshal, A.; Marquez, M.; Kik, P. G.: Single Particle Spectroscopy Study of Metal-Film-Induced Tuning of Silver Nanoparticle Plasmon Resonances. *J. Phys. Chem. C* **2010**, *114*, 7509-7514.

(42) Niu, W.; Zhang, L.; Xu, G. Seed-mediated growth of noble metal nanocrystals: crystal growth and shape control. *Nanoscale* **2013,** *5*, 3172-3181.

(43) Zhang, H.; Jin, M.; Xia, Y. Noble-Metal Nanocrystals with Concave Surfaces: Synthesis and Applications. *Angew. Chem. Int. Ed.* **2012,** *51*, 7656-7673.

(44) Quan, Z.; Wang, Y.; Fang, J. High-index faceted noble metal nanocrystals. *Acc. Chem. Res.* **2012,** *46*, 191-202.

(45) Lohse, S. E.; Burrows, N. D.; Scarabelli, L.; Liz-Marzán, L. M.; Murphy, C. J. Anisotropic Noble Metal Nanocrystal Growth: The Role of Halides. *Chem. Mater.* **2014,** *26*, 34-43.

(46) Burda, C.; Chen, X.; Narayanan, R.; El-Sayed, M. A. Chemistry and Properties of Nanocrystals of Different Shapes. *Chem. Rev.* **2005,** *105*, 1025-1102.

(47) Xia, Y. N.; Xiong, Y. J.; Lim, B.; Skrabalak, S. E. Shape-Controlled Synthesis of Metal Nanocrystals: Simple Chemistry Meets Complex Physics? *Angew. Chem. Int. Ed.* **2009,** *48*, 60-103.

(48) Turkevich, J.; Stevenson, P. C.; Hillier, J. A study of the nucleation and growth processes in the synthesis of colloidal gold. *Discuss. Faraday Soc.* **1951,** *11*, 55-75.

(49) Frens, G. Controlled nucleation for the regulation of the particle size in monodisperse gold suspensions. *Nature* **1973,** *241*, 20-22.

(50) Brust, M.; Walker, M.; Bethell, D.; Schiffrin, D. J.; Whyman, R. Synthesis of thiol-derivatised gold nanoparticles in a two-phase liquid–liquid system. *J. Chem. Soc., Chem. Commun.* **1994**, 801-802.

(51) Zhao, P.; Li, N.; Astruc, D. State of the art in gold nanoparticle synthesis. *Coord. Chem. Rev.* **2013,** *257*, 638-665.

(52) Brown, K. R.; Fox, A. P.; Natan, M. J. Morphology-Dependent Electrochemistry of Cytochrome c at Au Colloid-Modified SnO2 Electrodes. *J. Am. Chem. Soc.* **1996,** *118*, 1154-1157.

(53) Sun, Y.; Xia, Y. Shape-Controlled Synthesis of Gold and Silver Nanoparticles. *Science* **2002,** *298*, 2176-2179.

(54) Fievet, F.; Lagier, J. P.; Figlarz, M. Preparing Monodisperse Metal Powders in Micrometer and Submicrometer Sizes by the Polyol Process. *MRS Bull.* **1989,** *14*, 29-34.

(55) Wiley, B.; Herricks, T.; Sun, Y.; Xia, Y. Polyol Synthesis of Silver Nanoparticles: Use of Chloride and Oxygen to Promote the Formation of Single-Crystal, Truncated Cubes and Tetrahedrons. *Nano Lett.* **2004,** *4*, 1733-1739.

(56) Coskun, S.; Aksoy, B.; Unalan, H. E. Polyol Synthesis of Silver Nanowires: An Extensive Parametric Study. *Cryst. Growth Des.* **2011,** *11*, 4963-4969.

(57) Dongjo, K.; Sunho, J.; Jooho, M. Dongjo, K.; Sunho, J.; Jooho, M. Synthesis of silver nanoparticles using the polyol process and the influence of precursor injection. *Nanotechnology* **2006,** *17*, 4019.the polyol process and the influence of precursor injection. *Nanotechnology* **2006,** *17*, 4019-4024.

(58) Skrabalak, S. E.; Wiley, B. J.; Kim, M.; Formo, E. V.; Xia, Y. On the Polyol Synthesis of Silver Nanostructures: Glycolaldehyde as a Reducing Agent. *Nano Lett.* **2008,** *8*, 2077-2081.

(59) Feldmann, C. Polyol-Mediated Synthesis of Nanoscale Functional Materials. *Adv. Funct. Mater.* **2003,** *13*, 101-107.

(60) Sun, Y. G.; Xia, Y. N. Large-scale synthesis of uniform silver nanowires through a soft, self-seeding, polyol process. *Adv. Mater.* **2002,** *14*, 833-837.

(61) Wiley, B.; Sun, Y.; Xia, Y. Polyol Synthesis of Silver Nanostructures: Control of Product Morphology with Fe(II) or Fe(III) Species. *Langmuir* **2005,** *21*, 8077-8080.

(62) Sun, Y.; Mayers, B.; Herricks, T.; Xia, Y. Polyol Synthesis of Uniform Silver Nanowires: A Plausible Growth Mechanism and the Supporting Evidence. *Nano Lett.* **2003,** *3*, 955-960.

(63) Xia, Y.; Gilroy, K. D.; Peng, H.-C.; Xia, X. Seed-Mediated Growth of Colloidal Metal Nanocrystals. *Angew. Chem. Int. Ed.* **2017,** *56*, 60-95.

(64) Murphy, C. J.; Thompson, L. B.; Chernak, D. J.; Yang, J. A.; Sivapalan, S. T.; Boulos, S. P.; Huang, J.; Alkilany, A. M.; Sisco, P. N. Gold nanorod crystal growth: From seed-mediated synthesis to nanoscale sculpting. *Curr. Opin. Colloid Interface Sci.* **2011,** *16*, 128-134.

(65) Vigderman, L.; Khanal, B. P.; Zubarev, E. R. Functional Gold Nanorods: Synthesis, Self-Assembly, and Sensing Applications. *Adv. Mater.* **2012,** *24*, 4811-4841.

(66) Jana, N. R.; Gearheart, L.; Murphy, C. J. Wet Chemical Synthesis of High Aspect Ratio Cylindrical Gold Nanorods. *J. Phys. Chem. B* **2001,** *105*, 4065-4067.

(67) Sau, T. K.; Murphy, C. J. Seeded High Yield Synthesis of Short Au Nanorods in Aqueous Solution. *Langmuir* **2004,** *20*, 6414-6420.

(68) Carbó-Argibay, E.; Rodríguez-González, B.; Gómez-Graña, S.; Guerrero-Martínez, A.; Pastoriza-Santos, I.; Pérez-Juste, J.; Liz-Marzán, L. M. The Crystalline Structure of Gold Nanorods Revisited: Evidence for Higher-Index Lateral Facets. *Angew. Chem. Int. Ed.* **2010,** *49*, 9397-9400.

(69) Lohse, S. E.; Murphy, C. J. The Quest for Shape Control: A History of Gold Nanorod Synthesis. *Chem. Mater.* **2013,** *25*, 1250-1261.

(70) Eustis, S.; El-Sayed, M. A. Why gold nanoparticles are more precious than pretty gold: Noble metal surface plasmon resonance and its enhancement of the radiative and nonradiative properties of nanocrystals of different shapes. *Chem. Soc. Rev.* **2006,** *35*, 209-217.

(71) Jana, N. R.; Gearheart, L.; Murphy, C. J. Seed-mediated growth approach for shape-controlled synthesis of spheroidal and rod-like gold nanoparticles using a surfactant template. *Adv. Mater.* **2001,** *13*, 1389-1393.

(72) Zweifel, D. A.; Wei, A. Sulfide-Arrested Growth of Gold Nanorods. *Chem. Mater.* **2005,** *17*, 4256-4261.

(73) Ye, X.; Jin, L.; Caglayan, H.; Chen, J.; Xing, G.; Zheng, C.; Doan-Nguyen, V.; Kang, Y.; Engheta, N.; Kagan, C. R.et al. Improved Size-Tunable Synthesis of Monodisperse Gold Nanorods through the Use of Aromatic Additives. *ACS Nano* **2012,** *6*, 2804-2817.

(74) Langille, M. R.; Personick, M. L.; Zhang, J.; Mirkin, C. A. Defining Rules for the Shape Evolution of Gold Nanoparticles. *J. Am. Chem. Soc.* **2012,** *134*, 14542-14554.

(75) Scarabelli, L.; Coronado-Puchau, M.; Giner-Casares, J. J.; Langer, J.; Liz-Marzán, L. M. Monodisperse Gold Nanotriangles: Size Control, Large-Scale Self-Assembly, and Performance in Surface-Enhanced Raman Scattering. *ACS Nano* **2014,** *8*, 5833-5842.

(76) Niu, W.; Zheng, S.; Wang, D.; Liu, X.; Li, H.; Han, S.; Chen, J.; Tang, Z.; Xu, G. Selective Synthesis of Single-Crystalline Rhombic Dodecahedral, Octahedral, and Cubic Gold Nanocrystals. *J. Am. Chem. Soc.* **2009,** *131*, 697-703.

(77) Kumar, P. S.; Pastoriza-Santos, I.; Rodríguez-González, B.; De Abajo, F. J. G.; Liz-Marzan, L. M. High-yield synthesis and optical response of gold nanostars. *Nanotechnology* **2007,** *19*, 015606.

(78) Guerrero-Martínez, A.; Barbosa, S.; Pastoriza-Santos, I.; Liz-Marzán, L. M. Nanostars shine bright for you: Colloidal synthesis, properties and applications of branched metallic nanoparticles. *Curr. Opin. Colloid Interface Sci.* **2011,** *16*, 118-127.

(79) Ye, E.; Win, K. Y.; Tan, H. R.; Lin, M.; Teng, C. P.; Mlayah, A.; Han, M.-Y. Plasmonic Gold Nanocrosses with Multidirectional Excitation and Strong Photothermal Effect. *J. Am. Chem. Soc.* **2011,** *133*, 8506-8509.

(80) Niu, W.; Chua, Y. A. A.; Zhang, W.; Huang, H.; Lu, X. Highly Symmetric Gold Nanostars: Crystallographic Control and Surface-Enhanced Raman Scattering Property. *J. Am. Chem. Soc.* **2015,** *137*, 10460-10463.

(81) Mulvihill, M. J.; Ling, X. Y.; Henzie, J.; Yang, P. Anisotropic Etching of Silver Nanoparticles for Plasmonic Structures Capable of Single-Particle SERS. *J. Am. Chem. Soc.* **2010,** *132*, 268-274.

(82) Tao, A.; Sinsermsuksakul, P.; Yang, P. Polyhedral Silver Nanocrystals with Distinct Scattering Signatures. *Angew. Chem. Int. Ed.* **2006,** *45*, 4597-4601.

(83) Dass, A. Faradaurate Nanomolecules: A Superstable Plasmonic 76.3 kDa Cluster. *J. Am. Chem. Soc.* **2011,** *133*, 19259-19261.

(84) Kumara, C.; Zuo, X.; Ilavsky, J.; Chapman, K. W.; Cullen, D. A.; Dass, A. Super-Stable, Highly Monodisperse Plasmonic Faradaurate-500 Nanocrystals with 500 Gold Atoms: Au~500(SR)~120. *J. Am. Chem. Soc.* **2014,** *136*, 7410-7417.

(85) Zeng, C.; Chen, Y.; Kirschbaum, K.; Appavoo, K.; Sfeir, M. Y.; Jin, R. Structural patterns at all scales in a nonmetallic chiral Au133(SR)52 nanoparticle. *Science Advances* **2015,** *1*, e1500045.

(86) Zhou, M.; Zeng, C.; Chen, Y.; Zhao, S.; Sfeir, M. Y.; Zhu, M.; Jin, R. Evolution from the plasmon to exciton state in ligand-protected atomically precise gold nanoparticles. *Nat. Commun.* **2016,** *7*, 13240.

(87) Malola, S.; Lehtovaara, L.; Enkovaara, J.; Häkkinen, H. Birth of the Localized Surface Plasmon Resonance in Monolayer-Protected Gold Nanoclusters. *ACS Nano* **2013,** *7*, 10263-10270.

(88) Zhu, M.; Aikens, C. M.; Hollander, F. J.; Schatz, G. C.; Jin, R. Correlating the Crystal Structure of A Thiol-Protected Au25 Cluster and Optical Properties. *J. Am. Chem. Soc.* **2008,** *130*, 5883-5885.

(89) Salorinne, K.; Malola, S.; Wong, O. A.; Rithner, C. D.; Chen, X.; Ackerson, C. J.; Häkkinen, H. Conformation and dynamics of the ligand shell of a water-soluble Au102 nanoparticle. *Nat. Commun.* **2016,** *7*, 10401.

(90) Zeng, C.; Qian, H.; Li, T.; Li, G.; Rosi, N. L.; Yoon, B.; Barnett, R. N.; Whetten, R. L.; Landman, U.; Jin, R. Total Structure and Electronic Properties of the Gold Nanocrystal Au36(SR)24. *Angew. Chem. Int. Ed.* **2012,** *51*, 13114-13118.

(91) Chen, Y.; Zeng, C.; Liu, C.; Kirschbaum, K.; Gayathri, C.; Gil, R. R.; Rosi, N. L.; Jin, R. Crystal Structure of Barrel-Shaped Chiral Au130(p-MBT)50 Nanocluster. *J. Am. Chem. Soc.* **2015,** *137*, 10076-10079.

(92) Weissker, H. C.; Escobar, H. B.; Thanthirige, V. D.; Kwak, K.; Lee, D.; Ramakrishna, G.; Whetten, R. L.; López-Lozano, X. Information on quantum states pervades the visible spectrum of the ubiquitous Au144(SR)60 gold nanocluster. *Nat. Commun.* **2014,** *5*, 3785.

(93) Ma, Y.; Li, W.; Cho, E. C.; Li, Z.; Yu, T.; Zeng, J.; Xie, Z.; Xia, Y. Au@Ag Core−Shell Nanocubes with Finely Tuned and Well-Controlled Sizes, Shell Thicknesses, and Optical Properties. *ACS Nano* **2010,** *4*, 6725-6734.

(94) Tsao, Y.-C.; Rej, S.; Chiu, C.-Y.; Huang, M. H. Aqueous Phase Synthesis of Au–Ag Core–Shell Nanocrystals with Tunable Shapes and Their Optical and Catalytic Properties. *J. Am. Chem. Soc.* **2014,** *136*, 396-404.

(95) Chiu, C.-Y.; Huang, M. H. Polyhedral Au–Pd Core–Shell Nanocrystals as Highly Spectrally Responsive and Reusable Hydrogen Sensors in Aqueous Solution. *Angew. Chem. Int. Ed.* **2013,** *52*, 12709-12713.

(96) Chen, H.; Wang, F.; Li, K.; Woo, K. C.; Wang, J.; Li, Q.; Sun, L.-D.; Zhang, X.; Lin, H.-Q.; Yan, C.-H. Plasmonic Percolation: Plasmon-Manifested Dielectric-to-Metal Transition. *ACS Nano* **2012,** *6*, 7162-7171.

(97) Sugawa, K.; Tahara, H.; Yamashita, A.; Otsuki, J.; Sagara, T.; Harumoto, T.; Yanagida, S. Refractive Index Susceptibility of the Plasmonic Palladium Nanoparticle: Potential as the Third Plasmonic Sensing Material. *ACS Nano* **2015,** *9*, 1895-1904.

(98) DeSantis, C. J.; Sue, A. C.; Bower, M. M.; Skrabalak, S. E. Seed-Mediated Co-reduction: A Versatile Route to Architecturally Controlled Bimetallic Nanostructures. *ACS Nano* **2012,** *6*, 2617-2628.

(99) DeSantis, C. J.; Peverly, A. A.; Peters, D. G.; Skrabalak, S. E. Octopods versus Concave Nanocrystals: Control of Morphology by Manipulating the Kinetics of Seeded Growth via Co-Reduction. *Nano Lett.* **2011,** *11*, 2164-2168.

(100) Sun, Y.; Xia, Y. Increased Sensitivity of Surface Plasmon Resonance of Gold Nanoshells Compared to That of Gold Solid Colloids in Response to Environmental Changes. *Anal. Chem.* **2002,** *74*, 5297-5305.

(101) Khalavka, Y.; Becker, J.; Sönnichsen, C. Synthesis of Rod-Shaped Gold Nanorattles with Improved Plasmon Sensitivity and Catalytic Activity. *J. Am. Chem. Soc.* **2009,** *131*, 1871-1875.

(102) Skrabalak, S. E.; Chen, J.; Sun, Y.; Lu, X.; Au, L.; Cobley, C. M.; Xia, Y. Gold Nanocages: Synthesis, Properties, and Applications. *Acc. Chem. Res.* **2008,** *41*, 1587-1595.

(103) Zeng, J.; Zhang, Q.; Chen, J.; Xia, Y. A Comparison Study of the Catalytic Properties of Au-Based Nanocages, Nanoboxes, and Nanoparticles. *Nano Lett.* **2010,** *10*, 30-35.

(104) Hong, X.; Wang, D.; Cai, S.; Rong, H.; Li, Y. Single-Crystalline Octahedral Au–Ag Nanoframes. *J. Am. Chem. Soc.* **2012,** *134*, 18165-18168.

(105) Lu, X.; Tuan, H.-Y.; Chen, J.; Li, Z.-Y.; Korgel, B. A.; Xia, Y. Mechanistic Studies on the Galvanic Replacement Reaction between Multiply Twinned Particles of Ag and HAuCl4 in an Organic Medium. *J. Am. Chem. Soc.* **2007,** *129*, 1733-1742.

(106) Yang, Y.; Liu, J.; Fu, Z.-W.; Qin, D. Galvanic Replacement-Free Deposition of Au on Ag for Core–Shell Nanocubes with Enhanced Chemical Stability and SERS Activity. *J. Am. Chem. Soc.* **2014,** *136*, 8153-8156.

(107) Chen, Y.; Xiang, Q.; Li, Z.; Wang, Y.; Meng, Y.; Duan, H. "Sketch and Peel" Lithography for High-Resolution Multiscale Patterning. *Nano Lett.* **2016,** *16*, 3253-3259.

(108) Duan, H.; Hu, H.; Kumar, K.; Shen, Z.; Yang, J. K. W. Direct and Reliable Patterning of Plasmonic Nanostructures with Sub-10-nm Gaps. *ACS Nano* **2011,** *5*, 7593-7600.

(109) Malak, S. T.; König, T.; Near, R.; Combs, Z. A.; El-Sayed, M. A.; Tsukruk, V. V. Stacked Gold Nanorectangles with Higher Order Plasmonic Modes and Top-Down Plasmonic Coupling. *J. Phys. Chem. C* **2014,** *118*, 5453-5462.

(110) Koh, A. L.; Fernández-Domínguez, A. I.; McComb, D. W.; Maier, S. A.; Yang, J. K. W. High-Resolution Mapping of Electron-Beam-Excited Plasmon Modes in Lithographically Defined Gold Nanostructures. *Nano Lett.* **2011,** *11*, 1323-1330.

(111) Ah, C. S.; Yun, Y. J.; Park, H. J.; Kim, W.-J.; Ha, D. H.; Yun, W. S. Size-Controlled Synthesis of Machinable Single Crystalline Gold Nanoplates. *Chem. Mater*. **2005,** *17*, 5558-5561.

(112) Huang, J. S.; Callegari, V.; Geisler, P.; Bruning, C.; Kern, J.; Prangsma, J. C.; Wu, X. F.; Feichtner, T.; Ziegler, J.; Weinmann, P.et al. Atomically flat single-crystalline gold nanostructures for plasmonic nanocircuitry. *Nat. Commun.* **2010,** *1*, 150.

(113) Chen, Y.; Bi, K.; Wang, Q.; Zheng, M.; Liu, Q.; Han, Y.; Yang, J.; Chang, S.; Zhang, G.; Duan, H. Rapid Focused Ion Beam Milling Based Fabrication of Plasmonic Nanoparticles and Assemblies via "Sketch and Peel" Strategy. *ACS Nano* **2016**, *10*, 11228-11236

(114) Lee, J.; Lee, P.; Lee, H.; Lee, D.; Lee, S. S.; Ko, S. H. Very long Ag nanowire synthesis and its application in a highly transparent, conductive and flexible metal electrode touch panel. *Nanoscale* **2012,** *4*, 6408-6414.

(115) Wiley, B.; Sun, Y.; Xia, Y. Synthesis of Silver Nanostructures with Controlled Shapes and Properties. *Acc. Chem. Res.* **2007,** *40*, 1067-1076.

(116) Kang, M. G.; Xu, T.; Park, H. J.; Luo, X.; Guo, L. J. Efficiency enhancement of organic solar cells using transparent plasmonic Ag nanowire electrodes. *Adv. Mater.* **2010,** *22*, 4378-4383.

(117) Dickson, R. M.; Lyon, L. A. Unidirectional Plasmon Propagation in Metallic Nanowires. *J. Phys. Chem. B* **2000,** *104*, 6095-6098.

(118) Fang, Z.; Fan, L.; Lin, C.; Zhang, D.; Meixner, A. J.; Zhu, X. Plasmonic Coupling of Bow Tie Antennas with Ag Nanowire. *Nano Lett.* **2011,** *11*, 1676-1680.

(119) Johns, P.; Yu, K.; Devadas, M. S.; Hartland, G. V. Role of Resonances in the Transmission of Surface Plasmon Polaritons between Nanostructures. *ACS Nano* **2016,** *10*, 3375-3381.

(120) Netzer, N. L.; Gunawidjaja, R.; Hiemstra, M.; Zhang, Q.; Tsukruk, V. V.; Jiang, C. Formation and Optical Properties of Compression-Induced Nanoscale Buckles on Silver Nanowires. *ACS Nano* **2009,** *3*, 1795-1802.

(121) Gunawidjaja, R.; Ko, H.; Jiang, C.; Tsukruk, V. V. Buckling Behavior of Highly Oriented Silver Nanowires Encapsulated within Layer-by-Layer Films. *Chem. Mater.* **2007,** *19*, 2007-2015.

(122) Mahmoud, M. A.; El-Sayed, M. A. Gold Nanoframes: Very High Surface Plasmon Fields and Excellent Near-Infrared Sensors. *J. Am. Chem. Soc.* **2010,** *132*, 12704-12710.

(123) Sun, Y.; Mayers, B.; Xia, Y. Metal Nanostructures with Hollow Interiors. *Adv. Mater.* **2003,** *15*, 641-646.

(124) Smith, A. F.; Harvey, S. M.; Skrabalak, S. E.; Weiner, R. G. Engineering high refractive index sensitivity through the internal and external composition of bimetallic nanocrystals. *Nanoscale* **2016,** *8*, 16841-16845.

(125) El Badawy, A. M.; Scheckel, K. G.; Suidan, M.; Tolaymat, T. The impact of stabilization mechanism on the aggregation kinetics of silver nanoparticles. *Sci. Total Environ.* **2012**, 429, 325-331.

(126) Heinz, H.; Pramanik, C.; Heinz, O.; Ding, Y.; Mishra, R. K.; Marchon, D.; Flatt, R. J.; Estrela-Lopis, I.; Llop, J.; Moya, S.et al. Nanoparticle decoration with surfactants: Molecular interactions, assembly, and applications. *Surf. Sci. Rep.* **2017**, 72, 1-58.

(127) Smith, D. K.; Korgel, B. A. The Importance of the CTAB Surfactant on the Colloidal Seed-Mediated Synthesis of Gold Nanorods. *Langmuir* **2008**, 24, 644-649.

(128) Jana, N. R.; Gearheart, L.; Murphy, C. J. Wet chemical synthesis of silver nanorods and nanowires of controllable aspect ratio. *Chem. Commun.* **2001**, 617-618.

(129) da Silva, J. A.; Meneghetti, M. R. New Aspects of the Gold Nanorod Formation Mechanism via Seed-Mediated Methods Revealed by Molecular Dynamics Simulations. *Langmuir* **2018**, 34, 366-375.

(130) Park, J.-W.; Shumaker-Parry, J. S. Structural Study of Citrate Layers on Gold Nanoparticles: Role of Intermolecular Interactions in Stabilizing Nanoparticles. J. *Am. Chem. Soc.* **2014**, 136, 1907-1921.

(131) Venkataraman, L.; Klare, J. E.; Tam, I. W.; Nuckolls, C.; Hybertsen, M. S.; Steigerwald, M. L. Single-Molecule Circuits with Well-Defined Molecular Conductance. *Nano Lett.* **2006**, 6, 458-462.

(132) Xue, Y.; Li, X.; Li, H.; Zhang, W. Quantifying thiol–gold interactions towards the efficient strength control. *Nat. Commun.* **2014**, 5, 4348.

(133) Hoft, R. C.; Ford, M. J.; McDonagh, A. M.; Cortie, M. B. Adsorption of Amine Compounds on the Au(111) Surface: A Density Functional Study. *J. Phys. Chem. C* **2007**, 111, 13886-13891.

(134) Napper, D. H. Steric stabilization. *J. Colloid Interface Sci.* **1977**, 58, 390-407.

(135) Borodko, Y.; Humphrey, S. M.; Tilley, T. D.; Frei, H.; Somorjai, G. A. Charge-Transfer Interaction of Poly(vinylpyrrolidone) with Platinum and Rhodium Nanoparticles. *J. Phys. Chem. C* **2007**, 111, 6288-6295.

(136) Borodko, Y.; Habas, S. E.; Koebel, M.; Yang, P.; Frei, H.; Somorjai, G. A. Probing the Interaction of Poly(vinylpyrrolidone) with Platinum Nanocrystals by UV−Raman and FTIR. *J. Phys. Chem. B* **2006**, 110, 23052-23059.

(137) Manson, J.; Kumar, D.; Meenan, B. J.; Dixon, D. Polyethylene glycol functionalized gold nanoparticles: the influence of capping density on stability in various media. *Gold bulletin* **2011**, 44, 99-105.

(138) Khanna, P.; Gokhale, R.; Subbarao, V.; Vishwanath, A. K.; Das, B.; Satyanarayana, C. PVA stabilized gold nanoparticles by use of unexplored albeit conventional reducing agent. *Mater. Chem. Phys.* **2005**, 92, 229-233.

(139) Longenberger, L.; Mills, G. Formation of Metal Particles in Aqueous Solutions by Reactions of Metal Complexes with Polymers. *J. Phys. Chem.* **1995**, 99, 475-478.

(140) Fritz, G.; Schädler, V.; Willenbacher, N.; Wagner, N. J. Electrosteric Stabilization of Colloidal Dispersions. *Langmuir* **2002**, 18, 6381-6390.

(141) Jans, H.; Jans, K.; Lagae, L.; Borghs, G.; Maes, G.; Huo, Q. Poly (acrylic acid)-stabilized colloidal gold nanoparticles: synthesis and properties. *Nanotechnology* **2010**, 21, 455702.

(142) Zhang, Y.; Wen, S.; Zhao, L.; Li, D.; Liu, C.; Jiang, W.; Gao, X.; Gu, W.; Ma, N.; Zhao, J.et al. Ultrastable polyethyleneimine-stabilized gold nanoparticles modified with polyethylene glycol for blood pool, lymph node and tumor CT imaging. *Nanoscale* **2016**, 8, 5567-5577.

(143) Chen, H.; Wang, Y.; Wang, Y.; Dong, S.; Wang, E. One-step preparation and characterization of PDDA-protected gold nanoparticles. *Polymer* **2006**, 47, 763-766.

(144) Li, J.; Shi, L.; An, Y.; Li, Y.; Chen, X.; Dong, H. Reverse micelles of star-block copolymer as nanoreactors for preparation of gold nanoparticles. *Polymer* **2006**, 47, 8480-8487.

(145) Hsu, S.-W.; Rodarte, A. L.; Som, M.; Arya, G.; Tao, A. R. Colloidal Plasmonic Nanocomposites: From Fabrication to Optical Function. *Chem. Rev.* **2018**, 118, 3100-3120.

(146) Mohan, Y. M.; Premkumar, T.; Lee, K.; Geckeler, K. E. Fabrication of silver nanoparticles in hydrogel networks. *Macromol. Rapid Commun.* **2006**, 27, 1346-1354.

(147) Huang, H.; Yuan, Q.; Yang, X. Preparation and characterization of metal–chitosan nanocomposites. *Colloids Surf. B* **2004**, 39, 31-37.

(148) Porel, S.; Singh, S.; Harsha, S. S.; Rao, D. N.; Radhakrishnan, T. P. Nanoparticle-Embedded Polymer: In Situ Synthesis, Free-Standing Films with Highly Monodisperse Silver Nanoparticles and Optical Limiting. *Chem. Mater.* **2005**, 17, 9-12.

(149) Hashimoto, T.; Harada, M.; Sakamoto, N. Incorporation of Metal Nanoparticles into Block Copolymer Nanodomains via in-Situ Reduction of Metal Ions in Microdomain Space. *Macromolecules* **1999**, 32, 6867-6870.

(150) Wang, C.; Flynn, N. T.; Langer, R. Controlled structure and properties of thermoresponsive nanoparticle–hydrogel composites. *Adv. Mater.* **2004**, 16, 1074-1079.

(151) Marqués-Hueso, J.; Abargues, R.; Valdés, J. L.; Martínez-Pastor, J. P. Ag and Au/DNQ-novolac nanocomposites patternable by ultraviolet lithography: a fast route to plasmonic sensor microfabrication. *J. Mater. Chem.* **2010**, 20, 7436-7443.

(152) Mackay, M. E.; Tuteja, A.; Duxbury, P. M.; Hawker, C. J.; Van Horn, B.; Guan, Z.; Chen, G.; Krishnan, R. General strategies for nanoparticle dispersion. *Science* **2006**, 311, 1740-1743.

(153) Chiu, J. J.; Kim, B. J.; Kramer, E. J.; Pine, D. J. Control of Nanoparticle Location in Block Copolymers. *J. Am. Chem. Soc.* **2005**, 127, 5036-5037.

(154) Kundu, P. K.; Samanta, D.; Leizrowice, R.; Margulis, B.; Zhao, H.; Börner, M.; Udayabhaskararao, T.; Manna, D.; Klajn, R. Light-controlled self-assembly of non-photoresponsive nanoparticles. *Nat. Chem.* **2015**, 7, 646.

(155) Zijlstra, P.; Chon, J. W. M.; Gu, M. Five-dimensional optical recording mediated by surface plasmons in gold nanorods. *Nature* **2009**, 459, 410-413.

(156) Zhang, H.; Cadusch, J.; Kinnear, C.; James, T.; Roberts, A.; Mulvaney, P. Direct Assembly of Large Area Nanoparticle Arrays. *ACS Nano* **2018**, 12, 7529-7537.

(157) Montelongo, Y.; Yetisen, A. K.; Butt, H.; Yun, S.-H. Reconfigurable optical assembly of nanostructures. *Nat. Commun.* **2016**, 7, 12002.

(158) Mesch, M.; Zhang, C.; Braun, P. V.; Giessen, H. Functionalized hydrogel on plasmonic nanoantennas for noninvasive glucose sensing. ACS Photonics **2015**, 2, 475-480.

(159) Aldeanueva-Potel, P.; Faoucher, E.; Alvarez-Puebla, R. A.; Liz-Marzán, L. M.; Brust, M. Recyclable Molecular Trapping and SERS Detection in Silver-Loaded Agarose Gels with Dynamic Hot Spots. *Anal. Chem.* **2009**, 81, 9233-9238.

(160) Lv, S.-W.; Liu, Y.; Xie, M.; Wang, J.; Yan, X.-W.; Li, Z.; Dong, W.-G.; Huang, W.-H. Near-Infrared Light-Responsive Hydrogel for Specific Recognition and Photothermal Site-Release of Circulating Tumor Cells. *ACS Nano* **2016**, 10, 6201-6210.

(161) Xing, R.; Liu, K.; Jiao, T.; Zhang, N.; Ma, K.; Zhang, R.; Zou, Q.; Ma, G.; Yan, X. An Injectable Self-Assembling Collagen–Gold Hybrid Hydrogel for Combinatorial Antitumor Photothermal/Photodynamic Therapy. *Adv. Mater.* **2016**, 28, 3669-3676.

(162) Pastoriza-Santos, I.; Kinnear, C.; Pérez-Juste, J.; Mulvaney, P.; Liz-Marzán, L. M. Plasmonic polymer nanocomposites. *Nat. Rev. Mat.* **2018**, 3, 375-391.

(163) Faupel, F.; Zaporojtchenko, V.; Strunskus, T.; Elbahri, M. Metal-polymer nanocomposites for functional applications. *Adv. Eng. Mater.* **2010**, 12, 1177-1190.

(164) Monk, P.; Mortimer, R.; Rosseinsky, D. *Electrochromism and electrochromic devices*; Cambridge University Press, **2007**.

(165) Beaujuge, P. M.; Reynolds, J. R. Color control in π-conjugated organic polymers for use in electrochromic devices. *Chem. Rev.* **2010**, 110, 268-320.

(166) Ledin, P. A.; Jeon, J.-W.; Geldmeier, J. A.; Ponder, J. F.; Mahmoud, M. A.; El-Sayed, M.; Reynolds, J. R.; Tsukruk, V. V. Design of Hybrid Electrochromic Materials with Large Electrical Modulation of Plasmonic Resonances. *ACS Appl. Mater. Interfaces* **2016,** *8*, 13064-13075.

(167) König, T. A. F.; Ledin, P. A.; Kerszulis, J.; Mahmoud, M. A.; El-Sayed, M. A.; Reynolds, J. R.; Tsukruk, V. V. Electrically Tunable Plasmonic Behavior of Nanocube–Polymer Nanomaterials Induced by a Redox-Active Electrochromic Polymer. *ACS Nano* **2014,** *8*, 6182-6192.

(168) Dubois, L. H.; Nuzzo, R. G. Synthesis, structure, and properties of model organic surfaces. *Annu. Rev. Phys. Chem.* **1992,** *43*, 437-463.

(169) Nuzzo, R. G.; Zegarski, B. R.; Dubois, L. H. Fundamental studies of the chemisorption of organosulfur compounds on gold(111). Implications for molecular self-assembly on gold surfaces. *J. Am. Chem. Soc.* **1987,** *109*, 733-740.

(170) Esplandiú, M. J.; Hagenström, H.; Kolb, D. M. Functionalized Self-Assembled Alkanethiol Monolayers on Au(111) Electrodes: 1. Surface Structure and Electrochemistry. *Langmuir* **2001,** *17*, 828-838.

(171) Park, J.-W.; Shumaker-Parry, J. S. Strong Resistance of Citrate Anions on Metal Nanoparticles to Desorption under Thiol Functionalization. *ACS Nano* **2015,** *9*, 1665-1682.

(172) Oyelere, A. K.; Chen, P. C.; Huang, X.; El-Sayed, I. H.; El-Sayed, M. A. Peptide-Conjugated Gold Nanorods for Nuclear Targeting. *Bioconjugate Chem.* **2007,** *18*, 1490-1497.

(173) Yu, C.; Irudayaraj, J. Multiplex Biosensor Using Gold Nanorods. *Anal. Chem.* **2007,** *79*, 572-579.

(174) Chang, J.-Y.; Wu, H.; Chen, H.; Ling, Y.-C.; Tan, W. Oriented assembly of Au nanorods using biorecognition system. *Chem. Commun.* **2005**, 1092-1094.

(175) Yu, C.; Varghese, L.; Irudayaraj, J. Surface Modification of Cetyltrimethylammonium Bromide-Capped Gold Nanorods to Make Molecular Probes. *Langmuir* **2007,** *23*, 9114-9119.

(176) Thierry, B.; Ng, J.; Krieg, T.; Griesser, H. J. A robust procedure for the functionalization of gold nanorods and noble metal nanoparticles. *Chem. Commun.* **2009**, 1724-1726.

(177) Vigderman, L.; Manna, P.; Zubarev, E. R. Quantitative Replacement of Cetyl Trimethylammonium Bromide by Cationic Thiol Ligands on the Surface of Gold Nanorods and Their Extremely Large Uptake by Cancer Cells. *Angew. Chem. Int. Ed.* **2012,** *51*, 636-641.

(178) Moran, C. H.; Rycenga, M.; Zhang, Q.; Xia, Y. Replacement of Poly(vinyl pyrrolidone) by Thiols: A Systematic Study of Ag Nanocube Functionalization by Surface-Enhanced Raman Scattering. *J. Phys. Chem. C* **2011,** *115*, 21852-21857.

(179) Niu, Z. Q.; Li, Y. D. Removal and Utilization of Capping Agents in Nanocatalysis. *Chem. Mater.* **2014,** *26*, 72-83.

(180) Li, D.; Wang, C.; Tripkovic, D.; Sun, S.; Markovic, N. M.; Stamenkovic, V. R. Surfactant Removal for Colloidal Nanoparticles from Solution Synthesis: The Effect on Catalytic Performance. *ACS Catalysis* **2012,** *2*, 1358-1362.

(181) Shao, M.; Odell, J. H.; Choi, S.-I.; Xia, Y. Electrochemical surface area measurements of platinum- and palladium-based nanoparticles. *Electrochem. Commun.* **2013,** *31*, 46-48.

(182) Wilson, A. J.; Marchuk, K.; Willets, K. A. Imaging Electrogenerated Chemiluminescence at Single Gold Nanowire Electrodes. *Nano Lett.* **2015,** *15*, 6110-6115.

(183) Takahashi, H.; Niidome, Y.; Niidome, T.; Kaneko, K.; Kawasaki, H.; Yamada, S. Modification of Gold Nanorods Using Phosphatidylcholine to Reduce Cytotoxicity. *Langmuir* **2006,** *22*, 2-5.

(184) Jain, P. K.; El-Sayed, M. A. Plasmonic coupling in noble metal nanostructures. *Chem. Phys. Lett.* **2010,** *487*, 153-164.

(185) Tao, A.; Sinsermsuksakul, P.; Yang, P. Tunable plasmonic lattices of silver nanocrystals. *Nat. Nanotechnol.* **2007,** *2*, 435-440.

(186) Li, W.; Camargo, P. H. C.; Au, L.; Zhang, Q.; Rycenga, M.; Xia, Y. Etching and Dimerization: A Simple and Versatile Route to Dimers of Silver Nanospheres with a Range of Sizes. *Angew. Chem. Int. Ed.* **2010,** *49*, 164-168.

(187) Pietrobon, B.; McEachran, M.; Kitaev, V. Synthesis of Size-Controlled Faceted Pentagonal Silver Nanorods with Tunable Plasmonic Properties and Self-Assembly of These Nanorods. *ACS Nano* **2009,** *3*, 21-26.

(188) Novak, J. P.; Feldheim, D. L. Assembly of Phenylacetylene-Bridged Silver and Gold Nanoparticle Arrays. *J. Am. Chem. Soc.* **2000,** *122*, 3979-3980.

(189) Li, W.; Camargo, P. H. C.; Lu, X.; Xia, Y. Dimers of Silver Nanospheres: Facile Synthesis and Their Use as Hot Spots for Surface-Enhanced Raman Scattering. *Nano Lett.* **2009,** *9*, 485-490.

(190) Gao, B.; Arya, G.; Tao, A. R. Self-orienting nanocubes for the assembly of plasmonic nanojunctions. *Nat. Nanotechnol.* **2012,** *7*, 433-437.

(191) Gandra, N.; Abbas, A.; Tian, L.; Singamaneni, S. Plasmonic Planet–Satellite Analogues: Hierarchical Self-Assembly of Gold Nanostructures. *Nano Lett.* **2012,** *12*, 2645-2651.

(192) Kraus, T.; Malaquin, L.; Schmid, H.; Riess, W.; Spencer, N. D.; Wolf, H. Nanoparticle printing with single-particle resolution. *Nat. Nanotechnol.* **2007,** *2*, 570-576.

(193) Lee, S. Y.; Hung, L.; Lang, G. S.; Cornett, J. E.; Mayergoyz, I. D.; Rabin, O. Dispersion in the SERS Enhancement with Silver Nanocube Dimers. *ACS Nano* **2010,** *4*, 5763-5772.

(194) Henzie, J.; Andrews, S. C.; Ling, X. Y.; Li, Z.; Yang, P. Oriented assembly of polyhedral plasmonic nanoparticle clusters. *Proc. Natl. Acad. Sci. U.S.A.* **2013,** *110*, 6640-6645.

(195) Hanske, C.; Tebbe, M.; Kuttner, C.; Bieber, V.; Tsukruk, V. V.; Chanana, M.; König, T. A. F.; Fery, A. Strongly Coupled Plasmonic Modes on Macroscopic Areas via Template-Assisted Colloidal Self-Assembly. *Nano Lett.* **2014,** *14*, 6863-6871.

(196) Müller, M. B.; Kuttner, C.; König, T. A. F.; Tsukruk, V. V.; Förster, S.; Karg, M.; Fery, A. Plasmonic Library Based on Substrate-Supported Gradiential Plasmonic Arrays. *ACS Nano* **2014,** *8*, 9410-9421.

(197) Loweth, C. J.; Caldwell, W. B.; Peng, X.; Alivisatos, A. P.; Schultz, P. G. DNA-based assembly of gold nanocrystals. *Angew. Chem. Int. Ed.* **1999,** *38*, 1808-1812.

(198) Mastroianni, A. J.; Claridge, S. A.; Alivisatos, A. P. Pyramidal and Chiral Groupings of Gold Nanocrystals Assembled Using DNA Scaffolds. *J. Am. Chem. Soc.* **2009,** *131*, 8455-8459.

(199) Kuzyk, A.; Schreiber, R.; Fan, Z.; Pardatscher, G.; Roller, E.-M.; Hogele, A.; Simmel, F. C.; Govorov, A. O.; Liedl, T. DNA-based self-assembly of chiral plasmonic nanostructures with tailored optical response. *Nature* **2012,** *483*, 311-314.

(200) Pal, S.; Deng, Z.; Wang, H.; Zou, S.; Liu, Y.; Yan, H. DNA Directed Self-Assembly of Anisotropic Plasmonic Nanostructures. *J. Am. Chem. Soc.* **2011,** *133*, 17606-17609.

(201) Gwo, S.; Lin, M.-H.; He, C.-L.; Chen, H.-Y.; Teranishi, T. Bottom-Up Assembly of Colloidal Gold and Silver Nanostructures for Designable Plasmonic Structures and Metamaterials. *Langmuir* **2012,** *28*, 8902-8908.

(202) Raney, J. R.; Lewis, J. A. Printing mesoscale architectures. *MRS Bull.* **2015,** *40*, 943-950.

(203) Waheed, S.; Cabot, J. M.; Macdonald, N. P.; Lewis, T.; Guijt, R. M.; Paull, B.; Breadmore, M. C. 3D printed microfluidic devices: enablers and barriers. *Lab Chip* **2016,** *16*, 1993-2013.

(204) Tumbleston, J. R.; Shirvanyants, D.; Ermoshkin, N.; Janusziewicz, R.; Johnson, A. R.; Kelly, D.; Chen, K.; Pinschmidt, R.; Rolland, J. P.; Ermoshkin, A. Continuous liquid interface production of 3D objects. *Science* **2015,** *347*, 1349-1352.

(205) Morton, S. W.; Herlihy, K. P.; Shopsowitz, K. E.; Deng, Z. J.; Chu, K. S.; Bowerman, C. J.; DeSimone, J. M.; Hammond, P. T. Scalable Manufacture of Built-to-Order Nanomedicine: Spray-Assisted Layer-by-Layer Functionalization of PRINT Nanoparticles. *Adv. Mater.* **2013,** *25*, 4707-4713.

(206) Linas, J.; Marcus, L.; Peter, G.; Bilal, G.; Stephan, B.; Mangirdas, M.; Aleksandr, O. Plasmon assisted 3D microstructuring of gold nanoparticle-doped polymers. *Nanotechnology* **2016,** *27*, 154001.

(207) Wu, L.; Dong, Z.; Kuang, M.; Li, Y.; Li, F.; Jiang, L.; Song, Y. Printing Patterned Fine 3D Structures by Manipulating the Three Phase Contact Line. *Adv. Funct. Mater.* **2015,** *25*, 2237-2242.

(208) Skylar-Scott, M. A.; Gunasekaran, S.; Lewis, J. A. Laser-assisted direct ink writing of planar and 3D metal architectures. *Proc. Natl. Acad. Sci. U.S.A.* **2016,** *113*, 6137-6142.

(209) Lewis, J. A.; Ahn, B. Y. Device fabrication: Three-dimensional printed electronics. *Nature* **2015,** *518*, 42-43.

(210) Sydney Gladman, A.; Matsumoto, E. A.; Nuzzo, R. G.; Mahadevan, L.; Lewis, J. A. Biomimetic 4D printing. *Nat. Mater.* **2016,** *15*, 413-418.

(211) O'Brien, M. N.; Jones, M. R.; Mirkin, C. A. The nature and implications of uniformity in the hierarchical organization of nanomaterials. *Proc. Natl. Acad. Sci. U.S.A.* **2016,** *113*, 11717-11725.

(212) Xie, Z.; Zhou, Y.; Hedrick, J. L.; Chen, P.-C.; He, S.; Shahjamali, M. M.; Wang, S.; Zheng, Z.; Mirkin, C. A. On-Tip Photo-Modulated Molecular Printing. *Angew. Chem. Int. Ed.* **2015,** *54*, 12894-12899.

(213) He, S.; Xie, Z.; Park, D. J.; Liao, X.; Brown, K. A.; Chen, P.-C.; Zhou, Y.; Schatz, G. C.; Mirkin, C. A. Liquid-Phase Beam Pen Lithography. *Small* **2016,** *12*, 988-993.

(214) Li, C. C.; Cai, W. P.; Cao, B. Q.; Sun, F. Q.; Li, Y.; Kan, C. X.; Zhang, L. D. Mass Synthesis of Large, Single-Crystal Au Nanosheets Based on a Polyol Process. *Adv. Funct. Mater.* **2006,** *16*, 83-90.

(215) Nikoobakht, B.; El-Sayed, M. A. Preparation and Growth Mechanism of Gold Nanorods (NRs) Using Seed-Mediated Growth Method. *Chem. Mater.* **2003,** *15*, 1957-1962.

(216) Sau, T. K.; Murphy, C. J. Room Temperature, High-Yield Synthesis of Multiple Shapes of Gold Nanoparticles in Aqueous Solution. *J. Am. Chem. Soc.* **2004,** *126*, 8648-8649.

(217) Singamaneni, S.; Gupta, M.; Yang, R.; Tomczak, M. M.; Naik, R. R.; Wang, Z. L.; Tsukruk, V. V. Nondestructive In Situ Identification of Crystal Orientation of Anisotropic ZnO Nanostructures. *ACS Nano* **2009,** *3*, 2593-2600.

(218) Hagemann, H. J.; Gudat, W.; Kunz, C. Optical constants from the far infrared to the x-ray region: Mg, Al, Cu, Ag, Au, Bi, C, and Al2O3. *J. Opt. Soc. Am.* **1975,** *65*, 742-744.

(219) Mark, J. E. *Physical properties of polymers handbook*; Springer, **2007**, *1076*, 825.

(220) Jeon, J.-W.; Zhou, J.; Geldmeier, J. A.; Ponder Jr, J. F.; Mahmoud, M. A.; El-Sayed, M.; Reynolds, J. R.; Tsukruk, V. V. Dual-Responsive Reversible Plasmonic Behavior of Core–Shell Nanostructures with pH-Sensitive and Electroactive Polymer Shells. *Chem. Mater.* **2016,** *28*, 7551-7563.

(221) Love, J. C.; Estroff, L. A.; Kriebel, J. K.; Nuzzo, R. G.; Whitesides, G. M. Self-assembled monolayers of thiolates on metals as a form of nanotechnology. *Chem. Rev.* **2005,** *105*, 1103-1169.

(222) Taguchi, T.; Isozaki, K.; Miki, K. Enhanced Catalytic Activity of Self-Assembled-Monolayer-Capped Gold Nanoparticles. *Adv. Mater.* **2012,** *24*, 6462-6467.

(223) Schmaltz, T.; Amin, A. Y.; Khassanov, A.; Meyer-Friedrichsen, T.; Steinrück, H.-G.; Magerl, A.; Segura, J. J.; Voitchovsky, K.; Stellacci, F.; Halik, M. Low-Voltage Self-Assembled Monolayer Field-Effect Transistors on Flexible Substrates. *Adv. Mater.* **2013,** *25*, 4511-4514.

(224) Liu, J.; Lu, Y. Fast Colorimetric Sensing of Adenosine and Cocaine Based on a General Sensor Design Involving Aptamers and Nanoparticles. *Angew. Chem. Int. Ed.* **2006,** *45*, 90-94.

(225) Ko, H.; Singamaneni, S.; Tsukruk, V. V. Nanostructured Surfaces and Assemblies as SERS Media. *Small* **2008,** *4*, 1576-1599.

(226) Akkerman, H. B.; Blom, P. W. M.; de Leeuw, D. M.; de Boer, B. Towards molecular electronics with large-area molecular junctions. *Nature* **2006,** *441*, 69-72.

(227) Du, W.; Wang, T.; Chu, H.-S.; Wu, L.; Liu, R.; Sun, S.; Phua, W. K.; Wang, L.; Tomczak, N.; Nijhuis, C. A. On-chip molecular electronic plasmon sources based on self-assembled monolayer tunnel junctions. *Nat. Photon.* **2016,** *10*, 274-280.

(228) Kaganer, V. M.; Möhwald, H.; Dutta, P. Structure and phase transitions in Langmuir monolayers. *Rev. Mod. Phys.* **1999,** *71*, 779-819.

(229) Yourdshahyan, Y.; Rappe, A. M. Structure and energetics of alkanethiol adsorption on the Au (111) surface. *J. Chem. Phys.* **2002,** *117*, 825-833.

(230) Camillone, N.; Leung, T. Y. B.; Schwartz, P.; Eisenberger, P.; Scoles, G. Chain Length Dependence of the Striped Phases of Alkanethiol Monolayers Self-Assembled on Au(111): An Atomic Beam Diffraction Study. *Langmuir* **1996,** *12*, 2737-2746.

(231) Poirier, G.; Pylant, E. The self-assembly mechanism of alkanethiols on Au (111). *Science* **1996,** *272*, 1145-1148.

(232) Schwartz, D. K. Mechanisms and kinetics of self-assembled monolayer formation. *Annu. Rev. Phys. Chem.* **2001,** *52*, 107-137.

(233) Stranick, S. J.; Parikh, A. N.; Tao, Y. T.; Allara, D. L.; Weiss, P. S. Phase Separation of Mixed-Composition Self-Assembled Monolayers into Nanometer Scale Molecular Domains. *J. Phys. Chem.* **1994,** *98*, 7636-7646.

(234) Farrell, Z.; Merz, S.; Seager, J.; Dunn, C.; Egorov, S.; Green, D. L. Development of Experiment and Theory to Detect and Predict Ligand Phase Separation on Silver Nanoparticles. *Angew. Chem. Int. Ed.* **2015,** *54*, 6479-6482.

(235) Singh, C.; Jackson, A. M.; Stellacci, F.; Glotzer, S. C. Exploiting Substrate Stress To Modify Nanoscale SAM Patterns. *J. Am. Chem. Soc* **2009,** *131*, 16377-16379.

(236) Sondag-Huethorst, J. A. M.; Schonenberger, C.; Fokkink, L. G. J. Formation of Holes in Alkanethiol Monolayers on Gold. *J. Phys. Chem.* **1994,** *98*, 6826-6834.

(237) Schreiber, F. Structure and growth of self-assembling monolayers. *Progr. Surf. Sci.* **2000,** *65*, 151-257.

(238) Rouhana, L. L.; Moussallem, M. D.; Schlenoff, J. B. Adsorption of Short-Chain Thiols and Disulfides onto Gold under Defined Mass Transport Conditions: Coverage, Kinetics, and Mechanism. *J. Am. Chem. Soc.* **2011,** *133*, 16080-16091.

(239) Feng, Y.; Xing, S.; Xu, J.; Wang, H.; Lim, J. W.; Chen, H. Probing the kinetics of ligand exchange on colloidal gold nanoparticles by surface-enhanced Raman scattering. *Dalton Trans.* **2010,** *39*, 349-351.

(240) Feng, Y.; He, J.; Wang, H.; Tay, Y. Y.; Sun, H.; Zhu, L.; Chen, H. An Unconventional Role of Ligand in Continuously Tuning of Metal–Metal Interfacial Strain. *J. Am. Chem. Soc.* **2012,** *134*, 2004-2007.

(241) Guo, L.-H.; Facci, J. S.; McLendon, G.; Mosher, R. Effect of Gold Topography and Surface Pretreatment on the Self-Assembly of Alkanethiol Monolayers. *Langmuir* **1994,** *10*, 4588-4593.

(242) Kim, Y. T.; McCarley, R. L.; Bard, A. J. Observation of n-octadecanethiol multilayer formation from solution onto gold. *Langmuir* **1993,** *9*, 1941-1944.

(243) Koczkur, K. M.; Mourdikoudis, S.; Polavarapu, L.; Skrabalak, S. E. Polyvinylpyrrolidone (PVP) in nanoparticle synthesis. *Dalton Trans.* **2015,** *44*, 17883-17905.

(244) Schlenoff, J. B.; Li, M.; Ly, H. Stability and Self-Exchange in Alkanethiol Monolayers. *J. Am. Chem. Soc.* **1995,** *117*, 12528-12536.

(245) Poirier, G.; Tarlov, M. The c (4X2) superlattice of n-alkanethiol monolayers self-assembled on Au (111). *Langmuir* **1994,** *10*, 2853-2856.

(246) Camillone III, N.; Chidsey, C. E.; Liu, G. y.; Scoles, G. Superlattice structure at the surface of a monolayer of octadecanethiol self-assembled on Au (111). *J. Chem. Phys.* **1993,** *98*, 3503-3511.

(247) Balamurugan, S.; Obubuafo, A.; Soper, S. A.; Spivak, D. A. Surface immobilization methods for aptamer diagnostic applications. *Anal. Bioanal. Chem.* **2008,** *390*, 1009-1021.

(248) Villarrubia, J. S. Algorithm for scanned probe microscope image simulation, surface reconstruction, and tip estimation. *J. Res. Natl. Inst. Stand. Technol.* **1997,** *102*, 425-454.

(249) Nečas, D.; Klapetek, P. Gwyddion: an open-source software for SPM data analysis. *Open Phys.* **2012,** *10*, 181-188.

(250) Kirkland, A. I.; Jefferson, D. A.; Duff, D. G.; Edwards, P. P. High-Resolution Studies of Trigonal Lamellar Particles of Gold and Silver. *Inst. Phys. Conf. Ser.* **1990**, 375-378.

(251) Bastys, V.; Pastoriza-Santos, I.; Rodríguez-González, B.; Vaisnoras, R.; Liz-Marzán, L. M. Formation of Silver Nanoprisms with Surface Plasmons at Communication Wavelengths. *Adv. Funct. Mater.* **2006,** *16*, 766-773.

(252) McConney, M. E.; Singamaneni, S.; Tsukruk, V. V. Probing Soft Matter with the Atomic Force Microscopies: Imaging and Force Spectroscopy. *Polym. Rev.* **2010,** *50*, 235-286..

(253) Mullen, K.; Carron, K. Adsorption of Chlorinated Ethylenes at 1-Octadecanethiol-Modified Silver Surfaces. *Anal. Chem.* **1994,** *66*, 478-483.

(254) Cavalleri, O.; Oliveri, L.; Dacca, A.; Parodi, R.; Rolandi, R. XPS measurements on L-cysteine and 1-octadecanethiol self-assembled films: a comparative study. *Appl. Surf. Sci.* **2001,** *175*, 357-362.

(255) Vericat, C.; Vela, M.; Benitez, G.; Carro, P.; Salvarezza, R. Self-assembled monolayers of thiols and dithiols on gold: new challenges for a well-known system. *Chem. Soc. Rev.* **2010,** *39*, 1805-1834.

(256) Liu, G.-Y.; Xu, S.; Qian, Y. Nanofabrication of Self-Assembled Monolayers Using Scanning Probe Lithography. *Acc. Chem. Res.* **2000,** *33*, 457-466.

(257) Gates, B. D.; Xu, Q.; Love, J. C.; Wolfe, D. B.; Whitesides, G. M. Unconventional nanofabrication. *Annu. Rev. Mater. Res.* **2004,** *34*, 339-372.

(258) Chyasnavichyus, M.; Young, S. L.; Tsukruk, V. V. Probing of Polymer Surfaces in the Viscoelastic Regime. *Langmuir* **2014,** *30*, 10566-10582.

(259) Healey, J.; Rubinstein, M.; Walters, V. The mechanical properties of some binders used in tableting. *J. Pharm. Pharmacol.* **1974,** *26*, 41-46.

(260) Salmeron, M.; Neubauer, G.; Folch, A.; Tomitori, M.; Ogletree, D.; Sautet, P. Viscoelastic and electrical properties of self-assembled monolayers on gold (111) films. *Langmuir* **1993,** *9*, 3600-3611.

(261) Smith, R. K.; Reed, S. M.; Lewis, P. A.; Monnell, J. D.; Clegg, R. S.; Kelly, K. F.; Bumm, L. A.; Hutchison, J. E.; Weiss, P. S. Phase separation within a binary self-assembled monolayer on Au {111} driven by an amide-containing alkanethiol. *J. Phys. Chem. B* **2001,** *105*, 1119-1122.

(262) Tsukruk, V. V.; Bliznyuk, V. N.; Hazel, J.; Visser, D.; Everson, M. P. Organic Molecular Films under Shear Forces: Fluid and Solid Langmuir Monolayers. *Langmuir* **1996,** *12*, 4840-4849.

(263) Vanbellingen, Q. P.; Elie, N.; Eller, M. J.; Della-Negra, S.; Touboul, D.; Brunelle, A. Time-of-flight secondary ion mass spectrometry imaging of biological samples with delayed extraction for high mass and high spatial resolutions. *Rapid Commun. Mass Spectrom.* **2015,** *29*, 1187-1195.

(264) Saidi, W. A.; Feng, H.; Fichthorn, K. A. Binding of Polyvinylpyrrolidone to Ag Surfaces: Insight into a Structure-Directing Agent from Dispersion-Corrected Density Functional Theory. *J. Phys. Chem. C* **2013,** *117*, 1163-1171.

(265) Bain, C. D.; Troughton, E. B.; Tao, Y. T.; Evall, J.; Whitesides, G. M.; Nuzzo, R. G. Formation of monolayer films by the spontaneous assembly of organic thiols from solution onto gold. *J. Am. Chem. Soc.* **1989,** *111*, 321-335.

(266) Castelino, K.; Kannan, B.; Majumdar, A. Characterization of Grafting Density and Binding Efficiency of DNA and Proteins on Gold Surfaces. *Langmuir* **2005,** *21*, 1956-1961.

(267) Demers, L. M.; Mirkin, C. A.; Mucic, R. C.; Reynolds, R. A.; Letsinger, R. L.; Elghanian, R.; Viswanadham, G. A Fluorescence-Based Method for Determining the Surface Coverage and Hybridization Efficiency of Thiol-Capped Oligonucleotides Bound to Gold Thin Films and Nanoparticles. *Anal. Chem.* **2000,** *72*, 5535-5541.

(268) Torres, E.; Blumenau, A. T.; Biedermann, P. U. Steric and Chain Length Effects in the ($\sqrt{3} \times \sqrt{3}$) R30° Structures of Alkanethiol Self-Assembled Monolayers on Au (111). *ChemPhysChem* **2011,** *12*, 999-1009.

(269) Porter, M. D.; Bright, T. B.; Allara, D. L.; Chidsey, C. E. D. Spontaneously organized molecular assemblies. 4. Structural characterization of n-alkyl thiol monolayers on gold by optical ellipsometry, infrared spectroscopy, and electrochemistry. *J. Am. Chem. Soc.* **1987,** *109*, 3559-3568.

(270) Poirier, G.; Pylant, E.; White, J. Crystalline structures of pristine and hydrated mercaptohexanol self-assembled monolayers on Au (111). *J. Chem. Phys.* **1996,** *105*, 2089-2092..

(271) Cognard, J. Adhesion to gold: a review. *Gold Bull.* **1984,** *17*, 131-139.

(272) Smith, T. The hydrophilic nature of a clean gold surface. *J. Colloid Interface Sci.* **1980,** *75*, 51-55.

(273) Stewart, M. E.; Anderton, C. R.; Thompson, L. B.; Maria, J.; Gray, S. K.; Rogers, J. A.; Nuzzo, R. G. Nanostructured Plasmonic Sensors. *Chem. Rev.* **2008,** *108*, 494-521.

(274) Willets, K. A.; Van Duyne, R. P. Localized surface plasmon resonance spectroscopy and sensing. *Annu. Rev. Phys. Chem.* **2007,** *58*, 267-297.

(275) Kneipp, K.; Kneipp, H.; Itzkan, I.; Dasari, R. R.; Feld, M. S. Ultrasensitive chemical analysis by Raman spectroscopy. *Chem. Rev.* **1999,** *99*, 2957-2976.

(276) Zhang, S.; Geryak, R.; Geldmeier, J.; Kim, S.; Tsukruk, V. V. Synthesis, Assembly, and Applications of Hybrid Nanostructures for Biosensing. *Chem. Rev.* **2017,** *117*, 12942-13038.

(277) Betz, J. F.; Yu, W. W.; Cheng, Y.; White, I. M.; Rubloff, G. W. Simple SERS substrates: powerful, portable, and full of potential. *Phys. Chem. Chem. Phys.* **2014,** *16*, 2224-2239.

(278) Yang, J.; Palla, M.; Bosco, F. G.; Rindzevicius, T.; Alstrom, T. S.; Schmidt, M. S.; Boisen, A.; Ju, J. Y.; Lin, Q. Surface-Enhanced Raman Spectroscopy Based

Quantitative Bioassay on Aptamer-Functionalized Nanopillars Using Large-Area Raman Mapping. *ACS Nano* **2013,** *7*, 5350-5359.

(279) Lee, C. H.; Hankus, M. E.; Tian, L.; Pellegrino, P. M.; Singamaneni, S. Highly Sensitive Surface Enhanced Raman Scattering Substrates Based on Filter Paper Loaded with Plasmonic Nanostructures. *Anal. Chem.* **2011,** *83*, 8953-8958.

(280) Ross, M. B.; Ashley, M. J.; Schmucker, A. L.; Singamaneni, S.; Naik, R. R.; Schatz, G. C.; Mirkin, C. A. Structure–Function Relationships for Surface-Enhanced Raman Spectroscopy-Active Plasmonic Paper. *J. Phys. Chem. C* **2016,** *120*, 20789-20797.

(281) Chang, S.; Combs, Z. A.; Gupta, M. K.; Davis, R.; Tsukruk, V. V. In situ Growth of Silver Nanoparticles in Porous Membranes for Surface-Enhanced Raman Scattering. *ACS Appl. Mater. Interfaces* **2010,** *2*, 3333-3339.

(282) Kodiyath, R.; Malak, S. T.; Combs, Z. A.; Koenig, T.; Mahmoud, M. A.; El-Sayed, M. A.; Tsukruk, V. V. Assemblies of silver nanocubes for highly sensitive SERS chemical vapor detection. *J. Mater. Chem. A* **2013,** *1*, 2777-2788.

(283) Yu, W. W.; White, I. M. A simple filter-based approach to surface enhanced Raman spectroscopy for trace chemical detection. *Analyst* **2012,** *137*, 1168-1173.

(284) Yuan, Y.; Panwar, N.; Yap, S. H. K.; Wu, Q.; Zeng, S.; Xu, J.; Tjin, S. C.; Song, J.; Qu, J.; Yong, K.-T. SERS-based ultrasensitive sensing platform: An insight into design and practical applications. *Coord. Chem. Rev.* **2017,** *337*, 1-33.

(285) Fan, M.; Andrade, G. F. S.; Brolo, A. G. A review on the fabrication of substrates for surface enhanced Raman spectroscopy and their applications in analytical chemistry. *Anal. Chim. Acta* **2011,** *693*, 7-25.

(286) Pang, S.; Yang, T.; He, L. Review of surface enhanced Raman spectroscopic (SERS) detection of synthetic chemical pesticides. *TrAC, Trends Anal. Chem.* **2016,** *85*, 73-82.

(287)Lee, C. H.; Tian, L.; Singamaneni, S. Paper-Based SERS Swab for Rapid Trace Detection on Real-World Surfaces. *ACS Appl. Mater. Interfaces* **2010,** *2*, 3429-3435.

(288) Schmucker, A. L.; Tadepalli, S.; Liu, K.-K.; Sullivan, C. J.; Singamaneni, S.; Naik, R. R. Plasmonic paper: a porous and flexible substrate enabling nanoparticle-based combinatorial chemistry. *RSC Advances* **2016,** *6*, 4136-4144.

(289) Halas, N. J.; Lal, S.; Chang, W.-S.; Link, S.; Nordlander, P. Plasmons in Strongly Coupled Metallic Nanostructures. *Chem. Rev.* **2011,** *111*, 3913-3961.

(290) Hu, K.; Tsukruk, V. V. Tuning the Electronic Properties of Robust Bio-Bond Graphene Papers by Spontaneous Electrochemical Reduction: From Insulators to Flexible Semi-Metals. *Chem. Mater.* **2015,** *27*, 6717-6729.

(291) Xiong, R.; Kim, H. S.; Zhang, S.; Kim, S.; Korolovych, V. F.; Ma, R.; Yingling, Y. G.; Lu, C.; Tsukruk, V. V. Template-Guided Assembly of Silk Fibroin on Cellulose Nanofibers for Robust Nanostructures with Ultrafast Water Transport. *ACS Nano* **2017,** *11*, 12008-12019.

(292) Saito, T.; Kimura, S.; Nishiyama, Y.; Isogai, A. Cellulose nanofibers prepared by TEMPO-mediated oxidation of native cellulose. *Biomacromolecules* **2007**, 8, 2485-2491.

(293) Sezonov, G.; Joseleau-Petit, D.; D'Ari, R. Escherichia coli physiology in Luria-Bertani broth. *J. Bacteriol.* **2007,** *189*, 8746-8749.

(294) Chen, H.; Shao, L.; Li, Q.; Wang, J. Gold nanorods and their plasmonic properties. *Chem. Soc. Rev.* **2013,** *42*, 2679-2724.

(295) Isogai, A.; Saito, T.; Fukuzumi, H. TEMPO-oxidized cellulose nanofibers. *Nanoscale* **2011,** *3*, 71-85.

(296) Fukuzumi, H.; Saito, T.; Iwata, T.; Kumamoto, Y.; Isogai, A. Transparent and High Gas Barrier Films of Cellulose Nanofibers Prepared by TEMPO-Mediated Oxidation. *Biomacromolecules* **2009,** *10*, 162-165.

(297) Moon, R. J.; Martini, A.; Nairn, J.; Simonsen, J.; Youngblood, J. Cellulose nanomaterials review: structure, properties and nanocomposites. *Chem. Soc. Rev.* **2011,** *40*, 3941-3994.

(298) Xiong, R.; Grant, A. M.; Ma, R.; Zhang, S.; Tsukruk, V. V. Naturally-derived biopolymer nanocomposites: Interfacial design, properties and emerging applications. *Mater. Sci. Eng. R Rep.* **2018,** *125*, 1-41.

(299) Tian, L.; Jiang, Q.; Liu, K. K.; Luan, J.; Naik, R. R.; Singamaneni, S. Bacterial Nanocellulose-Based Flexible Surface Enhanced Raman Scattering Substrate. *Advanced Materials Interfaces* **2016,** *3*, 1600214.

(300) *Hendra*, P. J.; Agbenyega, J. K. *The Raman spectra of polymers*; John Wiley & Sons New York, **1993**.

(301) Colthup, N. B.; Daly, L. H.; Wiberley, S. E. *Introduction to infrared and Raman spectroscopy*; 3rd ed.; Academic Press: San Diego, **1990**.

(302) Sun, Y.; Liu, K.; Miao, J.; Wang, Z.; Tian, B.; Zhang, L.; Li, Q.; Fan, S.; Jiang, K. Highly Sensitive Surface-Enhanced Raman Scattering Substrate Made from Superaligned Carbon Nanotubes. *Nano Lett.* **2010,** *10*, 1747-1753.

(303) Danielson, T. L.; Rayson, G. D.; Anderson, D. M.; Estell, R.; Fredrickson, E. L.; Green, B. S. Impact of filter paper on fluorescence measurements of buffered saline filtrates. *Talanta* **2003,** *59*, 601-604.

(304) Ding, S.-Y.; Yi, J.; Li, J.-F.; Ren, B.; Wu, D.-Y.; Panneerselvam, R.; Tian, Z.-Q. Nanostructure-based plasmon-enhanced Raman spectroscopy for surface analysis of materials. *Nat. Rev. Mat.* **2016,** *1*, 16021.

(305) Schlücker, S. Surface-Enhanced Raman Spectroscopy: Concepts and Chemical Applications. *Angew. Chem. Int. Ed.* **2014,** *53*, 4756-4795.

(306) Funston, A. M.; Novo, C.; Davis, T. J.; Mulvaney, P. Plasmon Coupling of Gold Nanorods at Short Distances and in Different Geometries. *Nano Lett.* **2009,** *9*, 1651-1658.

(307) Shao, L.; Woo, K. C.; Chen, H.; Jin, Z.; Wang, J.; Lin, H.-Q. Angle- and Energy-Resolved Plasmon Coupling in Gold Nanorod Dimers. *ACS Nano* **2010,** *4*, 3053-3062.

(308) Zhang, S.; Tsukruk, V. V. In *Polymer and Biopolymer Brushes: for Materials Science and Biotechnology*; Azzaroni, O.;Szleifer, I., Eds.; John Wiley & Sons, Inc.: Hoboken, NJ, USA, **2017**.

(309) Jensen, L.; Schatz, G. C. Resonance Raman scattering of rhodamine 6G as calculated using time-dependent density functional theory. *J. Phys. Chem. A* **2006,** *110*, 5973-5977.

(310) Ngo, Y. H.; Li, D.; Simon, G. P.; Garnier, G. Gold Nanoparticle–Paper as a Three-Dimensional Surface Enhanced Raman Scattering Substrate. *Langmuir* **2012,** *28*, 8782-8790.

(311) Lee, M.; Oh, K.; Choi, H.-K.; Lee, S. G.; Youn, H. J.; Lee, H. L.; Jeong, D. H. Subnanomolar Sensitivity of Filter Paper-Based SERS Sensor for Pesticide Detection by Hydrophobicity Change of Paper Surface. *ACS Sensors* **2018,** *3*, 151-159.

(312) Zhang, P.; Huang, Y.; Lu, X.; Zhang, S.; Li, J.; Wei, G.; Su, Z. One-Step Synthesis of Large-Scale Graphene Film Doped with Gold Nanoparticles at Liquid–Air Interface for Electrochemistry and Raman Detection Applications. *Langmuir* **2014,** *30*, 8980-8989.

(313) Zhang, P.; Yang, S.; Wang, L.; Zhao, J.; Zhu, Z.; Liu, B.; Zhong, J.; Sun, X. Large-scale uniform Au nanodisk arrays fabricated via x-ray interference lithography for reproducible and sensitive SERS substrate. *Nanotechnology* **2014,** *25*, 245301.

(314) Chen, H.-Y.; Lin, M.-H.; Wang, C.-Y.; Chang, Y.-M.; Gwo, S. Large-Scale Hot Spot Engineering for Quantitative SERS at the Single-Molecule Scale. *J. Am. Chem. Soc.* **2015,** *137*, 13698-13705.

(315) Chen, H.-L.; Yang, Z.-H.; Lee, S. Observation of Surface Coverage-Dependent Surface-Enhanced Raman Scattering and the Kinetic Behavior of Methylene Blue Adsorbed on Silver Oxide Nanocrystals. *Langmuir* **2016,** *32*, 10184-10188.

(316) Xiao, G.-N.; Man, S.-Q. Surface-enhanced Raman scattering of methylene blue adsorbed on cap-shaped silver nanoparticles. *Chem. Phys. Lett.* **2007,** *447*, 305-309.

(317) Goeller, L. J.; Riley, M. R. Discrimination of bacteria and bacteriophages by Raman spectroscopy and surface-enhanced Raman spectroscopy. *Appl. Spectrosc.* **2007,** *61*, 679-685.

(318) Kong, K.; Kendall, C.; Stone, N.; Notingher, I. Raman spectroscopy for medical diagnostics — From in-vitro biofluid assays to in-vivo cancer detection. *Adv. Drug Deliv. Rev.* **2015,** *89*, 121-134.

(319) Byrne, H. J.; Knief, P.; Keating, M. E.; Bonnier, F. Spectral pre and post processing for infrared and Raman spectroscopy of biological tissues and cells. *Chem. Soc. Rev.* **2016,** *45*, 1865-1878.

(320) Wei, D.; Chen, S.; Liu, Q. Review of fluorescence suppression techniques in Raman spectroscopy. *Appl. Spectrosc. Rev.* **2015,** *50*, 387-406.

(321) Edwards, H. G. M.; Farwell, D. W.; Webster, D. FT Raman microscopy of untreated natural plant fibres. *Spectrochim. Acta A* **1997,** *53*, 2383-2392.

(322) Wiley, J. H.; Atalla, R. H. Band assignments in the raman spectra of celluloses. *Carbohydr. Res.* **1987,** *160*, 113-129.

(323) Kong, K.; Eichhorn, S. J. Crystalline and amorphous deformation of process-controlled cellulose-II fibres. *Polymer* **2005,** *46*, 6380-6390.

(324) Sengupta, A.; Mujacic, M.; Davis, E. J. Detection of bacteria by surface-enhanced Raman spectroscopy. *Anal. Bioanal. Chem* **2006,** *386*, 1379-1386.

(325) Wu, Q.; Hamilton, T.; Nelson, W. H.; Elliott, S.; Sperry, J. F.; Wu, M. UV Raman Spectral Intensities of E. Coli and Other Bacteria Excited at 228.9, 244.0, and 248.2 nm. *Anal. Chem.* **2001,** *73*, 3432-3440.

(326) Wu, Q.; Nelson, W. H.; Elliot, S.; Sperry, J. F.; Feld, M.; Dasari, R.; Manoharan, R. Intensities of E. coli Nucleic Acid Raman Spectra Excited Selectively from Whole Cells with 251-nm Light. *Anal. Chem.* **2000,** *72*, 2981-2986.

(327) Notingher, I.; Selvakumaran, J.; Hench, L. L. New detection system for toxic agents based on continuous spectroscopic monitoring of living cells. *Biosens. Bioelectron.* **2004,** *20*, 780-789.

(328) Ebbesen, T. W.; Lezec, H. J.; Ghaemi, H.; Thio, T.; Wolff, P. Extraordinary optical transmission through sub-wavelength hole arrays. *Nature* **1998,** *391*, 667-669.

(329) Garcia-Vidal, F. J.; Martin-Moreno, L.; Ebbesen, T.; Kuipers, L. Light passing through subwavelength apertures. *Rev. Mod. Phys.* **2010,** *82*, 729-787.

(330) Barnes, W. L.; Dereux, A.; Ebbesen, T. W. Surface plasmon subwavelength optics. *Nature* **2003,** *424*, 824-830.

(331) Genet, C.; Ebbesen, T. W. Light in tiny holes. *Nature* **2007,** *445*, 39-46.

(332) Shao, L.; Zhuo, X.; Wang, J. Advanced Plasmonic Materials for Dynamic Color Display. *Adv. Mater.* **2018,** *30*, 1704338.

(333) Lei, D. Y.; Li, J.; Fernández-Domínguez, A. I.; Ong, H. C.; Maier, S. A. Geometry Dependence of Surface Plasmon Polariton Lifetimes in Nanohole Arrays. *ACS Nano* **2010,** *4*, 432-438.

(334) Martin-Moreno, L.; Garcia-Vidal, F.; Lezec, H.; Pellerin, K.; Thio, T.; Pendry, J.; Ebbesen, T. Theory of extraordinary optical transmission through subwavelength hole arrays. *Phys. Rev. Lett.* **2001,** *86*, 1114-1117.

(335) Tang, Z.; Peng, R.; Wang, Z.; Wu, X.; Bao, Y.; Wang, Q.; Zhang, Z.; Sun, W.; Wang, M. Coupling of surface plasmons in nanostructured metal/dielectric multilayers with subwavelength hole arrays. *Phys. Rev. B* **2007,** *76*, 195405.

(336) Gao, F.; Li, D.; Peng, R.-W.; Hu, Q.; Wei, K.; Wang, Q.; Zhu, Y.; Wang, M. Tunable interference of light behind subwavelength apertures. *Appl. Phys. Lett.* **2009,** *95*, 011104.

(337) Yokogawa, S.; Burgos, S. P.; Atwater, H. A. Plasmonic Color Filters for CMOS Image Sensor Applications. *Nano Lett.* **2012,** *12*, 4349-4354.

(338) Chen, Q.; Cumming, D. R. High transmission and low color cross-talk plasmonic color filters using triangular-lattice hole arrays in aluminum films. *Opt. Express* **2010,** *18*, 14056-14062.

(339) Zeng, B.; Gao, Y.; Bartoli, F. J. Ultrathin nanostructured metals for highly transmissive plasmonic subtractive color filters. *Sci. Rep.* **2013,** *3*, 2840.

(340) Xu, T.; Wu, Y.-K.; Luo, X.; Guo, L. J. Plasmonic nanoresonators for high-resolution colour filtering and spectral imaging. *Nat. Commun.* **2010,** *1*, 59.

(341) Shu, F. Z.; Yu, F. F.; Peng, R. W.; Zhu, Y. Y.; Xiong, B.; Fan, R. H.; Wang, Z. H.; Liu, Y.; Wang, M. Dynamic Plasmonic Color Generation Based on Phase Transition of Vanadium Dioxide. *Adv. Opt. Mater.* **2018,** *6*, 1700939.

(342) Lee, Y.; Park, M.-K.; Kim, S.; Shin, J. H.; Moon, C.; Hwang, J. Y.; Choi, J.-C.; Park, H.; Kim, H.-R.; Jang, J. E. Electrical Broad Tuning of Plasmonic Color Filter Employing an Asymmetric-Lattice Nanohole Array of Metasurface Controlled by Polarization Rotator. *ACS Photonics* **2017,** *4*, 1954-1966.

(343) Xu, T.; Walter, E. C.; Agrawal, A.; Bohn, C.; Velmurugan, J.; Zhu, W.; Lezec, H. J.; Talin, A. A. High-contrast and fast electrochromic switching enabled by plasmonics. *Nat. Commun.* **2016,** *7*, 10479.

(344) Atighilorestani, M.; dos Santos, D. P.; Jaimes, R. F. V. V.; Rahman, M. M.; Temperini, M. L. A.; Brolo, A. G. Electrochemical Control of Light Transmission through Nanohole Electrode Arrays. *ACS Photonics* **2016,** *3*, 2375-2382.

(345) Xiong, K.; Emilsson, G.; Maziz, A.; Yang, X.; Shao, L.; Jager, E. W.; Dahlin, A. B. Plasmonic Metasurfaces with Conjugated Polymers for Flexible Electronic Paper in Color. *Adv. Mater.* **2016,** *28*, 9956-9960.

(346) Xiong, K.; Tordera, D.; Emilsson, G.; Olsson, O.; Linderhed, U.; Jonsson, M. P.; Dahlin, A. B. Switchable Plasmonic Metasurfaces with High Chromaticity Containing Only Abundant Metals. *Nano Lett.* **2017,** *17*, 7033-7039.

(347) Li, Z.; Clark, A. W.; Cooper, J. M. Dual Color Plasmonic Pixels Create a Polarization Controlled Nano Color Palette. *ACS Nano* **2016,** *10*, 492-498.

(348) Zhou, Z.; Yu, Y.; Sun, N.; Möhwald, H.; Gu, P.; Wang, L.; Zhang, W.; König, T. A. F.; Fery, A.; Zhang, G. Broad-Range Electrically Tunable Plasmonic Resonances of a Multilayer Coaxial Nanohole Array with an Electroactive Polymer Wrapper. *ACS Appl. Mater. Interfaces* **2017,** *9*, 35244-35252.

(349) Balakrishnan, S.; Najiminaini, M.; Singh, M. R.; Carson, J. J. A study of angle dependent surface plasmon polaritons in nano-hole array structures. *J. Appl. Phys.* **2016,** *120*, 034302.

(350) Baba, A.; Lübben, J.; Tamada, K.; Knoll, W. Optical Properties of Ultrathin Poly(3,4-ethylenedioxythiophene) Films at Several Doping Levels Studied by In Situ Electrochemical Surface Plasmon Resonance Spectroscopy. *Langmuir* **2003,** *19*, 9058-9064.

(351) Ponder, J. F.; Pittelli, S. L.; Reynolds, J. R. Heteroatom Role in Polymeric Dioxyselenophene/Dioxythiophene Systems for Color and Redox Control. *ACS Macro Letters* **2016,** *5*, 714-717.

(352) Teran, N. B.; Reynolds, J. R. Discrete Donor–Acceptor Conjugated Systems in Neutral and Oxidized States: Implications toward Molecular Design for High Contrast Electrochromics. *Chem. Mater.* **2017,** *29*, 1290-1301.

(353) Ponder, J. F.; Österholm, A. M.; Reynolds, J. R. Conjugated Polyelectrolytes as Water Processable Precursors to Aqueous Compatible Redox Active Polymers for Diverse Applications: Electrochromism, Charge Storage, and Biocompatible Organic Electronics. *Chem. Mater.* **2017,** *29*, 4385-4392.

(354) Mock, J. J.; Smith, D. R.; Schultz, S. Local Refractive Index Dependence of Plasmon Resonance Spectra from Individual Nanoparticles. *Nano Lett.* **2003,** *3*, 485-491.

(355) Jeon, J.-W.; Ledin, P. A.; Geldmeier, J. A.; Ponder, J. F.; Mahmoud, M. A.; El-Sayed, M.; Reynolds, J. R.; Tsukruk, V. V. Electrically Controlled Plasmonic Behavior of Gold Nanocube@Polyaniline Nanostructures: Transparent Plasmonic Aggregates. *Chem. Mater.* **2016,** *28*, 2868-2881.

(356) Zhou, J.; Jeon, J.-W.; Ponder, J. F.; Geldmeier, J. A.; Mahmoud, M. A.; El-Sayed, M.; Reynolds, J. R.; Tsukruk, V. V. Electrochromic tuning of transparent gold nanorods with poly [(3, 4-propylenedioxy) pyrrole] shells in the near-infrared region. *J. Mater. Chem. C* **2017,** *5*, 12571-12584.

(357) Jiang, N.; Zhuo, X.; Wang, J. Active Plasmonics: Principles, Structures, and Applications. *Chem. Rev.* **2018,** *118*, 3054-3099.

(358) Tan, S. J.; Zhang, L.; Zhu, D.; Goh, X. M.; Wang, Y. M.; Kumar, K.; Qiu, C.-W.; Yang, J. K. W. Plasmonic Color Palettes for Photorealistic Printing with Aluminum Nanostructures. *Nano Lett.* **2014,** *14*, 4023-4029.

(359) Roberts, A. S.; Pors, A.; Albrektsen, O.; Bozhevolnyi, S. I. Subwavelength Plasmonic Color Printing Protected for Ambient Use. *Nano Lett.* **2014,** *14*, 783-787.

(360) Olson, J.; Manjavacas, A.; Liu, L.; Chang, W.-S.; Foerster, B.; King, N. S.; Knight, M. W.; Nordlander, P.; Halas, N. J.; Link, S. Vivid, full-color aluminum plasmonic pixels. *Proc. Natl. Acad. Sci. U.S.A.* **2014,** *111*, 14348-14353.

(361) Gordon, R.; Hughes, M.; Leathem, B.; Kavanagh, K. L.; Brolo, A. G. Basis and Lattice Polarization Mechanisms for Light Transmission through Nanohole Arrays in a Metal Film. *Nano Lett.* **2005,** *5*, 1243-1246.

(362) Geldmeier, J. A.; Mahmoud, M. A.; Jeon, J.-W.; El-Sayed, M.; Tsukruk, V. V. The effect of plasmon resonance coupling in P3HT-coated silver nanodisk monolayers on their optical sensitivity. *J. Mater. Chem. C* **2016,** *4*, 9813-9822.

(363) Cohen, M.; Zalevsky, Z.; Shavit, R. Towards integrated nanoplasmonic logic circuitry. *Nanoscale* **2013,** *5*, 5442-5449.

(364) Fu, Y.; Hu, X.; Lu, C.; Yue, S.; Yang, H.; Gong, Q. All-optical logic gates based on nanoscale plasmonic slot waveguides. *Nano Lett.* **2012,** *12*, 5784-5790.

(365) Chang, W.-S.; Willingham, B. A.; Slaughter, L. S.; Khanal, B. P.; Vigderman, L.; Zubarev, E. R.; Link, S. Low absorption losses of strongly coupled surface plasmons in nanoparticle assemblies. *Proc. Natl. Acad. Sci. U.S.A.* **2011,** *108*, 19879-19884.

(366) Do, Y. S.; Park, J. H.; Hwang, B. Y.; Lee, S. M.; Ju, B. K.; Choi, K. C. Plasmonic Color Filter and its Fabrication for Large-Area Applications. *Adv. Opt. Mater.* **2013,** *1*, 133-138.

(367) Eftekhari, F.; Escobedo, C.; Ferreira, J.; Duan, X.; Girotto, E. M.; Brolo, A. G.; Gordon, R.; Sinton, D. Nanoholes as nanochannels: flow-through plasmonic sensing. *Anal. Chem.* **2009,** *81*, 4308-4311.

(368) Brolo, A. G.; Gordon, R.; Leathem, B.; Kavanagh, K. L. Surface plasmon sensor based on the enhanced light transmission through arrays of nanoholes in gold films. *Langmuir* **2004,** *20*, 4813-4815.

(369) Im, H.; Shao, H.; Park, Y. I.; Peterson, V. M.; Castro, C. M.; Weissleder, R.; Lee, H. Label-free detection and molecular profiling of exosomes with a nano-plasmonic sensor. *Nat. Biotechnol.* **2014,** *32*, 490-495.

(370) Couture, M.; Ray, K. K.; Poirier-Richard, H.-P.; Crofton, A.; Masson, J.-F. 96-Well Plasmonic Sensing with Nanohole Arrays. *ACS Sensors* **2016**, 1, 287-294.

(371) Jackman, J. A.; Ferhan, A. R.; Cho, N.-J. Nanoplasmonic sensors for biointerfacial science. *Chem. Soc. Rev.* **2017**, 46, 3615-3660.

(372) Canalejas-Tejero, V.; Herranz, S.; Bellingham, A.; Moreno-Bondi, M. C.; Barrios, C. A. Passivated Aluminum Nanohole Arrays for Label-Free Biosensing Applications. *ACS Appl. Mater. Interfaces* **2014**, 6, 1005-1010.

(373) Barbosa, S.; Agrawal, A.; Rodríguez-Lorenzo, L.; Pastoriza-Santos, I.; Alvarez-Puebla, R. A.; Kornowski, A.; Weller, H.; Liz-Marzán, L. M. Tuning Size and Sensing Properties in Colloidal Gold Nanostars. *Langmuir* **2010**, 26, 14943-14950.

(374) Polavarapu, L.; Liz-Marzán, L. M. Towards low-cost flexible substrates for nanoplasmonic sensing. *Phys. Chem. Chem. Phys.* **2013**, 15, 5288-5300.

(375) Zouhdi, S.; Sihvola, A. H.; Vinogradov, A. P. *Metamaterials and plasmonics : fundamentals, modelling, applications*; Springer : In cooperation with NATO Public Diplomacy Division: Dordrecht, **2009**.

(376) Rahimi, E.; Gordon, R. Nonlinear Plasmonic Metasurfaces. *Adv. Opt. Mater.* **2018,** *6*, 1800274.

(377) Zhang, S.; Xiong, R.; Mahmoud, M. A.; Quigley, E. N.; Chang, H.; El-Sayed, M.; Tsukruk, V. V. Dual-Excitation Nanocellulose Plasmonic Membranes for Molecular and Cellular SERS Detection. *ACS Appl. Mater. Interfaces* **2018,** *10*, 18380-18389.

(378) Chen, J.; Gan, F.; Wang, Y.; Li, G. Plasmonic Sensing and Modulation Based on Fano Resonances. *Adv. Opt. Mater.* **2018,** *6*, 1701152.

(379) Linic, S.; Christopher, P.; Ingram, D. B. Plasmonic-metal nanostructures for efficient conversion of solar to chemical energy. *Nat. Mater.* **2011,** *10*, 911-921.

(380) Wang, C.; Astruc, D. Nanogold plasmonic photocatalysis for organic synthesis and clean energy conversion. *Chem. Soc. Rev.* **2014,** *43*, 7188-7216.

(381) Li, J.; Cushing, S. K.; Meng, F.; Senty, T. R.; Bristow, A. D.; Wu, N. Plasmon-induced resonance energy transfer for solar energy conversion. *Nat. Photon.* **2015,** *9*, 601-607.

(382) Kawata, S.; Inouye, Y.; Verma, P. Plasmonics for near-field nano-imaging and superlensing. *Nat. Photon.* **2009,** *3*, 388-394.

(383) Kravtsov, V.; Ulbricht, R.; Atkin, J. M.; Raschke, M. B. Plasmonic nanofocused four-wave mixing for femtosecond near-field imaging. *Nat. Nanotechnol.* **2016,** *11*, 459-464.

(384) Palomba, S.; Novotny, L. Near-Field Imaging with a Localized Nonlinear Light Source. *Nano Lett.* **2009,** *9*, 3801-3804.

(385) Vahala, K. J. Optical microcavities. *Nature* **2003,** *424*, 839-846.

(386) Berman, P. R. Cavity quantum electrodynamics; Academic Press: Boston, 1994.

(387) Lončar, M.; Yoshie, T.; Scherer, A.; Gogna, P.; Qiu, Y. Low-threshold photonic crystal laser. Appl. Phys. Lett. 2002, 81, 2680-2682.

(388) Khajavikhan, M.; Simic, A.; Katz, M.; Lee, J.; Slutsky, B.; Mizrahi, A.; Lomakin, V.; Fainman, Y. Thresholdless nanoscale coaxial lasers. *Nature* **2012,** *482*, 204-207.

(389) Benson, O. Assembly of hybrid photonic architectures from nanophotonic constituents. *Nature* **2011,** *480*, 193-199.

(390) Hill, M. T.; Oei, Y.-S.; Smalbrugge, B.; Zhu, Y.; De Vries, T.; Van Veldhoven, P. J.; Van Otten, F. W.; Eijkemans, T. J.; Turkiewicz, J. P.; De Waardt, H. Lasing in metallic-coated nanocavities. *Nat. Photon.* **2007,** *1*, 589-594.

(391) Yang, X.; Ishikawa, A.; Yin, X.; Zhang, X. Hybrid Photonic−Plasmonic Crystal Nanocavities. *ACS Nano* **2011,** *5*, 2831-2838.

(392) Robbiano, V.; Giordano, M.; Martella, C.; Stasio, F. D.; Chiappe, D.; de Mongeot, F. B.; Comoretto, D. Hybrid Plasmonic–Photonic Nanostructures: Gold Nanocrescents Over Opals. *Adv. Opt. Mater.* **2013,** *1*, 389-396.

(393) Barth, M.; Schietinger, S.; Fischer, S.; Becker, J.; Nüsse, N.; Aichele, T.; Löchel, B.; Sönnichsen, C.; Benson, O. Nanoassembled Plasmonic-Photonic Hybrid Cavity for Tailored Light-Matter Coupling. *Nano Lett.* **2010,** *10*, 891-895.

(394) Zhang, T.; Callard, S.; Jamois, C.; Chevalier, C.; Feng, D.; Belarouci, A. Plasmonic-photonic crystal coupled nanolaser. *Nanotechnology* **2014,** *25*, 315201.

(395) De Angelis, F.; Patrini, M.; Das, G.; Maksymov, I.; Galli, M.; Businaro, L.; Andreani, L. C.; Di Fabrizio, E. A Hybrid Plasmonic−Photonic Nanodevice for Label-Free Detection of a Few Molecules. *Nano Lett.* **2008,** *8*, 2321-2327.

(396) Ameling, R.; Giessen, H. Microcavity plasmonics: strong coupling of photonic cavities and plasmons. *Laser & Photonics Reviews* **2013,** *7*, 141-169.

(397) Ameling, R.; Giessen, H. Cavity Plasmonics: Large Normal Mode Splitting of Electric and Magnetic Particle Plasmons Induced by a Photonic Microcavity. *Nano Lett.* **2010,** *10*, 4394-4398.

(398) Abhilash, T.; Balasubrahmaniyam, M.; Patra, A.; Kasiviswanathan, S. Plasmon resonance mediated enhancement in Fabry-Perot cavity modes. *Appl. Phys. Lett.* **2014,** *104*, 241112.

(399) Mehrzad, H.; Mohajerani, E. Liquid crystal mediated active nano-plasmonic based on the formation of hybrid plasmonic-photonic modes. *Appl. Phys. Lett.* **2018,** *112*, 061101.

(400) Ameling, R.; Langguth, L.; Hentschel, M.; Mesch, M.; Braun, P. V.; Giessen, H. Cavity-enhanced localized plasmon resonance sensing. *Appl. Phys. Lett.* **2010,** *97*, 253116.

(401) Schmidt, M. A.; Lei, D. Y.; Wondraczek, L.; Nazabal, V.; Maier, S. A. Hybrid nanoparticle–microcavity-based plasmonic nanosensors with improved detection resolution and extended remote-sensing ability. *Nat. Commun.* **2012,** *3*, 1108.

(402) Jiang, J.-J.; Xie, Y.-B.; Liu, Z.-Y.; Tang, X.-M.; Zhang, X.-J.; Zhu, Y.-Y. Amplified spontaneous emission via the coupling between Fabry–Perot cavity and surface plasmon polariton modes. *Opt. Lett.* **2014,** *39*, 2378-2381.

(403) Liu, H.; Erouel, M.; Gerelli, E.; Harouri, A.; Benyattou, T.; Orobtchouk, R.; Milord, L.; Belarouci, A.; Letartre, X.; Jamois, C. Nanoantenna-induced fringe splitting of Fabry-Perot interferometer: a model study of plasmonic/photonic coupling. *Opt. Express* **2015,** *23*, 31085-31097.

(404) Lin, T.-L.; Lin, J.-H.; Guo, J.-T.; Kan, H.-C. Suppression of Photonic Bandgap Reflection by Localized Surface Plasmons in Self-Assembled Plasmonic–Photonic Crystals. *Adv. Opt. Mater.* **2015,** *3*, 1470-1475.

(405) Abate, Y.; Schwartzberg, A.; Strasser, D.; Leone, S. R. Nanometer-scale size dependent imaging of cetyl trimethyl ammonium bromide (CTAB) capped and uncapped gold nanoparticles by apertureless near-field optical microscopy. *Chem. Phys. Lett.* **2009,** *474*, 146-152.

(406) Barrow, S. J.; Funston, A. M.; Gómez, D. E.; Davis, T. J.; Mulvaney, P. Surface Plasmon Resonances in Strongly Coupled Gold Nanosphere Chains from Monomer to Hexamer. *Nano Lett.* **2011,** *11*, 4180-4187.

(407) Silfvast, W. T. *Laser fundamentals*; Cambridge University Press: Cambridge, Eng. ; New York, NY, USA, **1996**.

(408) Demtröder, W. *Laser spectroscopy : basic concepts and instrumentation*; 3rd ed.; Springer: Berlin ; New York, **2003**.

(409) Perenboom, J. A. A. J.; Wyder, P.; Meier, F. Electronic properties of small metallic particles. *Phys. Rep.* **1981,** *78*, 173-292.

(410) Jain, P. K.; Huang, W.; El-Sayed, M. A. On the Universal Scaling Behavior of the Distance Decay of Plasmon Coupling in Metal Nanoparticle Pairs: A Plasmon Ruler Equation. *Nano Lett.* **2007,** *7*, 2080-2088.

(411) Muehlschlegel, P.; Eisler, H.-J.; Martin, O. J.; Hecht, B.; Pohl, D. Resonant optical antennas. *Science* **2005,** *308*, 1607-1609.

(412) Barnard, E. S.; White, J. S.; Chandran, A.; Brongersma, M. L. Spectral properties of plasmonic resonator antennas. *Opt. Express* **2008,** *16*, 16529-16537.

(413) Novotny, L.; Van Hulst, N. Antennas for light. *Nat. Photon.* **2011,** *5*, 83-90.

(414) Scriven, L. Physics and applications of dip coating and spin coating. *MRS Online Proceedings Library Archive* **1988,** *121*, 717-729.

(415) Grauer, Z.; Avnir, D.; Yariv, S. Adsorption characteristics of rhodamine 6G on montmorillonite and laponite, elucidated from electronic absorption and emission spectra. *Can. J. Chem.* **1984,** *62*, 1889-1894.

(416) Achermann, M.; Petruska, M. A.; Kos, S.; Smith, D. L.; Koleske, D. D.; Klimov, V. I. Energy-transfer pumping of semiconductor nanocrystals using an epitaxial quantum well. *Nature* **2004**, 429, 642-646.

(417) González-Rubio, G.; Díaz-Núñez, P.; Rivera, A.; Prada, A.; Tardajos, G.; González-Izquierdo, J.; Bañares, L.; Llombart, P.; Macdowell, L. G.; Palafox, M. A. Femtosecond laser reshaping yields gold nanorods with ultranarrow surface plasmon resonances. *Science* **2017**, 358, 640-644.

(418) Le Ru, E. C.; Etchegoin, P. G. *Principles of surface-enhanced Raman spectroscopy: and related plasmonic effects*; 1st ed.; Elsevier: Amsterdam ; Boston, **2009**.

(419) Bain, C. D.; Whitesides, G. M. Formation of two-component surfaces by the spontaneous assembly of monolayers on gold from solutions containing mixtures of organic thiols. *J. Am. Chem. Soc.* **1988**, 110, 6560-6561.